On Modeling Elastic and Inelastic Polarized Radiation Transport in the Earth Atmosphere with Monte Carlo Methods

Von der Fakultät für Physik und Geowissenschaften

der Universität Leipzig

genehmigte

DISSERTATION

zur Erlangung des akademischen Grades

Doktor der Naturwissenschaften

Dr. rer. nat.

vorgelegt von Dipl.-Phys. Tim Deutschmann

geboren am 22. Juni 1979 in Lübeck

Gutachter: Prof. Dr. Manfred Wendisch
          Prof. Dr. Detlev Reiter
          Prof. Dr. Ulrich Platt

Tag der Verleihung 26. Januar 2015

Bibliographische Beschreibung

Deutschmann, Tim

On Modeling Elastic and Inelastic Polarized Radiation Transport in the Earth Atmosphere with Monte Carlo Methods

Universität Leipzig, Dissertation

158 S., 95 Lit., 68 Abb.

Referat

Das dreidimensionale Monte Carlo Strahlungstransportmodell McArtim wird um die Simulation der Ausbreitung polarisierter Strahlung und inelastischer Streuung, der Rotations-Raman-Streuung, der Ursache des sogenannten Ring-Effekts erweitert. Mit der jetzt dadurch genügend genauen Berechenbarkeit des Ring Effekts entstehen neue Möglichkeiten in der optischen Absorptionsspektroskopie. Für die Berechnung kommt die Methode des sogenannten 'importance samplings' (IS) zum Einsatz. Damit erhält man von einem Monte Carlo Photonen-Trajektorienensemble je eine Intensität mit elastischer Aerosol-, Cabannes- sowie inelastischer Rotations-Raman-Streuung (RRS) und gleichzeitig eine Intensität, die die Rayleigh-Streuung als elastischen Streuvorgang behandelt. Durch die Kombination beider Intensitäten erhält man das filling-in (FI, engl. für das Auffüllen von Fraunhoferlinien) als das Maß der Stärke des Ringeffekts mit der gleichen relativen Genauigkeit wie die der Intensitäten selbst. Die Validierung der Polarisation und des Ringeffekts geschieht durch Vergleich mit teilweise veröffentlichten Ergebnissen anderer Strahlungstransportmodelle.

Desweiteren wird die Diskretisierung des optischen Gebiets in Gitterzellen erweitert, indem die Gitterzellen beliebig zu sogenannten Klustern, also Gitterzellaggregate, zusammenfügbar gemacht werden. Das Programm kann dadurch Ableitungen von radiometrisch zugänglichen Größen, nämlich den Intensitäten an bestimmten Orten des atmosphärischen Strahlungsfeldes und den den Orten zugeordneten Lichtweginte-grale von Spurengaskonzentrationen, den Ergebnissen der DOAS (engl. differential optical absorption spectroscopy) Methode, nach optischen Eigenschaften von Aerosolen und Gasen in zusammenhängenden räumlichen Bereichen berechnen. Die Ableitungen erster und zweiter Ordnung werden durch sogenannte Selbstkonsistenztests validiert. Diese Ableitungen ermöglichen die Inversion von dreidimensionalen Spurengas- und Aerosolkonzentrationsprofilen und ebnen den Weg hin zu optischer 3D Streulichttomographie. Ist ein derartiges tomographisches Inversionsschema auf spektrale Intensitäten basiert, ermöglichen die jetzt verfügbaren Ableitungen zweiter Ordnung die Berücksichtigung der Krümmung der Kostenfunktion und damit den Einsatz effizienter Verfahren.

Weiter wird der Einfluss der Instrumentenfunktion auf die Spektren analysiert um das Potential von DOAS mathematisch hinreichend genau erfassen zu können. Es stellt sich heraus, dass für eine weiter führende spektrale Analyse die detaillierte Kenntnis der Gerätefunktion notwendig ist.

Abschließend wird die mathematische Trennbarkeit von schmalbandigen Absorptionssignaturen und dem Ringsignal von dem eher breitbandingen Einfluss der nahezu elastischen Streuprozesse in den Spektren demonstriert, was genau dem DOAS Prinzip entspricht. Dabei wird das differentielle Signal durch die vorgestellte IS Technik um etwa 4 Größenordnungen schneller erhalten als wie bisher durch separate Modellierung mit und ohne schmalbandige Strukturen. Dadurch rückt die Zusammenführung der getrennten Auswertestufen DOAS und die darauffolgende Strahlungstransportmodellierung in rechenzeittechnisch greifbare Nähe.

Bibliographic Description

Deutschmann, Tim

On Modeling Elastic and Inelastic Polarized Radiation Transport in the Earth Atmosphere with Monte Carlo Methods

University of Leipzig, Dissertation

158 ps., 95 cits., 68 Figs.

Abstract

The three dimensional Monte Carlo radiation transport model McArtim is extended to account for the simulation of the propagation of polarized radiation and the inelastic rotational Raman scattering which is the cause of the so called Ring effect. From the achieved and now sufficient precision of the calculated Ring effect new opportunities in optical absorption spectroscopy arise. In the calculation the method of importance sampling (IS) is applied. Thereby one obtains from an ensemble of Monte Carlo photon trajectories an intensity accounting for the elastic aerosol particle-, Cabannes- and the inelastic rotational Raman scattering (RRS) and simultaneously an intensity, for which Rayleigh scattering is treated as an elastic scattering process. By combining both intensities one obtains the so called filling-in (FI, which quantifies the filling-in of Fraunhofer lines) as a measure for the strength of the Ring effect with the same relative precision as the intensities. The validation of the polarized radiometric quantities and the Ring effect is made by comparison with partially published results of other radiation transport models.

Furthermore the concept of discretisation of the optical domain into grid cells is extended by making grid cells arbitrarily joining into so called clusters, i.e. grid cell aggregates. Therewith the program is able to calculate derivatives of radiometrically or spectroscopically accessible quantities, namely the intensities at certain locations in the atmospheric radiation field and the light path integrals of trace gas concentrations associated thereto, i.e. the product of the DOAS (differential optical absorption spectroscopy) method, with respect to optical properties of aerosols and gases in connected spatial regions. The first and second order derivatives are validated through so called self-consistency tests. These derivatives allow the inversion of three dimensional tracegas and aerosol concentration profiles and pave the way down to 3D optical scattered light tomography. If such tomographic inversion scheme is based solely on spectral intensitites the available second order derivatives allows the consideration of the curvature in the cost function and therefore allows implementation of efficient optimisation algorithms.

The influence of the instrument function on the spectra is analysed in order to mathematically assess the potential of DOAS to a sufficient degree. It turns out that the detailed knowledge of the instrument function is required for an advanced spectral analysis.

Concludingly the mathematical separability of narrow band signatures of absorption and the Ring effect from the relatively broad band influence of the elastic scattering processes on the spectra is demonstrated which corresponds exactly to the DOAS principle. In that procedure the differential signal is obtained by approximately 4 orders of magnitude faster then by the separate modelling with and without narrow band structures. Thereby the fusion of the separated steps DOAS spectral analysis and subsequent radiation transport modeling becomes computationally feasible.

Contents

<div align="right">

1

</div>

<div align="right">

Introduction

</div>

The assessment of some components of the atmospheric state being relevant to life on our planet is possible through measurements of radiometric quantities of its radiation field. Atmospheric radiation transport (RT) modeling (M) is the mathematical and numerical discipline of implementing the knowledge on the physics thereon into a computer model. The most important of the modeled quantities are the spectrally resolved intensity, actinic flux densities and heating rates being relevant to transformation of solar energy into other forms of energy (e.g. chemical or mechanical) and derivatives of these quantities with respect to parameters of the transport process as for example the absorption coefficient somewhere in the simulated domain or the optical properties of particle scattering. The measurement methods applied in this context are subdivided into remote sensing (or tele metric) and the in situ methods. These two groups are distinguished by the spatial relationship between the scientific object of investigation and the observer, where the observer is at the location of the object in the in situ methods and at a certain distance in the remote sensing methods. It can loosely be said that in situ method provide more point-like measurements of the field of properties and remote sensing provide large scale integral-like information. Central to the evaluation of remote sensing data is therefore the question of the spatial sensitivity of the measured radiometric quantity with respect to the field of properties under investigation. If the sun is used as a light source the method is called passive whereas if an artificial light is used the remote sensing method is called active.

1.1. Radiation Transport Modeling and Atmospheric State Inversion

Passive optical remote sensing in the UV/vis/NIR (UV: **u**ltra**v**iolet, vis: **vis**ible, NIR **n**ear **infra**red) established as a valuable measurement technique to infer information on the atmospheric state [Platt and Stutz, 2008, Wendisch et al., 2013, Ben-Dor et al., 2013]. In order to use radiometric quantities for the inversion of atmospheric state parameters [Tarantola, 2005, Rodgers, 2000], the entire physics of the measurement process must be modeled (see [Wendisch and Yang, 2012] for a comprehensive treatment of the underlying theory). This comprises the modeling of the large scale atmospheric radiation transport, small scale transport inside molecules [Witschas, 2012, Hollas, 2004, Haken and Wolf, 2006] and particles [Huffman and Bohren, 1983, Mishchenko et al., 2006] and then also modeling the measurement device. In this thesis dispersive optical spectrometers [Platt and Stutz, 2008] are in focus. Given certain discrepancies between model results and measurements may then have three origins: Knowledge uncertainty on the measurement device, on uncertainty on the atmospheric state and uncertainties on the physics of radiation transport modeling. Nowadays, the dominating uncertainty in the whole measurement process are the atmospheric state parameters. In order to infer them from systematic inter comparisons of simulations and measurements the forward model (i.e. the physical model) must *in principle* be able to model the measurements. Depending on the purpose of the modeling, different degrees of approximations in the atmospheric RT physics modeling can be made. See for example [Marshak and Davis, 2005, Davis and Marshak, 2010] for quantifying errors by reduction of RT in three spatial dimensions to RT in a horizontally homogeneous optical medium relevant for climate modeling. The standard degree of accuracy in describing the phenomenon of radiation transport has long been and likely still is the scalar monochromatic radiative transfer equation (RTE) which is phenomenologically deduced, but can be related to its physical foundation, the Maxwell equations e.g. [Mishchenko, 2002]. Relative spectroscopy bases on ratios of spectra and is motivated by the idea that inherent instrumental factors cancel in the ratios. When comparing measurements obtained therewith to results from standard RT codes aiming at solving the scalar RTE, relative differences in the order of 10^{-2} of the relative radiance accuracy appear, depending on the spectral resolution. It is well known that the neglect of the polarization state is one of the

sources responsible for these deviations (e.g. [Lacis et al., 1998]). These broad band deviations tend to be less important than another source of uncertainty ranging in the 10^{-2} to 10^{-3} order of magnitude, the so called Ring effect. Discovered in the 1960s by [Shefov, 1959, Grainger and Ring, 1962], the Ring effect spectrally appears as a filling in of structures in the extraterrestrial solar irradiance spectrum [Pallamraju et al., 2000]. Since [Kattawar et al., 1973] the filling is commonly explained by inelastic rotational and vibrational Raman scattering (RRS and VRS) processes at air molecules N_2 and O_2. Its physically correct modeling comprises still an obstacle on the way to fit residuals smaller then 10^{-4}. However, there is some agreement within the atmospheric radiation community that the RTE is able to entirely assess these effects and that it is only a matter of creating accurate numerical methods in order to create radiation transport models (RTMs) performing at the aforementioned accuracy level.

The mathematical description of the physics of radiation transport requires introducing elements from classical electrodynamics. Algorithms for the exact solutions of the Maxwell equations in the context of atmospheric radiation transport modeling have been put forward by [Mishchenko et al., 2006]. Since in the UV/vis/NIR spectral range at atmospheric scales (km) it is not necessary to account for interference effects, the particle nature and also the propagation of the photon spin of light dominates the description of its transport. The reduction of the Maxwell equations to the explicit description of the spin and particle nature is called the vector radiation transport equation (RTE) [Mishchenko et al., 2006].

1.2. Vector RTE Solution Methods

The classes of solution methods for the vector RTE can roughly be divided into groups of fast and nearly exact methods operating on a horizontally homogeneous (1D) optical media and the exact three dimensional Monte Carlo methods (except the RTM SHDOM [Pincus and Evans, 2009]) being able to deal with arbitrary spatial heterogeneity (3D). Based on the RTE, fast 1D solvers (e.g. [Stamnes, 1986, Spurr, 2006, Rozanov et al., 2005]) describe the radiation field by orthogonal spherical functions and solve the RTE by a single matrix inversion. The derivation of the matrix to be inverted requires relating the radiation field at different discrete locations "seeing" each other under discrete ordinates, therefore these methods are called discrete ordinate methods and have been invented by [Chandrasekhar, 1960]. A prominent representative of these methods is the DISORT method [Stamnes, 1986]. The tradition in Monte Carlo atmospheric radiation transport modeling which is subject of the thesis dates back to the pioneering work of [Marchuk et al., 1976] who applied methods developed in the field of neutron transport modeling to atmospheric radiation problems. Since Marchuk several codes being able to deal with the full complexity of three dimensional and polarized radiation transport have been written (inter alia RTMs published by [O'Hirok and Gautier, 1998, Mayer, B., 2009, Cornet et al., 2010, Deutschmann et al., 2011]) and inter compared [Cahalan et al., 2005]. Regarding the linearisation of the simulated quantities also [Marchuk et al., 1976] laid the foundation but only few Monte Carlo models exist (e.g. MCC++ from Oleg Postylakov [Postylyakov, 2004]) and [Deutschmann et al., 2011]) being able to provide derivatives of the radiance with respect to optical parameters of the atmosphere. Monte Carlo modeling of the Ring effect goes back to some early attempts by [Kattawar et al., 1973] and subsequent publications on approximate treatments [Joiner et al., 1995, Chance and Spurr, 1997]. Since then a fast approximate treatment of RRS implemented into the prior version of McArtim was published [Wagner et al., 2009] but no publications exist on accurate (i.e. exact) Monte Carlo modeling the Ring effect. Some discrete ordinate codes exist [Vountas et al., 1998, Kylling et al., 2010] but only [Landgraf et al., 2004] and [van Deelen et al., 2005] employing the doubling adding method [Liu and Weng, 2006] were able to deal even with multiple RRS.

1.3. Scope of the Thesis

The Monte Carlo RTM method presented in this thesis bases on the integral form of the RTE and is presented as a certain form of high dimensional Monte Carlo integration. Different Monte Carlo techniques especially the so called importance sampling method are applied to obtain new model quantities such as second order radiance derivatives and radiances including rotational Raman scattering leading to the Ring effect. Some improvements such as the cluster concept suitable for efficient inversion schemes and an effective way to calculate bulk optical properties of size distributions of spherical particles using Gustav Mie's theory [Mie, 1908] are presented. Further, the DOAS method and the revision of the separated application of DOAS and radiative transfer modeling for the subsequent interpretation of the DOAS results is focused. Overall the

availability of a RTM combining of the Ring effect, polarization modeling and three dimensionality may be regarded as an important requirement for UV/vis/NIR remote sensing.

1.4. Outline of the Thesis

The thesis begins with the introduction chapter 2 on the atmospheres structure and its gaseous and particulates constituents. Basic theory and physical and photo chemical processes needed to describe thermal and pressure structure are presented. The focus is on aerosol and cloud particles morphology and transformation processes. The objects described in Chapter 2 are then analyzed for their optical properties and relevance for describing radiation transport in the atmosphere. Thus, the following Chapter 3 starts with the physical fundament of radiation transport theory, the Maxwell equations, and especially the description of the polarization state of electromagnetic waves. As important elements of the transport process, scattering elastic and inelastic scattering, especially rotational Raman scattering on molecules is introduced. Then, particle scattering in the spherical approximation, which contains Rayleigh scattering in the asymptotic limit is described. The influence of the scattering on the polarization state in a single scattering event is discussed. The Chapter is concluded by motivating the governing integro differential radiative transfer equation RTE. Chapter 4 starts with introducing fundamental concepts in the Monte Carlo integration theory. After describing how random numbers can be used to estimate complicated 1D integrals, the Metropolis-Hastings algorithm as an important Monte Carlo method is introduced. The second half of the chapter is dedicated to the Monte Carlo method of the thesis, the sequential importance sampling method, which serves as a radiation field sampling algorithm. A single sample or estimate of the collision density (directly related to the radiation field) is represented by a piece-wise linear path in the atmosphere where the connectors are scatter events. Such trajectories are used to obtain functionals of the polarized radiation field and their first and second order derivatives with respect to optical properties of the atmosphere which is discussed in Chapter 5. The chapter is concluded with results from validation exercises. Especially derivatives and polarization effects are evaluated. Chapter 6 is a mathematical analysis of the method of optical absorption spectroscopy. Both instrumental and modeling requirements for the detection of fine structures of signatures of weakly absorbing gases are discussed. The concept of cellular or cluster sensitivities is introduced from linearisation of the logarithm of the spectrum with respect to the number density of a trace gas. Chapter 7 the achieved improvements in the modeling of polarization and inelastic radiation transport caused by rotational Raman scattering are applied to simulate the Ring effect. Modifications of the path generation scheme are derived from the modified version of the RTE including inelastic scattering. Since the Ring signal which appears spectrally as a relative difference between radiances with and without RRS, is an effect in the order of 10^{-2} to 10^{-3} and thus MC modeling of the difference is unfeasible in reasonable time, therefore the importance sampling method is used in order to obtain the Ring signal from a single model run. Modeled Ring signals are validated through comparison with a discrete ordinate radiation transport code. Comparison to measurements are unfortunately unpleasing due to instrumental calibration uncertainties. The chapter is finished by the investigation of the strength of the Ring effect in the components of the Stokes vector. In the final Chapter 8 the technique of importance sampling is applied in order to numerically obtain the fraction of the radiance attributed to rotational Raman scattering and absorption which to significant extent cause the differential signal in measured UV/vis skylight spectra.

<div align="right">

2

</div>

Thermodynamic State and Composition of the Earth's Atmosphere

This chapter is dedicated to the chemical, dynamic and thermodynamic state of the Earth's atmosphere as far as it is relevant for understanding radiation processes therein. There is a strong coupling between the atmospheric thermal structure (giving names to vertical atmospheric segments) and gravitation, molecular diffusion and large scale air parcel transport and radiation processes. The thesis merely focuses on radiation processes taking place within a time frame of $t \approx 1 \cdot 10^{-3}s$ which is the time light needs to travel approximately 300km. This is approximately the time a single solar photon needs to intrude and interact with the atmosphere until it becomes part of the thermal equilibrium of the Earth system or exits the atmosphere without absorption. Many details of the atmospheric circulation patterns can only be assessed on time scales much larger than t. The thesis studies radiation processes in a temporal "snapshot" version of the atmosphere, i.e. the time dependence is dropped.

The chapter begins with an overview on the molecular composition of the gaseous atmosphere and the thermal vertical structure resulting from the interaction of the radiation with molecular constituents related to oxygen. The section is followed by discussing roughly abundances and dynamics of particulate solid or liquid suspensions of matter (known as aerosols and clouds) in the gas atmosphere. The knowledge discussed here is based on the books [Rödel, 2000], [Schwabl, 2004] and [Rogers and Yau, 2000].

2.1. General Structure

In this section the vertical atmospheric structure in terms of pressure and temperature is discussed. Once these quantities are known or given the molecular scattering and absorption cross sections can be related to number densities derived from the ideal gas law as long as the thermodynamic equilibrium is conserved. The second important aspect for radiative transfer (RT) modeling are the phases of water together with abundances of solid suspensions of matter known as aerosols.

2.1.1. Chemical Composition of the Gas Phase

Tab. 2.1 shows the volume abundances of molecules in the gaseous and mixed atmosphere. The table is ordered according to molecular volume mixing ratios (VMRs). Throughout the planetary layer the relative VMRs can change. In the troposphere and the stratosphere the VMRs can be assumed constant because there are turbulent mixing processes. The current chemical composition according to Tab. 2.1 can be regarded as the result of a long term (billions of years) and complex interaction of the biosphere, the oceans with its currents and glaciers, the Sun activity, Earth's rotation, gravitation and topology, volcanic and astronomical events such as asteroid impacts.

2.1.2. The Troposphere, Temperature and Pressure Vertical Structure

Gravitation and solar radiation in combination with the chemical composition can be regarded as determining the pressure and temperature profile $p(z)$ and $T(z)$ of the atmosphere. Absorption and the inelastic scattering processes are the main contributors to the radiation induced change of the energetic state of molecules and therewith of the temperature. For example the hard solar UV radiation leads to photo dissociation of oxygen

Name	Symbol	Abundance (ppmv)
Nitrogen	N_2	780,840
Oxygen	O_2	209,460
Argon	Ar	9,340
Carbon dioxide	CO_2	394.45
Neon	Ne	18.18
Helium	He	5.24
Methane	CH_4	1.79
Krypton	Kr	1.14
Hydrogen	H_2	0.55
Nitrous oxide	N_2O	0.3
Carbon monoxide	CO	0.1
Xenon	Xe	0.09
Ozone	O_3	0.0 to 0.07
Nitrogen dioxide	NO_2	0.02
Iodine	I_2	0.01
Ammonia	NH_3	trace

Table 2.1.: Composition of the gaseous atmosphere. Carbon dioxide, NOAA Earth System Research Laboratory, updated 2012.03. Methane, IPCC TAR Table 6.1. H_2O is not contained in the table its abundance is ~0.40% over full atmosphere, typically 1%-4% at surface
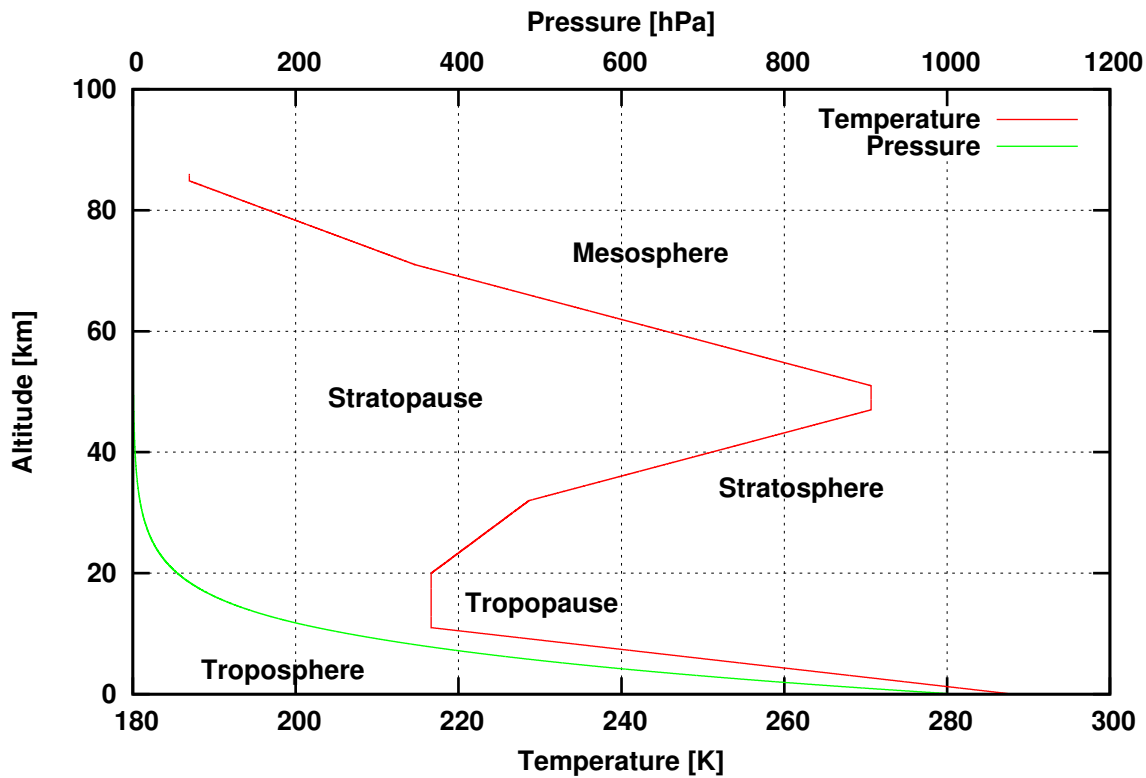
Figure 2.1.: US standard atmosphere 1976.

molecules. The molecules recombine to ozone molecules and the ozone layer forming an effective UV radiation barrier and causing thermal deposition of solar radiation energy in the stratosphere. In thermodynamic equilibrium, an air parcel of volume V in altitude layer z obeys the ideal gas equation

$$p(z)V = RT(z). \tag{2.1}$$

Fig. 2.1 shows the temperature and pressure profile according to the US standard atmosphere 1976 (U.S. Government Printing Office, Washington, D.C., 1976).

2.1.2.1. Hydrostatic Equation

The exponential shape of the pressure profile is the consequence of the balance between the force $F_p = pA$ resulting from the pressure p of an air parcel of volume $dV = A\,dz$, vertical extension dz and horizontal cross section A, and the gravitation force $F_g = -Mg$ where g is the gravitational acceleration (assumed constant in the atmosphere) and the integrated air mass above the air parcel. The differential form of the hydrostatic equation is found by considering infinitesimally small differences $dF_g = -\rho(z)A\,dz g = dF_p = dpA$

$$dp = -\rho_m(z)g\,dz = -p\frac{Mg}{RT}\,dz, \tag{2.2}$$

where the mass density ρ_m was replaced using the ideal gas equation and the molar mass of an air parcel (calculated according to Tab. 2.1). The pressure profile is found by inserting the ideal gas Eq. (2.1) into Eq. (2.2).

$$\frac{dp}{p(z)} = -\frac{Mg}{RT(z)}\,dz. \tag{2.3}$$

Since $T(z)$ varies with altitude z, integrating the differential hydrostatic equation solely is not a trivial task. However, when assuming approximately constant temperature $\overline{T}$ (obtained from more or less sophisticated averaging) the exponential form of the pressure profile becomes obvious by integrating the simplified equation:

$$p(z) \approx p_0 \exp\left(-\frac{Mgz}{R\overline{T}}\right). \tag{2.4}$$

Natural deviations from this law can be explained by variation in the water vapor concentration profile and variations in the temperature profile (radiative heating and latent heat release in phase transitions of water).

2.1.2.2. Adiabatic Temperature Profile

In order to understand the vertical variation of the temperature, a fictitious "dry" (without water vapor) air parcel is lifted slowly from the ground upward. The process is adiabatic because no heat is exchanged with the environment (i.e. $dQ = 0$ in the first principle of thermodynamics $dU = dQ + dW$). Therefore, as the parcel assumes its thermodynamic equilibrium, kinetic energy (described by the Maxwell-Boltzmann distribution) is transformed into gravitational potential energy and the parcel consequently cools down:

$$dU = dW \leftrightarrow C_v\,dT = -p(z)\,dV. \tag{2.5}$$

The work (right side) is obtained from the total differential of the ideal gas equation. Together with $C_p = R + C_V$ and by eliminating the volume using again the ideal gas equation one arrives at

$$\frac{dT}{dp} = \frac{RT}{C_p p} = \left(\frac{\kappa - 1}{\kappa}\right)\frac{T}{p}, \tag{2.6}$$

with the isentropic exponent $\kappa = C_p/C_V$. Eq. (2.6) is already the adiabatic temperature gradient. Using the differential hydrostatic equation Eq. (2.3) the gradient is expressed in terms of change of altitude dz:

$$\Gamma = \frac{dT}{dz} = -\frac{Mg}{C_p} \tag{2.7}$$

where Γ is called *dry adiabatic lapse rate*. Numerical values for dry air in the lower troposphere are $\Gamma \approx -0.981 K \cdot 100m^{-1}$. Eq. (2.6) can be integrated to obtain the following form:

$$\kappa \log{(T)}|_{\Theta}^{T} = (\kappa - 1)\log{(p)}|_{p_0}^{p} \leftrightarrow \Theta = T\left(\frac{p}{p_0}\right)^{\frac{\kappa - 1}{\kappa}}. \tag{2.8}$$

The expression $\Theta = T_0$ is called *potential temperature* and can be related directly to entropy. In regions with constant entropy (i.e. constant Θ) only reversible state changes take place (i.e. $dQ = 0$ and no phase transitions).
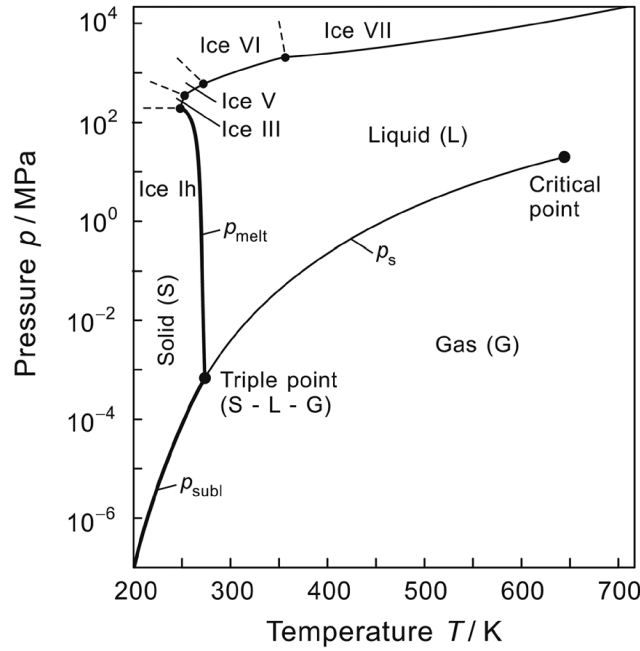
Figure 2.2.: Phase boundary curves of water in a *p-T* diagram. In order to obtain a reasonable pressure scale in this figure, the sublimation-pressure curve psubl was truncated at 200 K. Figure and caption from [Wagner et al., 2011].

2.1.2.3. Moist Lapse Rate and Water Phase Transitions

An air parcels thermodynamic "behavior" changes when water vapor is contained. Dalton's law states that the total pressure of a gas is the sum of the partial pressures of the gases constituents. Each of these constituents has in principle gas, liquid and solid phases. In the Earths atmosphere only water shows phase transitions. Fig. 2.2 shows the phase boundary curve diagram of water [Wagner et al., 2011]. The diagram is based on the assumption that the phase interface is plane and infinitely extended. The occurrence of phases depends on temperature and pressure. The state of the parcel corresponds to a point in the phase diagram Fig. 2.2. If the change in state variables of the air parcel implies crossing a phase boundary, a phase transition happens. Thus, if water vapor is contained in an atmospheric air parcel, a spatial displacement or mixing with parcels of different water content or state (e.g. of colder temperature) can lead to a phase transition of the gas phase into the liquid or solid (ice) phase. The condensation process depends on the saturation ratio

$$S_{v \leftrightarrow l|s}(T) = \frac{p_{H_2O}}{p_{H_2O, v \leftrightarrow l|s}(T)} \tag{2.9}$$

of the partial pressure of water vapor p_{H_2O} to the water saturation vapor pressure $p_{H_2O, v \leftrightarrow l|s}(T)$ ($v \leftrightarrow l|s$: vapor phase $\leftrightarrow$ liquid or solid phase) and on the occurrence of condensation nuclei CN, which are particles that tend to accumulate water molecules In the atmosphere, such CN can be regarded as omnipresent, such that condensation sets on once $S_{v \leftrightarrow l|s}(T) > 1$. The opposite process, evaporation, happens if $S_{v \leftrightarrow l|s}(T) < 1$. In order to evaporate liquid or solid water entirely into the gas phase a certain specific amount of energy, the *latent heat* $L(T) = Q_l - Q_v = \Delta Q$ is needed. It is called latent because the energy is deposited in the vapor phase and can be released again in a condensation process. $L(T)$ is obtained by integrating the first law of thermodynamics at constant pressure $p = p_{H_2O, v \leftrightarrow l|s}(T)$ and temperature:

$$L(T) = T \int_{Q_v}^{Q_l} \frac{dQ}{T} = \int_{U_v}^{U_l} dU + \int_{V_v}^{V_l} p \, dV. \tag{2.10}$$

The resulting integral can be sorted to phases 1 and 2:

$$G_v = U_v + p_{H_2O, v \leftrightarrow l|s}(T)V_v - TS_v = U_l + p_{H_2O, v \leftrightarrow l|s}(T)V_l - TS_l = G_l \tag{2.11}$$

The thermodynamic potential represented by both sides of the integral is called *Gibbs free energy G*. Homogeneous substances, as for example the vapor and the liquid phase, obey the so called *Gibbs-Duhem relation*

$$U = TS - pV + \mu N, \tag{2.12}$$

where μ is the so called *chemical potential* per molecule which originates from the molecular electronic, vibrational and rotational energies. Consequently, the Gibbs free energy of each phase can also be expressed by

$$G = \mu N. \tag{2.13}$$

The total differential of Eq. (2.11) for one phase is

$$dG = dpV - dTS \tag{2.14}$$

where the first law was used to eliminate dU. Equating the changes of $G_{1|2}$ for both phases $dG_v = dG_l$ in equilibrium, yields the *Clausius-Clapeyron* equation

$$\frac{df_{H_2O, v \leftrightarrow l|s}(T)}{dT} = \frac{S_l - S_v}{V_l - V_v} = \frac{L}{T(V_l - V_v)} \tag{2.15}$$

and relates the slope of the phase boundary curve (see Fig. 2.2) to the release of latent heat per phase volume difference times temperature. Explicit parametrizations of the phase boundary curves are found by integrating Eq. (2.15). First approximations are found by assuming $L = const.$, using the ideal gas equation and neglecting the liquid or solid volume (i.e. $V_l \gg V_v$). More sophisticated approximations consider the temperature dependence of the latent heat. For practical purposes, the so called *Magnus formulae* yield numerical values of $p_{H_2O, v \leftrightarrow l|s}(T)$ with an accuracy of a few per mill. As a result of phase transitions the dry adiabatic temperature gradient Γ is modified. The additional heat released in a condensation or resublimation process, lowers the vertical dry adiabatic temperature gradient Γ. The modified expression for Γ_{moist} is found by considering $L = \Delta Q$ in the derivation. Typical values of Γ_{moist} in the temperature range 0°C to 10°C are $\Gamma_{moist} \approx 0.5 K \cdot 100 m^{-1}$ i.e. half as much as the dry adiabatic gradient [Rödel, 2000].

2.1.3. The Stratosphere

In the course of discussing the thermal vertical structures, the processes causing the tropospheric temperature gradient were explained. The adiabatic temperature profile was obtained by assuming $\delta Q = 0$. Due to condensation processes the latent heat release decreases the temperature gradient. Above the tropopause region radiative heating increases the entropy of air parcels. Consequently the temperature gradient changes its sign in the stratosphere and becomes positive.

2.1.3.1. The Ozone Layer

The reason for the heating is absorption of ultraviolet radiation and transformation into unordered mechanical energy leading to increasing temperature in that region. The extraterrestrial solar irradiance is nearly that of a black body (see Fig. 2.3). Some of the high energetic ultraviolet radiation of the wavelength range 100nm to 210nm (*Schumann-Runge* bands and *Herzberg* continuum) (see Fig. 2.4) reaches the stratosphere and causes the photolysis of oxygen molecules [Chapman, 1930]:

$$O_2 + h\nu_{[100nm,210nm]} \rightarrow 2O, \tag{2.16}$$

these oxygen atoms have a relative short life time of seconds and recombine with oxygen molecules to form ozone:

$$O + O_2 + M \rightarrow O_3 + M^*, \tag{2.17}$$

where the asterisk indicates kinetic energy transferred to the molecule M. The ozone generated by the reaction (2.17) has a life time of minutes and forms an absorption barrier for ultraviolet Sun light of wavelengths 220nm to 320nm (*Hartley* bands):

$$O_3 + h\nu_{[220nm,320nm]} \rightarrow O_2 + O. \tag{2.18}$$
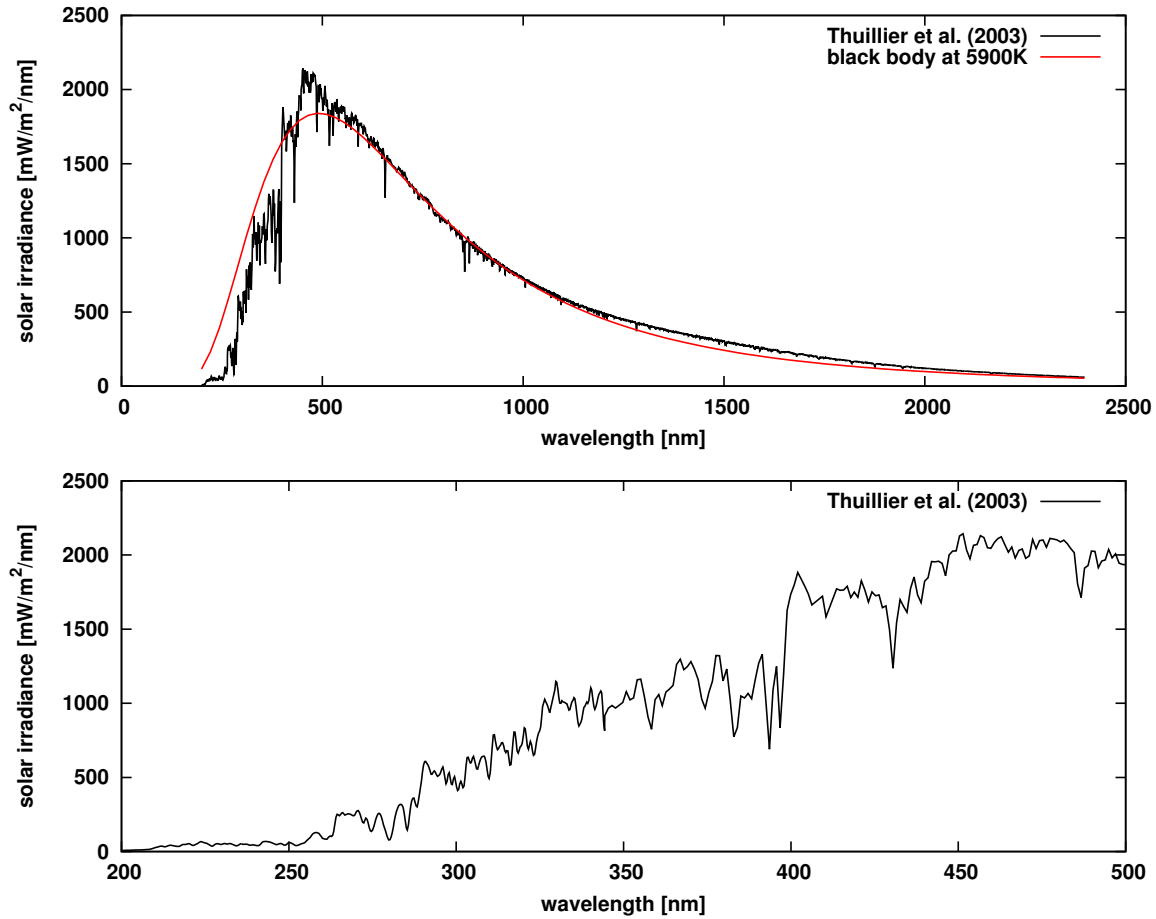
Figure 2.3.: Solar irradiance $F_0(\lambda)$ from [Thuillier et al., 2003]. Top panel: $200\,nm$ - $2400\,nm$, bottom panel: $200\,nm$ to $500\,nm$.

The other reaction [Chapman, 1930] considered as an ozone sink is the capture of a single oxygen atom and formation of two oxygen molecules:

$$O_3 + O \rightarrow 2O_2. \tag{2.19}$$

2.1.3.2. Stratospheric Ozone Sinks

These reactions found by [Chapman, 1930] could qualitatively explain the temperature profile and the existence of the ozone layer. However, observed stratospheric ozone concentrations where significantly smaller then predicted by the Chapman's model. In order to explain the discrepancies either additional sources of O_x must exist or chemical pathways that destroy ozone. Nowadays a couple of pathways are known that catalytically destroy ozone. A common type of a catalytic ozone destruction cycle is:

$$
\begin{align}
Y + O_3 &\rightarrow YO + O_2 \tag{2.20} \\
YO + O &\rightarrow Y + O_2 \tag{2.21}
\end{align}
$$

where for Y NO, OH, Cl or Br are prominent examples. NO_x has mostly natural sources, HO_x stems from tropospheric methane CH_4, hydrogen and also gaseous water and stratospheric halogens Cl and Br have mostly anthropogenic sources, as for example the famous chlorine, flour and carbon (CFC) species. Since the ozone layer and its UV absorbing capabilities are of great importance to human health e.g. [Norval et al., 2007], ozone depleting substances are in focus of atmospheric research. The reader interested in more details on the atmospheric scientific details is referred to [Seinfeld and Pandis, 2006].
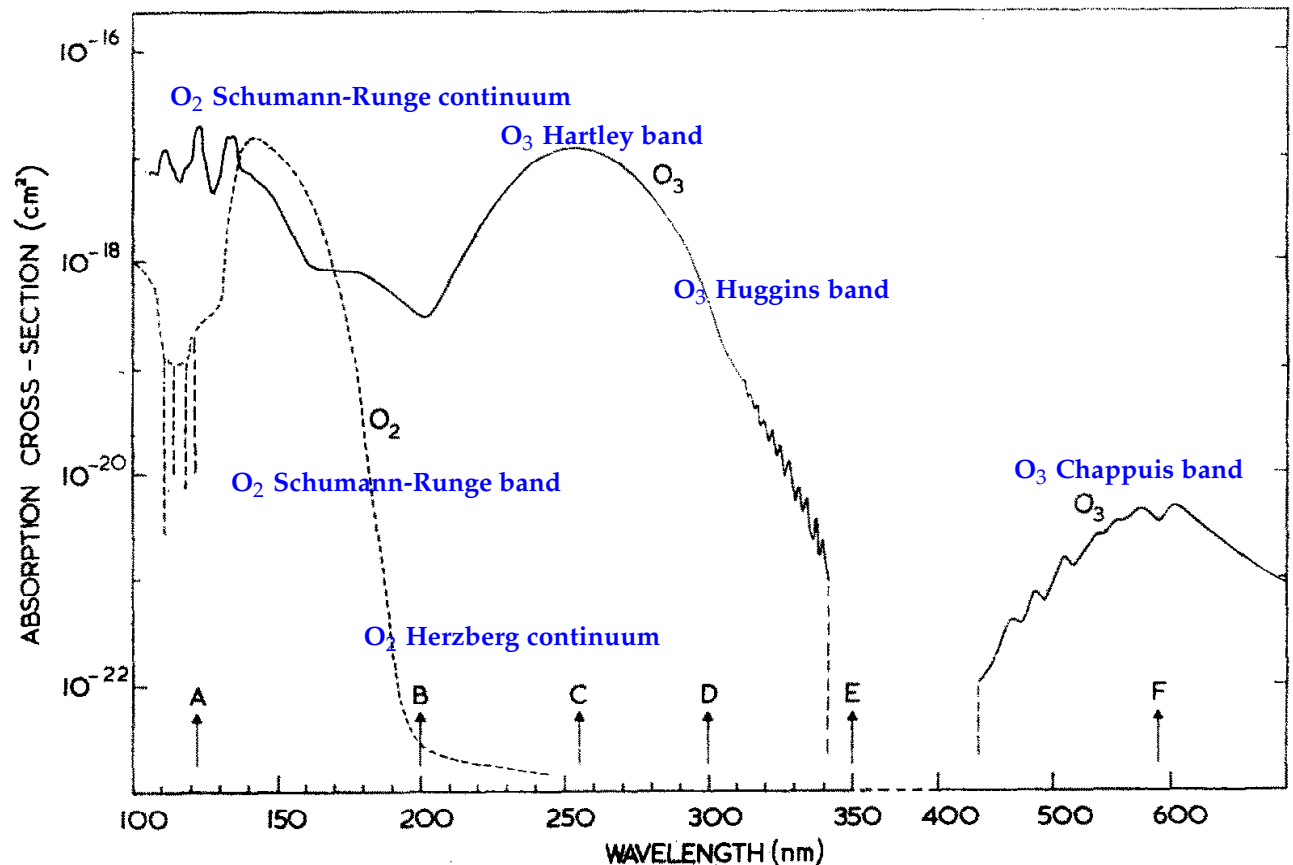
Figure 2.4.: Oxygen and Ozone absorption features in the UV/vis spectral range associated with their respective names. The fine structure of the O_2 Schumann-Runge band is suppressed in the figure. Plot without blue labels reproduced from [Thomas and Bowman, 1969].

2.2. Aerosols and Clouds

The most important physical aspects of aerosol and cloud particles with respect to their bulk optical properties are their size distribution, shape spectra and the average complex refractive index. The knowledge summarized here is presented in more detail in [Hoffmann et al., 2007, O'Dowd et al., 2012, Gilardoni et al., 2011, Guo et al., 2010]. For a global climatology of aerosol vertical profiles the reader is referred to [Clarke and Kapustin, 2010].

2.2.1. Classification and Morphology

Aerosol particles are discriminated into primary aerosol particles that are mechanically injected into the atmosphere and secondary particles that form within the atmosphere. *Primary aerosol particles* have numerous sources and are subdivided into three primary groups:

- Organic particles. Emission from plants such as pollen, spores and organic material originating from decomposition processes (see Fig. 2.6).

- An-organic particles:

    a) Mineral dust particles, as for example sand or clay or originating from erosive processes. These particles chemically consist of elements of the Earth, i.e. silicon, aluminium, iron and calcium, see Fig. 2.10.

    b) Sea salt and spray. The oceans are emission sources of these liquid and solid particles. Rising bubbles in sea water produce droplets when the reach the sea surface. Coastal winds carry sea salt particles inland.

Panel a (left)

Element	Weight%	Atomic%
C	38.91	54.62
O	24.42	25.74
Si	14.86	8.92
Al	4.15	2.59
Na	2.26	1.66
S	2.96	1.55
Ca	3.60	1.51
Cl	3.13	1.49
Fe	4.28	1.29
K	1.43	0.62

Panel a (right)

Element	Weight%	Atomic%
O K	21.60	34.50
Na K	2.51	2.79
Al K	9.92	9.39
Si K	47.58	43.28
K K	5.15	3.37
Ca K	3.42	2.18
Fe K	9.82	4.49

Panel b (left)

Element	Weight%	Atomic%
C	46.88	59.20
O	31.58	29.94
Si	11.07	5.98
Cl	3.01	1.29
Al	2.06	1.16
Na	1.27	0.84
Mg	0.78	0.48
Fe	1.57	0.43
Ca	1.08	0.41
K	0.71	0.28

Panel b (right)

Element	Weight%	Atomic%
C K	54.40	63.88
O K	36.09	31.82
Na K	1.69	1.04
Mg K	0.43	0.25
Al K	0.26	0.14
S K	3.70	1.63
Cl K	0.91	0.36
Ca K	2.51	0.88

Panel c (left)

Element	Weight%	Atomic%
O	56.95	70.13
Na	8.52	7.30
Cl	11.25	6.25
Mg	6.59	5.34
Al	6.49	4.74
Si	5.66	3.97
K	2.71	1.36
Ca	1.83	0.90

Panel c (right)

Element	Weight%	Atomic%
O K	60.49	78.76
Na K	2.08	1.89
Al K	5.71	4.41
Si K	8.45	6.27
Fe K	23.26	8.68

Panel d (left)

Element	Weight%	Atomic%
C	37.13	47.34
O	44.13	42.24
Si	11.94	6.51
Al	3.41	1.93
Na	2.36	1.57
K	1.03	0.40

Panel d (right)

Element	Weight%	Atomic%
C K	15.21	22.82
O K	49.08	55.27
Na K	3.35	2.62
Al K	5.23	3.49
Si K	20.94	13.43
K K	1.40	0.65
Ca K	1.36	0.61
Fe K	3.43	1.11

Figure 2.5.: SEM images and tables of the chemical composition of ash particles of the Eyjafjallajökull volcano, [O'Dowd et al., 2012].

c) Volcanic ash, ash of natural fires and SO_2. SO_2 is actually a gas, but once dissolved in water, as it often happens in the surrounding of volcanoes, the hygroscopic property of $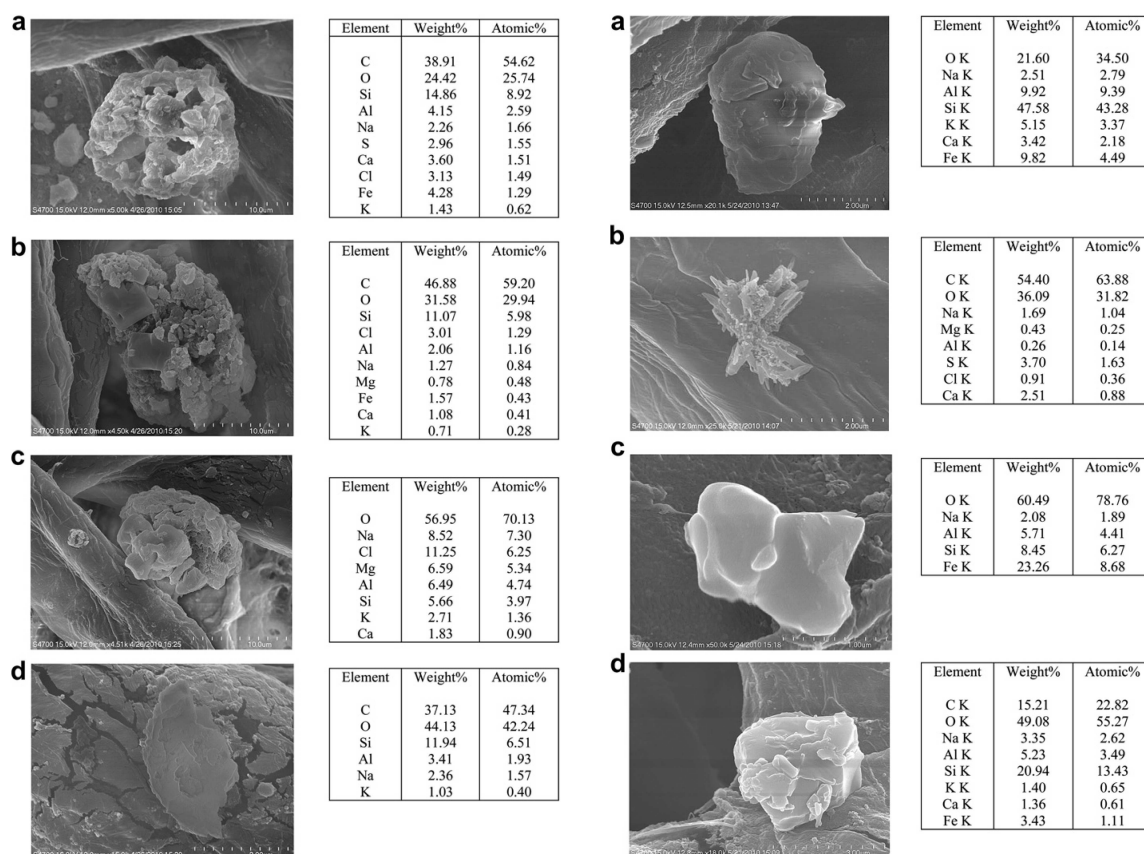SO_2$ triggers growth of particles. Volcanic activity around the world forms a permanent source of these particles. In large eruptions, volcanic aerosol can reach the stratosphere and influence the global radiation budget, see Fig. 2.5.

- Anthropogenic particles. The products of combustion processes of fossil fuels in turbines of air planes and car motors are the gases CO_2, H_2O, NO_x, C_xH_y, CO and SO_x and soot particles. The gaseous products dissolved in water act as condensation nuclei, see Fig. 2.6. Soot particles are often insoluble without modification, but act well as ice nucleation cores.

Secondary aerosol particles are result of the *gas-to-particle-conversion* and other transformation processes, see Fig. 2.7. The components of the particles may be organic or anorganic. Important anorganic constituent are water molecules H_2O and SO_2 that can react with atmospheric OH and a atomic oxygen to form the hygroscopic sulfuric acid H_2SO_4. The latter is of importance because it is able to chemically modify the surfaces of primary inert aerosol particles (e.g. soot) and make them therewith hydrophilic. Other gaseous particle precursor are ammonia NH_3 and nitric acid HNO_3. Organic gases are for example isoprene, mono- and sesquiterpene which are emitted by forests under strong solar radiation.

2.2.2. Water Related Particle Growth and Shrinking Processes

In this section the evolution of hydrophilic condensation nuclei is described. Much of the theory is related to cloud processing, but to some extent (depending on the saturation ratio) it applies also to aerosol particle processing. These processes depend on the chemical composition of the surrounding atmosphere and the particle. Later in the thesis particle optical properties (Chapter 3.2.4) are discussed which depend on the complex refractive index of the particle matter. The complex refractive index is related to the particle dielectric
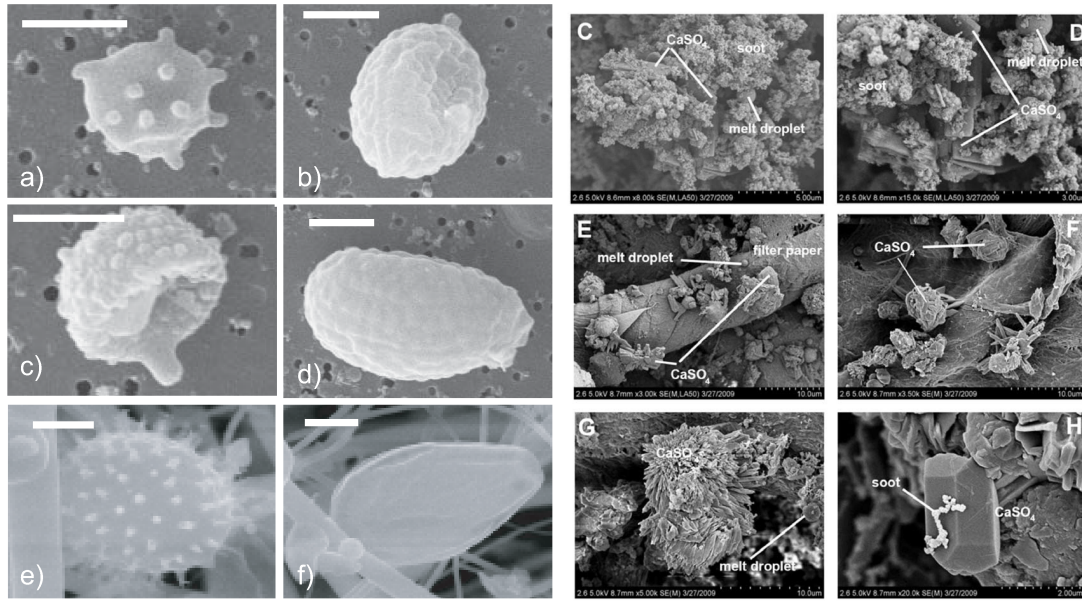
Figure 2.6.: SEM images of typical aerosol particles. Left panel (**a-f** from [Gilardoni et al., 2011]): primary biogenic aerosol particles found in the wet season over the amazon basin. The length of the white bar corresponds to $2\mu m$. Right panel (**C** to **H** from [Guo et al., 2010]): soot and ash aerosol particles with adsorbed sulfate crystals as a result of gas to particle conversion processes.
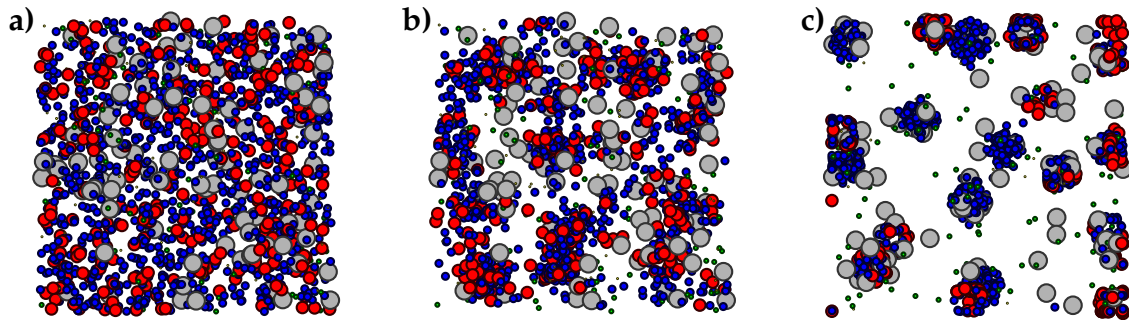
Figure 2.7.: Schematic for the nucleation process. Colors represent different molecule types. Panel **a**: molecules in the gas phase subject to Brownian motion, panel **b**: collisions form unstable clusters and panel **c**: formation of thermodynamically stable nuclei with sizes around a few *nm*.

properties (Chapter 3.2.2.1) and therewith depend on the chemical composition. In literature tables of refractive indices for pure substances (e.g. pure water or salt crystals) are given. In reality the complex refractive index is "a mixture" [1] of the refractive indices of the individual species and thus it is important to understand the microphysical mechanisms which cause the optical properties of the particles. In comparison with Section 2.1.2.3 the laws of phase transitions of water considering condensation and evaporation processes on atmospheric particles have to be modified. Differences arise due to the fact that the interface between the liquid and the gas phase is curved. According to [Pruppacher and Klett, 2010] the thermodynamic description can be done adding a surface energy term resulting from the surface curvature to the the second law. The curvature leads to in surface tension term which forms an energy barrier for condensing molecules of the gas phase. The consequence is that the saturation vapor pressure over curved surfaces is higher then over plane surfaces and increases with decreasing droplet radius (described by *Kelvin's* equation). Secondly, water is usually not present in pure form, but in solutions. Important solutes are sulfuric acid SO_4^{2-}, dissolved ammonia NH_4^+, nitric acid NO_3^-, different salts and also organic components as previously mentioned. The modification of $p_{H_2O,s}(T)$ due to the presence of these substances is called *Raoult's law*.

In the following discussion, it is assumed, that droplets or hydrophilic condensation nuclei defined by a

---

[1]this statement has to be treated with care, because the mixture is likely not additive with respect to volume or mass

Figure 2.8.: $\Delta G(r)$ for water at 20°C and different saturation ratios. The dashed line is the curve of the critical radii $\Delta G(r_*) = \frac{4}{3}\pi\sigma(T)r_*^2$.
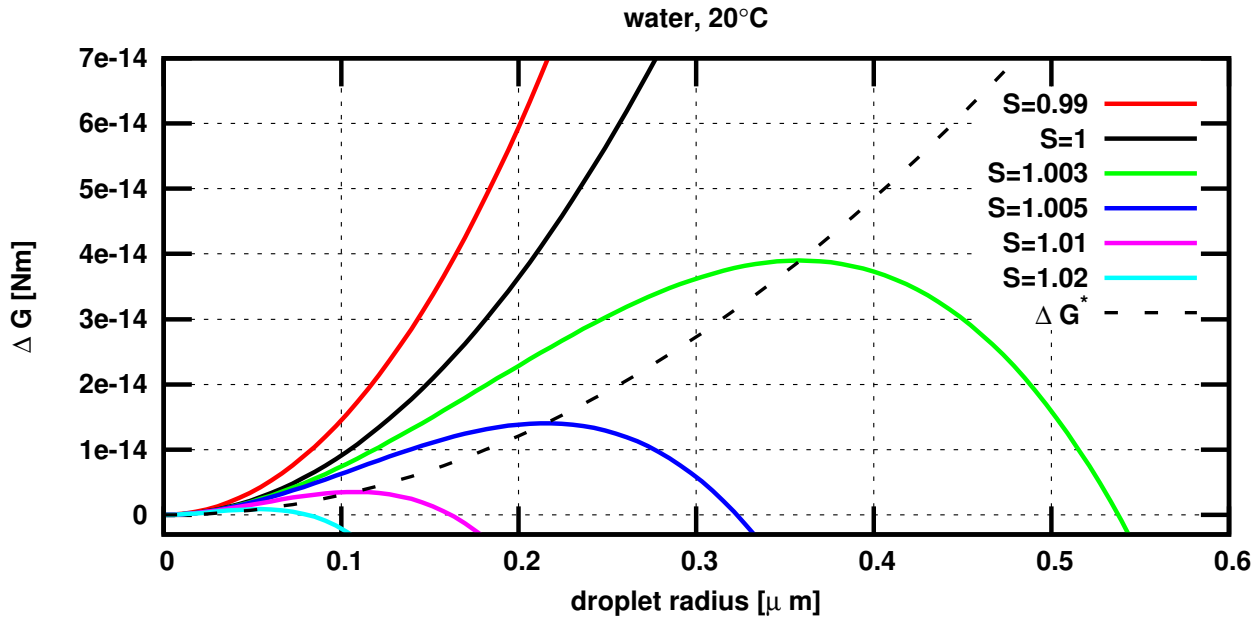
certain size distribution and chemical composition are already present. The formation of pure water droplets from the gas phase is called homogeneous nucleation and is up to now not entirely understood. Classical descriptions of homogeneous nucleation in the atmosphere suggest that this formation process is quite unlikely, since supersaturation of several hundred percent are required. In the presence of aerosol or ice particles, the so called heterogeneous nucleation takes place already at much lower supersaturations. Heterogeneous nucleation is considered to be the prevalent particle formation process in the atmosphere.

2.2.2.1. Kelvins Equation

In order to account for the liquid droplet curvature in phase transitions, an additional energy term $\sigma(T)A$ resulting from the work needed to form the droplet against the surface tension is introduced. $\sigma(T)$ is the so called surface energy in units $N \cdot m^{-1}$ or $J \cdot m^{-2}$ and $A = 4\pi r^2$ is the droplets surface. The temperature dependence of σ is nearly linear [Eötvös, 1886]. In order to derive the free enthalpy difference between the vapor phase and the liquid phase [Rödel, 2000] splits the transition into an adiabatic compression from the vapor volume to the volume of the liquid phase and the actual phase transition with the associated release of latent heat, balancing the work needed to compress the vapor. In a microscopic description, the transition happens because single vapor molecules with Maxwell-Boltzmann distributed velocities get stuck in the liquid phase, "depositing" their kinetic energy there. Consequently, the kinetic energy (the temperature) in the penetrating environment in the droplet rises and eventually single molecules are emitted back to the gas phase. In equilibrium, the rates of evaporation and condensation balance each other. Assuming a plane phase interface, the difference between the chemical potentials of the liquid and the vapor phase $\Delta G_{\text{plane}} = -N\Delta\mu_{\text{plane}}$ can be expressed by the work needed to isothermally compress N condensing H_2O molecules under environmental pressure p_{H_2O} to the saturation pressure $p_{H_2O,\,s}$

$$\Delta G_{\text{plane}} = -N\,\mathrm{d}\Delta\mu_{\text{plane}} = p\,\mathrm{d}V \overset{\text{i.g.e.}}{=} Nk_BT\frac{\mathrm{d}V}{V} \overset{pV=const.}{=} -Nk_BT\frac{\mathrm{d}P}{P}. \tag{2.22}$$

The absolute difference in the Gibbs free energy between the phases is found by integration:

$$\Delta G_{\text{plane}} = -N\Delta\mu_{\text{plane}} = -Nk_BT\ln\left(\frac{p_{H_2O}}{p_{H_2O,\,s}}\right) = -Nk_BT\ln\left(S_{v\leftrightarrow l|s}(T)\right). \tag{2.23}$$

If the molecules condense onto a spherical droplet of radius r and surface $A = 4\pi r^2$, the energy needed to form the droplet (the work to be done against the surface tension) is added to ΔG_{plane}:

$$\Delta G = -N k_B T \ln \left[S_{v \leftrightarrow l|s}(T) \right] + A\sigma \tag{2.24}$$

In terms of the droplet radius r ΔG becomes

$$\Delta G(r) = -\frac{4}{3}\pi r^3 \rho_{\text{H}_2\text{O,l}} k_B T \ln \left[S_{v \leftrightarrow l|s}(T) \right] + 4\pi r^2 \sigma \tag{2.25}$$

where the number density (number of molecules per volume) $\rho_{\text{H}_2\text{O,l}}$ was introduced. Fig. 2.8 shows ΔG for water at room temperature and different saturation ratios S. Equilibrium of vapor and liquid phase is assumed for a certain critical radius r_* for which the Gibbs energy difference assumes a maximum, i.e. $\frac{\text{d}\Delta G}{\text{d}r}\Big|_{r_*} = 0$:

$$r_* = \frac{2\sigma}{\rho_{\text{H}_2\text{O,l}} k_B T \ln \left(S_{v \leftrightarrow l|s}(T) \right)}. \tag{2.26}$$

Suppose, that a droplet with some radius r exists. According to Eq. (2.26) the pressure for which the droplet (i.e. the liquid in form of a sphere) is in equilibrium with the surrounding vapor is:

$$\frac{p_{\text{H}_2\text{O}, v \leftrightarrow l|s, r}(r, T)}{p_{\text{H}_2\text{O}, v \leftrightarrow l|s}(T)} = \exp \left(\frac{2\sigma}{r \rho_{\text{H}_2\text{O,l}} k_B T} \right). \tag{2.27}$$

This equation, the so called *Kelvin Equation*, shows that the saturation vapor pressure over liquid droplets is higher then over a plane phase interface. Furthermore, the saturation pressure increases with decreasing radius. In a water cloud or in an hygroscopic aerosol haze, the single particles radii show a certain distribution $\text{d}N_i / \text{d}r_i$. Relative to the surrounding pressure, each droplet i has a saturation ratio $S_i(T, r_i)$. For a certain pressure and temperature, a critical radius r_* in the radius distribution exists. Droplets i of radii smaller then r_* have higher saturation pressures, thus their saturation ratios fulfill $S_i(T, r_i) < 1$ which causes the droplets liquid to evaporate. Conversely droplets larger then r_* have lower saturation pressures such that their saturation ratios are $S_i(T, r_i) > 1$, i.e. these droplets will grow at the expense of smaller droplets. Another fact related to critical radii is that aerosol or cloud particles that are mechanically injected or formed through cloud processes (e.g. coalescence) and have super critical size will grow. Particles of super critical radii are therefore called *activated*.

2.2.2.2. Raoult's Law

The second modification of the saturation vapor pressure is due to solutes in the liquid stemming from the mother aerosol particle (e.g. sea salt, sulfuric or nitric acid). Suppose, the liquid phase of the particle consists of $N = N_0 + N_s$ particles where N_0 are number of solvent molecules and N_s is the number of solute molecules. *Raoult's Law* states that

$$\frac{p_{\text{solution}, v \leftrightarrow l|s, r}(r, T)}{p_{\text{H}_2\text{O}, v \leftrightarrow l|s, r}(r, T)} = \frac{N_0}{i N_s + N_0}. \tag{2.28}$$

i is the so called *van't Hoff factor* and accounts for the dissociation of the solute. NaCl or ammonium sulfate for example dissociate entirely, therefore a mole NaCl dissolves into two moles ions Na^+ and Cl^-, i.e. $i_{\text{NaCl}} = 2$. In dilute solutions $N_s \ll N_0$ and thus the right side of Eq. (2.28) can be developed into a Taylor series:

$$\frac{N_0}{i N_s + N_0} = \frac{N_0}{N_0 \left(1 + \frac{i N_s}{N_0} \right)} \approx 1 - \frac{i N_s}{N_0} = 1 - \frac{3 i N_s}{4\pi \rho_{\text{H}_2\text{O,l}} r^3}. \tag{2.29}$$

To give an example the saturation ratio as a function of droplet radius and N_s for the solute NaCl is plotted in Fig. 2.9. The graphs are called *Köhler curves*.

2.2.2.3. Transport and Size and Mass Population Dynamics

Some of the important particle formations process were discussed in previous sections. The role of reactive (organic or anorganic) gaseous constituents is twofold. First, by chance, molecules collide and form
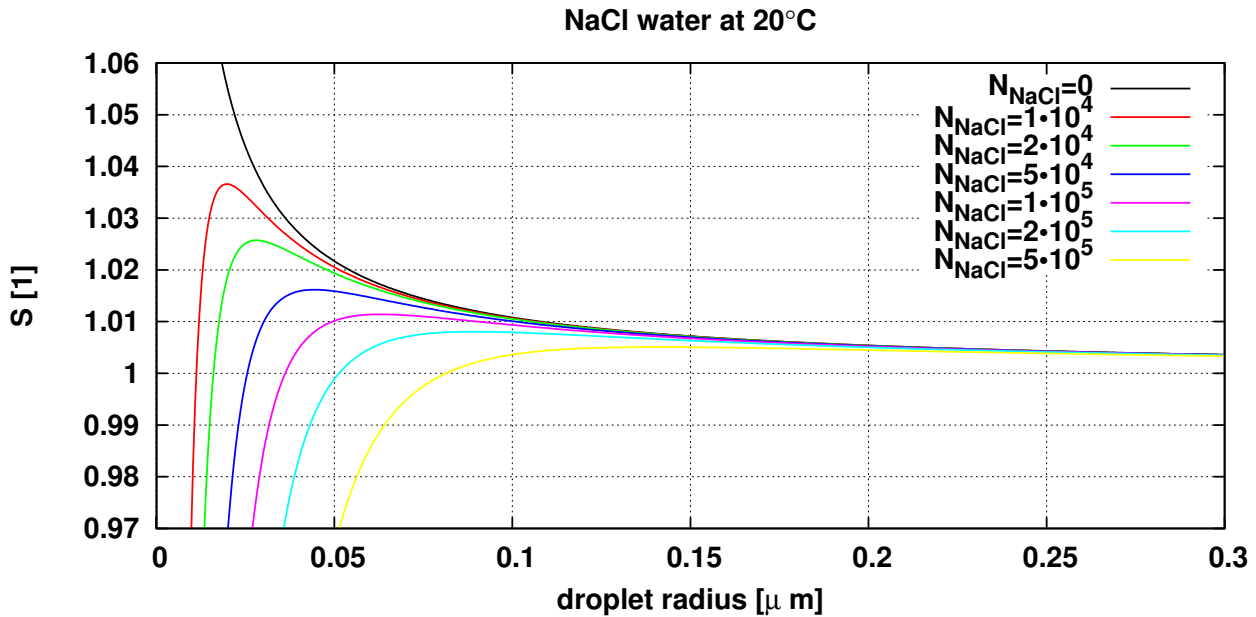
Figure 2.9.: *Köhler curves*, i.e. saturation ratio for NaCl-water solution droplets with different numbers of NaCl molecules dissolved.

thermodynamically stable and hydrophilic nuclei (secondary aerosol particles). Second, reactive gases chemically modify the surfaces of primary aerosol particles (this is called *aging*, see Fig. 2.10) and make them hydrophilic. If enough water vapor is present by chance these nuclei grow to the critical radius, become activated. With growing mass, the nuclei begin to sediment significantly. The more water these *cloud condensation nuclei* CCN collect, the more likely becomes CCN growth by collisions and coalescence. At the time heavier CCN sediment so fast that they fall down to altitudes with higher temperatures. So in this CCN size stage, evaporation competes with growth by condensation, collisions and coalescence. Furthermore the release of latent heat in the condensation causes the development of updrafts in the cloud. As one can imagine, the outlined processes are highly competitive and lead to complex particle trajectories.
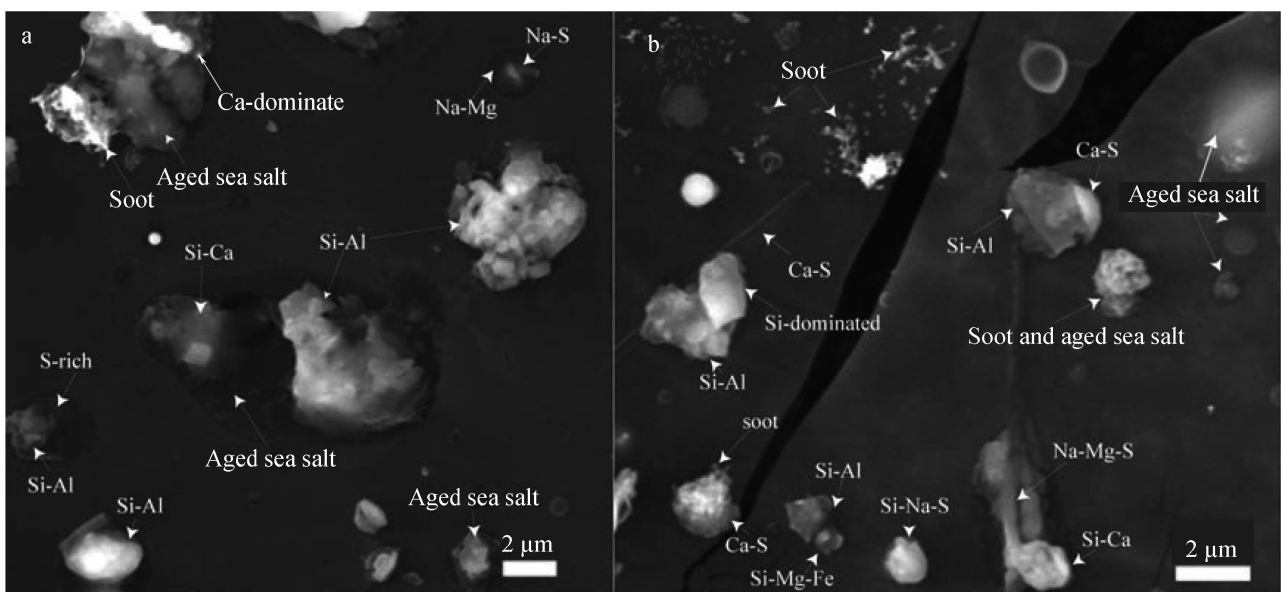
Figure 2.10.: Aged mineral, sea salt and soot aerosol particles over China. Images from [Li et al., 2010].

2.2.3. Size Spectra and Modes

The formation and transformation mechanism described earlier result in certain structures of the size spectra. Observed aerosol size spectra exhibit distinct size modes each of which can be described approximately by a log normal distribution [Seinfeld and Pandis, 2006]. The hole size distribution with M modes is a superposition of individual log normal distributions:

$$\frac{\mathrm{d}N}{\mathrm{dlog}\,(D)} = \frac{1}{\sqrt{2\pi}} \sum_{m=1}^{M} \frac{N_m}{\log\,(\sigma_m)} \exp\left\{ -\frac{1}{2} \left[\frac{\log\,(D) - \log\,(\overline{D}_m)}{\log\,(\sigma_m)} \right]^2 \right\}, \tag{2.30}$$

where the total number of particles in the respective mode m is N_m, the mean diameter is $\overline{D}_m$ and the width of the log-normal distribution is described by σ_m. The mean size of the mode depends on the respective processes and substances involved in the transformation processes. In literature different size ranges are given and thus only the naming and rough size specification is given in the following:

- Nucleation mode. Particles in the nucleation phase forming unstable molecular clusters.

- Aitken mode. Thermodynamically stable particles formed e.g. during gas to particle conversion and those with sizes around 10nm.

- Accumulation mode. Particles in the sub micrometer range that are subject to persistent growth processes and also to long range transport processes.

- Coarse mode. Large cloud particles or mechanically injected aerosols with sizes larger then $1\mu m$. An important sink for these particles is sedimentation.

In the thesis [Koponen, 2003] it is reported on measurements of particle size distributions. Fig. 2.11 shows examples for rural, maritime and continental aerosols. The continental and polluted air masses in Fig. 2.11 are traced back to coastal Africa. In these spectra Aitken and accumulation mode overlap representing therewith indications of transitions of Aitken mode particles to the accumulation mode. As it is stated in [Koponen, 2003], it is a typical feature of anthropogenic freshly polluted air masses. Spectra as in panel b, plot D with distinct mode features, are typical for cloud processing of remote marine boundary layer air masses. The air in (b,E) probably stems from continental Europe and passed a few days over the ocean. The total number of droplets is decreased in comparison with the spectra in panel a, probably due to dilution by entrainment (mixing with air masses of much lower particle concentrations). Panel b, F with a pronounced nucleation mode are typical for antarctic air masses.

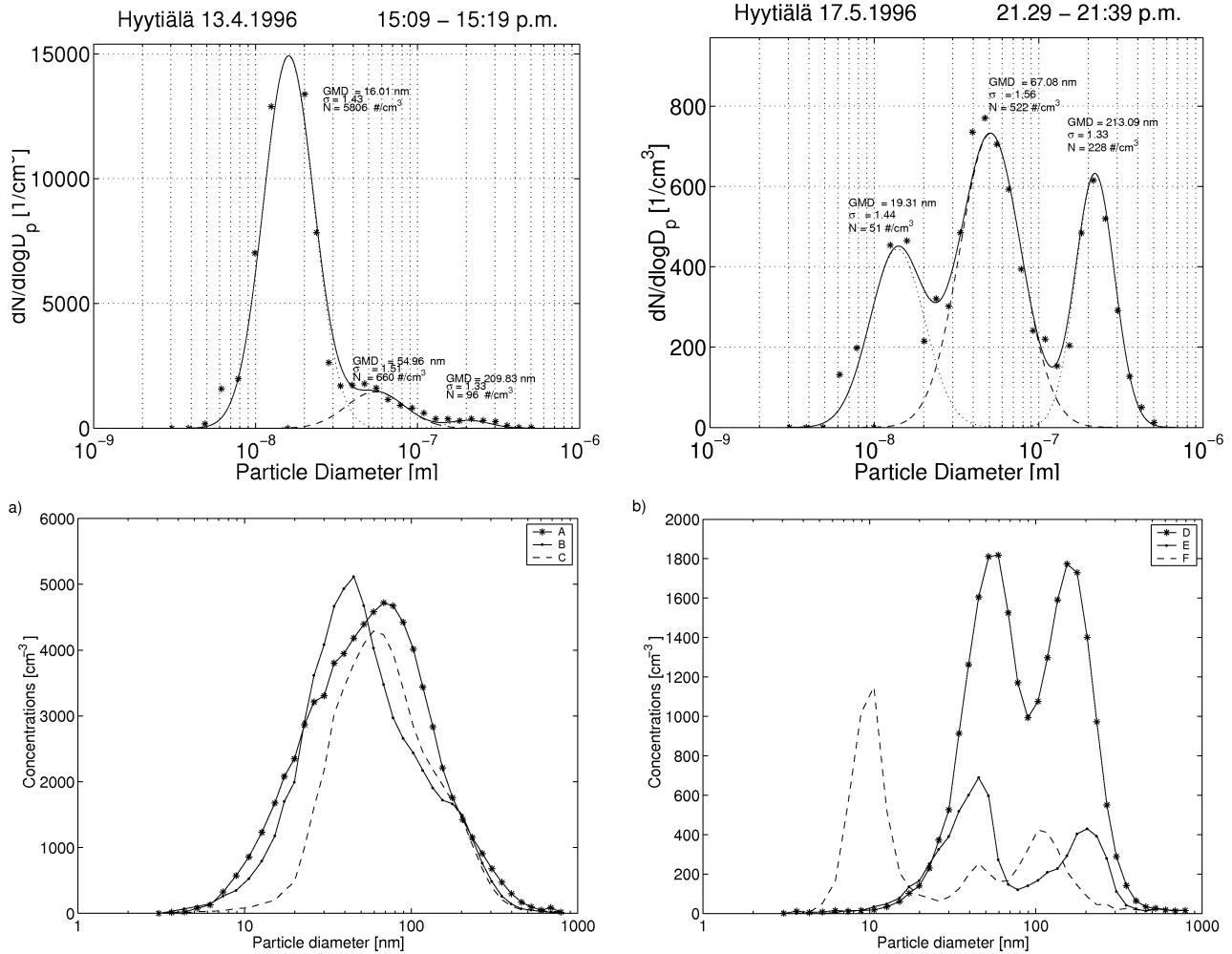Figure 2.11.: Top panel row: rural aerosol size distribution as measured in central Hyytiälä, Finland. Crosses are measurements, solid lines represent log-normal function fits to the data. Bottom panel row: continental aerosol (left, a), marine aerosol (right, b). The latitudes of the measurements are 50 N (for DSD A), 35 N (B), 7 N (C), 7 S (D), 25 N (E), and 55 N (F). Plots from [Koponen, 2003]

<p style="text-align: right; font-size: 3em; color: red;">3</p>

Radiative Transfer Theory

In this chapter some aspects of the physical and mathematical description of radiative transfer and the numerical treatment of problems in that context are presented. The description of the process is subdivided with respect to different spatial scales. On the outer scale the Maxwell equations form the basis, whereas regarding absorption (i.e. the wavelength of absorption lines) and also some molecular scattering processes like rotational and vibrational Raman scattering, also quantum mechanics needs to be taken into account.

The chapter is organized as follows. It begins with relevant considerations with respect to the interaction of radiation with molecular matter. After discussing the molecular processes it is proceeded to scattering on particles with dimensions larger than those of molecules. In that context, the quantum mechanical aspects are less important and the Maxwell equations dominate the description. A crude overview on numerical methods developed for the calculation of single scattering and absorption properties of particles and molecules is given. The chapter is concluded with the phenomenological deduction of the radiative transfer equation. For a more profound discussion the reader is referred e.g. to [Wendisch and Yang, 2012].

3.1. Electromagnetic Waves

In order to connect the theory presented in this chapter with the building of theoretical physics, the Maxwell equations are discussed in view of the relevant physics. Basis for the following derivations is a standard textbook on electrodynamics [Nolting, 1997].

3.1.1. Maxwell's Equations

Without the presence of free charges and currents Maxwell's equations describing the electric field $\vec{E}$ and the magnetic induction $\vec{B}$ are:

$$\begin{aligned} \vec{\nabla} \cdot \vec{E} = 0, \quad &\vec{\nabla} \times \vec{E} = -\dot{\vec{B}}, \\ \vec{\nabla} \cdot \vec{B} = 0, \quad &\vec{\nabla} \times \vec{B} = \epsilon \mu \dot{\vec{E}}. \end{aligned} \tag{3.1}$$

The dots over the fields symbolize taking the first derivative with respect to time, i.e. $\dot{\vec{X}} := \partial \vec{X}/\partial t$ and $\ddot{\vec{X}} := \partial^2 \vec{X}/\partial t^2$. The dielectric permeability ε and the magnetic susceptibility μ describe the electrical properties of the host medium in relation to the vacuum (index 0):

$$\varepsilon = \varepsilon_0 \varepsilon_r \quad \text{and} \quad \mu = \mu_0 \mu_r \tag{3.2}$$

In this introduction it is generally assumed, that ε_r and μ_r are scalars. Later in the chapter (Section 3.2.2), when describing the angular dependence of molecular scattering, ε_r is used as a tensor, describing therewith different electrical permeabilities parallel and perpendicular to the rotation axes of the diatomic molecules N_2 and O_2. Inserting the source-free Maxwell equations into each other leads to wave equations in the fields $\vec{E}$ and $\vec{B}$:

$$\Delta \vec{E} - \epsilon \mu \ddot{\vec{E}} \quad = \quad 0 \tag{3.3}$$

$$\Delta \vec{B} - \epsilon \mu \ddot{\vec{B}} \quad = \quad 0 \tag{3.4}$$

Homogeneous wave equations are generally defined as $\Delta \Psi - \frac{1}{u^2} \ddot{\Psi} = 0$ and motivate through comparison $(u^{-2} = \varepsilon_0 \varepsilon_r \mu_0 \mu_r)$ with the electromagnetic wave equations the introduction of the complex refractive index

$$n = \frac{c}{u} = \sqrt{\varepsilon_r \mu_r} \quad \text{where} \quad c = \frac{1}{\sqrt{\mu_0 \varepsilon_0}} \tag{3.5}$$

is the speed of light in the vacuum. In this work in particular the wavelength dependent refractive index $n(\lambda)$ of air is important in order to describe scattering on air molecules (Section 3.2.2). In the description of particle scattering (Section 3.2.4), the refractive indices of water and different solutes are used. As potential solutions of the wave equations in particular periodic functions

$$\vec{E}(\vec{r},t) = \vec{E}_0 e^{i(\vec{k}\vec{r} - \omega t)} \tag{3.6}$$

are investigated in the following. In Eq. (3.6), $\vec{k}$ is the so called wave vector oriented towards the propagation direction of the wave. $\vec{r}$ is the location and $\omega = 2\pi f$ is the waves angular frequency . Inserting Eq. (3.6) into Eq. (3.4) leads to the phase velocity

$$u = \frac{\omega}{k}. \tag{3.7}$$

Calculating the time integration of the curl of Eq. (3.6)

$$-i\vec{\nabla} \times \int_0^t \vec{E}(\vec{r},t)\,\mathrm{d}t = -i\vec{k} \times \vec{E}_0 \int_0^t e^{i(\vec{k}\vec{r} - \omega t)}\,\mathrm{d}t = \frac{1}{\omega}\vec{k}\vec{E}(\vec{r},t) \tag{3.8}$$

yields through comparison with the second Maxwell equation (going back to Faraday, induction law) the following relationship between the $\vec{E}$ and $\vec{B}$ fields

$$\vec{B}(\vec{r},t) = \frac{1}{\omega}\vec{k} \times \vec{E}(\vec{r},t). \tag{3.9}$$

It is thus sufficient to solve the inhomogeneous wave equation for $\vec{E}$ and apply Eq. (3.9) to obtain the magnetic induction $\vec{B}$.

3.1.2. Measurement of Electromagnetic Waves

Only effective values of the fields are measured, since it is often not possible or required to time-resolve the field oscillations. Furthermore, light is a mixture of plane waves of different frequencies and also different complex amplitudes. A natural electromagnetic wave can be constructed using the Fourier transformation. Time averaging is performed for the observable (real) parts of the complex fields $\vec{E}$ and $\vec{B}$. The electric field is expressed in Eq. (3.6). In view of calculating the energy flux density in terms of the Poynting vector

$$\vec{S} = \frac{1}{\mu}\vec{E} \times \vec{B}, \tag{3.10}$$

time averaging for the frequency-specific interval $2\pi/\omega$ yields [Nolting, 1997]:

$$\langle \vec{S} \rangle = \frac{1}{\mu}\frac{1}{\tau}\int_t^{t+2\pi/\omega} \Re(\vec{E}) \times \Re(\vec{B})\,\mathrm{d}t = \frac{1}{2\mu}\Re(\vec{E}_0 \times \vec{B}_0^*) \tag{3.11}$$

The $\vec{B}$ field amplitude $\vec{B}_0$ is obtained from Eq. (3.9):

$$\vec{B}_0 = \frac{1}{\omega}\vec{k} \times \vec{E}_0. \tag{3.12}$$

The time averaged Poynting vector is thus

$$\langle \vec{S} \rangle = \frac{1}{2\mu\omega}\Re(\vec{E}_0 \times \vec{k} \times \vec{E}_0^*) = \frac{1}{2\mu\omega}\Re(\vec{k}\cdot(\vec{E}_0 \cdot \vec{E}_0^*) - \vec{E}_0^*\cdot(\vec{k}\cdot\vec{E}_0)) = \frac{\vec{k}}{2\mu\omega}|\vec{E}_0|^2 \tag{3.13}$$

and describes the energy flux density of the EM wave. Resolved for wavelength $\langle \vec{S} \rangle$ has the unit $[W/m^2]$ (irradiance). In the derivation the product $\vec{k}\cdot\vec{E}_0$ vanishes because $\vec{E}_0$ is perpendicular to the propagation

direction $\vec{k}$. In the thesis the irradiance is used which is defined as follows:

$$F = \frac{k}{|\vec{k}|}\langle \vec{S} \rangle = \frac{k}{2\mu\omega}|\vec{E}_0|^2 \tag{3.14}$$

where $k = |\vec{k}|$.

3.1.3. Polarization State of EM Waves

Solutions in the homogeneous case are transverse waves, for which $\vec{E}$ and $\vec{B}$ are orthogonal to each other and to the propagation direction $\vec{k}/k$. It is customary (and it simplifies the equations) to restrict the considerations to the case $\vec{k} = k\vec{e}_z$, i.e. the wave propagates into the $\vec{e}_z$ direction of the coordinate system. With this simplification the electric field takes the following form:

$$\vec{E} = (E_{0x}\vec{e}_x + E_{0y}\vec{e}_y)e^{i(kz-\omega t)}. \tag{3.15}$$

Since E_{0x} and E_{0y} are complex numbers they can be expressed [Nolting, 1997] through

$$E_{0x} = |E_{0x}|e^{i\varphi} \quad \text{and} \quad E_{0y} = |E_{0y}|e^{i(\varphi+\delta)} \tag{3.16}$$

where φ is the angle of the E_{0x} in the complex number plane and δ is the angle (phase) difference between E_{0y} and E_{0x}. Depending on the exact choice of $|E_{0x}|$, $|E_{0y}|$ and δ linearly ($\delta = 0, \pm\pi$), circularly ($\delta = \pm\frac{\pi}{2}$, $|E_{0x}| = |E_{0y}|$) and elliptically polarized light is distinguished.

3.1.3.1. Linear Polarization Filters

In a measurement only time averaged characteristics of a field are determined. As a analysis tool polarization filters are used. Such a linear polarization filter can be seen as a projector $\vec{J}(\alpha)$. Its effect is mathematically described by the following expression:

$$\vec{J}(\alpha) = \cos{(\alpha)}\vec{e}_x + \sin{(\alpha)}\vec{e}_y. \tag{3.17}$$

For instance $\vec{J}(0)$ projects out electric field components in $\vec{e}_x$ direction and $\vec{J}(\frac{\pi}{2})$ projects the y component, see e.g. [Huffman and Bohren, 1983]. For other angles mixtures the E_{0x} and E_{0y} remain in the filtered light but with modified intensities. In order to analyze the effect of a polarizing filter for all possible orientations α, $\vec{J}(\alpha)$ is applied to Eq. (3.15):

$$\vec{J}_l(\alpha)\vec{E} = [\cos{(\alpha)}\vec{e}_x + \sin{(\alpha)}\vec{e}_y][E_{0x}\vec{e}_x + E_{0y}\vec{e}_y]e^{i(kz-\omega t)} \tag{3.18}$$

$$= [\cos{(\alpha)}E_{0x} + \sin{(\alpha)}E_{0y}]e^{i(kz-\omega t)}. \tag{3.19}$$

The EM wave behind the filter is again an EM wave which can be measured using its time averaged Poynting vector. According to Eq. (3.13) it is sufficient to calculate the absolute value of the field amplitude:

$$|\vec{J}_l(\alpha)\vec{E}|^2 = \cos^2{(\alpha)}|E_{0x}|^2 + \sin^2{(\alpha)}|E_{0y}|^2 + 2\sin{(\alpha)}\cos{(\alpha)}|E_{0x}||E_{0y}|\cos{(\delta)}. \tag{3.20}$$

It is therefore instructive to start with filters $\alpha = 0$ to obtain $|E_{0x}|$, $\alpha = \frac{\pi}{2}$ for $|E_{0x}|$ and then, for instance with choosing $\alpha = \frac{\pi}{4}$, to obtain $\cos(\delta)$. The irradiance which is measured after the linear polarizer is

$$F_l(\alpha) = \frac{k}{2\omega\mu}|\vec{J}_l(\alpha)\vec{E}|^2. \tag{3.21}$$

3.1.3.2. Circular Polarization Filters

From the above equations it becomes obvious that it is not possible to obtain information on the exact phase δ, see Eq. (3.16). This is only possible by using another optical element called circular polarizer. Such an element can be symbolized by

$$\vec{J}_c = \frac{\sqrt{2}}{2}(\vec{e}_x - i\vec{e}_y). \tag{3.22}$$

The sign of i may vary (left or right circular polarizer). The physical realization of a circular polarizer exploits the property of some dielectric materials to have different refractive indices along different axes of the crystal (birefringence). The difference in the refractive indices lead to a linearly propagating phase difference between $\vec{E}_{0x}$ and $\vec{E}_{0y}$. Through an appropriate choice of the path length of light through such a material the phase difference can be adjusted to a desired value e.g. $\Delta\varphi = \frac{\pi}{2}$. Since the refractive index is usually wavelength dependent, the relative phase of waves of different frequencies will deviate from the desired value, such that circular polarizers are more complicated to use then linear polarizers. However, in principle only the phase retardation must be known for each wavelength, then it is possible to exploit the complementary information coming from a circular polarizer. The effect on the electric field is:

$$\vec{J}_c \vec{E} = \frac{\sqrt{2}}{2} (|E_{0x}|e^{i\varphi} - i|E_{0y}|e^{i(\varphi+\delta)}) \tag{3.23}$$

The Poynting vector of the resulting field is proportional to

$$|\vec{J}_c \vec{E}|^2 = |E_{0x}|^2 + |E_{0y}|^2 + 2|E_{0x}||E_{0y}|\sin(\delta) \tag{3.24}$$

and the measured irradiance is

$$F_c = \frac{k}{2\omega\mu}|\vec{J}_c\vec{E}|^2. \tag{3.25}$$

Summarizing, together with the circular filter, the polarization state is entirely defined by

$$\{|E_{0x}|, |E_{0y}|, \delta\}. \tag{3.26}$$

3.1.4. Stokes Vectors

It is common practise to express the polarization state of light through its so called Stokes vector (F, Q, U, V) and relate it to measurements with polarization filters as described earlier. Following the convention of [Huffman and Bohren, 1983] the Stokes (irradiance) vector is defined as

$$\begin{pmatrix} F \\ Q \\ U \\ V \end{pmatrix} = \frac{k}{2\omega\mu} \begin{pmatrix} E_{0x}E_{0x}^* + E_{0y}E_{0y}^* \\ E_{0x}E_{0x}^* - E_{0y}E_{0y}^* \\ E_{0x}E_{0y}^* + E_{0y}E_{0x}^* \\ i(E_{0x}E_{0y}^* - E_{0y}E_{0x}^*) \end{pmatrix} = \frac{k}{2\omega\mu} \begin{pmatrix} |E_{0x}|^2 + |E_{0y}|^2 \\ |E_{0x}|^2 - |E_{0y}|^2 \\ 2|E_{0x}||E_{0y}|\cos(\delta) \\ 2|E_{0x}||E_{0y}|\sin(\delta) \end{pmatrix}. \tag{3.27}$$

3.1.4.1. Measurement of Stokes Vectors

Using in particular the set of operators, for instance the linear polarizers $F_l(\alpha)$ (Eq. (3.21)) and the circular polarizer F_c according to Eq. (3.21) that just have been investigated, the Stokes vector can be measured by linearely combining the filtered intensities:

$$\begin{pmatrix} F \\ Q \\ U \\ V \end{pmatrix} = \begin{pmatrix} F_l(0) + F_l(\frac{\pi}{2}) \\ F_l(0) - F_l(\frac{\pi}{2}) \\ 2F_l(\frac{\pi}{4}) - F_l(0) - F_l(\frac{\pi}{2}) \\ F_c - 2F_l(0) - 2F_l(\frac{\pi}{2}) \end{pmatrix}. \tag{3.28}$$

Instead of calculating the Stokes vector it is also possible to express the parameters of Eq. (3.26) by the measured intensities:

$$|E_{0x}| = \sqrt{\frac{2\omega\mu}{k}F_l(0)} \tag{3.29}$$

$$|E_{0y}| = \sqrt{\frac{2\omega\mu}{k}F_l\left(\frac{\pi}{2}\right)} \tag{3.30}$$

$$\delta = \arctan\left[F_c - 2F_l(0) - 2F_l\left(\frac{\pi}{2}\right), 2F_l\left(\frac{\pi}{4}\right) - F_l(0) - F_l\left(\frac{\pi}{2}\right)\right] \tag{3.31}$$

where for the inverse tangens the version $\arctan(y, x)$ is taken.

3.1.4.2. Mapping of Stokes Vectors and Electric Field Components

For later purposes it is necessary to introduce another set of independent variables $\{E_{0x}E_{0x}^*, E_{0y}E_{0y}^*, E_{0x}E_{0y}^*, E_{0y}E_{0x}^*\}$ and relate its elements to the Stokes vector

$$
\begin{pmatrix} E_{0x}E_{0x}^* \\ E_{0y}E_{0y}^* \\ E_{0x}E_{0y}^* \\ E_{0y}E_{0x}^* \end{pmatrix} = \frac{\omega\mu}{k} \begin{pmatrix} F+Q \\ F-Q \\ U-iV \\ U+iV \end{pmatrix} = \frac{\omega\mu}{k} \begin{pmatrix} 1 & 1 & 0 & 0 \\ 1 & -1 & 0 & 0 \\ 0 & 0 & 1 & -i \\ 0 & 0 & 1 & i \end{pmatrix} \begin{pmatrix} F \\ Q \\ U \\ V \end{pmatrix}
\tag{3.32}
$$

and vice versa:

$$
\begin{pmatrix} F \\ Q \\ U \\ V \end{pmatrix} = \frac{k}{2\omega\mu} \begin{pmatrix} 1 & 1 & 0 & 0 \\ 1 & -1 & 0 & 0 \\ 0 & 0 & 1 & 1 \\ 0 & 0 & i & -i \end{pmatrix} \begin{pmatrix} E_{0x}E_{0x}^* \\ E_{0y}E_{0y}^* \\ E_{0x}E_{0y}^* \\ E_{0y}E_{0x}^* \end{pmatrix}.
\tag{3.33}
$$

As symbols are used

$$
\mathbf{M}_{S\to J} := \frac{\omega\mu}{k} \begin{pmatrix} 1 & 1 & 0 & 0 \\ 1 & -1 & 0 & 0 \\ 0 & 0 & 1 & -i \\ 0 & 0 & 1 & i \end{pmatrix} \quad\text{and}\quad \mathbf{M}_{J\to S} := \frac{k}{2\omega\mu} \begin{pmatrix} 1 & 1 & 0 & 0 \\ 1 & -1 & 0 & 0 \\ 0 & 0 & 1 & 1 \\ 0 & 0 & i & -i \end{pmatrix}.
\tag{3.34}
$$

It is interesting to introduce also another set of parameters which is equivalent to Eq. (3.26):

$$
\{E, \varphi_E, \delta\} \leftrightarrow \{|E_{0x}| = \cos(\varphi_E)E, |E_{0y}| = \sin(\varphi_E)E, \delta\}
\tag{3.35}
$$

where

$$
\varphi_E = \arctan\left[\sqrt{F-Q}, \sqrt{F+Q}\right] = \arctan\left[\sqrt{F_l(\tfrac{\pi}{2})}, \sqrt{F_l(0)}\right].
\tag{3.36}
$$

With this set the orientation φ_E of the oscillating electric field vector is used in combination with the absolute field strength E.

3.1.4.3. Stokes Vector Transformations and Rotation Matrices

In optics, optical elements are used in a certain alignment. In such an alignment or configuration of elements it is frequently necessary to transform the electric field from one coordinate system to another. In this section it is shown how Stokes vectors transform in a change of the coordinate system. The amplitudes of E_x and E_y are multiplied with a cosine factor when projecting the propagation direction into the new coordinate system and then an additional rotation angle α (in the xy plane) around the $\vec{e}_z$ axis is introduced. A close inspection reveals that only α is a relevant parameter in such coordinate system transformation since the cosine factor only changes the amplitude but not the nature (i.e. the polarization state) of the light beam. The resulting transformation rule for the Stokes vector is investigated in the following:

$$
\begin{pmatrix} E'_{x0} \\ E'_{y0} \end{pmatrix} = \begin{pmatrix} \cos(\alpha) & \sin(\alpha) \\ -\sin(\alpha) & \cos(\alpha) \end{pmatrix} \begin{pmatrix} E_{x0} \\ E_{y0} \end{pmatrix}.
\tag{3.37}
$$

In the system $\{E_{0x}E_{0x}^*, E_{0y}E_{0y}^*, E_{0x}E_{0y}^*, E_{0y}E_{0x}^*\}$ the rotation writes as follows:

$$
\begin{pmatrix} E_{0x}E_{0x}^* \\ E_{0y}E_{0y}^* \\ E_{0x}E_{0y}^* \\ E_{0y}E_{0x}^* \end{pmatrix}' = \begin{pmatrix} c^2 & s^2 & sc & sc \\ s^2 & c^2 & -sc & sc \\ -sc & sc & c^2 & s^2 \\ -sc & sc & -s^2 & c^2 \end{pmatrix} \begin{pmatrix} E_{0x}E_{0x}^* \\ E_{0y}E_{0y}^* \\ E_{0x}E_{0y}^* \\ E_{0y}E_{0x}^* \end{pmatrix}
\tag{3.38}
$$

where $s = \sin(\alpha)$ and $c = \cos(\alpha)$ and the matrix is defined as $\mathbf{R}(\alpha)$. Using the matrices defined in Section 3.1.4.2 the Stokes vectors transform as follows:

$$
\begin{pmatrix} F' \\ Q' \\ U' \\ V' \end{pmatrix} = \mathbf{M}_{S \to J} \mathbf{R}(\alpha) \mathbf{M}_{J \to S} \begin{pmatrix} F \\ Q \\ U \\ V \end{pmatrix} \tag{3.39}
$$

$$
= \frac{1}{2} \begin{pmatrix} 1 & 1 & 0 & 0 \\ 1 & -1 & 0 & 0 \\ 0 & 0 & 1 & 1 \\ 0 & 0 & i & -i \end{pmatrix} \begin{pmatrix} c^2 & s^2 & sc & sc \\ s^2 & c^2 & -sc & sc \\ -sc & sc & c^2 & s^2 \\ -sc & sc & -s^2 & c^2 \end{pmatrix} \begin{pmatrix} 1 & 1 & 0 & 0 \\ 1 & -1 & 0 & 0 \\ 0 & 0 & 1 & -i \\ 0 & 0 & 1 & i \end{pmatrix} \begin{pmatrix} F \\ Q \\ U \\ V \end{pmatrix}
$$

$$
= \frac{1}{2} \begin{pmatrix} 1 & 1 & 0 & 0 \\ c^2 - s^2 & s^2 - c^2 & 2sc & 2sc \\ -2sc & s2c & c^2 - s^2 & c^2 - s^2 \\ 0 & 0 & i & -i \end{pmatrix} \begin{pmatrix} 1 & 1 & 0 & 0 \\ 1 & -1 & 0 & 0 \\ 0 & 0 & 1 & -i \\ 0 & 0 & 1 & i \end{pmatrix} \begin{pmatrix} F \\ Q \\ U \\ V \end{pmatrix}. \tag{3.40}
$$

With the identities $\cos(\alpha) = \frac{1}{2}(e^{i\alpha} + e^{-i\alpha})$ and $\sin(\alpha) = -\frac{i}{2}(e^{i\alpha} - e^{-i\alpha})$ it follows that

$$
c^2 - s^2 = \frac{1}{4}(e^{2i\alpha} + 2 + e^{-2i\alpha}) + \frac{1}{4}(e^{2i\alpha} - 2 + e^{-2i\alpha}) = \frac{1}{2}(e^{2i\alpha} + e^{-2i\alpha}) = \cos(2\alpha) \tag{3.41}
$$

$$
2sc = \frac{-i}{2}(e^{i\alpha} + e^{-i\alpha})(e^{i\alpha} - e^{-i\alpha}) = \frac{-i}{2}(e^{2i\alpha} - e^{-2i\alpha}) = \sin(2\alpha). \tag{3.42}
$$

The final result (also e.g. [Kattawar et al., 1973]) is thus

$$
\begin{pmatrix} F' \\ Q' \\ U' \\ V' \end{pmatrix} = \begin{pmatrix} 1 & 0 & 0 & 0 \\ 0 & \cos(2\alpha) & \sin(2\alpha) & 0 \\ 0 & -\sin(2\alpha) & \cos(2\alpha) & 0 \\ 0 & 0 & 0 & 1 \end{pmatrix} \begin{pmatrix} F \\ Q \\ U \\ V \end{pmatrix} =: \mathbf{L}(\alpha) \begin{pmatrix} F \\ Q \\ U \\ V \end{pmatrix}. \tag{3.43}
$$

Later in the thesis it is shown that scatter events on molecules and particles are in principle treated like optical elements, describing therewith the propagation of electromagnetic radiation in such event. In each scatter order the Stokes vector of the incoming model photon has to be transformed into the scattering plane spanned by the incident ($\vec{k}_{\text{inc}}$) and outgoing ($\vec{k}_{\text{sca}}$) propagation direction. After the scattering interaction, the modified Stokes vector needs to be related to the outgoing direction $\vec{k}_{\text{sca}}$ (see Fig. 3.1). The angles i_{inc} and i_{sca} are calculated by means of spherical trigonometry. Their identity as shown in the figure can be found by a thorough analysis of the location of the scattering plane and how it intersects the xy plane.

3.2. Scattering and Absorption of EM Waves by Molecules and Particles

To better understand large scale radiation transport, one has to understand its "atomic" elements. The following discussion is be based on the idea that a single molecule or particle with certain dielectric properties (in the continuum or classical picture) respectively with certain transitions between internal states (in the quantum mechanical picture) is exposed to an electromagnetic wave described through its electrical field vector $\vec{E}_{\text{inc}}$ oscillating with frequency ω_{inc}. As a result of the exposure and due to the internal energy states, a purely scattering object will cause an additional electrical field $\vec{E}_{\text{sca}}$ (i.e. a *specific response*) which adds to $\vec{E}_{\text{inc}}$. In case of a quantum mechanical inner molecular electronic or mechanical transitions (of changing the rotational or vibrational molecular state) single photons of the "radiation field photon bath" are absorbed and excite the molecule either electronically or mechanically. In the latter case it might happen, that a photon is emitted when the excited state decays again. This process is called spontaneous emission if no outer cause is present and it is called induced if the decay of the excited state is caused by the interaction with another molecule, particle or photon. In molecular scattering, one distinguishes elastic and inelastic scattering processes. Whereas elastic scattering processes conserve the energy of the incident photons (the oscillation frequency of the scattered electric field ω_{sca} is equal to ω_{inc}), inelastic processes remove photons
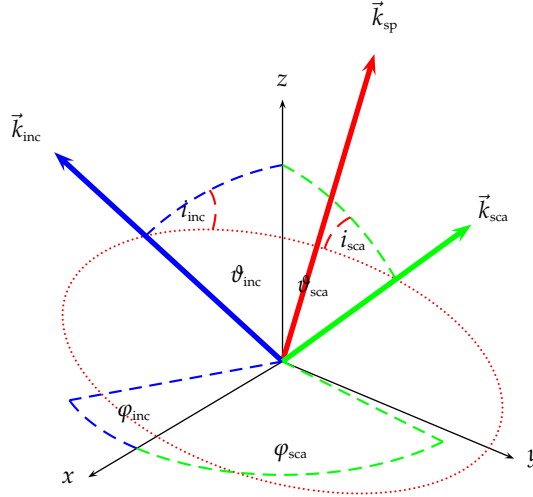
Figure 3.1.: Definition of angles used for the calculation of the angles i_{inc} and i_{sca} after [Chandrasekhar, 1960]. The angle i_{inc} is needed in order to relate Stokes vector of the incident wave with propagation direction $\vec{k}_{\mathrm{inc}}$ to the scattering plane (circle with dots, and normal $\vec{k}_{\mathrm{sp}}$). The second angle i_{sca} relates the Stokes vector in the scattering plane to the Stokes vector of the outgoing waves with propagation direction $\vec{k}_{\mathrm{sca}}$. The source code of this plot is found in Appendix A.5.

of frequency ω_{inc} from the radiation field and emit photons of altered frequency ω_{sca} as a result of an inner molecular process called rotational and/or vibrational Raman scattering which is discussed further below. As a consequence of such an inelastic scattering process, the internal energy state of the scatter object is altered.

3.2.1. General Description of Scattering and Coordinate Systems

For the theoretical description of scattering in the classical (Maxwell) picture it is sufficient to regard the incident electric field as a plane wave. Scattering happens when a wave travels through a medium with fluctuations in the refractive index. The phenomenon is well known for sharp discontinuities like sudden transitions between two media with notably different refractive indices like water and air, or air and glass, but it happens also in air. Microscopically small fluctuations in the pressure, i.e. in principle mechanical (sound) waves are believed to be the reason for the fluctuations in the refractive index of air. Scattering is associated also with dielectric molecular properties like the (effective) molecular polarizability and also mechanical excitations. Scattering at large particles can thus be explained by the difference between the refractive index of the surrounding medium (i.e. air) and the particles refractive index. The particle picture of scattering motivates analyzing the involved electrical fields respectively in two coordinate systems which share the normal of the scattering plane as a basis vector (see Fig. 3.1). Let the scatter location be in the center of the coordinate system. The following two unit vectors are defined:

$$\vec{e}_{\mathrm{inc}} := \frac{\vec{k}_{\mathrm{inc}}}{|\vec{k}_{\mathrm{inc}}|} \quad \text{and analogously} \quad \vec{e}_{\mathrm{sca}} := \frac{\vec{k}_{\mathrm{sca}}}{|\vec{k}_{\mathrm{sca}}|} \tag{3.44}$$

which determine the vector orthogonal to the scattering plane:

$$\vec{e}_{\mathrm{sp}} := \vec{e}_{\mathrm{inc}} \times \vec{e}_{\mathrm{sca}} \tag{3.45}$$

Using these unit vectors, two coordinate systems of respectively three right handed vectors

$$\{\vec{e}_{\mathrm{inc}}, \vec{e}_{\mathrm{inc}\perp}, \vec{e}_{\mathrm{inc}\|}\} \quad \text{and} \quad \{\vec{e}_{\mathrm{sca}}, \vec{e}_{\mathrm{sca}\perp}, \vec{e}_{\mathrm{sca}\|}\}. \tag{3.46}$$

are defined

$$\vec{e}_{\text{inc}\perp} = \vec{e}_{\text{sp}} \tag{3.47}$$

$$\vec{e}_{\text{inc}\parallel} = \vec{e}_{\text{inc}} \times \vec{e}_{\text{sp}} = \vec{e}_{\text{inc}} \times (\vec{e}_{\text{inc}} \times \vec{e}_{\text{sca}}) = \vec{e}_{\text{inc}} \cos(\theta_S) - \vec{e}_{\text{sca}} \tag{3.48}$$

$$\vec{e}_{\text{sca}\perp} = \vec{e}_{\text{sp}} \tag{3.49}$$

$$\vec{e}_{\text{sca}\parallel} = \vec{e}_{\text{sca}} \times \vec{e}_{\text{sp}} = \vec{e}_{\text{sca}} \times (\vec{e}_{\text{inc}} \times \vec{e}_{\text{sca}}) = \vec{e}_{\text{inc}} - \vec{e}_{\text{sca}} \cos(\theta_S) \tag{3.50}$$

using the Graßman identity and $\cos(\theta_S) = \vec{e}_{\text{inc}}\vec{e}_{\text{sca}}$ for the scatter angle θ_s. Incident and scattered electric field and are then expressed through projections to the respective $\{\vec{e}_\perp, \vec{e}_\parallel\}$, furthermore the time dependence is dropped in the notation. For electric field vectors $\vec{E}$ the expansion writes:

$$\vec{E}_{\text{inc/sca}} = E_{\text{inc/sca}\parallel}\vec{e}_{\text{inc/sca}\parallel} + E_{\text{inc/sca}\perp}\vec{e}_{\text{inc/sca},\perp}. \tag{3.51}$$

For example, the incident plane wave amplitudes parallel and perpendicular to the scattering plane are:

$$E_{\text{inc}\parallel} = (\vec{e}_{\text{inc}} \cos(\theta_S) - \vec{e}_{\text{sca}})\vec{E}_{\text{inc}} = -\vec{e}_{\text{sca}}\vec{E}_{\text{inc}} \tag{3.52}$$

$$E_{\text{inc}\perp} = \vec{e}_{\text{sp}}\vec{E}_{\text{inc}}. \tag{3.53}$$

The right side of Eq. (3.52) follows because light is a transverse wave, i.e. projection of the field strength onto the propagation direction vanishes.

3.2.1.1. Complex Scattering Amplitudes

In the far field zone, i.e. in sufficient distance (compared to the size of the scattering object) away from the scatter location, the scattered electrical field is a spherical wave. In order to describe the response of the scatter object to the incident electric field, scattered and incident electrical fields are related to each other through [Huffman and Bohren, 1983]:

$$\vec{E}_{\text{sca}}(\vec{r}) = \frac{ie^{ik(r-z)}}{kr}\mathbf{S}_J(\vec{k}_{\text{inc}}, \vec{k}_{\text{sca}})\vec{E}_{\text{inc}} \tag{3.54}$$

respectively

$$\begin{pmatrix} E_{\parallel\text{sca}} \\ E_{\perp\text{sca}} \end{pmatrix} = \frac{ie^{ik(r-z)}}{kr}\begin{pmatrix} S_2 & S_3 \\ S_4 & S_1 \end{pmatrix}\begin{pmatrix} E_{\parallel\text{inc}} \\ E_{\perp\text{inc}} \end{pmatrix} \tag{3.55}$$

in the scattering coordinate systems Eq. (3.46). $\mathbf{S}_J$ is called complex scattering matrix. In principle for any relevant atmospheric scattering object the angular distribution and the absolute cross section can be obtained by solving the Maxwell equations. In case of molecular scattering the (first order) physics is found in standard textbooks (dipole radiation, Section 3.2.2.3). For larger speherical particles (in comparison to the wavelength) Mie's theory [Mie, 1908] is applied. The corresponding scattering amplitudes are briefly discussed in Section 3.2.4. For other than spherically shaped particles different methods are applied. If symmetries can be exploited the so called T-matrix method [Mishchenko et al., 1996] is useful, for arbitrarily shaped particles with a heterogeneous distribution of the dielectric properties the discrete dipole approximation (DDA, [Draine and Flatau, 1994]) is available. The scattered field adds to the incident field to form the total electric field:

$$\vec{E} = \vec{E}_{\text{inc}} + \vec{E}_{\text{sca}}. \tag{3.56}$$

Fig. 3.2 shows the electric fields involved in a scattering process [Mishchenko, 2009]. The description of scattering of polarized EM waves in this thesis uses the Stokes vector language. Similarly as in Section 3.1.4, the transformation of the electric field can be described by a single matrix. It is again started with the system

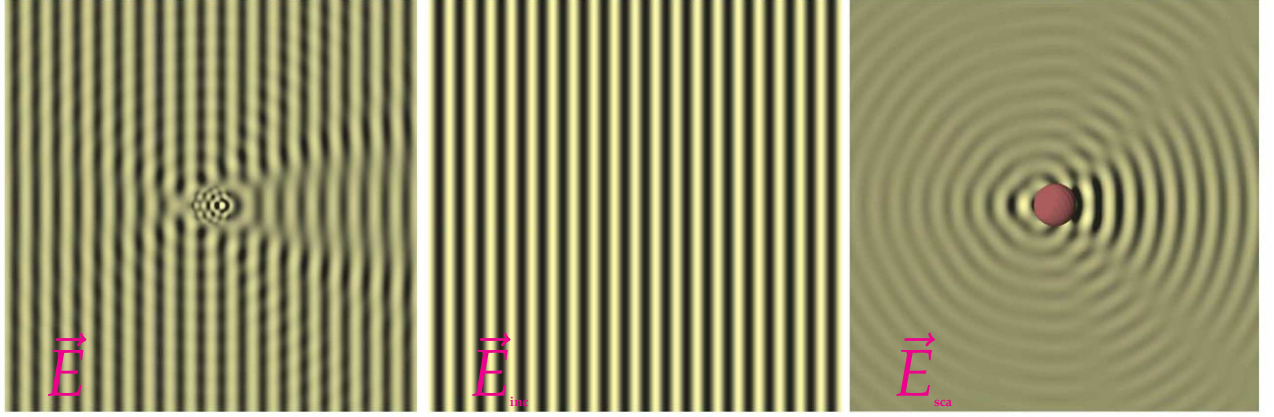$$\{E_\parallel E_\parallel^*, E_\perp E_\perp^*, E_\parallel E_\perp^*, E_\perp E_\parallel^*\}$$

Figure 3.2.: The total, incident and scattered field in a scattering process. The incident wave is a linearly polarized plane wave. The refractive index of the particle (red ball) is considerably larger causing a fine ripple structure in the internal field in $\vec{E}$. Figure taken and modified from [Mishchenko, 2009].

$$
\begin{pmatrix}
E_{\parallel\mathrm{sca}} E^*_{\parallel\mathrm{sca}} \\
E_{\perp\mathrm{sca}} E^*_{\perp\mathrm{sca}} \\
E_{\parallel\mathrm{sca}} E^*_{\perp\mathrm{sca}} \\
E_{\perp\mathrm{sca}} E^*_{\parallel\mathrm{sca}}
\end{pmatrix}
=
\frac{S}{k^2 r^2}
\begin{pmatrix}
E_{\parallel\mathrm{inc}} E^*_{\parallel\mathrm{inc}} \\
E_{\perp\mathrm{inc}} E^*_{\perp\mathrm{inc}} \\
E_{\parallel\mathrm{inc}} E^*_{\perp\mathrm{inc}} \\
E_{\perp\mathrm{inc}} E^*_{\parallel\mathrm{inc}}
\end{pmatrix}
\tag{3.57}
$$

$$
S =
\begin{pmatrix}
S_2 S_2^* & S_3 S_3^* & S_2 S_3^* & S_3 S_2^* \\
S_4 S_4^* & S_1 S_1^* & S_4 S_1^* & S_1 S_4^* \\
S_2 S_4^* & S_3 S_1^* & S_2 S_1^* & S_3 S_4^* \\
S_4 S_2^* & S_1 S_3^* & S_4 S_3^* & S_1 S_2^*
\end{pmatrix}.
\tag{3.58}
$$

In the Stokes vector language the scattering matrix $\mathbf{S}_{\mathrm{Stokes}}$ relating to each other the Stokes parameters of the scattered and the incident wave is

$$
S_{\mathrm{Stokes}} = \mathbf{M}_{S \to J} \mathbf{S} \mathbf{M}_{J \to S}.
\tag{3.59}
$$

The detailed elements of S_{Stokes} are found e.g. in [Huffman and Bohren, 1983]. The modulus of the scattered waves Poynting vector, i.e. the scattered wave irradiance is

$$
S_{\mathrm{sca}} = F_{\mathrm{sca}} = \frac{k}{2\omega\mu} \vec{E}_{\mathrm{sca}} \vec{E}^*_{\mathrm{sca}} = \frac{1}{k^2 r^2} S_{\mathrm{Stokes},11} F_{\mathrm{inc}}
\tag{3.60}
$$

using Eq. (3.59).

3.2.1.2. Differential and Total Scattering Cross Section, Phase Matrix

Due to their rapid oscillations, the fields can not be measured directly. When measuring the direction characteristics of the scattered electric field the modulus of the Poynting vector $\vec{S}_{\mathrm{sca}}$, resp. the irradiance is used. Suppose the observer is located in the radiation zone of the scattered electrical field at $\vec{r}$ and exposes an area of $\mathrm{d}\vec{A} = r^2 \mathrm{d}\vec{\Omega} = \vec{n} r^2 \mathrm{d}\Omega$ with $\vec{n} = \vec{r}/r$ to the scattered electric field, then the observer measures a power $\mathrm{d}P_{\mathrm{rad}}$ of

$$
\mathrm{d}P_{\mathrm{rad}}(\vec{\Omega}, S_{\mathrm{inc}}) = \mathrm{d}\vec{A} \vec{S}_{\mathrm{sca}}(\vec{\Omega}, S_{\mathrm{inc}}) = r^2 \vec{S}_{\mathrm{sca}}(\vec{\Omega}, S_{\mathrm{inc}}) \mathrm{d}\vec{\Omega} = r^2 \vec{n} \vec{S}_{\mathrm{sca}}(\vec{\Omega}, S_{\mathrm{inc}}) \mathrm{d}\Omega.
\tag{3.61}
$$

$\mathrm{d}P_{\mathrm{rad}}$ depends in magnitude on the incident energy flux density $S_{\mathrm{inc}} = |\vec{S}_{\mathrm{inc}}|$. In order to obtain a normalized measure of the interaction probability, the differential scattering cross section is introduced using $S_{\mathrm{inc}} = F_{\mathrm{inc}}$:

$$
\frac{\mathrm{d}\sigma_S}{\mathrm{d}\Omega} = \frac{1}{S_{\mathrm{inc}}} \frac{\mathrm{d}P_{\mathrm{rad}}}{\mathrm{d}\Omega} = r^2 \frac{S_{\mathrm{sca}}}{S_{\mathrm{inc}}} = \frac{1}{k^2} S_{\mathrm{Stokes},11}.
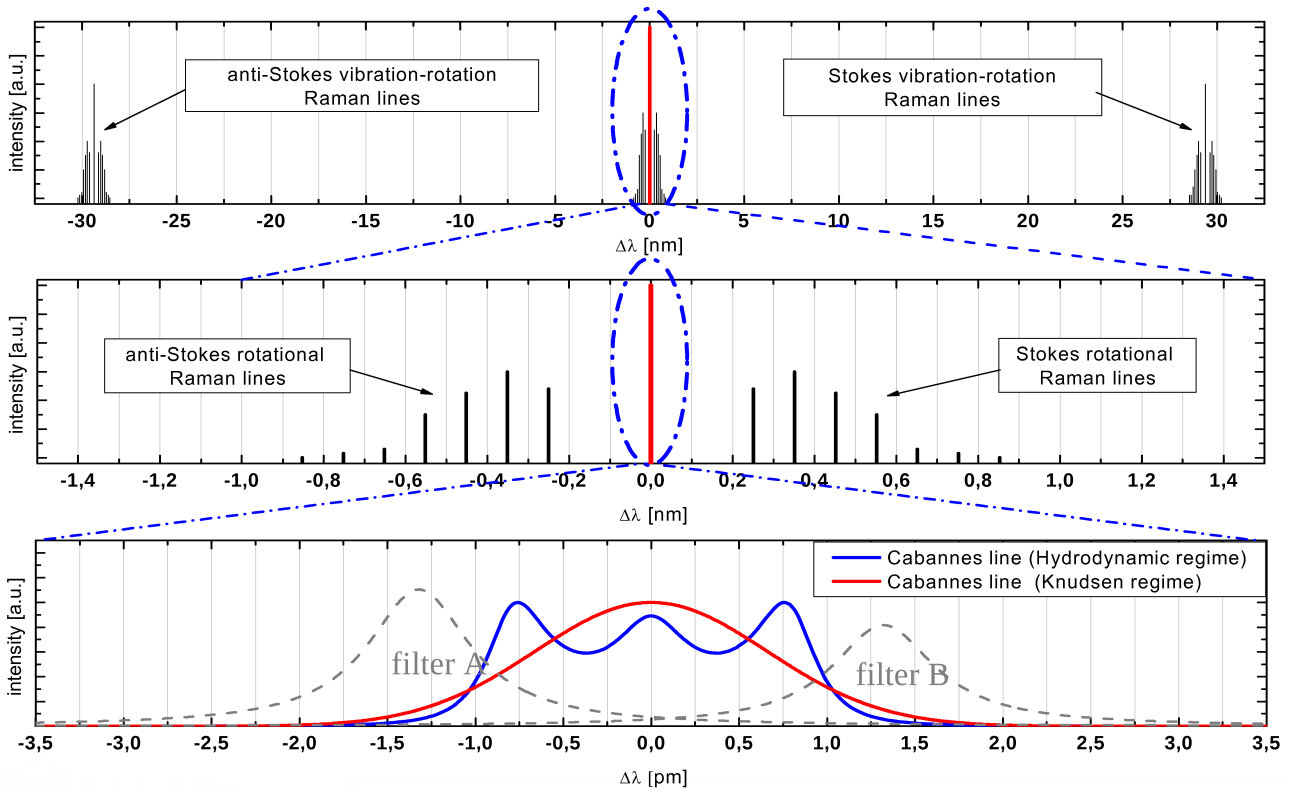\tag{3.62}
$$

Figure 3.3.: Plot from: Oliver Reitebuch, Benjamin Witschas, Ofelia Vieitez, Eric-Jan van Duijn, Willem van de Water, Wim Ubachs: Rayleigh-Brillouin Scattering in N_2, O_2, and Air, 33rd Lidar Working Group, Destin (FL), 2-4 Feb 2010 Institut für Physik der Atmosphäre, DLR Oberpfaffenhofen. Details in the main text.

Through integration over all directions using Eq. (3.60), the total scattering cross section is obtained

$$\sigma_S = \frac{r^2}{S_{\text{inc}}} \int_{4\pi} \vec{S}_{\text{sca}}(\vec{\Omega}, S_{\text{inc}}) \, d\vec{\Omega}. = \frac{1}{k^2} \int_{4\pi} S_{\text{Stokes},11}(\vec{\Omega}) \, d\Omega. \tag{3.63}$$

In atmospheric optics, the differential cross section is separated into a part depending on the total cross section and a purely directional part, the so called phase function $P(\vec{\Omega})$, i.e.:

$$\frac{d\sigma_S}{d\Omega} = \frac{\sigma_S}{4\pi} P(\vec{\Omega}) \rightarrow P(\vec{\Omega}) := \frac{4\pi}{\sigma_S} \frac{d\sigma_S}{d\Omega} = \frac{4\pi r^2 S_{\text{sca}}}{\sigma_S S_{\text{inc}}} = \frac{4\pi S_{\text{Stokes},11}(\vec{\Omega})}{\int_{4\pi} S_{\text{Stokes},11}(\vec{\Omega}) \, d\Omega} \tag{3.64}$$

which is found using Eq. (3.60). For the full description of polarized radiation transport in a single scattering event the phase matrix is defined as:

$$\boldsymbol{P}(\vec{\Omega}) = \frac{4\pi \boldsymbol{S}_{\text{Stokes}}(\vec{\Omega})}{\int_{4\pi} S_{\text{Stokes},11}(\vec{\Omega}) \, d\Omega}. \tag{3.65}$$

3.2.2. Molecular Scattering

When spectrally analyzing the electromagnetic response of an air parcel entirely consisting of molecules at a certain pressure and temperature illuminated with a laser beam, certain spectral structures appear at different wavelength scales (see Fig. 3.3) in the back-scattered direction. At this point it is probably most instructive to cite Andrew Young's definition [Young, 1981] of terms in the context of molecular scattering (compare to Figs. 3.3 and 3.4):

> *Molecular scattering consists of Rayleigh scattering and vibrational Raman scattering. The Rayleigh scattering consists of rotational Raman lines and the central Cabannes line. The Cabannes line is composed of the Brillouin doublet and the central Gross or Landau-Placzek line. None of the above is completely coherent. The term "Rayleigh line" should never be used.*
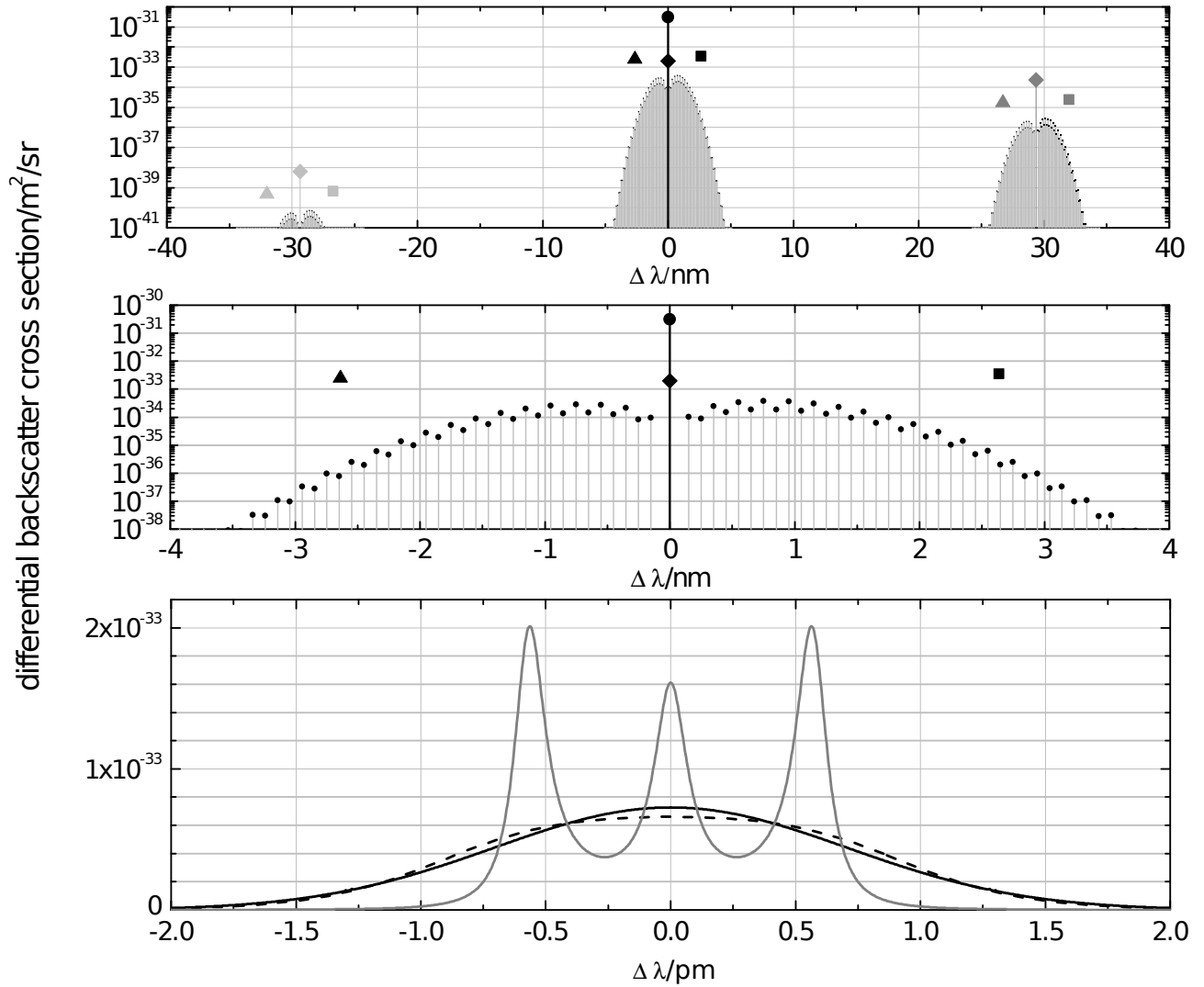
Figure 3.4.: Back-scattered laser light of wavelength 355nm in N_2 at 300K. **Top Panel:** vibration-rotation Raman scattering signatures. The triangles, squares and circles symbolize integrated cross sections for the respective branches. The circle at the center symbolizes cross sections for integrated Rayleigh-Brillouin scattering cross sections. **Middle Panel:** pure rotational Raman transitions. The **bottom panel** shows the Rayleigh-Brillouin scattering cross sections. Plot with courtesy of Benjamin Witschas. More information is found in [Witschas, 2012].

The importance of the different molecular scattering processes can be related to their respective scattering cross sections in the backward direction (Fig. 3.4). From the figure the relative magnitudes of the scattering cross sections can roughly be estimated as $1 : 10^{-2} : 10^{-3}$ Cabannes : rotational Raman : rotational-vibrational Raman scattering. The physical origin of Cabannes scattering is discussed in Section 3.2.2.3. The physics of vibrational and rotational Raman scattering can roughly be described as inelastic scattering caused by the electromagnetic interaction of light with the change of polarizability induced by mechanical vibration and rotation of diatomic molecules (Section 3.2.2.4). The deep reason of rotational Raman scattering is the anisotropy of the polarizability of rotating air molecules. The anisotropy is also the origin of deviations of differential scattering cross section from the ideal dipole scattering characteristic.

3.2.2.1. Molecular Polarizability

The relationship between the macroscopic dielectric permittivity and the refractive index with the molecular polarizability is discussed. Since the underlying theory presented here forms the basis of branches of analytic and physical chemistry the reader interested in details thereof is referred to the relevant literature e.g. [Hollas, 2004, Haken and Wolf, 2006]. If an insulator (or a gas consisting of diatomic molecules) is exposed to an
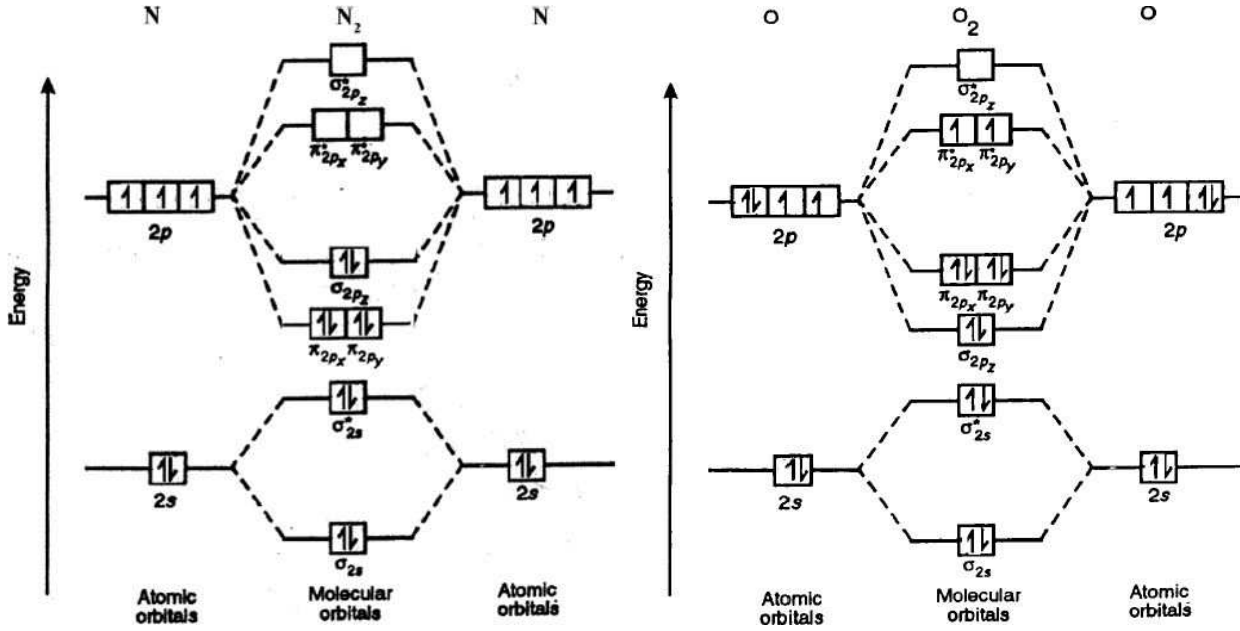
Figure 3.5.: Nitrogen (**left**) and oxygen (**right**) electronic configuration and molecular obitals. The terms on the left and right in each plot show the electronic orbitals in the isolates atoms, the middle terms show the molecular electronic orbitals. Asterisk stands for anti-bond, i.e. the electron densities (squared wave functions) are zero between the molecules. Source: internet, standard textbook

electric field, the molecules become polarized, i.e. internal charges q are displaced by a distance $\vec{d}$ according to the strength of the local electric field, see Fig. 3.5 in order to gain an impression on the detailed electronic configuration of N_2 and O_2 molecules. The induced dipole moment p_{ind} is

$$q\vec{d} = \vec{p}_{\text{ind}} = \boldsymbol{\alpha}\vec{E} = \begin{pmatrix} \alpha_{xx} & \alpha_{xy} & \alpha_{xz} \\ \alpha_{yx} & \alpha_{yy} & \alpha_{yz} \\ \alpha_{zx} & \alpha_{zy} & \alpha_{zz} \end{pmatrix} \begin{pmatrix} E_x \\ E_y \\ E_z \end{pmatrix}. \tag{3.66}$$

The elements ij of the polarizability tensor $\boldsymbol{\alpha}$ describe thus the strength the component i of the induced dipole momentum as a linear function of the component j of the electric field. Without the presence of a magnetic field the rotation axes of the diatomic molecules are uniformly distributed in the direction space and therefore a direction averaging has to be performed in order to obtain effective polarizabilities. There are two characteristic quantities that are conserved in a rotation of the coordinate system. These are the average molecular polarizability $\bar{\alpha}$ (related to the trace of $\boldsymbol{\alpha}$):

$$\bar{\alpha} = \frac{1}{3}(\alpha_{xx} + \alpha_{yy} + \alpha_{zz}) \tag{3.67}$$

and the squared anisotropy of the polarizability γ^2 defined as

$$\gamma^2 = \frac{1}{2}\left[(\alpha_{xx} - \alpha_{yy})^2 + (\alpha_{yy} - \alpha_{zz})^2 + (\alpha_{zz} - \alpha_{xx})^2 + 6(\alpha_{xy}^2 + \alpha_{yz}^2 + \alpha_{zx}^2)\right]. \tag{3.68}$$

For rotating diatomic molecules N_2 and O_2 with rotation axis oriented along the z direction, the polarizability tensor assumes the following form

$$\boldsymbol{\alpha} = \begin{pmatrix} \alpha_\perp & 0 & 0 \\ 0 & \alpha_\perp & 0 \\ 0 & 0 & \alpha_\| \end{pmatrix} \tag{3.69}$$

i.e. the polarizabilities in x and y direction are equal to $\alpha_\perp$ and differ from the polarizability $\alpha_\parallel$ in z direction. Average polarizability and anisotropy are thus

$$\gamma(\lambda) = \alpha_\parallel(\lambda) - \alpha_\perp(\lambda) \tag{3.70}$$

$$\bar{\alpha}(\lambda) = \frac{1}{3}[\alpha_\parallel(\lambda) + 2\alpha_\perp(\lambda)]. \tag{3.71}$$
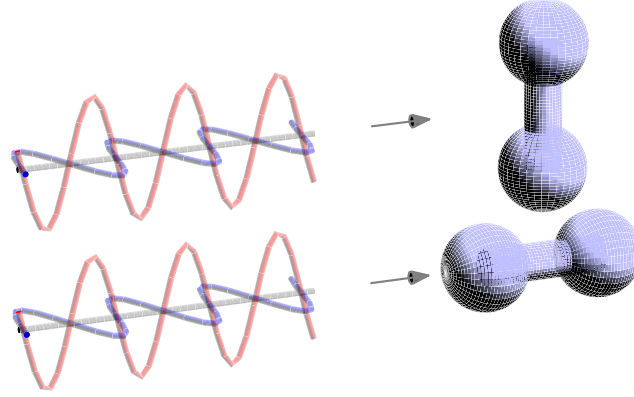

Figure 3.6.: Illustration of the relation between axis of a diatomic molecule (shown as a rigid rotator) and the polarization state of an incident wave. For many diatomic molecules, polarizability is largest along the axis between the atoms (red sine wave on top).

3.2.2.2. Clausius-Mosotti Relation

It is important to understand how the macroscopic dielectric permittivity is related to the (microscopic) molecular polarizability. This relation can be found by equating the induced dipole strength $\vec{P}$ for molecules with number density n_{air} using both descriptions. The polarization described with the dielectric constants is

$$\vec{P} = (\varepsilon_r - 1)\varepsilon_0\vec{E} \tag{3.72}$$

where $\vec{E}$ is the external (incident) field. On the microscopic scale, $\vec{P}$ is the displacement of charges caused by the local electric field $\vec{E}_l$ which is the superposition of the external with the electric field caused by the induced dipoles on a sphere around the volume of interest (after Lorentz):

$$\vec{E}_l = \vec{E} + \frac{1}{3\varepsilon_0}\vec{P} \tag{3.73}$$

where Eq. (3.72) is used in order to substitute $\vec{P}$. The microscopic description of the polarization is related to the respective local field:

$$\vec{P} = n_{\text{air}}\bar{\alpha}\vec{E}_l \tag{3.74}$$

Inserting Eq. (3.73) into Eq. (3.74) yields the following equilibrium condition for the macroscopic polarization

$$\vec{P} = n_{\text{air}}\bar{\alpha}\vec{E} + \frac{n_{\text{air}}\bar{\alpha}}{3\varepsilon_0}\vec{P}. \tag{3.75}$$

It is interesting to note that this equation is formally very similar to the radiation transport equation derived later in this chapter. Substituting $\vec{P}$ with its macroscopic description Eq. (3.72) yields the so called Clausius-Mosotti relation:

$$\frac{\varepsilon_r - 1}{\varepsilon_r + 2} = \frac{n_{\text{air}}\bar{\alpha}}{3\varepsilon_0}. \tag{3.76}$$

In air the magnetic permeability can safely be approximated as $\mu_r = 1$, such that ε_r can be substituted with the squared refractive index $n^2 = \varepsilon_r\mu_r$:

$$\frac{n^2 - 1}{n^2 + 2} = \frac{n_{\text{air}}\bar{\alpha}}{3\varepsilon_0}. \tag{3.77}$$

which is called Lorentz-Lorenz equation. Therefore, in the following derivation of the Cabannes and Rayleigh cross section, expressions

$$\frac{n^2 - 1}{n_{\text{air}}(n^2 + 2)} \left(= \frac{\bar{\alpha}}{3\varepsilon_0} \right) \tag{3.78}$$

are directly related to the molecular polarizability.

3.2.2.3. Rayleigh and Cabannes Scattering

Before the development of quantum mechanics Lord Rayleigh (1842-1919) approximated the scattered electrical field $\vec{E}_{\text{sca}}$ of molecules using the assumption that molecules can be described by dielectric homogeneous spheres with relative dielectric permeability ε_r. With this simple model Rayleigh was able to obtain expressions for both, the scattering cross section and the angular dependence of molecular elastic scattering. How the macrophysical permeability is effectively linked to the electronic degrees of freedom is not trivial to explain. A direct approach is to regard the first order of a (periodical) perturbation to the energetic levels (see Fig. 3.5) of an air molecule. The expressions occurring therein must be identical to the result of the classical approach, see [Hohm and Kerl, 1990] for measurements and theory. In the macroscopic description the wavelength dependence of the Rayleigh scattering cross section σ_{Rayleigh} is related to the refractive index of air, Eq. (3.77). Despite Young's statement (see p. 34), at some places in this work elastic (Cabannes) scattering is sometimes loosely called Rayleigh scattering in order to maintain compatibility with literature of spectroscopic measurements with wavelength resolution insensitive to the physics detailed in [Young, 1981, Witschas, 2012]. From electromagnetic theory it is known, that the scattered electromagnetic field of a molecule has a dipole characteristic (e.g. [Nolting, 1997]), caused by the periodically induced charge displacement. In the near field (measured with wavelength comparable to the "size" of the molecule) the electric field at the observer position has not only transverse character but also shows longitudinal patterns which rapidly decay in the far field, such that in large distance from the center of scattering the EM wave is purely transverse. In the radiation zone, i.e. far away from the molecule, the electric field assumes the form

$$\vec{E}(\vec{r}) = \frac{k^2}{4\pi\varepsilon_0} \frac{e^{ikr}}{r} (\vec{e}_{\text{sca}} \times \vec{p}) \times \vec{e}_{\text{sca}} = \frac{k^2}{4\pi\varepsilon_0} \frac{e^{ikr}}{r} (\vec{p} - \vec{e}_{\text{sca}}(\vec{e}_{\text{sca}} \cdot \vec{p})) \tag{3.79}$$

where $\vec{e}_{\text{sca}} = \vec{r}/r$ and $\vec{p}$ is the induced dipole momentum. The orientation of the dipole moment $\vec{p}$ depends on the polarization of the incident light and will be specified further below. Depending on $\vec{p}$, the expansion of the scattered electric field $\vec{E}$ into the scattered coordinate system (Chapter 3.2.1) is

$$\vec{E}_{\text{sca}\parallel}(\vec{r}) = \vec{E}(\vec{r})\vec{e}_{\text{sca}\parallel} \tag{3.80}$$

$$= \frac{k^2}{4\pi\varepsilon_0} \frac{e^{ikr}}{r} (\vec{p} - \vec{e}_{\text{sca}}(\vec{e}_{\text{sca}} \cdot \vec{p}))(\vec{e}_{\text{inc}} - \vec{e}_{\text{sca}} \cos(\theta_S)) \tag{3.81}$$

$$= \frac{k^2}{4\pi\varepsilon_0} \frac{e^{ikr}}{r} (\vec{p}\vec{e}_{\text{inc}} - \vec{p}\vec{e}_{\text{sca}} \cos(\theta_S)) \tag{3.82}$$

$$= \frac{k^2}{4\pi\varepsilon_0} \frac{e^{ikr}}{r} \vec{p}(\vec{e}_{\text{inc}} - \vec{e}_{\text{sca}} \cos(\theta_S)) \tag{3.83}$$

for the parallel component and

$$\vec{E}_{\text{sca}\perp}(\vec{r}) = \vec{E}(\vec{r})\vec{e}_{\text{sca}\perp} \tag{3.84}$$

$$= \frac{k^2}{4\pi\varepsilon_0} \frac{e^{ikr}}{r} (\vec{p} - \vec{e}_{\text{sca}}(\vec{e}_{\text{sca}} \cdot \vec{p}))\vec{e}_{\text{inc}} \times \vec{e}_{\text{sca}} \tag{3.85}$$

$$= \frac{k^2}{4\pi\varepsilon_0} \frac{e^{ikr}}{r} \vec{p} \cdot (\vec{e}_{\text{inc}} \times \vec{e}_{\text{sca}}) \tag{3.86}$$

for the perpendicular component with respect to the scattered coordinate system. At this point the induced dipole momentum for a molecule $X = N_2, O_2$ with polarizability tensor $\boldsymbol{\alpha}_X$ is substituted:

$$\vec{p}(\theta_X, \varphi_X) = \mathbf{R}(\theta_X, \varphi_X)\boldsymbol{\alpha}_X \mathbf{R}^T(\theta_X, \varphi_X)\vec{E}_{\text{inc}} \tag{3.87}$$
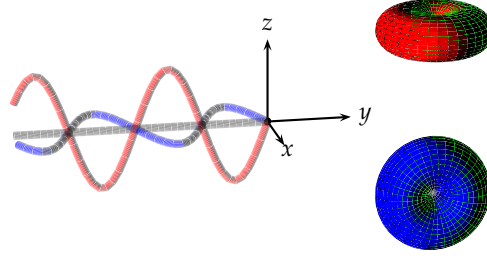
Figure 3.7.: Differential induced dipole scattering cross sections for light linearly polarized in z direction (red) and in x direction (blue).

where θ_X and φ_X represent the orientation angles of the molecule and **R** are combined (multiplied) y-axis-and-then-z-axis rotation matrices, where the molecule axis is oriented along the z axis. For diatomic symmetric molecules only two angles are needed. In order to describe all "effects" of Rayleigh scattering related to the anisotropy of the polarisability, the electric field components need to be averaged (or integrated, [Eberhard, 2010]) over all orientations of the molecule leading to Tab. 3.1. For sake of simplicity in discussing major angular features I continue the derivation assuming isotropic polarizability. This assumption merely affects Eq. (3.83) because in case of isotropic polarizability $\vec{p}$ is parallel to $\vec{E}_{\text{inc}}$ and Eq. (3.87) becomes

$$\vec{p} \approx \bar{\alpha} \vec{E}_{\text{inc}} \tag{3.88}$$

i.e. $\vec{p}$ is exactly perpendicular to the incident direction $\vec{e}_{\text{inc}}$. Fig. 3.7 shows the angular characteristics of dipole scattering for two different orientations of the incident electric field vector. As a consequence of $\boldsymbol{\alpha} \approx \bar{\alpha}$ Eq. (3.83) simplifies as follows:

$$\vec{E}_{\text{sca}\|}(\vec{r}) \overset{\boldsymbol{\alpha} \approx \bar{\alpha}}{\approx} -\frac{k^2}{4\pi\varepsilon_0} \frac{e^{ikr}}{r} \vec{p} \vec{e}_{\text{sca}} \cos(\theta_s). \tag{3.89}$$

By relating $\{\vec{E}_{\text{inc}\|}, \vec{E}_{\text{inc}\perp}\}$ defined in Equ.s (3.52) and (3.53) to $\{\vec{E}_{\text{sca}\|}, \vec{E}_{\text{sca}\perp}\}$ according to Eq. (3.55), the complex scattering amplitude matrix for dipole scattering is found:

$$\frac{1}{kr} \begin{pmatrix} S_{2,\text{dipole}} & 0 \\ 0 & S_{1,\text{dipole}} \end{pmatrix} = \frac{k^2\bar{\alpha}}{4\pi\varepsilon_0 r} \begin{pmatrix} \cos(\theta_S) & 0 \\ 0 & 1 \end{pmatrix} \tag{3.90}$$

(purely complex phases cancel in the Poynting vector calculation and are thus not important). Applying Eq. (3.58) and subsequently Eq. (3.59) leads to the Rayleigh-Stokes scattering matrix:

$$S_{\text{Stokes, dipole}} = \frac{k^6\bar{\alpha}^2}{16\pi^2\varepsilon_0^2} \begin{pmatrix} \frac{1}{2}(1+\mu_s^2) & \frac{1}{2}(\mu_s^2-1) & 0 & 0 \\ \frac{1}{2}(\mu_s^2-1) & \frac{1}{2}(1+\mu_s^2) & 0 & 0 \\ 0 & 0 & \mu_s & 0 \\ 0 & 0 & 0 & \mu_s \end{pmatrix}. \tag{3.91}$$

Following the derivation of properties of Rayleigh scattering according to Section 3.2.1.2, the differential scattering cross section is deduced from its definition Eq. (3.62) and Eq. (3.91):

$$\frac{\mathrm{d}\sigma_{\text{dipole}}}{\mathrm{d}\Omega} = \frac{1}{k^2} S_{\text{Stokes,dipole},11} = \frac{k^4\bar{\alpha}^2}{32\pi^2\varepsilon_0^2}(1+\mu_s^2) \tag{3.92}$$

The total cross section is calculated by integrating the 11 element of the Stokes scattering matrix (see Eq. (3.63)). Since the 11 element only depends on the cosine of the scatter angle, the solid angle integration of the directional part yields

$$\int_0^{2\pi} \int_{-1}^{1} \frac{1}{2}(1+\mu^2) \, \mathrm{d}\mu \, \mathrm{d}\varphi = 2\pi \frac{1}{2} \left[\mu + \frac{1}{3}\mu^3\right]_{-1}^{1} = \frac{8\pi}{3} \tag{3.93}$$

i.e.

$$\sigma_{\text{dipole}} = \int_{4\pi} \frac{d\sigma_{\text{dipole}}}{d\Omega} \, d\Omega = \frac{k^4 \bar{\alpha}^2}{16\pi^2 \varepsilon_0^2} \frac{8\pi}{3} \overset{k=\frac{2\pi}{\lambda}}{=} \frac{24\pi^3}{\lambda^4} \frac{\bar{\alpha}^2}{9\varepsilon_0^2}. \tag{3.94}$$

Finally, the phase matrix of dipole scattering is derived according to Eq. (3.65):

$$\boldsymbol{P}_{\text{dipole}}(\mu_S) = \frac{4\pi}{\sigma_{\text{dipole}}} \frac{d\sigma_{\text{dipole}}}{d\Omega} = \frac{3}{2} \begin{pmatrix} \frac{1}{2}(1+\mu_s^2) & \frac{1}{2}(\mu_s^2-1) & 0 & 0 \\ \frac{1}{2}(\mu_s^2-1) & \frac{1}{2}(1+\mu_s^2) & 0 & 0 \\ 0 & 0 & \mu_S & 0 \\ 0 & 0 & 0 & \mu_S \end{pmatrix} \tag{3.95}$$

with its famous 11 element

$$P_{\text{dipole}}(\mu_S) = \frac{3}{4}(1+\mu_s^2). \tag{3.96}$$

In literature several different methods to calculate σ_{Rayleigh} are presented. Using one of these, σ_{Rayleigh} differs from σ_{dipole} only with respect to using a the tensor instead of a scalar (average) polarizability. The authors of [Bodhaine et al., 1999] for example state that the newest available data for the refractive index considering the detailed composition of an air parcel should be used. Using the Lorentz-Lorenz Eq. (3.77) the fraction on the right side of Eq. (3.94) containing the molecular polarizability is expressed through the macroscopic refractive index. This is the reason why Bodhaine et al.'s suggestion relies on deep physical arguments. In order to account for the anisotropy, the total cross sections averaged over all possible orientations of the molecular rotation axis must be calculated. Doing this and given $n(\lambda)$ for example from [Ciddor, 1996], one obtains the effective molecular Rayleigh cross section [Bodhaine et al., 1999] :

$$\sigma_{\text{Rayleigh}} = \frac{24\pi^3}{\lambda^4} \left(\frac{n^2(\lambda)-1}{n_{\text{air}}(n^2(\lambda)+2)} \right)^2 F_{\text{air}}(\lambda) \tag{3.97}$$

where n_{air} is the number density at the respective pressure and temperature taken for the refractive index. With respect to σ_{dipole} in Eq. (3.94), the cross section is modified by the factor $F_{\text{air}}(\lambda)$. The King correction factor $F_{\text{air}}(\lambda)$ accounts for the anisotropy of the polarizability and is defined as [Bates, 1984]

$$F_{\text{air}}(\lambda) = 1 + \frac{2}{9}\varepsilon(\lambda) \quad \text{with} \quad \varepsilon(\lambda) = \left(\frac{\gamma(\lambda)}{\alpha(\lambda)} \right)^2. \tag{3.98}$$

In $F_{\text{air}}(\lambda)$ the ratio of the anisotropy of the polarizability $\gamma(\lambda)$ and the average polarizability $\bar{\alpha}(\lambda)$ appear. $F_{\text{air}}(\lambda)$ is obtained by performing the orientation averaging of Eq. (3.87). The reader interested in details of this procedure is again referred to [Eberhard, 2010]. In this work, the King correction factor F_{air} is calculated as suggested by [Bates, 1984] using the correction factors of the individual air constituents. The anisotropy $\gamma(\lambda)$ is calculated using the parametrization obtained by [Chance and Spurr, 1997]. The angular dependence of the differential scattering cross section depends on the polarization of the incident wave. [Landgraf et al., 2004] present unified expressions for the scattering phase matrices of molecular scattering according to [Kattawar et al., 1981]. Tab. 3.1 contains also a parametrization of the phase matrix for rotational Raman scattering

	A	B	C	N
Rayleigh	$3(45+\varepsilon)$	$30(9-\varepsilon)$	36ε	$(180+40\varepsilon)$
Cabannes	$3(180+\varepsilon)$	$30(36-\varepsilon)$	36ε	$40(18+\varepsilon)$
rot. Raman	3	-10	36	40

Table 3.1.: Parametrization of Phase Matrices reproduced from [Landgraf et al., 2004] based on [Kattawar et al., 1981]. King factors F_{air} are used to obtain squared ratios ε (not to be confused with extinction coefficients!) of γ and $\bar{\alpha}$
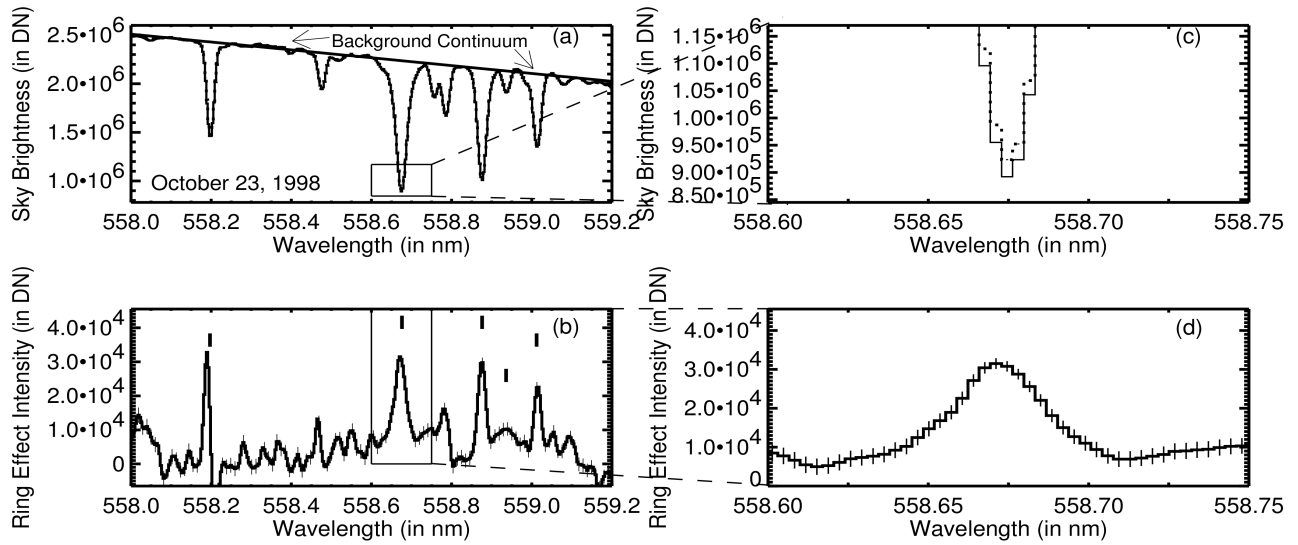
Figure 3.8.: **a)** measured daylight spectrum. **b)** measurement - **elastic** RT model. **c)** and **d)**: blown-up versions of **a** and **b**. Plot from [Pallamraju et al., 2000].

presented later in the following section. The unified phase matrix is [Landgraf et al., 2004]:

$$\mathbf{P}(\mu_s) = \frac{1}{N} \begin{pmatrix} A(1+\mu_s^2)+C & -A(1-\mu_s^2) & 0 & 0 \\ -A(1-\mu_s^2) & A(1+\mu_s^2) & 0 & 0 \\ 0 & 0 & 2A\mu_s & 0 \\ 0 & 0 & 0 & B\mu_s \end{pmatrix} \tag{3.99}$$

with parameters according to Tab. 3.1. In contrast to Eq. (3.92), θ_s is the scatter angle and $\mu_s = \cos(\theta_s)$.

3.2.2.4. Rotational Raman Scattering (RRS)

In the early 1960s it was discovered independently by [Shefov, 1959] and [Grainger and Ring, 1962] that direct light intensities in of scattered Sun light are brighter then predicted by radiation transport theory. Fig. 3.8 shows the effect of RRS in a day light spectrum. When comparing simulated and measured signal, it becomes obvious (panels **b** and **d** in Fig. 3.8) that there is light where no light should be. After controversial discussion about the underlying physics it was suggested by [Kattawar et al., 1981] that rotational and vibrational Raman scattering is the most likely mechanism of causing the filling in of Fraunhofer lines. [Kattawar et al., 1981] also collected earlier results from [Placzek and Teller, 1933] in order to present a entire set of formulas necessary to describe the phenomenon. In these inelastic scattering processes the rotational and/or the vibrational state of the molecule is changed, and energy is added/removed to/from the radiation field by a small wavelength shift of the scattered photons. The quantitative simulation of these processes is a challenging task [Joiner et al., 1995, M.Vountas et al., 1998, van Deelen et al., 2005, Landgraf et al., 2004]. In this work it is described how the Monte Carlo method is applied to account for the rotational Raman scattering (RRS) in atmospheric radiation transport. After motivating the rotational Raman effect by classical arguments, the following quantum mechanical treatment is based on the diploma thesis of Markus Bussemer [Bussemer, 1993]. Bussemer implemented a single scattering radiative transfer code in order to obtain an approximate Ring spectrum for the DOAS (see Chapter 6) fit routine. A central part of his algorithm is to calculate cross sections for RRS causing a wavelength (i.e. energy) shift of the incident photon. From the view point of Monte Carlo radiative transfer modeling, the change of wavelength is computationally challenging because the optical properties of the medium change and thus have to be recalculated after a RRS event.

3.2.2.5. Classical Description of RRS

A rotating diatomic molecule has an oscillating polarizability with twice the molecular rotation frequency ω_r, see Fig. 3.9. In order to qualitatively understand the rotational Raman effect, one considers the time dependence of the polarizability along an axis perpendicular transverse to the propagation direction as fol-
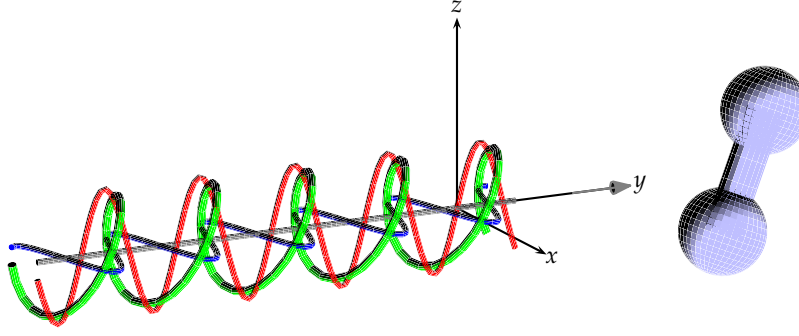
Figure 3.9.: The general case of the rotation axis orientation of a diatomic molecule (again symbolized as a rigid rotator) with anisotropic polarizability and an arbitrarily polarized wave. The components of the electric field vectors are in red and blue and have a relative phase shift, the trajectory of the tip of the associated $\vec{E}$ is shown in green. The molecule rotates around the z-axis. Therefore, the incident wave "sees" an oscillating polarizability in x direction. Due to the symmetry of the polarizability tensor, polarization is equal after a half rotation of the molecule. Therefore the induced dipole is modulated with twice the molecular rotation frequency, motivating the $\Delta J = \pm 2$ selection rule .

lows. Let the atom-atom axis rotate in the xy plane around the z axis. Then the propagation direction of the incident wave is pointing along the y axis and the wave is linearly polarized in x direction, i.e. the electric field oscillates along the x axis. The polarizability tensor reduces to two dimensions and becomes

$$\boldsymbol{\alpha} = \begin{pmatrix} c & -s \\ s & c \end{pmatrix} \begin{pmatrix} \alpha_{\parallel} & 0 \\ 0 & \alpha_{\perp} \end{pmatrix} \begin{pmatrix} c & s \\ -s & c \end{pmatrix} = \begin{pmatrix} \alpha_{\parallel} c^2 + \alpha_{\perp} s^2 & (\alpha_{\parallel} - \alpha_{\perp})sc \\ (\alpha_{\parallel} - \alpha_{\perp})sc & \alpha_{\parallel} s^2 + \alpha_{\perp} c^2 \end{pmatrix} \tag{3.100}$$

which is the inverse of the transformation to principal axes, $c = \cos(\omega_r t)$ and $s = \sin(\omega_r t)$. The electric field is oscillating along the x-direction, so the induced dipole moment is:

$$\vec{p} = \boldsymbol{\alpha} \begin{pmatrix} E_x \cos(\omega_{inc} t) \\ 0 \end{pmatrix} = \begin{pmatrix} (\alpha_{\parallel} c^2 + \alpha_{\perp} s^2) \\ (\alpha_{\parallel} - \alpha_{\perp})sc \end{pmatrix} E_x \cos(\omega_{inc} t). \tag{3.101}$$

Only the x component of the dipole moment is considered further:

$$p_x \quad = \quad (\alpha_{\parallel} \cos^2(\omega_r t) + \alpha_{\perp} \sin^2(\omega_r t)) E_x \cos(\omega_{inc} t) \tag{3.102}$$

$$\overset{\sin^2(x) = 1 - \cos^2(x)}{=} \quad ((\alpha_{\parallel} - \alpha_{\perp})\cos^2(\omega_r t) + \alpha_{\perp}) E_x \cos(\omega_{inc} t) \tag{3.103}$$

$$\overset{\cos^2(\omega_r t) = \frac{1}{2} + \frac{1}{2}\cos(2\omega_r t)}{=} \quad \left(\frac{1}{2}(\alpha_{\parallel} + \alpha_{\perp}) + \frac{1}{2}(\alpha_{\parallel} - \alpha_{\perp})\cos(2\omega_r t)\right) E_x \cos(\omega_{inc} t) \tag{3.104}$$

$$= \quad \bar{\alpha} E_x \cos(\omega_{inc} t) + \frac{\gamma}{2} \cos(2\omega_r t) E_x \cos(\omega_{inc} t). \tag{3.105}$$

Using the identity $\cos(x)\cos(y) = \frac{1}{2}(\cos(x+y) + \cos(x-y))$, one finally arrives at the remarkable result

$$p_x = \bar{\alpha} E_x \cos(\omega_{inc} t) + \frac{\gamma}{4}\left(\cos(\omega_{inc} + 2\omega_r)t + \cos(\omega_{inc} - 2\omega_r)t\right) E_x \tag{3.106}$$

which is interpreted as follows. If the rotating molecule has a anisotropic polarizability $\gamma \neq 0$, the scattered electric field consists of light with modified frequencies $\omega_{inc} \pm 2\omega_r$ and Rayleigh scattered light at the incident wave length $\lambda_{inc} = 2\pi c/\omega_{inc}$. Due to energy conservation the molecules rotational momentum changes about the energy corresponding to two light quanta of the frequency ω_r. The amplitude of the RR scattered light must be proportional to γ^2, because the differential scattering cross section depends in the second order on the induced dipole momentum. The classical description can only explain qualitatively the physics of rotational Raman scattering. Results from a more detailed quantum mechanical treatment are presented in
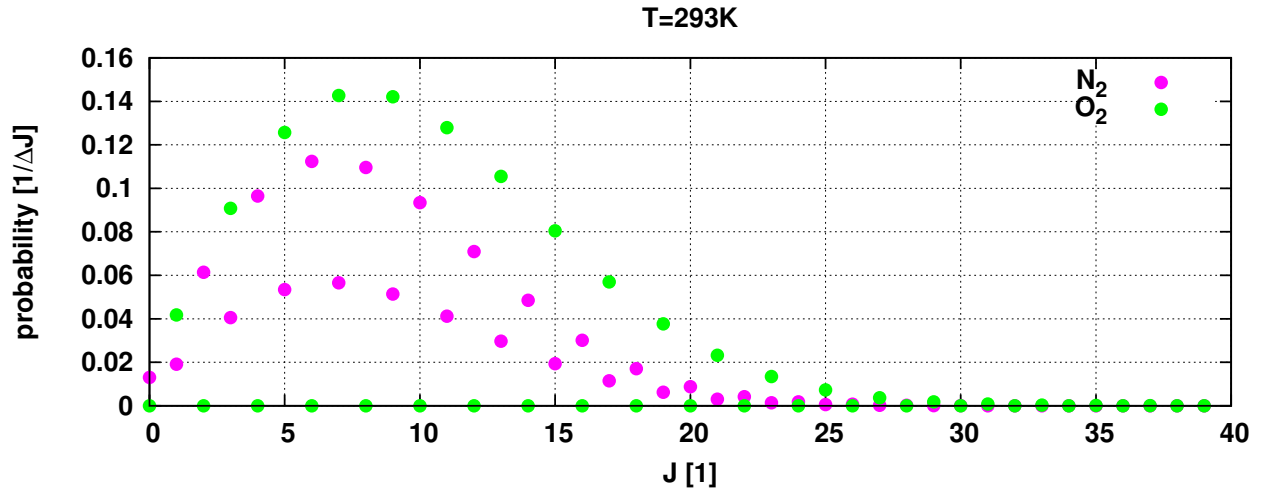
Figure 3.10.: Thermal probabilities $w(J, T)$ of encountering (if) N_2 and O_2 molecules in certain rotational states J at 293K. Note that the statistical weights $g_{J=\text{even/odd}}$ of oxygen (Tab. 3.2) are the reason for the exclusive presence of odd J rotational states.

the following section.

3.2.2.6. Rotational State of N_2 and O_2

As a simple model for the inertial properties of N_2 and O_2, which can probably derived from first order approximations to the general case, the model of the rigid rotator is used. Quantum mechanical rigid rotators have the rotational energy

$$E_{\text{rot}}(J) = hcB_0 J(J+1) \tag{3.107}$$

where the inertial constants B_0 for N_2 and O_2 are given in Tab. 3.2. In thermodynamic equilibrium the

gas	$B_0[\text{cm}^{-1}]$	$g_{J=\text{even}}$	$g_{J=\text{odd}}$	I
$^{14}N_2$	1.98973	6	3	1
$^{14}O_2$	1.4378	0	1	0

Table 3.2.: from [Bussemer, 1993], p. 20, after [Penney et al., 1974].

occurrences of rotational energies are Boltzmann distributed according to the local temperature (heat bath):

$$z(J, T) = g_J(2J + 1) \exp\left(-\frac{E(J)}{k_B T}\right) \tag{3.108}$$

The factor $(2J + 1)$ stems from the degeneracy of J, and g_J is a statistical weight originating from a selection rule for the nuclear spin (see [Chance and Spurr, 1997] for some more details or [Placzek and Teller, 1933] for a deep discussion). It is useful to define the thermodynamic probabilities:

$$w(J, T) = \frac{z(J, T)}{Z(J, T)} \quad \text{with} \quad Z(T) = \sum_{J=0}^{\infty} z(J, T) \tag{3.109}$$

where $Z(J, T)$ is the rotational energy partition function of the respective molecule. $w(J, T)$ can be interpreted as the probability to encounter a molecule in rotational energy state J. Fig. 3.10 shows the thermodynamic probabilities $w(J, T)$ of encountering either a N_2 or O_2 at 293K is a certain rotational state J.

3.2.2.7. RRS Cross Sections and Phase Matrix

RRS is the inelastic interaction of photons of the radiation field with the diatomic molecules being in rotational state J through the anisotropic polarizability γ. The energy balance equation is

$$E_{\text{rot}}(J_i) + h\nu_i = E_{\text{rot}}(J_f) + h\nu_f \tag{3.110}$$

where $E_{\text{rot}}(J_{i/f})$ is the rotational energy of the molecule in the initial / final state, ν_i is the frequency of the incident photon before scattering and ν_f is the frequency after scattering. In a RRS event, the interaction of the photons with the molecule cause a change in the rotational quantum number of the molecule. As already mentioned before, the selection rule is $\Delta J = \pm 2$. Absorption lines originating from transitions $J \to J + 2$ are called Stokes lines, $J \to J - 2$ are Anti-Stokes lines. The energy of a photon with wavelength λ is $h\nu = h/\lambda$. The energy balance Eq. (3.110) becomes

$$\frac{1}{\lambda_i} - \frac{1}{\lambda_f} = \frac{\Delta E_{\text{rot}}(J_i \to J_f)}{hc} \tag{3.111}$$

with

$$\Delta E_{\text{rot}}(J_i \to J_f) = E_{\text{rot}}(J \pm 2) - E_{\text{rot}}(J) \tag{3.112}$$

$$= \begin{cases} \Delta E_{\text{rot}}^+(J) := hcB_0(4J + 6) & \text{Stokes transitions} \\ \Delta E_{\text{rot}}^-(J) := hcB_0(2 - 4J) & \text{Anti-Stokes transitions} \end{cases} . \tag{3.113}$$

The scattering cross section for a single transition $J_i \to J_f$ in a RRS event ([Chance and Spurr, 1997] or [Bussemer, 1993]) is:

$$\sigma_{J_i \to J_f}(\lambda_i) = \frac{256\pi^5}{27\lambda_f^4} b_{J_i \to J_f} \gamma^2(\lambda_i) \tag{3.114}$$

with the Placzek-Teller coefficients obtained from first order perturbation theory (see [Penney et al., 1974] for a derivation from transition matrix elements)

$$b_{J \to J'} = \begin{cases} b_J^+ := \frac{3(J+1)(J+2)}{2(2J+1)(2J+3)} & \text{for } J' = J + 2 \\ b_J^- := \frac{3J(J-1)}{2(2J+1)(2J-1)} & \text{for } J' = J - 2 \\ 0 & \text{else} \end{cases} . \tag{3.115}$$

The total RRS cross section for scattering of light away from λ is obtained by adding the individual cross sections for transitions for all states of thermodynamic relevance (according to the local Boltzmann distribution $w(J, T)$):

$$\sigma_{\text{RRS}}(\lambda) = \sum_{J=0}^{\infty} w(J, T)(\sigma_{J \to J-2})(\lambda) + \sigma_{J \to J+2})(\lambda)) \tag{3.116}$$

Fig. 3.11 shows the cross sections. The line intensity shape exhibits only a weak variation with temperature. In contrast, the wavelength dependence is significant. The width of the line shape (the redistribution interval) increases with wavelength. Light of 300nm wavelength for example is redistributed into a wavelength region of 2nm around the so called Cabannes (Rayleigh scattering) line, at 500nm the redistribution range is already 4nm and at around 800nm the redistribution interval has a width of 7nm. The scattering phase matrix for RRS according to the unified molecular Stokes scattering matrix scheme is given in Tab. 3.1.

3.2.3. Molecular Absorption Processes and Electronic Molecular States

The second important interaction mechanism between molecules and the radiation field is absorption by excitation of electronic states. Electrons are bound to the atomic nuclei through the Coulomb and mutual spin interaction (leading to the Pauli principle and other population rules). Due to the wave nature (and the uncertainty principle) of electrons the energy levels associated with the spatial areas in which electrons reside are discrete. As a consequence, molecules absorb and emit photons of certain energies being representable
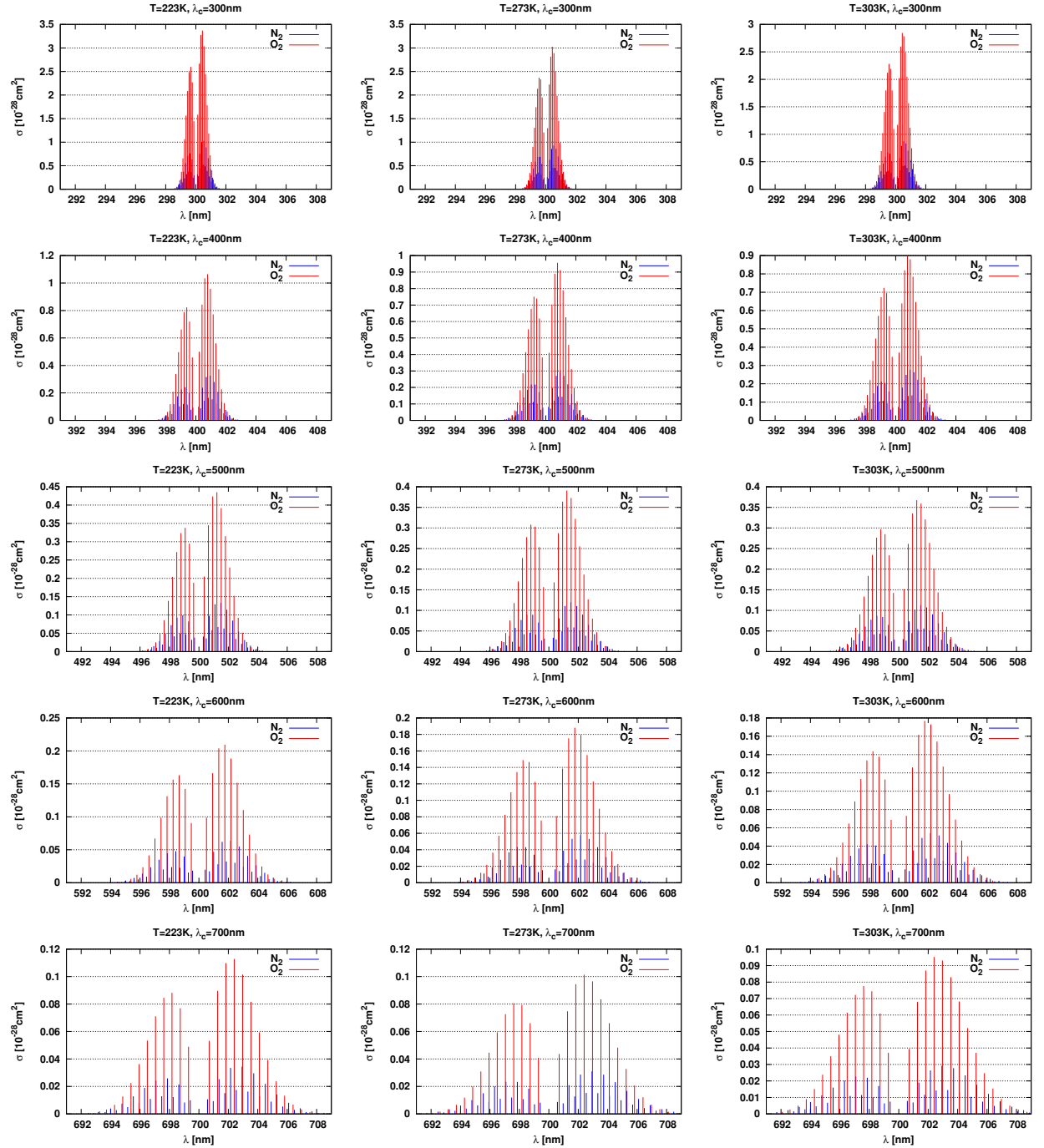
Figure 3.11.: RRS line intensities for 300, 400, 500, 600 and 700nm (panel rows top to bottom) and T=-50, 0 and 30°C (columns left to right).

by differences between the discrete energy levels of the molecule:

$$h\nu = E_f - E_i. \tag{3.117}$$

The uncertainty principle expressed in terms energy and time uncertainty

$$\Delta E \Delta t \geq \frac{\hbar}{2} \tag{3.118}$$

establishes a relation between the lifetime of the excited state Δt and its energy difference to the ground state ΔE. For most absorption lines in the UV-IR spectral range of atmospheric constituents, the life times of isolated (i.e. non interacting) molecules is in the order of a second leading to negligible natural line widths [Liou, 1980]. Two other mechanisms influence the line shape of molecular absorption lines. These are the shortening of the lifetime caused by collisions between the molecules and the broadening of lines due to the Maxwell-Boltzmann distributed velocity related Doppler shift. In case of collision broadening the resulting Lorentzian line shape follows then by assuming that the behavior of the electric field strength of the released photons behaves similarly to a damped harmonic oscillator with damping constant corresponding to the collision-reduced lifetime τ. The line shape caused by the Doppler shift is Gaussian (Boltzmann distributed kinetic energies). Both line shapes need to be combined through a convolution in order to obtain the effective line shape, see appendix C of [Frankenberg, 2004] or Chapter 8 of [Wendisch and Yang, 2012] for practical instructions for line shape calculations and details on the theory.

3.2.4. Scattering On Spherical Particles - Mie Theory

In view of the morphological complexity of aerosol particles (see pictures in Chapter 2.2) it seems impossible to describe the scattered radiation emerging from such particles without detailed knowledge of their exact shape. In remote sensing applications it is thus necessary to approximate the single scattering properties of particle with a simple model. This is to assume that particles are optically homogeneous spheres (i.e. with respect to the refractive index) and that they can be described by a single complex refractive index. The approach is justified up to a reasonable extent, because the multiple scattering radiation transport process tends to "smear out" to some extent but not entirely some details of radiation patterns originating from distinctive microphysical structures and optical resonances of the particles. Furthermore, their are indeed some particles such as fog and cloud droplets, i.e. liquid suspensions of matter in the gaseous atmosphere, that nearly fulfill the assumption of spherical shape. Only the shape of larger droplets show deviations from the spherical shape (e.g. [Pruppacher and Klett, 2010, Rogers and Yau, 2000]) during sedimentation.

The first complete and exact physical description of the scattering of electromagnetic radiation on a dielectric sphere was put forward 1908 by Gustav Mie when he published his theoretic work on the electromagnetic properties of conducting spheres. In [Mie, 1908], Mie calculated the electromagnetic field outside a metal sphere with a radius comparable to the wavelength and exposed to a plane electromagnetic wave. The nature of the paper is rather mathematical and many reviews (e.g. [Huffman and Bohren, 1983]) have been made to restructure Mie's achievement. In this section only results are presented that are relevant to atmospheric radiation transport. Motivation for introducing Mie theory results is to document how the extinction coefficient, single scattering albedo and elements of the phase matrix for a size distribution of spheres are efficiently calculated in the program.

3.2.4.1. Parameters of Mie's Theory

With a constant (with wavelength) refractive index, the electromagnetic properties would be scale-invariant and would only depend on the ratio of the sphere radius and the wavelength. Fundamental to Mie's theory is the so called size parameter

$$x = \frac{2\pi r}{\lambda} = kr. \tag{3.119}$$

The plane electromagnetic wave, which the sphere with refractive index m_{sphere} is exposed to, propagates in a medium with refractive index m_{bath}. The ratio of both indices is

$$m_r = \frac{m_{\text{sphere}}}{m_{\text{bath}}}. \tag{3.120}$$

In atmospheric optics, where the refractive index m_{bath} is close to one it is often loosely set $m_r \approx m_{\text{sphere}}$. In this work the following convention according to [Wiscombe, 1979], i.e. to restrict the imaginary part of m to negative values, is used:

$$m_r = m_{\text{re}} - i|m_{\text{im}}|. \tag{3.121}$$

Another quantity which frequently occurs in the derivation is $z = m_r x$ and the wave number $k = \frac{2\pi}{\lambda}$

3.2.4.2. Optical Properties of a Dielectric Sphere with Large Diameter in Comparison with the Wavelength

Central to calculating optical properties of a single dielectric sphere are the so called (complex) Mie coefficients a_n and b_n. To summarize [Wiscombe, 1979] or the relevant chapters in [Huffman and Bohren, 1983], Mies coefficients are the expansion coefficients of the electric and magnetic fields inside and outside the dielectric sphere with respect to a certain set of orthogonal functions. The a_n and b_n are obtained by exposing the expansion to the continuity conditions of the fields tangentially and across the interface between the particle and the surrounding atmosphere. In [Wiscombe, 1979] recommendations are given how to obtain a_n and b_n in a numerically stable way. If the Mie coefficients are given, the optical properties can be calculated as follows. The extinction and scattering cross sections are given by

$$\sigma_e = \frac{2\pi}{k^2} \sum_{n=1}^{N} (2n+1)\Re(a_n + b_n) \tag{3.122}$$

$$\sigma_s = \frac{2\pi}{k^2} \sum_{n=1}^{N} (2n+1)(|a_n|^2 + |b_n|^2) \tag{3.123}$$

Single scattering albedos are obtained from the relationship $\varpi_0 = \frac{\sigma_s}{\sigma_e}$.

3.2.4.3. Mie Stokes Scattering Phase Matrix

In RTM the phase matrix and its (11) element, the phase function is of central importance. The asymmetry parameter of the Mie phase function is given by (e.g. [Wiscombe, 1979]):

$$g = \frac{1}{2} \int_{-1}^{+1} \mu P_{\text{Mie}}(\mu) \, d\mu \tag{3.124}$$

$$= \frac{4\pi}{k^2 \sigma_s} \sum_{n=1}^{N} \left\{ \frac{n(n+2)}{n+1} \Re(a_n a_{n+1}^* + b_n b_{n+1}^*) + \frac{2n+1}{n(n+1)} \Re(a_n b_n^*) \right\} \tag{3.125}$$

In order to describe the scattered electric field the so called scattering amplitudes are needed. According to [Wiscombe, 1979] instead of calculating S_1 and S_2 ($S_3 = S_4 = 0$ for spherical and optically homogeneous particles) in Eq. (3.55) it is computationally more effective to calculate the following related quantities $S_{\pm}(\mu)$:

$$S_+(\mu) = \sum_{n=1}^{N} \frac{2n+1}{n(n+1)} (a_n + b_n)[\pi_n(\mu) + \tau_n(\mu)] \tag{3.126}$$

$$S_-(\mu) = \sum_{n=1}^{N} \frac{2n+1}{n(n+1)} (a_n - b_n)[\pi_n(\mu) - \tau_n(\mu)]. \tag{3.127}$$

Using the $S_{\pm}(\mu)$, the relationship between incident and scattered Stokes vectors is

$$\begin{pmatrix} F_{\text{sca}} \\ Q_{\text{sca}} \\ U_{\text{sca}} \\ V_{\text{sca}} \end{pmatrix} = \frac{1}{x^2} \begin{pmatrix} S_{11} & S_{12} & 0 & 0 \\ S_{12} & S_{11} & 0 & 0 \\ 0 & 0 & S_{33} & S_{34} \\ 0 & 0 & -S_{34} & S_{33} \end{pmatrix} \begin{pmatrix} F_{\text{inc}} \\ Q_{\text{inc}} \\ U_{\text{inc}} \\ V_{\text{inc}} \end{pmatrix} \tag{3.128}$$
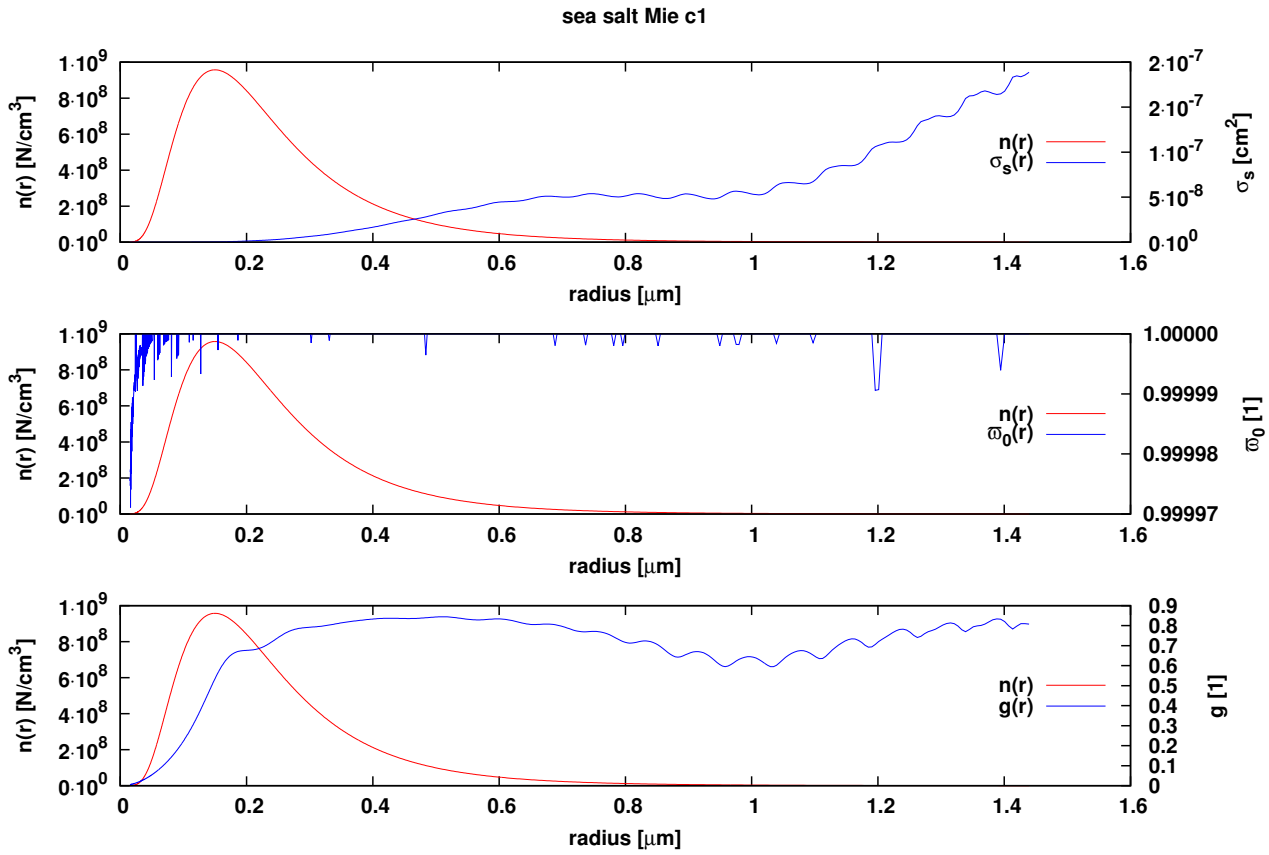
Figure 3.12.: Optical properties (scattering coefficient σ_s, single scattering albedo ϖ_0 and asymmetry parameter g) at λ=577nm of a distribution of sea salt particles with $N = 300cm^{-3}$, mean radius $0.15\mu m$, $\sigma = 1.76$ and refractive index $1.349082 - i6.789928 \cdot 10^{-9}$. The resulting total extinction is 0.081743 km^{-1} and the effective asymmetry parameter $g = 0.785944$.

with

$$S_{11} = \tfrac{1}{4}(S_+^* S_+ + S_-^* S_-) \tag{3.129}$$

$$S_{12} = -\tfrac{1}{4}(S_+^* S_- + S_-^* S_+) \tag{3.130}$$

$$S_{33} = \tfrac{1}{4}(S_+^* S_+ - S_-^* S_-) \tag{3.131}$$

$$S_{34} = \tfrac{i}{4}(S_+^* S_- - S_-^* S_+). \tag{3.132}$$

3.2.4.4. Bulk Optical Properties

In the atmosphere, aerosol particles are present in different sizes described by the size distributions (see Chapter 2.2.3). Aerosol particles associated with the same class have equal or at least nearly equal refractive indices. In order to obtain the effective (bulk) optical properties for a distribution of such particles with equal refractive index, the optical properties of each size have to be integrated with the size distribution $N(r)$. Extinction and scattering coefficients are obtained by

$$\varepsilon_{e|s} = \int \sigma_{e|s}(r)N(r)\,\mathrm{d}r \approx \sum_i \sigma_{e|s}(r_i)N(r_i)\Delta r_i. \tag{3.133}$$

Analogously the bulk phase matrix is calculated with

$$\mathbf{P}(\mu) = \frac{1}{\varepsilon_s} \int \mathbf{P}(\mu, r) \sigma_s(r) N(r) \, dr \tag{3.134}$$

$$\approx \frac{1}{\varepsilon_s} \sum_i \mathbf{P}(\mu, r_i) \sigma_s(r_i) N(r_i) \Delta r_i \tag{3.135}$$

$$= \frac{4\pi}{\varepsilon_s k^2} \sum_i \mathbf{S}(\mu, r_i) N(r_i) \Delta r_i. \tag{3.136}$$

Carrying out the integration as it is suggested by Eq. (3.136) in a direct way is inefficient, because for every phase matrix element evaluation the size integration has to be repeated. There is a way to circumvent this problem by separating the angle dependent functions $\pi_n(\mu)$ and $\tau_n(\mu)$ from the Mie coefficients and carrying out the size integration once for the Mie coefficients.
First it is defined:

$$\alpha_{n\pm}(x, m_r) = \frac{2n+1}{n(n+1)} (a_n(x, m_r) \pm b_n(x, m_r)) \tag{3.137}$$

$$\gamma_{n\pm}(\mu) = \pi_n(\mu) \pm \tau_n(\mu). \tag{3.138}$$

This separates the μ dependent functions from the rest. Since the scattering amplitudes in form of the $S_\pm$ are products

$$S_\pm(\mu) = \sum_{n=1}^{N} \alpha_{n\pm}(x, m_r) \gamma_n^\pm(\mu), \tag{3.139}$$

the size integration can be conducted once for all angles. Looking at Eqs. (3.129-3.132) the relevant complex summands are $S_+ S_+^*$, $S_+ S_-^*$, $S_- S_+^*$ and $S_- S_-^*$:

$$S_+^* S_+(x, m_r, \mu) = \sum_{m=1}^{N} \sum_{n=1}^{N} \alpha_{m+}^*(x, m_r) \alpha_{n+}(x, m_r) \gamma_{m+}(\mu) \gamma_{n+}(\mu) \tag{3.140}$$

$$S_+^* S_-(x, m_r, \mu) = \sum_{m=1}^{N} \sum_{n=1}^{N} \alpha_{m+}^*(x, m_r) \alpha_{n-}(x, m_r) \gamma_{m+}(\mu) \gamma_{n-}(\mu) \tag{3.141}$$

$$S_-^* S_+(x, m_r, \mu) = \sum_{m=1}^{N} \sum_{n=1}^{N} \alpha_{m-}^*(x, m_r) \alpha_{n+}(x, m_r) \gamma_{m-}(\mu) \gamma_{n+}(\mu) \tag{3.142}$$

$$S_-^* S_-(x, m_r, \mu) = \sum_{m=1}^{N} \sum_{n=1}^{N} \alpha_{m-}^*(x, m_r) \alpha_{n-}(x, m_r) \gamma_{m-}(\mu) \gamma_{n-}(\mu) \tag{3.143}$$

The size spectrum integration is carried out for the products $\alpha_{m\pm}^*(x, m_r) \alpha_{n\pm}(x, m_r)$ which form a matrix:

$$\overline{\alpha_{m\pm}^* \alpha_{n\pm}} \approx \sum_i \alpha_{m\pm}^*(x_i, m_r) \alpha_{n\pm}(x_i, m_r) N(r_i) dr_i \tag{3.144}$$

with $x_i = r_i k$. Phase matrix elements then are obtained by adding all elements *mn* with the products of the angle dependent functions $\gamma_{m\pm}(\mu) \gamma_{n\pm}(\mu)$ analog to Eqs. (3.140-3.143), but with $\overline{\alpha_{m\pm}^* \alpha_{n\pm}}$ instead of $\alpha_{m\pm}^*(x, m_r) \alpha_{n\pm}(x, m_r)$. In Fig. 3.13 phase matrix elements for a sea salt particle distribution are shown. The log normal distribution parameters are given in the caption of Fig. 3.12.

3.3. Mathematical Description of Radiation Transport

In the previous sections all necessary components needed to describe radiation transport in the atmosphere are presented. In this section, the integro-differential radiation transport equation RTE is introduced. Although it is possible to derive this equation from the Maxwell equations this is not done here. The more interested reader is referred to [Mishchenko, 2002]. It is important to note that in this case the RTE is phenomenologically motivated and not deduced from first principles. The gap to the fundamentals of the governing physical Maxwell equations expresses itself in the inability of the RTE to describe phenomena like weak localization and other wave interference effects [Mishchenko, 2009]. The mathematical objects of the RTE are single-velocity and non-interfering particles. However, as is known from model comparison to
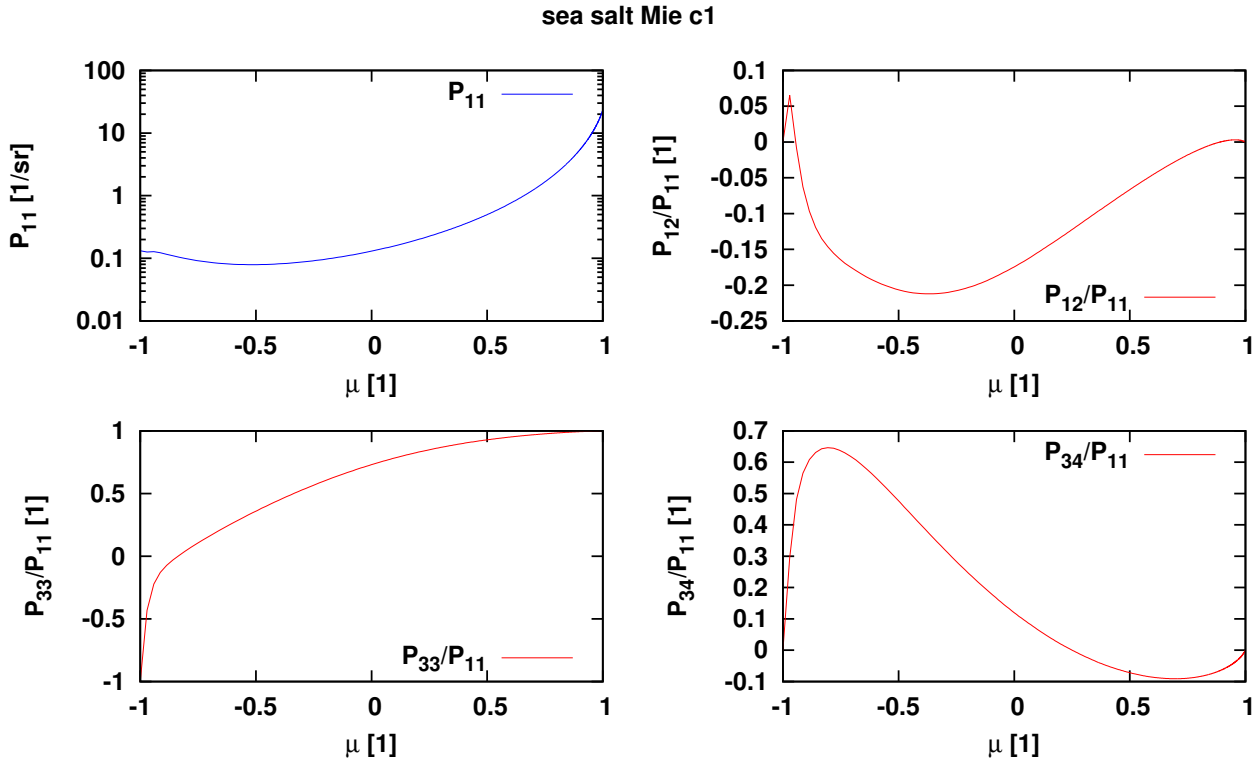
sea salt Mie c1

Figure 3.13.: Phase matrix elements of the sea salt particle distribution. Log normal distribution parameters are given in the caption of Fig. 3.12.

observations, the approach is well justified in the UV/vis/NIR range for most situations in atmospheric RT.

3.3.1. Radiance and Irradiance

In order to describe the strength, the location and direction dependence of a radiation field the concept of the radiance $R(\vec{r}, \vec{\omega}, \lambda)$ in $[W \cdot m^{-2} \cdot sr^{-1} \cdot nm^{-1}]$ (power per unit area and per unit solid angle and per unit wavelength) and the irradiance $F(\vec{r}, \vec{\omega}, \lambda)$ in $[W \cdot m^{-2} \cdot nm^{-1}]$ is introduced. The relationship between R and F is not trivial. As a reference for the more interested reader [Hovenier et al., 2004] is recommended and also [Ramamoorthi and Hanrahan, 2001] may serve as a starting point. In order to summarize the most important aspects of the relationship, think about a small plane area dA which is oriented according to its surface normal $\vec{n}$. Suppose that the area dA is exposed to an isotropic radiation field and that the radiation power per square meter and wavelength is P_{rad}. Then the irradiance F impinging $d\vec{A}$ is

$$F = \frac{dP_{\text{rad}}}{dA} = \int_{2\pi} R \cos(\theta_i) \, d\Omega \tag{3.145}$$

which is closely related to the time averaged Poynting vector (see Eq. (3.14)). Here, the solid angle integration is done over the half sphere 2π obtained when slicing a small sphere around the center $\vec{r}$ of the area element dA perpendicular to the surface normal $\vec{n}$. The angle θ_i is the incident angle between the negative transmitted directed radiance with the surface normal $\vec{n}$. Eq. (3.145) motivates the following definition of the radiance:

$$R = \frac{1}{\cos(\theta_i)} \frac{dP_{\text{rad}}^2}{dA \, d\Omega} = \frac{1}{\cos(\theta_i)} \frac{dF}{d\Omega}. \tag{3.146}$$

To give an example, the solar irradiance $F_0(\lambda)$, a plot of which is shown in Fig. 2.3, is given in $[W \cdot m^{-2} \cdot nm^{-1}]$.

3.3.2. Absorption, Scattering and Extinction Coefficients

In order to describe radiation transport, effective or cumulative optical properties as a function of space and direction are needed. In this work, the direction dependence of the optical properties is dropped. This

approach is well justified when thinking of nearly spherical or at least randomly oriented particles and molecules. In case of crystals occurring for example in cirrus clouds or in the solid phase of clouds which tend to orient themselves during sedimentation the assumption of isotropy fails and biases the model. A thinkable mechanism of orienting molecules are strong magnetic or electric fields attached to permanent electric or magnetic molecular dipole moments. None of the latter fields are usually present in the atmosphere, such that optical anisotropy of molecules can be considered negligible. Instead of cross sections $\sigma_{e|a|s}$ given in [cm^2] and number densities of species i with n_i in [cm^{-3}], so called coefficients $\varepsilon_{e|a|s}$ in [km^{-1}] are used. Coefficients can be regarded as a measure for number of events per unit length, i.e. they are densities with respect to length. Extinction is defined as the sum of absorption and scattering

$$\varepsilon_{(e)}(\vec{r}, \lambda) = \varepsilon_a(\vec{r}, \lambda) + \varepsilon_s(\vec{r}, \lambda). \tag{3.147}$$

Where it is allowed by the context, the index e for "extinction" is dropped.

3.3.2.1. Absorption Coefficients

In a small region (in units of some wavelengths) around a location in the atmosphere, molecules can be considered homogeneously distributed. Absorption of an electromagnetic wave with an intensity according to its Poynting vector is quantified by the respective wavelength depending cross section. The total absorption coefficient is

$$\varepsilon_a(\vec{r}, \lambda) = \sum_i^{N_a} n_{a,i}(\vec{r})\sigma_{a,i}(\vec{r}, \lambda) = \sum_i^{N_a} \varepsilon_{a,i}(\vec{r}, \lambda) \tag{3.148}$$

where $n_{a,i}$ is the absorber number density, and N_a: is the number of considered absorbers. In the equation the dependence on the location $\vec{r}$ is shown in order to remind that cross sections depend on thermodynamic properties like pressure and temperature and also the specific chemical composition at $\vec{r}$. At some places in the text, also the symbol $\beta(\lambda, \vec{r})$ is used for the absorption coefficient.

3.3.2.2. Scattering and Differential Scattering Coefficients

The second important element in the description of the transport process (besides absorption) is scattering. According to Eq. (3.64) the differential scattering cross section is separated into the total cross section and the phase matrix. Phase functions are the (11) elements of the phase matrices. Molecular phase matrices are defined in Section 3.2.2.3, Tab. 3.1. Particle phase matrices obtained from Gustav Mie's theory are given in Section 3.2.4.4. The total scattering cross section is defined similarly as Eq. (3.148) by

$$\varepsilon_s(\vec{r}, \lambda) = \sum_i^{N_s} \varepsilon_{s,i}(\vec{r}, \lambda) = \sum_i^{N_s} n_{s,i}(\vec{r})\sigma_{s,i}(\vec{r}, \lambda) \tag{3.149}$$

where i is again the species index, but this time for scattering molecules and particles. $n_{s,i}$ is the scatterer number density and N_s is the number of considered scatterers. The effective phase matrix is the scattering cross section-weighted (effective) phase matrix of all scatterers

$$\mathbf{P}(\vec{r}, \mu, \lambda) = \frac{1}{\varepsilon_s(\lambda, \vec{r})} \sum_i n_i(\vec{r})\sigma_{s,i}(\vec{r}, \lambda)\mathbf{P}_i(\mu_s), \tag{3.150}$$

where $\mu = \cos(\theta)$ is the cosine of scattering angle. Elements of the phase matrix are normalized to 2. In order to describe the intensity of light scattered on the particle the so called phase function, the 11 element of the phase matrix is used:

$$P(\vec{r}, \mu, \lambda) = \mathbf{P}_{11}(\vec{r}, \mu, \lambda). \tag{3.151}$$

3.3.3. Optical Thickness and Transmission

The next important descriptive element for the radiation transport in an optical medium is the transmission function:

$$T(\tau) := \exp(-\tau). \tag{3.152}$$

Transmission is a function of the optical thickness

$$\tau(\vec{r}_1 \to \vec{r}_2) := \int_0^{|\vec{r}_2 - \vec{r}_1|} \varepsilon\left(\vec{r}_1 + l \cdot \frac{\vec{r}_2 - \vec{r}_1}{|\vec{r}_2 - \vec{r}_1|}\right) dl \tag{3.153}$$

which is in general defined as the extinction coefficient integrated over a path in the medium (in this case a finite linear path $\vec{r}_1 \to \vec{r}_2$). The transmission function is naturally obtained by considering the change of the intensity dI of light traversing a small differential distance dl

$$dI = -\varepsilon \cdot I \cdot dl, \tag{3.154}$$

i.e. the differential intensity change is proportional to the incident intensity, the extinction coefficient and the differential length (Beer-Lambert-Bougert law). For an interval $[0, l]$ the solution of the differential equation above contains the transmission function:

$$I(l)/I(0) = T(\varepsilon \cdot l) := \exp\left(-\varepsilon \cdot l\right). \tag{3.155}$$

3.3.4. Scattering

In an optical medium the number of extinction/absorption/scattering events on a differential path with length dl is

$$\text{\# ext./abs./sca. events on } dl = \varepsilon_{e|a|s} \cdot dl. \tag{3.156}$$

Given an extinction event, the probability for scattering is quantified by the single scattering albedo (SSA):

$$\omega_0(\vec{r}, \lambda) = \frac{\varepsilon_s(\vec{r}, \lambda)}{\varepsilon(\vec{r}, \lambda)} \tag{3.157}$$

Provided that scattering of radiation $R(\vec{r}, \vec{\omega}, \lambda)$ at $\vec{r}$ occurs, the amount of radiation scattered into a cone of "polar" thickness $d\mu$ with direction $\vec{\omega}$ and with cosine of the cone angle μ is

$$\frac{d\mu}{2} P(\vec{r}, \vec{\omega}' \cdot \vec{\omega}, \lambda) \cdot R(\vec{r}, \vec{\omega}, \lambda) \tag{3.158}$$

where $\mu = \vec{\omega}' \cdot \vec{\omega}$. The total amount of radiation $R_s(\vec{r}, \vec{\omega}, \lambda)$ scattered into direction $\vec{\omega}$ is

$$R_s(\vec{r}, \vec{\omega}, \lambda) = \varepsilon(\vec{r})\omega_0(\vec{r}) \, dl \cdot \frac{1}{4\pi} \int_0^{2\pi} \int_{-1}^{+1} P(\vec{r}, \vec{\omega}' \cdot \vec{\omega}, \lambda) \cdot R(\vec{r}, \vec{\omega}, \lambda) \, d\phi \, d\mu \tag{3.159}$$

$$= \frac{\varepsilon_s(\vec{r}) \, dl}{4\pi} \int_0^{4\pi} P(\vec{r}, \vec{\omega} \to \vec{\omega}_0, \lambda) \cdot R(\vec{r}, \vec{\omega}, \lambda) \, d\vec{\omega}. \tag{3.160}$$

In the following $R_s(\vec{r}, \vec{\omega}, \lambda)$ is also called source term.

3.3.5. Incident (Ir)Radiance

In the UV/vis/NIR spectral range in the atmosphere the dominating light source is the extinction-attenuated irradiance of the sun:

$$F(\vec{r}, \lambda) := F_0(\lambda) \cdot T(\tau^*(\vec{r})) = F_0(\lambda) \cdot \exp\left(-\tau^*(\vec{r})\right) \tag{3.161}$$

where $\vec{r}_*$ is the sun position and $\tau^*(\vec{r}) := \tau(\vec{r}_* \to \vec{r})$ is the optical thickness between the sun and the point of interest $\vec{r}$. In the further description it is useful to introduce the incident radiance

$$R^*(\vec{r}, \vec{\omega}, \lambda) := F(\vec{r}, \lambda)\chi^*(\vec{r}, \vec{\omega}) \tag{3.162}$$

where

$$\chi^*(\vec{r}, \vec{\omega}) = \frac{1}{\Delta\Omega^*} \begin{cases} 1 & \vec{\omega} \cdot \frac{\vec{r} - \vec{r}_*}{|\vec{r} - \vec{r}_*|} > \cos\left(\sqrt{\Delta\Omega^*/\pi}\right) \\ 0 & \text{else} \end{cases} \tag{3.163}$$

is the characteristic function in $[\mathrm{sr}^{-1}]$ and $\Delta\Omega^*$ is the solid angle of the sun disc.

3.3.6. The Black Surface Single Scattering Approximation

In some situations in atmospheric RT, it is allowed to approximate the physics by the single scattering model. In such case, the light is emitted by the sun, enters the atmosphere, is transmitted on the linear path originating in the sun to the field of view (FOV) of the detector and is scattered therein into the direction of the detector. After scattering the light is transmitted to the detector. For later purposes a simple single scattering model is introduced. The FOV is δ-function-like, which describes that the detector measures the strength of the radiation field of a singular direction. This device is of course a pure hypothetical construction which can only be approximated in reality, because all physical detectors have a FOV larger then zero in order to be able to collect any amount of light at all, however, in the limit of very small FOVs and/or a sufficiently homogeneous radiation field within the FOV the δ-FOV approximation is well justified. The next approximation taken here is to set the surface albedo to zero. The effect of a purely absorbing (i.e. black) surface is that only light scattered in the atmosphere contributes to the measurement, if the detector is not oriented directly at the sun. This also serves the purpose to maximize the fraction of the relevant processes under investigation, i.e atmospheric scattering.

In this single scattering model, the line of sight (LOS) is defined by the observation point $\vec{r}_\bullet$ and the observation direction $\vec{\omega}_\bullet$ as a parametrized straight line:

$$\vec{r}_l = \vec{r}_\bullet + l \cdot \vec{\omega}_\bullet : \tag{3.164}$$

The upper integration boundary is $l_{\max}$:

$$l_{\max} = \begin{cases} l_g & \text{distance to ground (if)} \\ \infty & \text{else} \end{cases} . \tag{3.165}$$

In the single scattering approximation the solar light illuminates the FOV. For sake of readability the wavelength dependence is dropped, as also only elastic scattering is considered. The measured irradiance F_{ssa} (in the single scattering approximation) is

$$F_{\mathrm{ssa}} = \int\limits_0^{l_{\max}} T(\vec{r}_l \to \vec{r}_\bullet) R_s(\vec{r}_l, -\vec{\omega}_\bullet)\, \mathrm{d}l, \tag{3.166}$$

i.e. the intensity is the integral of all light scattered along the line of sight at $\vec{r}$ and transmitted to the detector. The light scattered at $\vec{r}_l$ is measured by the source term R_s with respect to the incident radiance Eq. (3.162) according to Eq. (3.160):

$$R_s(\vec{r}, \vec{\omega}) = \frac{1}{4\pi} \int\limits_{-\Delta\Omega^*(\vec{r})} \varepsilon_s(\vec{r}) P(\vec{r}, \vec{\omega}' \to \vec{\omega}) \cdot F_0 \cdot T(\vec{r}_*(\vec{\omega}') \to \vec{r})\, \mathrm{d}\vec{\omega}'. \tag{3.167}$$

Inserting Eq. (3.167) into Eq. (3.166) yields

$$F_{\mathrm{ssa}} = \frac{1}{4\pi} \int\limits_0^{l_{\max}} T(\vec{r}_l \to \vec{r}_\bullet) \int\limits_{-\Delta\Omega^*(\vec{r})} \varepsilon_s(\vec{r}_l) P(\vec{r}_l, \vec{\omega}' \to -\vec{\omega}_\bullet) \cdot F_0 \cdot T(\vec{r}_*(\vec{\omega}') \to \vec{r}_l)\, \mathrm{d}\vec{\omega}'\, \mathrm{d}l. \tag{3.168}$$

In total Eq. (3.168) calculates the amount of light emitted by the sun, F_0, transmitted from the sun to the point $\vec{r}_l$ on the LOS $T(\vec{r}_*(\vec{\omega}') \to \vec{r}_l)$, scattered inside the FOV, i.e. the LOS, $\varepsilon_s(\vec{r}_l)P(\vec{r}_l, \vec{\omega}' \to -\vec{\omega}_\bullet)$ and then transmitted to the detector $T(\vec{r}_l \to \vec{r}_\bullet)$. The justification of the single scattering approximation breaks down, if the mean free path length with respect to the mean scattering coefficient in the medium is in the range of $l_{\max}$ or smaller, then multiple scattering needs to be considered. The applicability of the single scattering model is investigated in chapter 7.4.1, where the simple model is checked for validity and then extended to account for inelastic scattering.

3.3.7. Radiative Transfer Equations

The correct description of a radiation transport process must conserve energy in the whole transport domain (i.e. the atmosphere). One way to achieve this is to discretize the whole into sub regions and to assure energy conservation in all of these. The characteristic quantity which is used to describe the radiation field is the spectral radiance R. The term spectral is associated with "per unit wavelength interval". In the following, the term "spectral" is dropped and the irradiance F and the radiance R are used, but it is kept in mind that R and F both are resolvable for wavelength.

3.3.7.1. Scalar RTE

To the first approximation, radiation transport is described by the so called scalar radiative transfer equation, in which it is assumed that the elements of radiation can be described as single velocity, non interfering, unpolarized (i.e. scalar) and weightless particles. Furthermore it is assumed that all optical properties are isotropic, i.e. direction independent $\mathrm{d}\varepsilon_{e|s|a}/\mathrm{d}\vec{\omega} = 0$). In the scalar approximation the radiative transfer equation (scalar RTE) is:

$$\vec{\omega} \cdot \vec{\nabla} R(\vec{r}, \vec{\omega}) = -\varepsilon_e(\vec{r}) R(\vec{r}, \vec{\omega}) + \frac{\varepsilon_s(\vec{r})}{4\pi} \int_{4\pi} R(\vec{r}, \vec{\omega}') P(\vec{r}, \vec{\omega} \cdot \vec{\omega}') \, \mathrm{d}\vec{\omega}. \tag{3.169}$$

where $P(\vec{r}, \vec{\omega} \cdot \vec{\omega}')$ is the 11 element of the effective phase matrix $\mathbf{P}(\vec{r}, \mu)$. This reduction of the phase matrix to its 11 element is central to the scalar approach. The boundary conditions describe the light source and are given as

$$S_0(\vec{r}, \vec{\omega}) = \varepsilon_a(\vec{r}) B_\lambda(T(\vec{r})) + P_0(\lambda) \Theta_{\text{Sun}}(\vec{r}). \tag{3.170}$$

S_0 has the units of $W/(m^3 sr)$ and is the density of thermally emitted photons (B_λ is the Planck function) plus a term describing solar photons, where $P_0(\lambda)$ is the emitting power per solid angle of the Sun at its surface in units of $\frac{W}{sr\mu m}$ and

$$\Theta_{\text{Sun}}(\vec{r}) = \begin{cases} \frac{3}{4\pi R_{\text{Sun}}^3} & \text{if } \vec{r} \text{ is in the Sun} \\ 0 & \text{else} \end{cases}. \tag{3.171}$$

In the UV/vis/NIR the thermal emission $B_\lambda(T(\vec{r}))$ is negligible and therefore omitted in this work.

3.3.7.2. Vector RTE

With respect to the neglect of polarization, the systematic error introduced in the scalar RTE can be assessed as follows. Using solely the 11 element of the phase matrix implicitly assumes that electromagnetic wave reaching a scatter object is unpolarized and that also the scattered radiation is unpolarized. From [Lacis et al., 1998] it is known that the systematic error introduced by neglecting the polarization state and its propagation during transport is in the range of some percent. In Chapter 5.3.1 these discrepancies are investigated for an example case. The error of the scalar approach correlates positively with the amount of molecular scattering in the light path, because Rayleigh scattering is much more polarizing incident unpolarized light than scattering on larger particles. If the polarization state of light is taken into account in the description, the radiative transfer equation assumes the same algebraic form, but the radiance is replaced by the respective Stokes vector and instead of the phase function the phase matrix is used

$$\vec{\omega} \cdot \vec{\nabla} \vec{R}(\vec{r}, \vec{\omega}) = -\varepsilon_e(\vec{r}) \vec{R}(\vec{r}, \vec{\omega}) + \frac{\varepsilon_s(\vec{r})}{4\pi} \int_{4\pi} \vec{R}(\vec{r}, \vec{\omega}') \mathbf{Z}(\vec{r}, \vec{\omega}, \vec{\omega}') \, \mathrm{d}\vec{\omega}'. \tag{3.172}$$

where

$$\mathbf{Z}(\vec{r}, \vec{\omega}, \vec{\omega}') = \mathbf{L}(i_{\text{sca}}(\vec{\omega}', \vec{\omega})) \mathbf{P}(\vec{r}, \vec{\omega} \cdot \vec{\omega}') \mathbf{L}(i_{\text{inc}}(\vec{\omega}', \vec{\omega})). \tag{3.173}$$

Details on how the i_{inc} and i_{sca} are calculated are found in Chapter 3.1.4.3. In this work Eq. (3.172) is referred to as the vector RTE. The boundary conditions of the vector RTE are those of the scalar case but put into the first component of the vector source $\vec{S}_0(\vec{r}, \vec{\omega})$, which is zero in other respects, implying that emerging radiation from the Sun is unpolarized.

Monte Carlo Methods in Radiation Transport Calculations

This chapter describes the usage of random numbers in the context of high and variable dimensional numerical integration. The underlying integrals appear in certain integral representations of functionals of the radiative transfer equation (RTE). It is shown that by randomly sampling ordinates of the integration domain, the so called ray tracing or random quadrature method, estimates of functionals of the RTE solution are obtained. In order to introduce the reader to the field, the chapter begins with an introduction of Monte Carlo concepts in 1D integration problems. Random quadrature methods in the context of radiative transfer modeling can be divided into subgroups of which two methods, the so called sequential importance sampling (SIS) and the Metropolis Hastings (Markov chain Monte Carlo, MCMC) methods. Both methods are compared to some extent in the middle section of the chapter. It turns out that, probably owed to current knowledge about the underlying math, the choice of the respective method (i.e. SIS or MCMC) depends on the dimensionality of the problem. The section which follows treats the application of the crude SIS method of solving the scalar RTE. It is shown, how estimates of algebraically similar RTE functionals can be obtained from and related to estimates of the scalar solution using the so called importance sampling technique. This concerns not only the simulation of polarization but also the estimation of 1st and 2nd order radiance derivatives.

4.1. General Monte Carlo Methods

4.1.1. Numerical Integration

It is instructive to formally reduce the dimensionality of an integration problem to one dimension. Basis of the following considerations is the general integration problem:

$$I = \int_a^b g(x)\, \mathrm{d}x. \tag{4.1}$$

4.1.1.1. Crude Monte Carlo

The Riemann method to obtain I is to sub divide the integration domain $X = [a,b]$ into N equally spaced portions and to let $N \to \infty$:

$$I = \lim_{N\to\infty} \frac{1}{N} \sum_{n=1}^{N} (b-a)g(x_n) \quad \text{with} \quad x_n = a + \frac{n-\frac{1}{2}}{N}(b-a). \tag{4.2}$$

In other words: the Riemann method is to *systematically* take x samples x_n of the integration domain, and to calculate the mean value of $(b-a)g(x_n)$, i.e.

$$I = \langle (b-a)g \rangle_{[a,b]}. \tag{4.3}$$

As suggested by Eq. (4.2), the expression

$$I_n = (b-a)g(x_n) \tag{4.4}$$

is an estimate of the integral I. Conversely, the Monte Carlo method to obtain I is to *randomly* sample from $[a, b]$ and apply Eq. (4.3). The most direct way (crude Monte Carlo) of calculating Eq. (4.1) is to use the uniform probability density function (PDF) over the interval $[a, b]$:

$$p_{[a,b]}(x) = \frac{1}{b-a} \underbrace{\begin{cases} 1 & \text{if } x \in [a, b] \\ 0 & \text{else} \end{cases}}_{\chi_{[a,b]}(x)}. \tag{4.5}$$

where $\chi_{[a,b]}(x)$ is called the characteristic function of the interval $[a, b]$. Using $p_{[a,b]}(x)$ Eq. (4.1) becomes:

$$I = (b-a) \int_{-\infty}^{+\infty} p_{[a,b]}(x) g(x) \, dx = \int_{-\infty}^{+\infty} \chi_{[a,b]}(x) g(x) \, dx. \tag{4.6}$$

Estimates of the integral are given for each integration domain sample $x_n \sim p_{[a,b]}(x)$. For a series of samples, the arithmetic sample mean gives an approximation of I:

$$I = \lim_{N \to \infty} \frac{1}{N} \sum_{n=1}^{N} (b-a) g(x_n) \quad \text{with} \quad x_n \sim p_{[a,b]}(x), \tag{4.7}$$

compare to Eq. (4.2).

4.1.1.2. Variance of Functional Estimates

Using random numbers, it can be expected that the functional estimates and the sample mean fluctuates randomly. The variance quantifies these fluctuations. Variance is defined as the mean squared difference to the sample mean and can be calculated as follows:

$$\text{var}(I) = \langle (I - \langle I \rangle)^2 \rangle = \langle I^2 \rangle - \langle I \rangle^2. \tag{4.8}$$

According to Eq. (4.8) the variance can be related to the moments M_n of the integrand g, with respect to the probability density function (PDF) from which samples are drawn:

$$M_n = \langle g^n(x) \rangle := \int_{-\infty}^{\infty} g^n(x) p(x) \, dx. \tag{4.9}$$

Expressed through the moments, the variance is:

$$\text{var}(I) = M_2 - M_1^2 \tag{4.10}$$

Given a finite number of functional estimates, the variance can be approximated using

$$\text{var}(I) \approx \frac{1}{N} \sum_{n=1}^{N} I_n^2 - \left(\frac{1}{N} \sum_{n=1}^{N} I_n \right)^2. \tag{4.11}$$

4.1.2. Importance Sampling and Zero Variance Estimates

For sake of simplicity the integration problem is modified and replaced with

$$I = \int_{-\infty}^{+\infty} g(x) \, dx \quad \text{with} \quad g(x) > 0 \tag{4.12}$$

The following identity (importance sampling identitiy) offers an alternate way of obtaining I:

$$I = \int_{-\infty}^{+\infty} g(x) \, dx = \int_{-\infty}^{+\infty} \frac{g(x)}{q(x)} q(x) \, dx. \tag{4.13}$$

Interpreted as a Monte Carlo method this means that samples x_n are drawn from $q(x)$ and that a functional estimate is given by

$$I_n = \frac{g(x_n)}{q(x_n)}.$$ (4.14)

The mean is identical, but the variance changes depend on the choice of $q(x)$:

$$\text{var}(I) = \int_{-\infty}^{+\infty} \left(\frac{g(x)}{q(x)} \right)^2 q(x)\,dx - \left(\int_{-\infty}^{+\infty} g(x)\,dx \right)^2.$$ (4.15)

Of course, it is desired to have as few variance of the functional estimates as possible, so it may be asked which $q(x)$ minimizes the variance. [Kahn, 1950] proved that estimates with zero variance are obtained if

$$q(x) = \frac{g(x)}{I}.$$ (4.16)

The detailed proof can be found in Appendix A.1. Zero variance estimates have the fantastic property that already a single functional estimate is the solution of the integral (insert Eq. (4.16) into Eq. (4.14)). This fact of course reveals the fundamental problem of constructing estimates with zero variance: the solution I must be known in Eq. (4.16) in order to obtain $q(x)$. That circular relationship also sketches another important fact: prior knowledge about the solution can help to construct functional estimates with reduced variance.

The importance sampling technique can be understood also in another way. If it is not possible to draw samples of the integration domain from the normalized $g(x)$ (because the norm is not known) another density $q(x)$ can be used that has a similar shape. Source of the functional variance is then always the ratio Eq. (4.14).

4.1.3. Optimal Sampling

In principle, variance reduced estimates of an integral

$$I = \int f(x)p(x)\,dx$$ (4.17)

are obtained by sampling from the overlap function

$$o(x) := f(x)p(x).$$ (4.18)

Suppose that this is not possible due to the nature of the function $f(x)$ and the density $p(x)$. Considering this situation makes also sense, because calculating the norm of $o(x)$ is the integration problem itself. During the sampling, however, it is possible to obtain a representation of $o(x)$ by collecting values of $o(x_n)$ at the $p(x)$-sampled ordinates. Numerous strategies are thinkable. One is to gradually develop $o(x)$ into a set of orthogonal functions and to sample from the surrogate obtained therewith. An adaptive method is demonstrated in the following.

4.1.3.1. Discretized Importance Sampling (DISIS)

The integration domain is subdivided into $G-2$ discrete portions and the two edge intervals $[\xi_1 = -\infty, \xi_2]$ and $[\xi_{G-1}, \xi_G = \infty]$. While sampling ordinates x_n from $p(x)$, the algorithm collects values $o(x_n)$ and stores them by simple adding and averaging into the bins corresponding to $[\xi_g, \xi_{g+1}]$ where $g = 1, \ldots, G-1$. After having drawn N samples, some information in form of samples $o(x_n \in [\xi_g, \xi_{g+1}])$ for the bin g has been collected and an intermediate estimate $\tilde{I}$ of I is calculated by averaging the $f(x_n)$. A discrete representation of $o(x)$ on the intervals g is obtained:

$$\tilde{o}_g = \frac{\sum_{n=1}^{N} f(x_n)\chi_g(x_n)}{\sum_{n=1}^{N} \chi_g(x_n)}$$ (4.19)

where

$$\chi_g(x) = \begin{cases} 1 & \text{if } x_n \in [\xi_g, \xi_{g+1}] \\ 0 & \text{else} \end{cases}.$$ (4.20)

The expectation of $\tilde{o}_g$ is

$$o_g = \frac{1}{\xi_{g+1} - \xi_g} \int_{\xi_g}^{\xi_{g+1}} f(x)p(x)\,\mathrm{d}x. \tag{4.21}$$

The number of samples N after which $o(x)$ is estimated after Eq. (4.19) in the *normalization step* could be determined according to the standard deviation of the o_g, i.e. normalization is triggered after a certain degree of accuracy has been reached in each bin. Then, in principle two strategies are available: a) continue sampling from $p(x)$ or b) using the discrete PDF

$$\tilde{q}(x) = \frac{1}{\tilde{I}} \sum_{g=1}^{G} \chi_g(x)\tilde{o}_g. \tag{4.22}$$

$\tilde{q}(x)$ is an estimate of

$$q(x) = \frac{1}{I} \sum_{g=1}^{G} \frac{\chi_g(x)}{\xi_{g+1} - \xi_g} \int_{\xi_g}^{\xi_{g+1}} f(x)p(x)\,\mathrm{d}x. \tag{4.23}$$

To some extent, the normalization step could be termed *burn-in period* (compare to the terminology of MCMC). In case of b) the importance sampling math $I = \int f(x)p(x)\,\mathrm{d}x = \int \frac{f(x)p(x)}{\tilde{q}(x)}\tilde{q}(x)\,\mathrm{d}x$ requires introducing weights $w(x) = \frac{p(x)}{\tilde{q}(x)}$. Using the weights, the integral becomes

$$\tilde{I}_{\text{DISIS}} = \frac{\tilde{I}}{N} \sum_{n=1}^{N} \frac{f(x_n)p(x_n)}{\sum_{g=1}^{G} \chi_g(x_n)\tilde{o}_g} \tag{4.24}$$

with samples x_n taken from $\tilde{q}(x)$. Again, the exact/mean expression of I_{DISIS} is:

$$I_{\text{DISIS}} = \tilde{I} \int \frac{f(x)p(x)}{\sum_{g=1}^{G} \chi_g(x)\tilde{o}_g} \tilde{q}(x)\,\mathrm{d}x = I. \tag{4.25}$$

4.1.3.2. Variance of DISIS Estimates

According to Eq. (4.8), the difference in the variance for different estimate ordinate PDF's $p(x)$ and $q(x)$ originates from the second moment M_2 of the estimates:

$$M_2 \quad = \quad \int \left(\frac{f(x)p(x)}{q(x)} \right)^2 q(x)\,\mathrm{d}x \tag{4.26}$$

$$= \quad \int f(x)f(x)\frac{p(x)}{q(x)}p(x)\,\mathrm{d}x \tag{4.27}$$

$$\overset{\text{Eq. (4.23)}}{=} \quad I \int f(x)f(x)\frac{p(x)}{\sum_{g=1}^{G} \frac{\chi_g(x)}{\xi_{g+1} - \xi_g} \int_{\xi_g}^{\xi_{g+1}} f(x')p(x')\,\mathrm{d}x'} p(x)\,\mathrm{d}x \tag{4.28}$$

$$= \quad I \sum_{g=1}^{G} \int_{\xi_g}^{\xi_{g+1}} \frac{f(x)f(x)p(x)p(x)}{\frac{1}{\xi_{g+1} - \xi_g} \int_{\xi_g}^{\xi_{g+1}} f(x')p(x')\,\mathrm{d}x'}\,\mathrm{d}x \tag{4.29}$$

In case of $G \to \infty$ and $\xi_{g+1} \to \xi_g$ it follows from Eq. (4.19):

$$\lim_{\xi_{g+1} \to \xi_g} \frac{1}{\xi_{g+1} - \xi_g} \int_{\xi_g}^{\xi_{g+1}} f(x')p(x')\,\mathrm{d}x' = f(x_g)p(x_g) \tag{4.30}$$
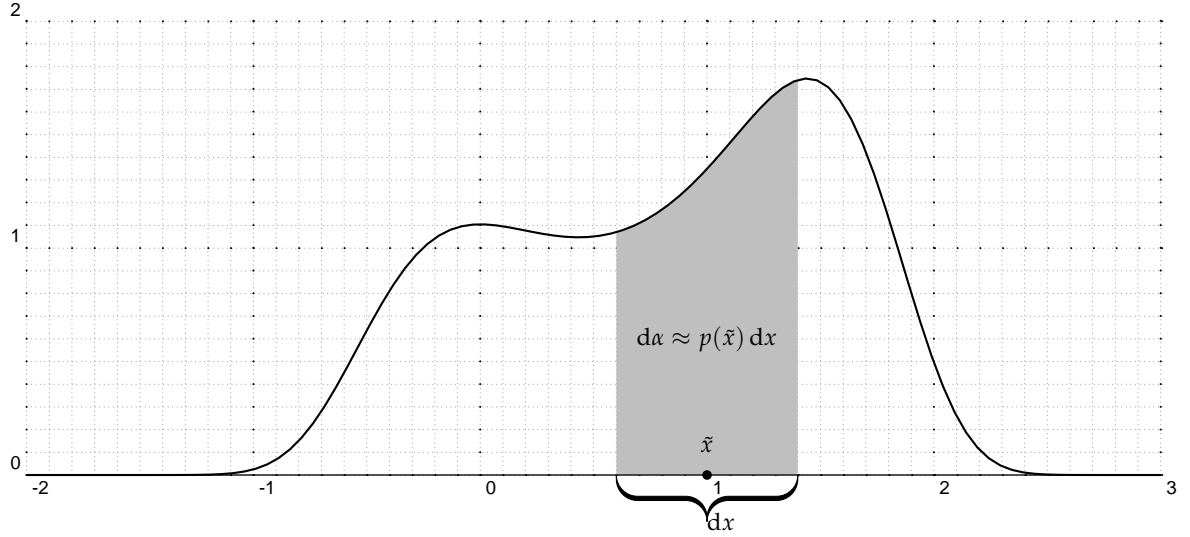
Figure 4.1.: Graph of a pdf $p(x) = \exp\left(-0.8x^4 + 2x^3 - x^2 + 0.1\right)$.

for $x_g = \frac{1}{2}(\xi_{g+1} + \xi_g)$ and

$$\lim_{\xi_{g+1} \to \xi_g} \frac{f(x)}{f(x_g)} = 1 \tag{4.31}$$

$$\lim_{\xi_{g+1} \to \xi_g} \frac{p(x)}{p(x_g)} = 1. \tag{4.32}$$

The consequence is:

$$\lim_{\xi_{g+1} \to \xi_g} M_2 = M_1^2 = I^2 \tag{4.33}$$

i.e. the variance according to Eq. (4.10) vanishes in the limit $G \to \infty$. It becomes also obvious that any variance reduction according or related to DISIS requires computer memory resources, in form of the o_g. Therefore the best (machine dependent) compromise between variance (and computation time) reduction and memory consumption needs to be found. It is also possible to refine the DISIS e.g. by representing $o(x)$ piece-wise by linear functions.

4.1.4. Sampling from Arbitrary Distributions

So far it is assumed that a method to draw samples from arbitrary PDF is given. Here it is discussed how this is done in practice. In the previous section it was concluded that in integration problems one should, if possible, draw samples directly from the respective integration kernel. Let the PDF of interest be $p(x)$.

4.1.4.1. Inverse Transform Sampling (ITS)

The key idea of sampling is that the number of x samples in an interval of extension dx around some $\tilde{x}$ is proportional to the area under the graph of $p(x)$ (see Fig. 4.1). On the other hand, the number of samples is also proportional to the interval $d\alpha$ from which random numbers are taken. In the limit $dx \to 0$ (i.e. $\tilde{x} \to x$) one must thus require

$$d\alpha = p(x)\, dx. \tag{4.34}$$

It follows:

$$\frac{d\alpha}{dx} = p(x) \quad \to \quad \alpha(x) = \int_{-\infty}^{x} p(x')\, dx = P(x), \tag{4.35}$$

where $P(x)$ is called the *cumulative distribution function* (CDF). Using a single $\alpha \in [0,1]$ a x sample is obtained from the inverse relationship:

$$x = P^{-1}(\alpha). \tag{4.36}$$
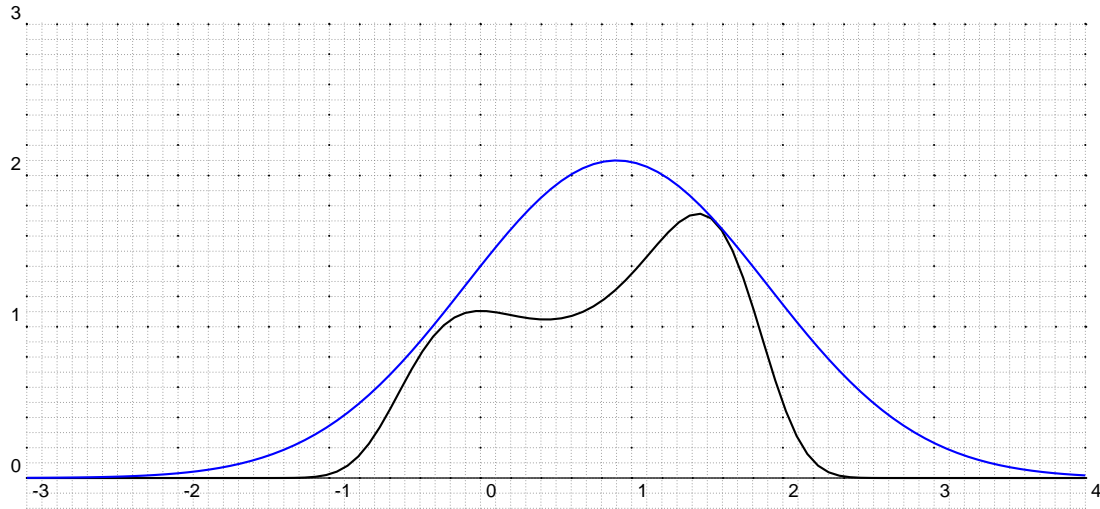
Figure 4.2.: Rejection sampling method to sample from $p(x)$. In this example $q(x) \propto \exp\left(-0.5(x-0.9)^2\right)$ (blue) and $M = 2.1$ is chosen. It is important that $Mq(x) > p(x)$.

Using Eq. (4.36) for sampling is called *inverse transform sampling* (ITS) method. In order to apply Eq. (4.36) to an arbitrary $p(x)$ the inverse of the CDF must be calculated. Sometimes $p(x)$ is given in tabulated form or it is represented by coefficients with respect to an orthonormal function system such as the Legendre polynomials. In these cases $P^{-1}(\alpha)$ is obtained by means of numerical integration. For a given α the area under the graph is integrated until a x is found that fulfills

$$\alpha = \int_{-\infty}^{x} p(x')\,\mathrm{d}x'. \tag{4.37}$$

4.1.4.2. Rejection Sampling (RS)

If the norm of a sample distribution $p(x)$ can not be calculated then there is the method of rejection sampling (RS, [von Neumann, 1951]) to draw samples. The RS method requires, as the importance sampling integration method, a proposal distribution $q(x)$ of similar shape that fulfills the condition

$$Mq(x) \leq p(x) \tag{4.38}$$

with a constant M (see Fig. 4.2). The method is to draw samples from $q(x)$ and accept them with probability $r_a(x) = \frac{p(x)}{Mq(x)}$. The acceptance step can be understood with simulating the weight of the sample according to the importance sampling integration method, since a single sample must have a weight of 1. r_a can also be understood as a survival probability in a Russian roulette game. If the game is survived, the state is alive (i.e. has weight 1) else it is dead (with weight 0).

How efficient is RS? In order to answer this, the proposal density $q(x)$ and the acceptance rate $r_a(x)$ are compared (Fig. 4.3). Proposed state state candidates stem from $q(x)$ and they are accepted with probability $r_a(x)$ it is first desired to have an acceptance ratio close to one. If that is not possible $r_a(x)$ should be at least close to one in important (high density) regions of $q(x)$, or in other words. $q(x)$ should be chosen such that important regions of $p(x)$ correspond to important regions in $q(x)$.

4.1.4.3. The Metropolis Algorithm

Another quite flexible method to draw samples from arbitrary distributions with unknown norm is the Metropolis (M) method. The original method of Metropolis is an extension of the RS method and was published in [Metropolis et al., 1953]. The intention was to generate statistically representative samples of states of a complex thermodynamic system consisting of a large number of particles in order to calculate thermodynamic variables from the accumulated mean of the partition function. Central to the M method is to create a so called Markov chain of $x \in \Omega$ samples $x_0, x_1, \ldots, x_N$. The chain is started in some arbitrary "state" x_0. A new state x_{n+1} is generated using its predecessor x_n by sampling from a symmetric, $x = x_n$
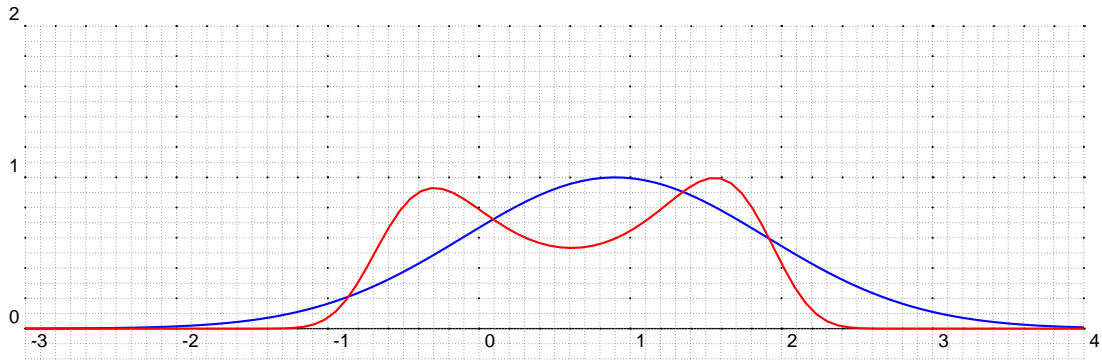
Figure 4.3.: Rejection sampling acceptance ratio $r_a(x) = \frac{p(x)}{Mq(x)}$ in red, proposal density $q(x)$ in blue. The norm of $q(x)$ is irrelevant in the depiction.

depending jumping proposal density $q(y,x) = q(x,y)$. The proposed state y is accepted (i.e. $x_{n+1} = y$) with a certain probability, which is

$$\alpha_{\text{Metropolis}}(x_n \to y) = \min\left\{\frac{\pi(y)}{\pi(x_n)}, 1\right\} \tag{4.39}$$

else the new state is the old state $x_{n+1} = x_n$. Adjacent samples x_n and x_{n+1} are thus correlated whereas samples from the ITS method are not. The performance of the Metropolis algorithm is controlled by the acceptance ratio. "Uphill jumps", i.e. states y that fulfill $\pi(y) > \pi(x_n)$ are always accepted as successors, whereas states "downhill" are only taken with probability $\alpha_{\text{Metropolis}}(x_n \to y)$. In Eq. (4.39) it becomes also obvious that any norm of $\pi(x)$ cancels in the ratio. The algorithm is thus norm-independent.

4.1.4.4. The Metropolis-Hastings Algorithm

Later in the 1970s the random walk Metropolis method was generalized by Hastings [Hastings, 1970] with the intention to improve the acceptance rate. In the Metropolis algorithm the acceptance rate depends on the ratio $\pi(y \sim q(x_n \to y))/\pi(x_n)$. It is thus predictable, which proposals of $q(x_n \to y)$ are likely accepted and therefore Hastings idea was to bias the proposal density to regions near x_n with a high acceptance rate by modifying the proposal density $q(x \to y)$. Hastings version of the Metropolis algorithm is:

1. choose $x_{n=0}$

2. sample y from $q(x_n \to y)$

3. calculate
$$\alpha(x_n \to y) = \min\left\{\frac{\pi(y)q(y \to x_n)}{\pi(x_n)q(x_n \to y)}, 1\right\} \tag{4.40}$$

4. set
$$x_{n+1} = \begin{cases} y & \text{with probability } \alpha(x_n \to y) \\ x_n & \text{else} \end{cases} \tag{4.41}$$

5. go to 2.

Why does running this algorithm produce a growing ensemble of states distributed according to $\pi(x)$? What has to be shown is that $\pi(x)$ is the invariant distribution under an redistribution operation (Eqs. 4.40 and 4.41), i.e. that

$$\int_\Omega \pi(x)k(x \to y)\,\mathrm{d}x = \pi(y). \tag{4.42}$$

But what is the absolute transition density (Markov kernel) $k(x \to y)$ according to the MH algorithm? With a certain *acceptance probability* $p_a(x)$ a new state, sampled from the proposal density $q(x \to y)$ is accepted, else the chain remains in state $y = x$. This is expressed as follows:

$$k(x \to y) = \alpha(x \to y)q(x \to y) + (1 - p_a(x))\delta_y(x), \tag{4.43}$$

where the acceptance probability is

$$
p_a(x) \quad = \quad \int\limits_{\Omega=\Omega_+\cup\Omega_-} q(x \to y) \min\left\{ \frac{\pi(y)q(y \to x)}{\pi(x)q(x \to y)}, 1 \right\} dy \tag{4.44}
$$

$$
= \quad \frac{1}{\pi(x)} \int\limits_{\Omega_+} \pi(y)q(y \to x)\,dy + \int\limits_{\Omega_-} q(x \to y)dy. \tag{4.45}
$$

The term $1 - p_a(x)$ can be interpreted as a rejection probability. The set Ω_+ is

$$
\Omega_+ := \{y | \pi(x)q(x \to y) > \pi(y)q(y \to x)\} \tag{4.46}
$$

and accordingly $\Omega_- = \Omega \setminus \Omega_+$. Ω_+ is thus the set in which the min argument assumes the ratio of "stream densities" $\pi(x)q(x \to y)$ and $\pi(y)q(y \to x)$. Inserting Eq. (4.43) into the left hand side of the invariance equation Eq. (4.42) yields

$$
\int\limits_{\Omega} \pi(x)k(x \to y)\,dx \quad = \quad \int\limits_{\Omega} \pi(x)\{\alpha(x \to y)q(x \to y) + (1 - a(x))\delta_y(x)\}\,dx \tag{4.47}
$$

$$
= \quad \int\limits_{\Omega} \pi(x)\alpha(x \to y)q(x \to y)\,dx + (1 - a(y))\pi(y) \tag{4.48}
$$

$$
= \quad \pi(y)\int\limits_{\Omega_+} q(y \to x)\,dx + \int\limits_{\Omega_-} \pi(x)q(x \to y)\,dx + \pi(y)
$$

$$
-\pi(y)\left\{ \frac{1}{\pi(y)} \int\limits_{\Omega_+} \pi(x)q(x \to y)\,dx + \int\limits_{\Omega_-} q(y \to x)\,dx \right\} \tag{4.49}
$$

$$
= \quad \pi(y) \quad \text{q.e.d..} \tag{4.50}
$$

The proof that the Metropolis algorithm yields x samples distributed like $\pi(x)$ follows by using a symmetric proposal density $q(x \to y) = q(y \to x)$ in Hastings version. Up to today numerous extensions of the MHA (such as the delayed rejection in reversible jump [Green and Mira, 1999] or the multiple try [Liu et al., 2000] method) were proposed. Central to the development of new algorithms is to reduce the burn-in period, to decorrelate adjacent samples (i.e. to improve chain mixing) and to improve the acceptance rate by finding suitable jump proposal densities.

The reason to include these powerful sampling methods in the thesis is the following. First, it is believed that the MCMC method is also suited to simulate atmospheric radiation transport. It was already shown by Eric Veach that MCMC is well suited for the physically correct treatment of the so called global illumination problem [Veach and Guibas, 1997], i.e. solving the radiation transport equation. An enthusiastic reader of this thesis on atmospheric radiation transport shall find all necessary (at least the basic) Monte Carlo techniques available for the atmospheric radiation problem. Second, the path generation algorithm has formal similarities with the generation of states of a Markov chain as is shown in the following section of this chapter. By introducing the MCMC method, the similarities and differences in the method become more transparent to the reader. Furthermore it is believed that for the problem of variance reduction in atmospheric RT the comparison of both methods will result in new very powerful methods.

4.2. Path Generation or Collision Density Estimation

The focus in this section is on the application of the Monte Carlo integration method to the problem of atmospheric radiation transport. The section starts with introducing an important concept of describing the optical medium in discretized form. The next step is to derive the integral form and the formal solution of the scalar RTE. This was done before in very similar form by [Marchuk et al., 1976]. Much of the derivation presented here is taken with some few modifications from the thesis [Deutschmann, 2009]. Finally the (already decades old) path generation algorithm is derived from the integral form.

4.2.1. Discretization of the Optical Domain into Cells and Clusters

The cluster concept is introduced. The implemented algorithm presented in this thesis knows four types of spatial grids. There are the spherical 1D (sp1D) and 3D (sp3D) and the plane parallel 1D (pp1D) and 3D (pp3D) grids. Only the 3D grids are considered here, the 1D versions are obtained by dropping the horizontal heterogeneity. The pp3D grid is defined using three independent coordinate lists for the x,y and z coordinates $\{x_i\},\{y_j\}$ and $\{z_k\}$. A location expressed in spherical coordinates is

$$\vec{r} = \begin{pmatrix} r\sin(\theta)\cos(\varphi) \\ r\sin(\theta)\sin(\varphi) \\ r\cos(\theta) \end{pmatrix}, \tag{4.51}$$

the coordinate lists are accordingly $\{\varphi_i\},\{\theta_j\}$ and $\{r_k\}$.

4.2.1.1. Cells or Voxels

For sake of simplicity the rest of the description of the domain discretization is done using the pp3D grid, but applies analogously to sp3D grid using the mapping

$$x \leftrightarrow \varphi, y \leftrightarrow \theta, z \leftrightarrow r. \tag{4.52}$$

An elemental cell of the grid is termed *cell* or *voxel* and is expressed by the eight corner points (x_i,y_j,z_k), (x_{i+1},y_j,z_k), (x_i,y_{j+1},z_k), (x_{i+1},y_{j+1},z_k), (x_i,y_j,z_{k+1}), (x_{i+1},y_j,z_{k+1}), (x_i,y_{j+1},z_{k+1}) and $(x_{i+1},y_{j+1},z_{k+1})$. In case of the cartesian grid, the cell boundaries are all planes, whereas sp3D grids have spherical slices with $r_k = const.$, cone slices with $\theta_j = const.$ and also planes with $\phi_i = const.$. A significant part of the solution algorithm presented in this section relies therefore on intersection point calculations of a ray with spheres, cones and planes. Details on the numerically stable implementation of the intersection point calculationare presented in [Deutschmann et al., 2011]. In the cells all properties such as extinction coefficients, pressure, temperature, etc. are constant.

4.2.1.2. Clusters

For many applications it is desired to simulate radiation transport on a fine discretized grid but simultaneously allow for a somewhat coarser grid sufficient to describe a certain optical property. Suppose for instantce that the radiation transport in the first km shall be simulated using air optical properties defined on a 100m grid but the aerosol extinction coefficient shall be defined on a 200m grid. The solution for an efficient calculation is regrouping or *clustering* of cells into cell compounds called . A cluster is thus nothing else but a compound of N individual cells:

$$\text{cluster} = \{\text{cell}_{i_1 j_1 k_1}, \ldots, \text{cell}_{i_N j_N k_N}\}. \tag{4.53}$$

The association of cells with clusters is done in the program by definition of a mapping of cells to clusters:

$$(i,j,k) \rightarrow \text{cluster id}. \tag{4.54}$$

An example application is to collect cells with similar micro physical or optical properties and associate them with one cluster in order to reduce for example the optical property calculation time or to reduce the dimension or the state space in a 3D retrieval problem.

4.2.2. RTE Integral Form

Basis of the following discussion is the introducing Chapter 3.3. In order to derive the integral form of the RTE, the boundary conditions are included into the RTE:

$$\vec{\omega}\vec{\nabla}R(\vec{r},\vec{\omega}) = -\varepsilon(\vec{r})R(\vec{r},\vec{\omega}) + \frac{\varepsilon_s(\vec{r})}{4\pi}\int_{4\pi} R(\vec{r},\vec{\omega}')P(\vec{r},\vec{\omega}\cdot\vec{\omega}')\,\mathrm{d}\vec{\omega}' + S_0(\vec{r},\vec{\omega}) \tag{4.55}$$

with the boundary conditions (BC)

$$S_0(\vec{r}, \vec{\omega}) = \varepsilon_a(\vec{r}) B_\lambda(T(\vec{r})) + F_0(\lambda) \Theta_{\text{Sun}}(\vec{r}), \tag{4.56}$$

where $B(T(\vec{r}), \lambda)$ is the Planck function. Since S_0 only differs from zero at locations where the solution R is prescribed by S_0, the BC may be included in the transfer equation.

4.2.2.1. Derivation

Rearranging the RTE yields:

$$\underbrace{\left(1 + \frac{1}{\varepsilon(\vec{r})} \vec{\omega} \vec{\nabla}\right)}_{:=A} R(\vec{r}, \vec{\omega}) = \frac{1}{4\pi} \underbrace{\frac{\varepsilon_S(\vec{r})}{\varepsilon(\vec{r})}}_{\omega_0(\vec{r})} \int_{4\pi} R(\vec{r}, \vec{\omega}') P(\vec{r}, \vec{\omega} \cdot \vec{\omega}') \, d\vec{\omega}' + \frac{1}{\varepsilon(\vec{r})} S_0(\vec{r}, \vec{\omega}). \tag{4.57}$$

For further manipulation Green's function $G_{\vec{\omega}}(\vec{r}, \vec{r}')$ of the A operator is needed. Motivated by the result obtained in Appendix A.4, Green's function of the operator A is

$$G_{\vec{\omega}}(x, \vec{r}') \begin{cases} 0 & \text{if } x < x' \\ \varepsilon(\vec{r}') e^{-\tau(\vec{r}, \vec{r}')} & \text{else} \end{cases} \tag{4.58}$$

where

$$\tau(\vec{r}, \vec{r}') = \int_{x'}^{x} \varepsilon(\vec{r}' + (t - x')\vec{\omega}) \, dt \tag{4.59}$$

with the optical thickness $\tau(\vec{r}', \vec{r})$ between $\vec{r}'$ and $\vec{r}$. In order to convolve the right side of (4.57) with $G(\vec{r}, \vec{r}')$ (to apply A^{-1}), one has to integrate over $x \in [a, b]$ where b is the distance from $\vec{r}'$ to the boundary of the medium along the direction $\vec{\omega}$. The integration along that direction is then substituted by the integration over the whole medium [Marchuk et al., 1976]. For $G_{\vec{\omega}}(\vec{r}', \vec{r})$ it is used:

$$G_{\vec{\omega}}(\vec{r}, \vec{r}') = \varepsilon(\vec{r}') e^{-\tau(\vec{r}, \vec{r}')} \frac{\delta\left(\vec{\omega} - \frac{\vec{r} - \vec{r}'}{|\vec{r} - \vec{r}'|}\right)}{|\vec{r} - \vec{r}'|^2}. \tag{4.60}$$

The δ function selects $\vec{r}$ that fit to the direction $\vec{\omega}$ and the reference point $\vec{r}'$ From 4.57 the integral RTE in terms of the collision density

$$f(\vec{r}, \vec{\omega}) = \varepsilon(\vec{r}) R(\vec{r}, \vec{\omega}) \tag{4.61}$$

is obtained by convolution with $G_{\vec{\omega}}(\vec{r}, \vec{r}')$ and multiplication with $\varepsilon(\vec{r})$:

$$f(\vec{r}, \vec{\omega}) = \int_D \int_{4\pi} \frac{\omega_0(\vec{r}')}{4\pi} P(\vec{r}', \vec{\omega} \cdot \vec{\omega}') \underbrace{R(\vec{r}', \vec{\omega}') \varepsilon(\vec{r}')}_{f(\vec{r}', \vec{\omega}')} \varepsilon(\vec{r}) e^{-\tau(\vec{r}, \vec{r}')} \dots$$

$$\frac{\delta\left(\vec{\omega} - \frac{\vec{r} - \vec{r}'}{|\vec{r} - \vec{r}'|}\right)}{|\vec{r} - \vec{r}'|^2} \, d\vec{\omega}' \, d\vec{r}' + \Psi(\vec{r}, \vec{\omega}) \tag{4.62}$$

with the initial collision density

$$\Psi(\vec{r}, \vec{\omega}) = \Psi_{\text{thermal}}(\vec{r}, \vec{\omega}) + \Psi_{\text{solar}}(\vec{r}, \vec{\omega}) \tag{4.63}$$

$$\Psi_{\text{thermal}}(\vec{r}, \vec{\omega}) = \varepsilon(\vec{r}) \int_D \varepsilon_a(\vec{r}') B_\lambda(T(\vec{r})) e^{-\tau(\vec{r}, \vec{r}')} \frac{\delta\left(\vec{\omega} - \frac{\vec{r} - \vec{r}'}{|\vec{r} - \vec{r}'|}\right)}{|\vec{r} - \vec{r}'|^2} \, d\vec{r}' \tag{4.64}$$

and

$$\Psi_{\text{solar}}(\vec{r}, \vec{\omega}) = F_0(\lambda) \varepsilon(\vec{r}) \int_D \Theta_{\text{Sun}}(\vec{r}') e^{-\tau(\vec{r}, \vec{r}')} \frac{\delta\left(\vec{\omega} - \frac{\vec{r} - \vec{r}'}{|\vec{r} - \vec{r}'|}\right)}{|\vec{r} - \vec{r}'|^2} \, d\vec{r}'. \tag{4.65}$$

D symbolizes the whole integration domain.

4.2.2.2. Interpretation

Terms in Eq. (4.62) are regrouped to obtain the following compact form of the IRTE

$$f(\vec{r}, \vec{\omega}) = \int\limits_{D} \int\limits_{4\pi} k\left[(\vec{r}', \vec{\omega}') \to (\vec{r}, \vec{\omega})\right] f(\vec{r}', \vec{\omega}') \, \mathrm{d}\vec{\omega}' \, \mathrm{d}\vec{r}' + \Psi(\vec{r}, \vec{\omega}) \tag{4.66}$$

or more short

$$f = Kf + \Psi \tag{4.67}$$

with the *transport kernel* k

$$k\left[(\vec{r}', \vec{\omega}') \to (\vec{r}, \vec{\omega})\right] = k_p\left[(\vec{r}', \vec{\omega}') \to (\vec{r}, \vec{\omega})\right] \frac{\delta\left(\vec{\omega} - \frac{\vec{r} - \vec{r}'}{|\vec{r} - \vec{r}'|}\right)}{|\vec{r} - \vec{r}'|^2} \tag{4.68}$$

and the *transport transition density* $k_p\left[(\vec{r}', \vec{\omega}') \to (\vec{r}, \vec{\omega})\right]$

$$k_p\left[(\vec{r}', \vec{\omega}') \to (\vec{r}, \vec{\omega})\right] = \varpi_0(\vec{r}') \cdot \frac{P(\vec{r}', \vec{\omega} \cdot \vec{\omega}')}{4\pi} \cdot \varepsilon(\vec{r}) e^{-\tau(\vec{r}', \vec{r})}, \tag{4.69}$$

which can be interpreted as a probability density of photons to perform the transition $(\vec{r}', \vec{\omega}') \to (\vec{r}, \vec{\omega})$. The factor between k and k_p in Eq. (4.68) is found when integration over space instead of using the "linear" Greens function Eq. (4.58). To avoid it, an equivalent expression of the IRTE is given from using Green's function in the variant Eq. (4.58):

$$f(\vec{r}, \vec{\omega}) = \int\limits_{0}^{t} \int\limits_{4\pi} k_p\left[(\vec{r}'(\xi), \vec{\omega}') \to (\vec{r}, \vec{\omega})\right] f(\vec{r}'(\xi), \vec{\omega}') \, \mathrm{d}\vec{\omega}' \, \mathrm{d}\xi + \Psi(\vec{r}, \vec{\omega}) \tag{4.70}$$

with $\vec{r}'(\xi) = \vec{r} - \xi\vec{\omega}$ and the distance t to the boundary of the domain D from $\vec{r}$ into direction $-\vec{\omega}$. Fig. 4.4
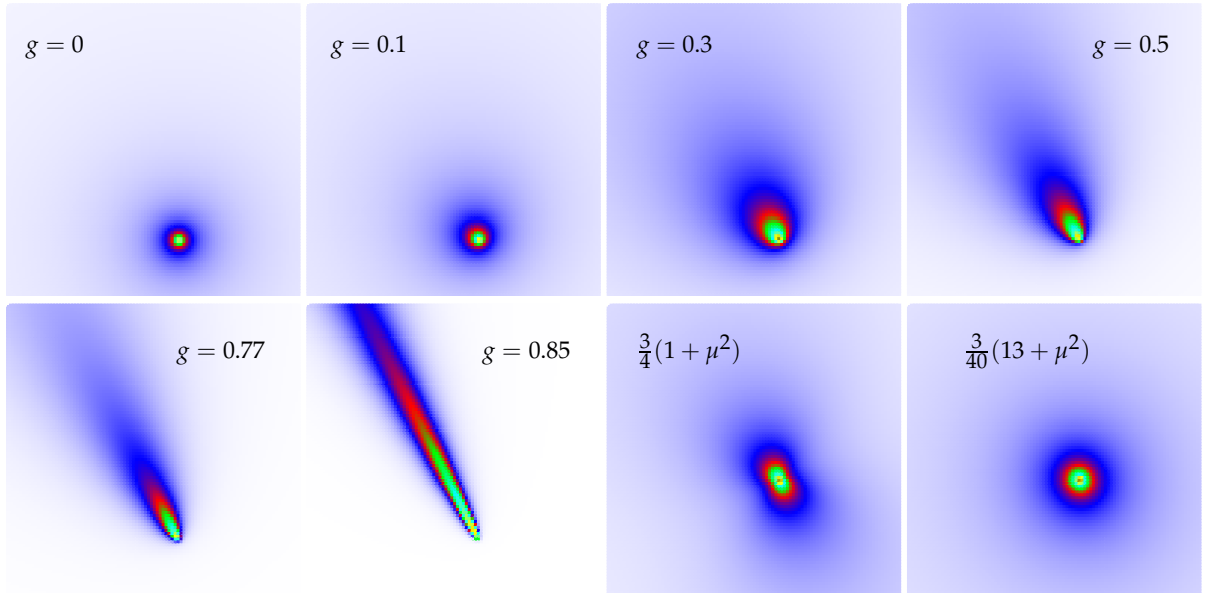
Figure 4.4.: Transport kernels for different phase functions reduced to two dimensions. Top panel: Henyey-Greenstein phase function model with asymmetry parameters g. Bottom panels on the right side, left: Rayleigh phase function, right: rotational Raman phase function. Color gradients correspond to gradients in the square of the electric field strength.

shows two-dimensional transport kernels for different phase functions. $\Psi(\vec{r}, \vec{\omega})$ in (4.66) is called *initial collision density* because it symbolizes the density of initially extinct (i.e. absorbed or scattered) photons.

4.2.3. Formal Solution of the IRTE

In order to facilitate the readability, the five dimensional phase space point $\vec{x} := (\vec{r}, \vec{\omega})$ containing both location and direction with elements $\vec{x} \in X$ is used. By applying Banach's fixed point theorem, i.e. iterating the IRTE which is a fix point equation, a formal and explicit expression of the collision density is obtained. Consider the following operator T by writing the right side of the IRTE Eq. (4.67), $f = Kf + \Psi$ in operator form, where the argument $\vec{x}$ is omitted for the sake of simplicity:

$$Tg := Kg + \Psi. \tag{4.71}$$

Using T, equation (4.66) can be interpreted as the condition for a fixed point $\tilde{f}(\vec{x})$:

$$\tilde{f} = T\tilde{f}. \tag{4.72}$$

Banach's theorem allows one to construct the fixed point $\tilde{f}(\vec{x})$ by successive application of T on an initial guess $g(\vec{x})$:

$$
\begin{aligned}
\tilde{f} &= \lim_{n \to \infty} T^n g \tag{4.73}\\
&= \lim_{n \to \infty} T^{n-1}(Kg + \Psi)\\
&= \lim_{n \to \infty} T^{n-2}(K^2 g + K\Psi + \Psi)\\
&= \lim_{n \to \infty} T^{n-3}(K^3 g + K^2\Psi + K\Psi + \Psi)\\
&= \lim_{n \to \infty} \left(K^n g + \sum_{i=0}^{n-1} K^i \Psi \right) \tag{4.74}\\
&= \sum_{n=0}^{\infty} K^n \Psi \quad \text{if} \quad \|K\| < 1 \tag{4.75}
\end{aligned}
$$

The last representation of the solution is called *Neumann series*. Prerequisite for the application of the theorem is that T is a contraction, respectively that T has a Lipschitz constant $L < 1$:

$$L := \frac{\|Tg_2(\vec{x}) - Tg_1(\vec{x})\|}{\|g_2(\vec{x}) - g_1(\vec{x})\|} = \frac{\|K[g_2(\vec{x}) - g_1(\vec{x})]\|}{\|g_2(\vec{x}) - g_1(\vec{x})\|} \leq \sup_{g(\vec{x}) \neq 0} \frac{\|Kg(\vec{x})\|}{\|g(\vec{x})\|} = \|K\|. \tag{4.76}$$

Indeed the analysis of the transport kernel (4.68) shows, that $\|K\| < 1$ if M is bounded, because $\int_0^{x < \infty} \varepsilon e^{-\varepsilon l}\, \mathrm{d}l = -\left[\exp\left(-\varepsilon l\right)\right]_0^{x < \infty} < 1$ or at least if the single scattering albedo $\varpi_0(\vec{r}) < 1$ in the case that M is not bounded. If $\|K\| < 1$ the initial guess g is not important, because its contribution tends to zero for large n. A more detailed and mathematically more stringent analysis of the convergence for a special case can be found in [Caballero, 2006].

4.2.3.1. Principle of Reciprocity

Looking forward to numerical solutions of the RTE, the so called *principle of reciprocity* (also called *theorem of optical mutuality*) is introduced. It allows to describe the radiative transfer process in reverse direction. In order to do this, a minus sign[1] before the direction $\vec{\omega}$ in the RTE (Eq. (3.169)) is introduced, i.e. one applies the time reversal operator. This results in the so called *adjoint RTE* containing the adjoint transport operator $K^\dagger$. In integral form the adjoint RTE is written as

$$f^\dagger = K^\dagger f^\dagger + \varphi, \tag{4.77}$$

where φ is the detector function. For example

$$\varphi(\vec{r}, \vec{\omega}) = \delta(\vec{r} - \vec{r}^*)\chi_{\text{FOV}}(\vec{\omega}) \tag{4.78}$$

describes a detector at $\vec{r}^*$ with the characteristic function of its field of view χ_{FOV}. By regarding the direction-reversed transport process, sources Ψ (Sun, thermal emission) and sinks φ (detector) are exchanged. The

---

[1]see [Marchuk et al., 1976] or [Marshak and Davis, 2005], chapter 3 for a detailed discussion

solution of (4.77) can be found in the same manner as for the forward time direction:

$$f^\dagger = \sum_{n=0}^{\infty} K^{\dagger n} \varphi. \tag{4.79}$$

The adjoint transport operator $K^\dagger$ therewith is defined as

$$[K^\dagger g](\vec{x}) = \int_X k^\dagger[\vec{x} \to \vec{x}'] g(\vec{x}') \, d\vec{x}', \tag{4.80}$$

in detail:

$$k_p^\dagger[\vec{x} \to \vec{x}'] = \omega_0(\vec{r}) \varepsilon(\vec{r}') e^{-\tau(\vec{r}, \vec{r}')} \frac{P(\vec{r}, \vec{\omega}' \cdot \vec{\omega})}{4\pi} \tag{4.81}$$

and

$$k^\dagger[\vec{x} \to \vec{x}'] = k_p^\dagger[\vec{x} \to \vec{x}'] \frac{\delta\left(\vec{\omega}' - \frac{\vec{r}' - \vec{r}}{|\vec{r}' - \vec{r}|}\right)}{|\vec{r}' - \vec{r}|^2}. \tag{4.82}$$

By using the inner product $(f, g) = \int_X f(x)g(x) \, dx$ the following identity (see e.g. [Marshak and Davis, 2005], p. 268) helps to reveal the relation between φ and Ψ. Let $f(\vec{x}^*)$ be the collision density at a certain position $\vec{r}^*$ and direction $\vec{\omega}^*$:

$$
\begin{aligned}
f(\vec{x}^*) &= (f, \delta_{\vec{x}^*}) \quad \text{with} \quad \delta_{\vec{x}^*} = \delta(\vec{r} - \vec{r}^*)\delta(\vec{\omega} - \vec{\omega}^*) & (4.83)\\
&= \left(\sum_{n=0}^{\infty} K^n \Psi, \delta_{\vec{x}^*}\right) = \sum_{n=0}^{\infty} (K^n \Psi, \delta_{\vec{x}^*}) & (4.84)\\
&= (\Psi, \delta_{\vec{x}^*}) + (K\Psi, \delta_{\vec{x}^*}) + (K^2\Psi, \delta_{\vec{x}^*}) + (K^3\Psi, \delta_{\vec{x}^*}) + \cdots & (4.85)\\
&= (\Psi, \delta_{\vec{x}^*}) + (\Psi, K^\dagger \delta_{\vec{x}^*}) + (\Psi, K^{\dagger 2} \delta_{\vec{x}^*}) + (\Psi, K^{\dagger 3} \delta_{\vec{x}^*}) + \cdots & (4.86)\\
&= \sum_{n=0}^{\infty} (\Psi, K^{\dagger n} \delta_{\vec{x}^*}) = \left(\Psi, \sum_{n=0}^{\infty} K^{\dagger n} \delta_{\vec{x}^*}\right) & (4.87)\\
&= (\Psi, f^\dagger). & (4.88)
\end{aligned}
$$

This means that the collision density at a certain point of the phase space can be found by either determining the solution of the RTE f and calculating $(f, \delta_{\vec{x}^*})$ or by determining the solution of the adjoint RTE $f^\dagger = \sum_{n=0}^{\infty} K^{\dagger n} \delta_{\vec{x}^*}$ and calculating $(\Psi, f^\dagger)$. As will be shown later, this theorem is the basis for the so called *backward* Monte Carlo methods, used to estimate measured radiances of small FOV detectors. Without the Neumann series the theorem can also be obtained by multiplying the RTE by $f^\dagger$:

$$(f, f^\dagger) = (Kf + \Psi, f^\dagger) = (Kf, f^\dagger) + (\Psi, f^\dagger) \tag{4.89}$$

and vice versa (4.77) by f:

$$(f, f^\dagger) = (f, K^\dagger f^\dagger + \varphi) = (f, K^\dagger f^\dagger) + (f, \varphi). \tag{4.90}$$

Because $(f, K^\dagger f^\dagger) = (Kf, f^\dagger)$, it follows $(\Psi, f^\dagger) = (f, \varphi)$.

4.2.4. Overview on Monte Carlo RTE Solution Algorithms

In order to compare different Monte Carlo methods another representation of the collision density is introduced:

$$\vec{f} = \left(\Psi, K\Psi, K^2\Psi, K^3\Psi, \cdots\right). \tag{4.91}$$

which is called collision density vector. The nth component of $\vec{f}$ is the phase space density of the n times scattered photons. In the particle picture (scalar approach) $\vec{f}$ can be interpreted as a PDF in the ∞-dimensional path space Ω:

$$\Omega = \mathbb{R}^5 \otimes \mathbb{R}^5 \otimes \cdots \tag{4.92}$$

where a component $\vec{x}_n = (\vec{r}_n \in \mathbb{R}^3, \vec{\omega}_n \in {}^3)$, $\vec{r}_n$ is the location of a scatter event in the path and

$$\vec{\omega}_n = \frac{\vec{r}_n - \vec{r}_{n-1}}{|\vec{r}_n - \vec{r}_{n-1}|}. \tag{4.93}$$

In this section Monte Carlo methods to draw samples of $\vec{f}$ are discussed. The difference to the "1D methods" discussed in the previous section is that the states are elements of a ∞-dimensional space. Despite the higher dimension of the integration domain, the formalism can be translated analogously to radiation transport. The underlying algorithms in different implementations of Monte Carlo radiation transport codes can be subdivided into two groups: algorithms applying Markov chain (MCMC) methods (such as Metropolis Hastings) and the sequential importance sampling (SIS) group. It apparently depends on the expected dimensionality of the path space whether MCMC or SIS is applied. Eric Veach first applied the MCMC method to radiation transport in computer graphics. His thesis [Veach and Guibas, 1997] is a good starting point in the question how and if to apply MCMC to atmospheric radiation transport. In computer graphics as in atmospheric radiation transport the dimensionality of the path space suggests to use Monte Carlo methods since systematic integration is not feasible. In the following section, the SIS method which is topic of this thesis is described in detail. The SIS method stems from neutron transport simulations and was later applied to atmospheric radiation transport by Marchuk et al. [Marchuk et al., 1976]. For understanding the SIS method it is best to think about model photons as non interfering (the so called independent particle approximation) single velocity, weight less particles (see also introducing Chapter 3.3.7.1). The algorithm explained below has already been published (from the authors side most recently in [Deutschmann et al., 2011]) and is somewhat the standard in the field since Marchuk's pioneering work.

The motivation to effectively sample from $\vec{f}$ is to calculate functionals $I(\vec{f})$ with an integrand $\vec{g}(\vec{X})$ such as the radiance at a certain position in the medium or derivatives of the radiance with respect to parameters of the radiation transport process:

$$I(\vec{f}) = \int_\Omega \vec{g}(\vec{X})\vec{f}(\vec{X}) \, d\vec{X}. \tag{4.94}$$

4.2.5. Crude Monte Carlo

The crude Monte Carlo method to estimate the radiation field is to randomly select scatter event locations uniformly distributed over the integration domain (atmosphere and ocean D). The question that arises in that approach is, how many scatter orders should be considered. In order to answer this the propagation mechanism is examined. The model photons originate at the Sun and enter into the atmosphere. Let the norm of the initial collision density $f_0 = \Psi$ be $|f_0|$. According to the transition kernel k the model photons are then redistributed resulting in the density of double scattered model photons:

$$f_1(\vec{x}) = [K\Psi](\vec{x}) = \int_D k(\vec{x}_1 \to \vec{x})\Psi(\vec{x}_1) \, d\vec{x}_1. \tag{4.95}$$

Since D is a finite domain, the transition density $k(\vec{x} \to \vec{y})$ is not unity-normalized, i.e. $|K| \leq 1$. Therefore $|f_1| \leq |f_0|$ and in general

$$|f_{n+1}| \leq |f_n|. \tag{4.96}$$

The consequence is that the expectation value of the number of scatter orders is finite. A detailed proof of this fact can be found in [Marchuk et al., 1976]. However it should be said, that for infinite precision of numerically (this is already a paradox) constructing the density f, infinite scatter orders need to be considered. The expectation $N_{\text{s.o.}}$ of the number of scatter orders is

$$N_{\text{s.o.}} = \frac{\sum_{n=0}^\infty n|f_n|}{\sum_{n=0}^\infty |f_n|} \tag{4.97}$$

As becomes obvious, already the estimation of $N_{\text{s.o.}}$ involves high dimensional integration. Suppose for the moment that $N_{\text{s.o.}}$ is known. The procedure of estimating f in Eq. 4.94 is then to calculate:

$$f \approx \Psi(x_1) \cdot k(\vec{x}_1 \to \vec{x}_2) \cdots \cdots k(\vec{x}_{N_{\text{s.o.}}-1} \to \vec{x}_{N_{\text{s.o.}}}). \tag{4.98}$$

From the deduction of the scalar IRTE it is already known, that $k(\vec{x} \to \vec{y})$ is a heterogeneous function varying over some orders of magnitude. It thus can be expected, that estimates using Eq. 4.98 inherit enormous
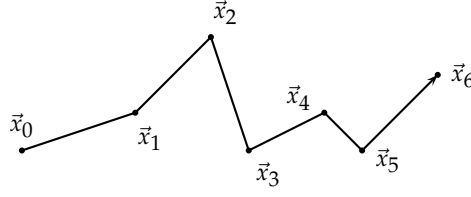
Figure 4.5.: Sequential importance sampling. Adjacent components $\vec{x}_{i=n,n+1} = (\vec{r}_i, \vec{\omega}_i)$ of the state $\vec{X} = (\vec{x}_0, \vec{x}_1, \ldots)$ are correlated according to $k_p[\vec{x}_n \to \vec{x}_{n+1}]$.
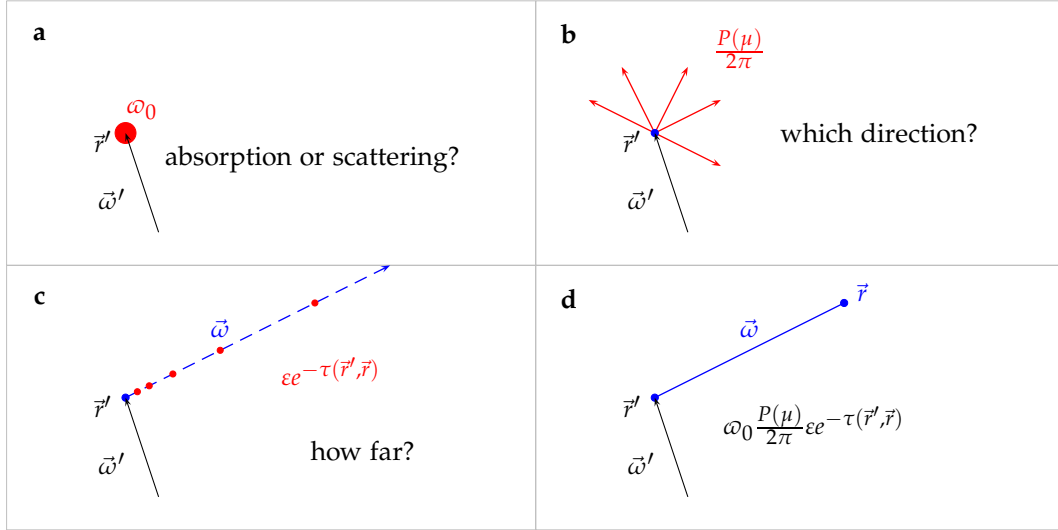
Figure 4.6.: Schematic depictions of the random samplings described in the Sections 4.2.6.1 (panel **a**), 4.2.6.2 (panel **b**) and 4.2.6.3 (panel **c**). In total, the procedure generates an event $\vec{x}_{n+1} = (\vec{r}, \vec{\omega})$ from its predecessor $\vec{x}_n$ represented here by $\vec{r}'$ and $\vec{\omega}'$ (panel **d**).

noise. The origin of that noise are adjacent samples of the location of scatter orders, since these samples are entirely uncorrelated (because locations are independently sampled). The solution of the noise problem and the problem to obtain $N_{\text{s.o.}}$ is presented in the following section.

4.2.6. Sequential Importance Sampling (SIS) or Path Generation

One way to overcome the aforementioned noise problem of the crude Monte Carlo method is to select components (i.e. scatter event locations) sequentially and according to their importance. Given a location $\vec{r}_n$ together with the current propagation direction $\vec{\omega}_n$ the next scatter event location $\vec{r}_{n+1}$ (if any) is sampled using the transition kernel $k_p[\vec{x}_n \to \vec{x}_{n+1}]$. The resulting procedure (*ray tracing*) is called *sequential importance sampling* (SIS) and is at the same time the direct simulation of the (scalar) radiation propagation process (see Fig. 4.5). Sampling a new $\vec{X}$ component (see Fig. 4.6) consists of simulating the free path length or escape from the medium (Section 4.2.6.3), the survival probability in the collision i.e. type of collision: absorption or scattering (Section 4.2.6.1) and sampling of the scattered direction (Section 4.2.6.2). The separability of these steps relies on the factorization of the corresponding densities in the transition kernel of which only the k_p factor is relevant:

$$k_p\left[(\vec{r}_n, \vec{\omega}_n) \to (\vec{r}_{n+1}, \vec{\omega}_{n+1})\right] = \omega_0(\vec{r}_n)\frac{\Phi(\vec{r}_n, \vec{\omega} \cdot \vec{\omega}_n)}{4\pi}\varepsilon(\vec{r}_{n+1})e^{-\tau(\vec{r}_n, \vec{r}_{n+1})}. \tag{4.99}$$

The procedure starts with sampling an initial extinction event (i.e. a free path length) either from $\Psi(\vec{x})$ or from $\varphi(\vec{x})$ depending on whether one wants to solve the RTE or its adjoint version.

4.2.6.1. Simulation of the Absorption or Scattering

Once a free path length is sampled a collision point $\vec{r}_{n+1} = \vec{r}_n + l\vec{\omega}_n$ is given. This collision point could be the location of the first scatter event in a forward or backward trajectory. Regarding the question whether the state sampling procedure shall be continued, the type of collision is sampled. The probability of scattering in a collision is given by the ratio of the scatter and the extinction coefficient called single scattering albedo:

$$\omega_0(\vec{r}_{n+1}) = \frac{\varepsilon_s(\vec{r}_{n+1})}{\varepsilon(\vec{r}_{n+1})}. \tag{4.100}$$

If $\alpha < \omega_0(\vec{r}_{n+1})$ the model photon survives the collision being scattered else, the trajectory is terminated and a sample of the phase space is complete.

4.2.6.2. Simulation of the Differential Scatter Cross Section

In case of scattering, the scatter angle has to be sampled from the scalar density (phase function):

$$P(\mu) = \left(\sum_{i=1}^{N_s} \varepsilon_{si} \right)^{-1} \cdot \sum_{i=1}^{N_s} \varepsilon_{si} P_i(\mu). \tag{4.101}$$

$P(\mu)$ is the 11 element of the scattering matrix $\mathbf{P}(\mu)$. In the scalar approach (neglecting polarization and interference), $P(\mu) = \mathbf{P}_{11}(\mu)$ is used for scatter angle sampling. Solving the vector form of the RTE, it is corrected for the resulting bias by an appropriate weight (again importance sampling). This is explained in chapter 5.1.3 in detail. The functions P_i are the scatter angle densities for the respective particles or molecules present at the collision point. There are N_s of these scatterers. In the UV-vis spectral range, molecular scattering is always accounted for. There are two relevant molecular scatter processes: Cabannes scattering and Raman scattering consisting of rotational and vibrational scattering. The individual scatter coefficients ε_{si} depend on the respective number densities $n_i(\vec{r})$ and single scattering cross sections $\sigma_{si}(\lambda, p, T)$:

$$\varepsilon_{si}(\vec{r}, \lambda) = n_i(\vec{r})\sigma_{si}(\lambda, p, T). \tag{4.102}$$

For the simulation of differential scattering cross sections different methods are applied depending on the respective mathematical representation (i.e. closed formulae, Legendre series expansion or tables, see App. A.3). In order to complete sampling of a new direction, also the azimuth angle φ is sampled:

$$\varphi = 2\pi\alpha. \tag{4.103}$$

The new direction $\vec{k}_{n+1}$ is therewith given by:

$$\vec{k}_{n+1} = \begin{pmatrix} \mu \cos(\varphi) \\ \mu \sin(\varphi) \\ \sqrt{1 - \mu^2} \end{pmatrix}. \tag{4.104}$$

In case of an (inelastic) RRS event, the wavelength of the incident photon is changed according to the line intensities of the wavelength shifted photon energies (See chapters 3.2.2.4 and 7). Basis for sampling the RRS shifted wavelength λ_n is the PDF

$$p_{\text{RRS}}(\lambda_n) = \frac{\sigma_n}{\sum_n \sigma_n} \tag{4.105}$$

which is more precisely formulated in Eq. (7.20) and also explained in much more detail in Chapter 7.2.1. σ_n is any of the considered and properly numbered RRS cross sections (corresponding to allowed rotational momentum changes) of N_2 or O_2. After a wavelength shift, the optical properties of a medium cell are recalculated for the new wavelength λ_n.

4.2.6.3. Simulation of the Free Path Length

The remaining part is sampling the path lengths to the next scatter event respectively escape from the medium. For a heterogeneous medium, with $\varepsilon(\vec{r})$ varying over space, the sampling method is analog to

sampling in a homogeneous medium (see App. A.2). The free path length density is:

$$p_{\text{fpl}}(l) \propto e^{-\tau(l)} \quad \text{where} \quad \tau(l) = \int_0^l \varepsilon(\vec{r} + l'\vec{\omega})\,dl'. \tag{4.106}$$

The norm N_{fpl} of $p_{\text{fpl}}(l)$ is as usually calculated:

$$N_{\text{fpl}} = \int_0^\infty e^{-\tau(l')}\,dl'. \tag{4.107}$$

An explicit expression of N_{fpl} is however not needed for the sampling procedure. Basis for the ITS method in heterogeneous medium is Eq. A.11 which states that the CDF of the free path length is the collision probability for the distance l. The analog expression is $P_{\text{fpl}}(l) = 1 - e^{-\tau(l)}$, therefore a free path length sample $l(\alpha)$ is found by gradual integration (see Fig. 4.7) :

$$\int_0^{l(\alpha)} \varepsilon(\vec{r}_n + l'\vec{\omega}_n)\,dl' = -\log(1-\alpha). \tag{4.108}$$

It may happen during the integration procedure along the propagation direction $\vec{\omega}$ that the ray leaves the
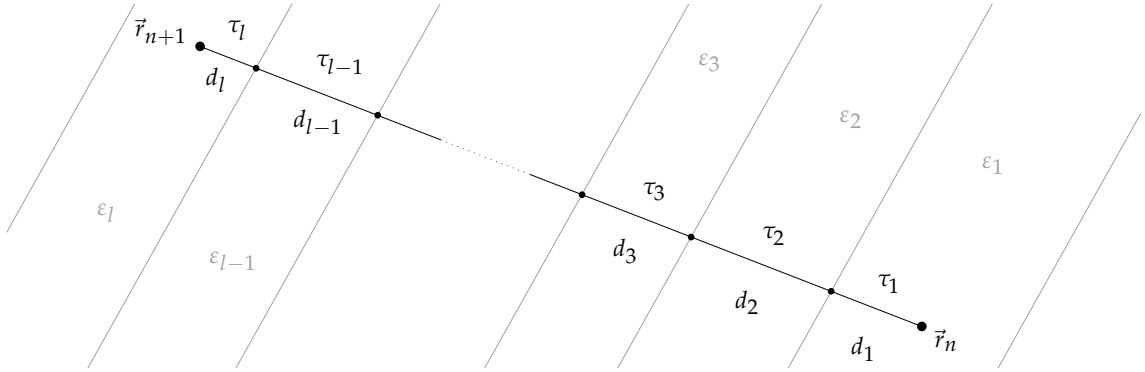
Figure 4.7.: Estimation of the free photon path length $|\vec{r}_{n+1} - \vec{r}_n|$ (schematic in Fig 4.6, panel **c)**. The ray tracer subdivides the medium into τ-segments according to the spatial grid and determines $\vec{r}_{n+1}$ by sampling of the optical density τ_l between $\vec{r}_n$ and $\vec{r}_{n+1}$.

atmosphere. In such case the trajectory is terminated and the phase space sample is also complete.

4.2.6.4. Summary on Sequential Importance Sampling / Path Generation

The result of the ray tracing algorithm described in the sections 4.2.6.1, 4.2.6.2 and 4.2.6.3 are model photon trajectories each consisting of individual scatter event locations $\vec{r}_1, \vec{r}_2, \ldots, \vec{r}_n$. Adjacent locations are correlated according to $k_p[\vec{x}_n \to \vec{x}_{n+1}]$. A trajectory represents also a state $\vec{X} = (\vec{x}_0, \vec{x}_1, \ldots, \vec{x}_n) \in \Omega$ distributed like $f(\vec{X})$, where $\vec{x}_0$ is a sample from the source distribution Ψ. In the adjoint formulation the source Ψ (physical photon sources) is replaced with the sinks φ (detection devices, absorption regions). However due to Helmholtz's principle of reversibility of propagation direction under time reversal, the ray tracing algorithm is identical.

4.3. Importance Sampling in Monte Carlo SIS Radiative Transfer

In chapter 4.1.2 the importance sampling method is introduced. Importance sampling offers a way of modifying the variance (more specifically: the second moment) of functional estimates. In atmospheric radiative transport modeling, the method is of great importance and shall here be transferred from 1D integration to high and variable dimensional integration. Particularly, the focus in this section is on combining sequential importance sampling (Monte Carlo ray tracing) with importance sampling. Motivation for the application of the concept is to obtain estimates of functionals with more complicated kernels (chapter 5). According to the significance for the following two chapters this sections should be understood well.

4.3.1. Weights for Alternate Kernels

In chapter 4.2, *sequential* importance sampling was used in order to construct samples of f respectively of $f^{\dagger}$ ($f^{(\dagger)}$). The algorithm is called sequential because the collision densities $f^{(\dagger)}$ are estimated gradually and component wise in a sequential manner. In each iteration step an estimate of the nth component of $f^{(\dagger)}$ is used to estimate the $n+1^{\text{th}}$ component according to its importance or relevance. Therewith the correlation between two subsequent components of a $f^{(\dagger)}$ sample is kept large in order to avoid large fluctuations in functional estimates originating from adjacent otherwise uncorrelated scatter orders. In the context of RTE functional estimation which is subject of the following chapter 5, IS is used to estimate RTE functionals based on SIS-generated $f^{(\dagger)}$ samples.

4.3.1.1. 1D Case

The IS equation in 1D is

$$I = \int g(x)p(x)\,\mathrm{d}x = \int g(x)w(x)q(x)\,\mathrm{d}x \quad \text{with} \quad w(x) = \frac{p(x)}{q(x)} \tag{4.109}$$

In the following chapter $q(x)$ samples in form of $f^{(\dagger)}$ are given and it is desired to calculate $\int g(x)p(x)\,\mathrm{d}x$. In order to correct for differences in the densities $p(x)$ and $q(x)$, a weight $w(x) = \frac{p(x)}{q(x)}$ is introduced. For a finite number N of samples drawn from $q(x)$ an estimate of I is obtained:

$$I \approx g(x_n)w(x_n) \quad \text{with} \quad x \sim q(x). \tag{4.110}$$

4.3.2. Weights in the Calculation of RTE Functional Estimates

In the high dimensional case the importance sampling equation assumes the following form

$$I = \int \cdots \int g(x_n)p(x_n, x_{n-1}) \cdot \cdots \cdot p(x_1, x_0)\,\mathrm{d}x_0 \cdots \mathrm{d}x_n \tag{4.111}$$

$$= \int \cdots \int g(x_n)w(x_n, \cdots, x_0)q(x_n, x_{n-1}) \cdot \cdots \cdot q(x_1, x_0)\,\mathrm{d}x_0 \cdots \mathrm{d}x_n \tag{4.112}$$

where the weight $w(x_n, \cdots, x_0)$ is defined as

$$w(x_n, \cdots, x_0) = \frac{p(x_n, x_{n-1}) \cdot \cdots \cdot p(x_1, x_0)}{q(x_n, x_{n-1}) \cdot \cdots \cdot q(x_1, x_0)}. \tag{4.113}$$

In chapter 5, $f^{(\dagger)}$ samples are be used to estimate RTE functionals. In the IS frame work, $f^{(\dagger)}$ samples correspond to $q(x)$ samples and RTE functionals contain different kernels $p(x)$. The advantage of this technique is that a single $f^{(\dagger)}$ sample can be used to estimate all desired functionals simultaneously. Drawback is a relatively stronger fluctuation of the estimates due to the weights that are involved.

4.3.3. Application of IS to Mie Phase Functions Scatter Angle Sampling

In McArtim the importance sampling technique is implemented to allow for using Mie phase functions and therewith to improve the physical realism of the calculated functionals. One implemented method is to take the Henyey-Greenstein (HG) model as an approximation to Mie phase functions and correct for the bias by the corresponding importance sampling weight $w_{\text{Mie/HG}}(\mu)$:

$$w_{\text{Mie/HG}}(\mu) = \frac{P_{\text{Mie}}(\mu)}{P_{\text{HG}}(\mu)} \tag{4.114}$$

Motivation of the approach is that formulas for the inverse CDF of the HG phase function exist whereas for Mie phase functions expressions for the inverse CDF are not available. The asymmetry parameter of the Mie phase function used in the Henyey-Greenstein phase function is given by Eq. (3.125). The other implemented importance sampling method is to create a discrete representation of the Mie phase function on a μ grid, to sample scatter angles from the resulting table according to appendix A.3.5 and to correct for the bias using the ratio of the true Mie phase function and the table entry.

Functionals of the Collision Density

With a sample of the collision density consisting of scatter event locations, functionals such as the flux densities, radiances or derivatives of these quantities with respect to optical parameters of the atmosphere can be calculated. The resulting formulas for radiances are called local estimates [Marchuk et al., 1976]. Radiance estimates are the basis for all functionals derived in the following. In order to calculate 1st and 2nd order radiance derivatives, polarized radiances (i.e. components of the Stokes vector) but also for the application of variance reduction techniques, the importance sampling method is used. The notation used, is identical to the notation in [Marchuk et al., 1976] and [Deutschmann, 2009].

5.1. Radiances, Intensities and the Reciprocity Theorem

For sake of completeness some definitions are recalled. Using the collision density f obtained from a direct simulation, the intensity I^a at some location $\vec{r}_d$ (d for detector) is found by integrating the collision density (proportional to the radiance of the local radiation field) at $\vec{r}_d$ over the detector's FOV:

$$I^a(\vec{r}_d, \mathbf{\Omega}_{\text{FOV}}) = \frac{1}{\varepsilon(\vec{r}_d)} \int\limits_{\mathbf{\Omega}_{\text{FOV}}} f(\vec{r}_d, \vec{\omega}) \, \mathrm{d}\vec{\omega} = \frac{1}{\varepsilon}(f, \varphi) \tag{5.1}$$

where the inner product of f and

$$\varphi(\vec{r}, \vec{\omega}) = \delta(\vec{r} - \vec{r}_d)\chi_{\text{FOV}}(\vec{\omega}) \tag{5.2}$$

$$\chi_{\text{FOV}}(\vec{\omega}) = \begin{cases} 1 & \text{if } \vec{\omega} \in \mathbf{\Omega}_{\text{FOV}} \\ 0 & \text{else} \end{cases} \tag{5.3}$$

is used. The initial collision density $\Psi(\vec{x})$ is given by

$$\Psi(\vec{r}, \vec{\omega}) = \chi_{\text{Sun}}(\vec{r}, \vec{\omega})\varepsilon(\vec{r}) \exp\left(-\tau(\vec{r}_{\text{Sun}}, \vec{r})\right). \tag{5.4}$$

Since the integration over the detector field of view for small FOV's (!) corresponds to averaging the radiance in the FOV and subsequently multiplying with the FOV solid angle, the intensity sometimes is loosely called radiance. But in fact the intensity I^a is an irradiance and in case of large FOV's the terminology becomes even wrong because the cosine weighting in the transformation from radiances to irradiances needs to be taken into account. In the following, I explicitly use the reciprocity theorem, i.e. the adjoint or backward method discussed in chapter 4.2.3.1 and work with trajectory samples from the adjoint collision density $f^\dagger$. Applied to radiances, the theorem states

$$I^a = \frac{1}{\varepsilon}(f, \varphi) = \frac{1}{\varepsilon} \sum_{n=0}^{\infty} (K^n\Psi, \varphi) = \frac{1}{\varepsilon} \sum_{n=0}^{\infty} (\Psi, K^{\dagger n}\varphi) = \frac{1}{\varepsilon}(\Psi, f^\dagger). \tag{5.5}$$

Fig. 5.1 shows two estimates of f and $f^\dagger$ respectively.

5.1.1. Scalar Radiance Estimates

[Marchuk et al., 1976] obtained estimates of radiances according to Eq. (5.5) using the so called local estimates formulas which are derived here. The following passages are taken from chapter 5 of my Diploma thesis
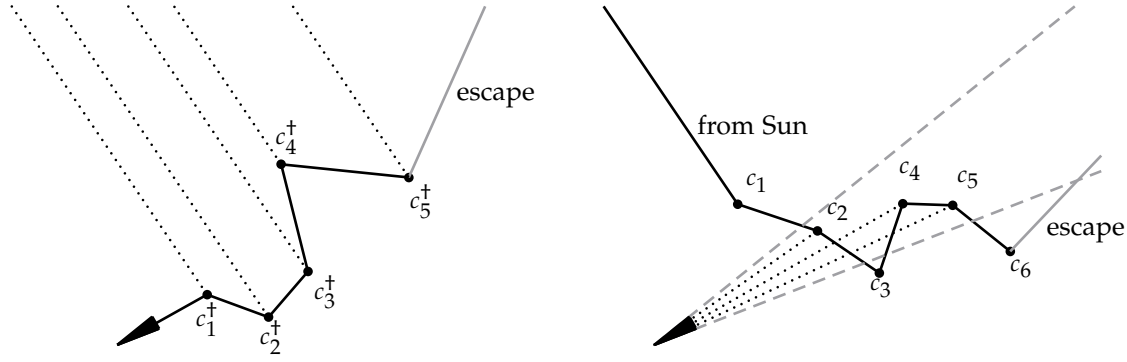
Figure 5.1.: $f^{(\dagger)}$ estimates and associated sub trajectories. **Left**: backward trajectory ($f^\dagger$ estimate) originating at the detector. For each scatter event n on a trajectory a contribution $c_n^\dagger$ is calculated. **Right**: forward trajectory (f estimate) originating at the Sun. Only scatter events inside the FOV (i.e. n=2, 4 and 5) contribute c_n to the Neumann series. A sub trajectory with index n consists of n scatter events and contains segments sampled by the ray tracer and the segment ending in the detector respectively starting at the Sun (dashed lines).

[Deutschmann, 2009] and contain only some few modifications. Using the RTE solution f the radiance at the position $\vec{r}_d$ with a FOV Ω_{FOV} is

$$
\begin{aligned}
I^a &= \frac{1}{\varepsilon}(f, \varphi) &(5.6)\\[2mm]
&= \frac{1}{\varepsilon(\vec{r}_d)} \sum_{n=0}^{\infty} \int_{\mathbf{X}} [K^n \Psi](\vec{x}) \varphi(\vec{x})\, d\vec{x} &(5.7)\\[2mm]
&=: \sum_{n=0}^{\infty} I_n^a &(5.8)\\[2mm]
&= \frac{1}{\varepsilon(\vec{r}_d)} \Bigg[\int_{\mathbf{X}} \varphi(\vec{x}) \Psi(\vec{x})\, d\vec{x} + \int_{\mathbf{X}} \varphi(\vec{x}) \int_{\mathbf{X}} k[\vec{x}_1 \to \vec{x}] \Psi(\vec{x}_1)\, d\vec{x}_1\, d\vec{x} + \\
&\qquad \int_{\mathbf{X}} \varphi(\vec{x}) \int_{\mathbf{X}} k[\vec{x}_2 \to \vec{x}] \int_{\mathbf{X}} k[\vec{x}_1 \to \vec{x}_2] \Psi(\vec{x}_1)\, d\vec{x}_1\, d\vec{x}_2\, d\vec{x} + \cdots \Bigg]. &(5.9)
\end{aligned}
$$

5.1.1.1. Scalar Radiance Neumann Series

The Neumann series is analyzed summand-wise. The first expression I_0^L is the contribution of direct light:

$$
\begin{aligned}
I_0^a &= \frac{1}{\varepsilon(\vec{r}_d)} \int_A \int_{4\pi} \Psi(\vec{r}, \vec{\omega}) \delta(\vec{r} - \vec{r}_d) \chi_{\text{FOV}}(\vec{\omega})\, d\vec{\omega}\, d\vec{r} &(5.10)\\[2mm]
&= \frac{1}{\varepsilon(\vec{r}_d)} \int_{\Omega_{\text{FOV}}} \Psi(\vec{r}_d, \vec{\omega})\, d\vec{\omega} &(5.11)\\[2mm]
&= \int_{\Omega_{\text{FOV}}} \chi_{\text{Sun}}(\vec{r}_d, \vec{\omega}) e^{-\tau(\vec{r}_{\text{Sun}}, \vec{r}_d)}\, d\vec{\omega} &(5.12)\\[2mm]
&=: I_{\text{direct}}^a. &(5.13)
\end{aligned}
$$

The rest of the Neumann series consists of integrals which partially have been estimated by the ray tracer. Investigating the $n + 1^{\text{th}}$ contribution I_n^L in Eq. (5.9) leads to:

$$
\begin{aligned}
I_n^a &= \frac{1}{\varepsilon(\vec{r}_d)} \int_{\mathbf{X}} \varphi(\vec{x}) \int_{\mathbf{X}} k[\vec{x}_n \rightarrow \vec{x}] \cdots \\
&\quad \underbrace{\int_{\mathbf{X}} \cdots \int_{\mathbf{X}}}_{n-1} \prod_{i=1}^{n-1} k[\vec{x}_j \rightarrow \vec{x}_{j+1}] \Psi(\vec{x}_1) \, \mathrm{d}\vec{x}_1 \cdots \mathrm{d}\vec{x}_{n-1} \, \mathrm{d}\vec{x}_n \, \mathrm{d}\vec{x}
\end{aligned}
\tag{5.14}
$$

$$
\begin{aligned}
&= \frac{1}{\varepsilon(\vec{r}_d)} \int_A \int_{4\pi} \delta(\vec{r} - \vec{r}_d) \chi_{\text{FOV}}(\vec{\omega}) \int_{\mathbf{X}} k[\vec{x}_n \rightarrow \vec{x}] \cdots \\
&\quad \int_{\mathbf{X}} \cdots \int_{\mathbf{X}} \prod_{i=1}^{n-1} k[\vec{x}_j \rightarrow \vec{x}_{j+1}] \Psi(\vec{x}_1) \, \mathrm{d}\vec{x}_1 \cdots \mathrm{d}\vec{x}_{n-1} \, \mathrm{d}\vec{x}_n \, \mathrm{d}\vec{\omega} \, \mathrm{d}\vec{r}
\end{aligned}
\tag{5.15}
$$

$$
\begin{aligned}
&= \frac{1}{\varepsilon(\vec{r}_d)} \int_{\mathbf{\Omega}_{\text{FOV}}} \int_A \int_{4\pi} \varpi_0(\vec{r}_n) \underbrace{\frac{P(\vec{r}_n, \vec{\omega}_n \cdot \vec{\omega})}{4\pi} \varepsilon(\vec{r}_d) e^{-\tau(\vec{r}_n \rightarrow \vec{r}_d)} \frac{\delta\left(\vec{\omega} - \frac{\vec{r}_d - \vec{r}_n}{|\vec{r}_d - \vec{r}_n|}\right)}{|\vec{r}_d - \vec{r}_n|^2}}_{k[\vec{x}_n \rightarrow (\vec{r}_d, \vec{\omega})]} \cdots \\
&\quad \int_{\mathbf{X}} \cdots \int_{\mathbf{X}} \prod_{i=1}^{n-1} k[\vec{x}_j \rightarrow \vec{x}_{j+1}] \Psi(\vec{x}_1) \, \mathrm{d}\vec{x}_1 \cdots \mathrm{d}\vec{x}_{n-1} \, \mathrm{d}\vec{\omega}_n \, \mathrm{d}\vec{r}_n \, \mathrm{d}\vec{\omega}.
\end{aligned}
\tag{5.16}
$$

We observe, that $\varepsilon(\vec{r}_d)$ cancels. In order to simplify the notation, the contribution function $C_n(\vec{r}, \vec{\omega})$ is introduced:

$$
C_n(\vec{r}, \vec{\omega}) = \frac{P(\vec{r}_n, \vec{\omega} \cdot \vec{\omega}_n) e^{-\tau(\vec{r}_n, \vec{r})}}{4\pi |\vec{r} - \vec{r}_n|^2} \quad \text{with} \quad \vec{\omega} = \frac{\vec{r} - \vec{r}_n}{|\vec{r} - \vec{r}_n|}
\tag{5.17}
$$

I_n^a then is:

$$
\begin{aligned}
I_n^a &= \int_{\mathbf{\Omega}_{\text{FOV}}} \int_A \int_{4\pi} C_n(\vec{r}_d, \vec{\omega}) \delta\left(\vec{\omega} - \frac{\vec{r}_d - \vec{r}_n}{|\vec{r}_d - \vec{r}_n|}\right) \cdots \\
&\quad \underbrace{\varpi_0(\vec{r}_n) \int_{\mathbf{X}} \cdots \int_{\mathbf{X}} \prod_{i=1}^{n-1} k[\vec{x}_j \rightarrow \vec{x}_{j+1}] \Psi(\vec{x}_1) \, \mathrm{d}\vec{x}_1 \cdots \mathrm{d}\vec{x}_{n-1} \, \mathrm{d}\vec{\omega}_n \, \mathrm{d}\vec{r}_n \, \mathrm{d}\vec{\omega}.}_{\text{estimated by the } n^{\text{th}} \text{ scatter event}}
\end{aligned}
\tag{5.18}
$$

5.1.1.2. Forward Monte Carlo Scalar Radiance Estimates

In order to understand the intention behind the manipulations undertaken, think again about the "simple" 1D problem $\int g(x) p(x) \, \mathrm{d}x$. Estimates of the integral are obtained by evaluating $g(x)$ at positions sampled from $p(x)$ (see chapter 4.1.3):

$$
\int g(x) p(x) \, \mathrm{d}x \approx g(x_n) \quad \text{with} \quad x_n \sim p(x).
\tag{5.19}
$$

In that sense Eq. (5.18) consists formally of two parts: the under braced expression corresponds to $p(x)$ (the algorithm to draw samples from that distribution is the ray tracer) and the rest in the integrand is the function $g(x)$ to be evaluated at the sampled coordinate (the local estimate). To conclude: for each scatter order n a contribution estimate is given by

$$
c_n = \begin{cases} C_n(\vec{r}_d) & \text{if } \vec{r}_n \text{ is inside the FOV} \\ 0 & \text{else} \end{cases}
\tag{5.20}
$$

(compare to right side of figure 5.1). For a large ensemble of N trajectories the radiance is obtained by averaging the sums of all contribution estimates:

$$
I^a = \sum_{n=0}^{\infty} \langle I_n^* \rangle = \sum_{n=0}^{\infty} \langle C_n(\vec{r}_d) \rangle_{f_n} \approx I_{\text{direct}}^* + \sum_{n=1}^{N} c_n,
\tag{5.21}
$$

where f_n symbolizes the sampling density of the nth scatter event location, N is the number of scatter events on the trajectory and c_n is the contribution of the nth scatter order.

5.1.2. Backward Monte Carlo Scalar Radiance

The fact that only scatter events inside the FOV contribute to the measurement when using the forward Monte Carlo path generation algorithm has significant effects on the variance of the estimates. This is comprehensible by decreasing gradually the FOV. In the extreme case of a delta function as aperture function all contributions in the sum of Eq. (5.21) become zero, simply because the probability of scattering inside the FOV is zero (see right side of Fig. 5.1). For these small FOV cases the backward Monte Carlo method can be the method of choice since the variance is smaller. The difference to the forward Monte Carlo method is to begin sampling trajectories (ray tracing) at the detector, resulting in a sample of the adjoint collision density $f^\dagger$. The radiance functional derived from the adjoint RTE (compare to Eq. (5.5)) is

$$I^a = \frac{1}{\varepsilon} \sum_{n=0}^{\infty} (\Psi, K^{\dagger n} \varphi) = \frac{1}{\varepsilon(\vec{r}_d)} \sum_{n=0}^{\infty} \int_{\mathbf{X}} \Psi(\vec{x})[K^{\dagger n}\varphi](\vec{x}) \, d\vec{x} =: \sum_{n=0}^{\infty} I_n^{a\dagger}. \tag{5.22}$$

The method to derive the radiance estimate from an adjoint collision density sample (a backward trajectory) is basically the same as for the forward case.

5.1.2.1. Adjoint Reduced Transport Density

Since the backward Monte Carlo method is the basis of the following considerations, the derivation of local estimates will be repeated here. As a side product, an expression is deduced which is later used with the importance sampling technique in order to obtain polarized radiances, radiance derivatives and Ring spectra in Chapter 7.3. It is started with the expression for the nth component of the adjoint Neumann series $I_n^{a\dagger}$:

$$
\begin{aligned}
I_n^{a\dagger} &= \int \Psi(\vec{x}) \int k^\dagger[\vec{x} \to \vec{x}_{n-1}] \int k^\dagger[\vec{x}_{n-1} \to \vec{x}_{n-2}] \cdots \\
&\qquad \int k^\dagger[\vec{x}_2 \to \vec{x}_1] \int k^\dagger[\vec{x}_1 \to \vec{x}_0] \varphi(\vec{x}_0) \, d\vec{x}_0 \, d\vec{x}_1 \cdots d\vec{x}_{n-1} \, d\vec{x} \tag{5.23} \\
&= \underbrace{\int \cdots \int}_{n+1} \Psi(\vec{x}) k^\dagger[\vec{x} \to \vec{x}_{n-1}] \prod_{j=1}^{n-1} k^\dagger[\vec{x}_j \to \vec{x}_{j-1}] \varphi(\vec{x}_0) \, d\vec{x}_0 \, d\vec{x}_1 \cdots d\vec{x}_{n-1} \, d\vec{x}. \tag{5.24}
\end{aligned}
$$

In order to simplify the notation the *adjoint reduced transport density* $T_n^\dagger$ of order n

$$T_n^\dagger[\vec{x} \to \vec{x}_{n-1} \to \cdots \to \vec{x}_0] = \frac{1}{\varepsilon(\vec{r}_d)} \Psi(\vec{x}) k_p^\dagger[\vec{x} \to \vec{x}_{n-1}] \prod_{j=1}^{n-1} k_p^\dagger[\vec{x}_j \to \vec{x}_{j-1}] \varphi(\vec{x}_0) \tag{5.25}$$

and the helper function Δ_n

$$\Delta_n = \frac{\delta\left(\vec{\omega}_{n-1} - \frac{\vec{r}_{n-1} - \vec{r}}{|\vec{r}_{n-1} - \vec{r}|}\right)}{|\vec{r} - \vec{r}_{n-1}|^2} \prod_{j=1}^{n-1} \frac{\delta\left(\vec{\omega}_{j-1} - \frac{\vec{r}_{j-1} - \vec{r}_j}{|\vec{r}_{j-1} - \vec{r}_j|}\right)}{|\vec{r}_j - \vec{r}_{j-1}|^2} \tag{5.26}$$

are introduced. A closer look at $T_n^\dagger$ reveals that many factors in the product cancel each other:

$$
\begin{aligned}
T_n^\dagger &= \frac{1}{\varepsilon(\vec{r}_d)} \underbrace{\varepsilon(\vec{r}) e^{-\tau(\vec{r}_{\text{Sun}} \to \vec{r})} \chi_{\text{Sun}}(\vec{r}, \vec{\omega})}_{\Psi(\vec{x})} \underbrace{\omega_0(\vec{r}) \frac{P(\vec{r}, \vec{\omega} \cdot \vec{\omega}_{n-1})}{4\pi} \varepsilon(\vec{r}_{n-1}) e^{-\tau(\vec{r} \to \vec{r}_{n-1})}}_{k_p^\dagger[\vec{x} \to \vec{x}_{n-1}]} \cdots \\
&\qquad \underbrace{\prod_{j=1}^{n-1} \omega_0(\vec{r}_j) \frac{P(\vec{r}_j, \vec{\omega}_j \cdot \vec{\omega}_{j-1})}{4\pi} \varepsilon(\vec{r}_{j-1}) e^{-\tau(\vec{r}_j \to \vec{r}_{j-1})}}_{k_p^\dagger[\vec{x}_j \to \vec{x}_{j-1}]} \underbrace{\delta(\vec{r}_0 - \vec{r}_d) \chi_{\text{FOV}}(\vec{\omega}_0)}_{\varphi(\vec{x}_0)} \tag{5.27}
\end{aligned}
$$

$$= \frac{1}{\varepsilon(\vec{r}_d)} \chi_{\text{Sun}}(\vec{r},\vec{\omega}) e^{-\tau(\vec{r}_{\text{Sun}} \to \vec{r} \to \vec{r}_{n-1} \to \cdots \to \vec{r}_0)} (4\pi)^{-n} \sum_{t=1}^{N_s} \varepsilon_{st}(\vec{r}) P_t(\vec{r},\vec{\omega} \cdot \vec{\omega}_{n-1}) \cdots$$

$$\prod_{j=1}^{n-1} \left(\sum_{t=1}^{N_s} \varepsilon_{st}(\vec{r}_j) P_t(\vec{r}_j,\vec{\omega}_j \cdot \vec{\omega}_{j-1}) \right) \varepsilon(\vec{r}_0) \delta(\vec{r}_0 - \vec{r}_d) \chi_{\text{FOV}}(\vec{\omega}_0) \tag{5.28}$$

$$\overset{\vec{r}_0 = \vec{r}_d}{=} \quad \chi_{\text{Sun}}(\vec{r},\vec{\omega}) e^{-\tau(\vec{r}_{\text{Sun}} \to \vec{r} \to \vec{r}_{n-1} \to \cdots \to \vec{r}_0)} (4\pi)^{-n} \sum_{t=1}^{N_s} \varepsilon_{st}(\vec{r}) P_t(\vec{r},\vec{\omega} \cdot \vec{\omega}_{n-1}) \cdots$$

$$\prod_{j=1}^{n-1} \left(\sum_{t=1}^{N_s} \varepsilon_{st}(\vec{r}_j) P_t(\vec{r}_j,\vec{\omega}_j \cdot \vec{\omega}_{j-1}) \right) \chi_{\text{FOV}}(\vec{\omega}_0). \tag{5.29}$$

Most of the replacements follow from the definition of the single scattering albedo $\varpi_0(\vec{r}) = \varepsilon_s(\vec{r})/\varepsilon(\vec{r})$, the effective phase function $P(\vec{r},\mu) = \varepsilon_s(\vec{r})^{-1} \sum_{t=1}^{N_s} \varepsilon_{st} P_t(\vec{r},\mu)$ and the free path length density. When "realized", the delta function from $\varphi(\vec{x})$ finally cancels $\varepsilon(\vec{r}_0)/\varepsilon(\vec{r}_d) = 1$. The delta function in $\vec{r}$ and the $\chi(\vec{\omega})$ function in $\varphi(\vec{x})$ cause the evaluation of the leading K integral at the observer position and ε^{-1} before the Neumann series cancels the factor ε in k.

5.1.2.2. Backward Monte Carlo Radiance Local Estimates

When carrying out the integration in Eq. (5.24) with the results just obtained, one observes that the contributions are nonzero only if direct sunlight reaches the associated scatter events, i.e. if it is no twilight situation. Due to the large distance between a scatterer in the atmosphere and the Sun the contributions are approximately

$$c_j^\dagger \approx \frac{\Omega_{\text{Sun}}}{4\pi^2 R^2} e^{-\tau(\vec{r}_i,\vec{r}_{\text{Sun}})} P\left(\vec{r}_i,\vec{\omega}_{\text{Sun},j} \cdot \vec{\omega}_i\right) \quad \text{with} \quad \vec{\omega}_{\text{Sun},j} = \frac{\vec{r}_{\text{Sun}} - \vec{r}_j}{|\vec{r}_{\text{Sun}} - \vec{r}_j|} \tag{5.30}$$

where the solid angle of the Sun disc is denoted by Ω_{Sun} and the Sun radius by R. The difference between the radiance I^a and the I is only a constant factor. Through the rest of the chapter, the focus is on the backward Monte Carlo method according to which estimates of the scalar radiance (silently omitting the factor I^a/I) are given by

$$I \approx \sum_{n=1}^{N} e^{-\tau^*(\vec{r}_n)} P(\vec{r}_n,\mu_n^*). \tag{5.31}$$

where $\tau^*(\vec{r})$ is the optical thickness from the location $\vec{r}$ to the Sun, and μ_n^* is the cosine of the angle between the negative direction of backward trajectory at the nth scatter event and the incoming Sun light direction (compare to Fig. 5.2).

5.1.3. Vector Radiances

So far, Monte Carlo approaches to solve the scalar RTE were discussed. In this section an algorithm to solve the vector form of the RTE (compare to Chapter 3.3) is presented. Central to that approach is the importance sampling technique as outlined in Chapter 4.3. The key idea is to assume that the integration kernels that lead to "scalar radiation transport" (the resulting method is called *scalar approach*) are good approximations for the vector radiation transport integration kernels. In the language of Chapter 4.3, the scalar (adjoint) kernels are written as $k^\dagger[\vec{x} \to \vec{y}]$ (corresponds to $q(x)$) and the (physically more correct) vector kernels are 4×4 matrices $\mathbf{k}[\vec{x} \to \vec{y}]$ (analogous to $p(x)$). The method described here was published earlier by [Emde et al., 2010].

5.1.3.1. Importance Sampling Weights for Vector Radiances

In order to correct for the scalar approach the ratio of the vector and the scalar integration kernel (i.e. the weight $w(x) = \frac{q(x)}{p(x)}$) has to be calculated for each scatter order. Since $q(x)$ are samples of the adjoint IRTE solution, the order of scatter events has to be inverted (see Fig. 5.2). Basis for the following considerations is Eq. (5.24) and the adjoint reduced transport density $T_n^\dagger$. The ratio (i.e. the importance sampling weight) is

$$\mathbf{w}(\vec{x}_0,\ldots,\vec{x}_n) = \frac{\mathbf{T}_n^\dagger}{T_n^\dagger} = \frac{\boldsymbol{\varphi}(\vec{x}_0^\dagger)}{\varphi^\dagger(\vec{x}_0^\dagger)} \cdot \frac{\mathbf{k}[\vec{x}_1^\dagger \to \vec{x}_0^\dagger]}{k^\dagger[\vec{x}_1^\dagger \to \vec{x}_0^\dagger]} \cdot \ldots \cdot \frac{\mathbf{k}[\vec{x}_n^\dagger \to \vec{x}_{n-1}^\dagger]}{k^\dagger[\vec{x}_n^\dagger \to \vec{x}_{n-1}^\dagger]} \cdot \frac{\vec{\Psi}(\vec{x}_n^*)}{\Psi(\vec{x}_n^*)}, \tag{5.32}$$
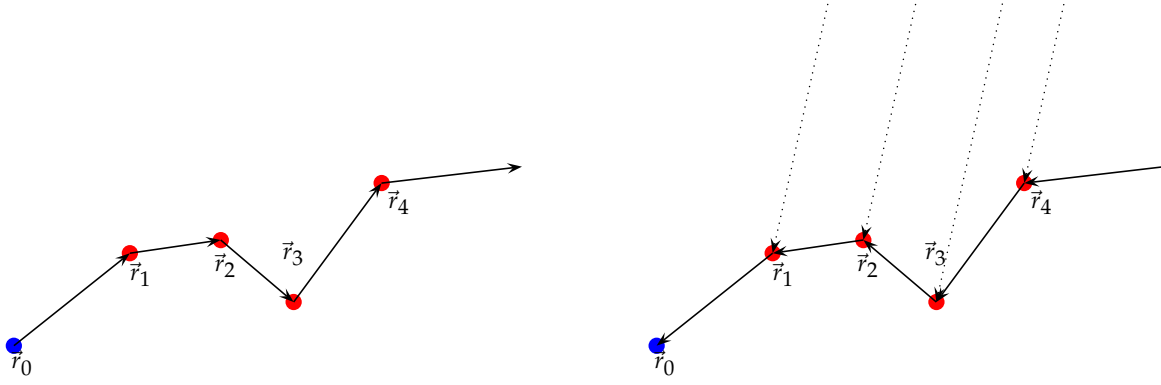
Figure 5.2.: **Left:** Backward trajectory sample. The detector location is blue, scatter events are red. The orientation of the path elements $\vec{\omega}_i = (\vec{r}_{i+1} - \vec{r}_i)/|\vec{r}_{i+1} - \vec{r}_i|$ point along the backward ray tracing direction. In the local estimation phase (**right**), the orientation of the trajectory elements is reversed (arrows).

where

$$\vec{x}^\dagger = \left(\begin{array}{c} \vec{r} \\ \vec{\omega} \end{array} \right)^\dagger = \left(\begin{array}{c} \vec{r} \\ -\vec{\omega} \end{array} \right) \quad \text{and} \quad \vec{x}_n^* = \left(\begin{array}{c} \vec{r}_n \\ \vec{\omega}_n^* \end{array} \right) \tag{5.33}$$

with $\vec{\omega}_n^*$ pointing from the nth scatter event to the Sun. The 4×4 matrix $\varphi(\vec{x})$ describes the polarization sensitivity of the measurement device. In many applications it is desired to keep the sensitivity of the measured radiance to the Stokes vector components 2, 3 and 4 as low as possible. The 2, 3 and 4 components of the (polarized) initial collision density vector $\vec{\Psi}(x)$ are zero, and the 1$^{\text{st}}$ coordinate is $\Psi(\vec{x})$. These values reflect the physical fact that sun light reaching the Earths atmosphere is unpolarized.

5.1.3.2. Locally Isotropic Optical Media and a Simple Measurement Device

In locally isotropic media, the extinction coefficient, the single scattering albedo and the phase matrix do not depend on the orientation of the particles or molecules. This assumption (A) is justified for a molecular atmosphere containing only spherical macroscopic particles. Then, the free path length densities in the scalar and in the vector kernel cancel each other and in Eq. (5.32) the ratio of the effective scatter phase matrix and the phase function (the 11 element of the scatter phase matrix) remains. The second assumption (B) is that $\varphi(\vec{x})$ is the unity matrix times the scalar detector function, implying that the detector directly measures the polarization state of the incident scattered light. It turns out that only the ratio of the phase matrix with its 11 element contributes to the total importance sampling weight. The effective total phase matrix is

$$\mathbf{P}(\vec{r}, \mu) = \frac{\sum_i \varepsilon_{s,i}(\vec{r}) \mathbf{P}_i(\vec{r}, \mu)}{\sum_i \varepsilon_{s,i}(\vec{r})} \tag{5.34}$$

where $\varepsilon_{s,i}$ is the scatter coefficient for scatterer i and $\mathbf{P}_i$ is the associated phase matrix. For a single scatter event at location $\vec{r}$ (omitted in the notation) the ratio is

$$\mathbf{W}(\vec{x}_{\text{in}} \to \vec{x}_{\text{out}}) = \frac{\mathbf{Z}(\vec{x}_{\text{in}} \to \vec{x}_{\text{out}})}{P_{11}(\vec{r}_{\text{in}}, \mu_{\text{in} \to \text{out}})} \tag{5.35}$$

where

$$\mathbf{Z}(\vec{x}_{\text{in}} \to \vec{x}_{\text{out}}) = \mathbf{L}(i_{\text{out}}(\vec{\omega}_{\text{in}}, \vec{\omega}_{\text{out}})) \mathbf{P}(\vec{r}_{\text{in}}, \mu_{\text{in} \to \text{out}}) \mathbf{L}(i_{\text{in}}(\vec{\omega}_{\text{in}}, \vec{\omega}_{\text{out}})), \tag{5.36}$$

$$\mu_{\text{in} \to \text{out}} = \vec{\omega}_{\text{in}} \cdot \vec{\omega}_{\text{out}} \tag{5.37}$$

The Stokes rotation matrix $\mathbf{L}(\alpha)$ is defined in Eq. (3.43). Details on the calculation of the angles $i_{\text{in}}(\vec{\omega}_{\text{in}}, \vec{\omega}_{\text{out}})$ and $i_{\text{out}}(\vec{\omega}_{\text{in}}, \vec{\omega}_{\text{out}})$ are found in Chapter 3.1.4.3, Fig. 3.1. Taken together, both assumptions (A+B) lead to the following importance sampling weights (see Fig. 5.2):

$$\mathbf{w}(\vec{x}_0, \ldots, \vec{x}_n) = \mathbf{W}(\vec{x}_1^\dagger \to \vec{x}_0^\dagger) \cdot \ldots \cdot \mathbf{W}(\vec{x}_{n-1}^\dagger \to \vec{x}_{n-2}^\dagger) \mathbf{W}(\vec{x}_n^{\dagger*} \to \vec{x}_{n-1}^\dagger). \tag{5.38}$$

In analogously applying Eq. (5.19), the modified version of a vector radiance estimate (a single summand $g(x_n)w(x_n)$ in Eq. (4.110) with $x_n \sim q(x)$) including the importance sampling weights is

$$\vec{I} \approx \sum_{n=1}^{N} e^{-\tau(\vec{x}_n^{\dagger *})} \prod_{i=1}^{n-1} \mathbf{W}(\vec{x}_i^{\dagger} \to \vec{x}_{i-1}^{\dagger}) \mathbf{Z}(\vec{x}_n^{\dagger *} \to \vec{x}_{n-1}^{\dagger}) \begin{pmatrix} F_0 \\ 0 \\ 0 \\ 0 \end{pmatrix} \tag{5.39}$$

where N is the number of scatter events of the backward trajectory. The weight matrix multiplication order is identical to Eq. (5.38), F_0 is the extraterrestrial solar irradiance and the integrated extinction along direction $\vec{\omega}$ starting at $\vec{r}$

$$\tau(\vec{x}) = \int_0 \varepsilon(\vec{r} + l\vec{\omega}) \, dl. \tag{5.40}$$

The structure of Eq. (5.39) is identical to Eq. (5.31) which can be seen by setting the importance weight matrices to unity matrices. In Section 5.3.1 vector radiances are validated.

5.2. Radiance Derivatives

In the tomographic inversion of scattered Sun light spectra radiative transfer models are used as parts of the so called forward model. A forward model $\vec{F}(\vec{x})$ can be thought of as a set of mathematical formulas that establish a functional model relationship of the observable vector $\vec{y}$ and the parameters $\vec{x}$, the *state*. that shall be determined by a process called inversion, i.e. the forward model shall simulate the measurement as a function of the state $\vec{y} = \vec{F}(\vec{x})$. In such inversion process first derivatives $\partial \vec{F}(\vec{x})/\partial \vec{x}$ and, if possible, second derivatives $\partial^2 \vec{F}(\vec{x})/\partial \vec{x}^2$ are needed. For a comprehensive and profound treatment of the quantitative evaluation and interpretation of a indirect measurements the reader is referred to [Tarantola, 2005]. In appendix B the method to obtain radiance derivative estimates is described in principle.

5.2.1. Variables for Radiance Derivatives

All cases of interest are covered in an atmospheric radiative transfer situation in which gases and two particle types are present. The integration domain is the high and variable dimensional phase space, consisting of the spatial coordinates of the individual scatter events symbolized by $\vec{x}$. The following passages are again taken from chapter 5.2 of the thesis [Deutschmann, 2009] and contain only minor modifications. With regard to optical properties ξ which influence the radiance, possible parameters are 1.) the absorption coefficient of any trace gas, 2.) the particle extinction coefficient in a cell, 3.) the particle single scattering albedo and 4.) particle phase function parameters like the asymmetry parameter g. More specifically, ξ influences the trajectories via the adjoint transport kernel $k^{\dagger}[\vec{x} \to \vec{x}]$ (during the $f^{\dagger}$ estimate sampling) and the initial collision density $\Psi(\vec{x})$. In order to understand the method, it is again sufficient to analyze a single contribution $I_n^{a\dagger}$ of the Neumann series in Eq. (5.22).

5.2.1.1. Logarithmic n^{th} Order Radiance Contributions

Using $T_n^{\dagger}$ and Δ_n the derivative becomes[1]

$$\frac{\partial}{\partial \xi} I_n^{a\dagger} = \int \cdots \int T_n^{\dagger} \frac{\partial}{\partial \xi} \log\left(T_n^{\dagger}\right) \Delta_n \, d\vec{x}_0 \, d\vec{x}_1 \cdots d\vec{x}_{n-1} \, d\vec{x}. \tag{5.41}$$

With regard to the importance sampling technique, the derivative of $T_n^{\dagger}$ in Eq. (5.41) is expressed as a logarithmic derivative. The logarithm of $T_n^{\dagger}$ is introduced:

$$\Gamma_n := \log\left(T_n^{\dagger}\right). \tag{5.42}$$

For sake of simplicity but without loss of generality and as aforementioned the special case of an atmosphere containing two sorts of particles (indices 1 and 2), and absorbing and scattering gases (with index m) is

---

[1]The principle of derivative calculation is discussed in appendix B. The results obtained therein are carried over to the more complex RT case.

discussed. The total scattering coefficient at location $\vec{r}$ thus is

$$\varepsilon_s(\vec{r}) = [\varepsilon_m + \varpi_{01}\varepsilon_1 + \varpi_{02}\varepsilon_2](\vec{r}) \tag{5.43}$$

and the total extinction is

$$\varepsilon(\vec{r}) = [\beta + \varepsilon_m + \varepsilon_1 + \varepsilon_2](\vec{r}) \tag{5.44}$$

where $\beta(\vec{r})$ is the absorption coefficient of the molecular absorbers. The total optical thickness along the backward trajectory until the n scatter order is

$$\tau_{\vec{r}_0 \to \cdots \to \vec{r}_n} = \int_{\vec{r}_0}^{\vec{r}_1} \varepsilon(\vec{r}) \, |d\vec{r}| + \int_{\vec{r}_1}^{\vec{r}_2} \varepsilon(\vec{r}) \, |d\vec{r}| + \cdots + \int_{\vec{r}_{n-1}}^{\vec{r}_n} \varepsilon(\vec{r}) \, |d\vec{r}| \,. \tag{5.45}$$

Furthermore, in order to improve the readability, the following symbolic abbreviation is introduced

$$\varepsilon_s P := \varepsilon_m P_m + \varpi_{01}\varepsilon_1 P_1 + \varpi_{02}\varepsilon_2 P_2. \tag{5.46}$$

In this notation the logarithm of $T_n^\dagger$ is accordingly

$$\Gamma_n = -\tau_{\vec{r}_0 \to \cdots \to \vec{r}_n} - \tau^*_{\vec{r}_n \to \vec{r}_{\text{Sun}}} + \sum_{i=1}^{n-1} \log\left(\varepsilon_s P(\vec{r}_i, \mu_i)\right) + \log\left(\varepsilon_s P(\vec{r}_n, \mu_n^*)\right). \tag{5.47}$$

Symbols tagged with * indicate contributions associated with the respective scatter order (n^{th} scatter event and associated dashed lines in Fig. 5.2). The cosines are defined as follows:

$$\mu_n \quad := \quad \vec{\omega}_{n-1} \cdot \vec{\omega}_n \tag{5.48}$$
$$\mu_n^* \quad := \quad \vec{\omega}_{n-1} \cdot \vec{\omega}_n^*. \tag{5.49}$$

Two more symbolic abbreviations are defined:

$$S_n \circ [A]_c := \sum_{i=1}^{n-1} \left[A(\vec{r}_i, \mu_i)\right]_c + \left[A(\vec{r}_n, \mu_n^*)\right]_c, \tag{5.50}$$

where

$$\left[A(\vec{r})\right]_c := \chi_c(\vec{r}) A(\vec{r}) \tag{5.51}$$

and $\chi_c(\vec{r})$ is 1 if $\vec{r}$ is located in the cluster with index c. Eq. (5.50) restricts the summation over contributions A to those located in the cluster with index c.

5.2.1.2. 1ˢᵗ Order Derivatives

The most important radiance derivatives are those with respect to the cluster absorption coefficient β_c and the particle js extinction coefficient ε_{cj}, single scattering albedo ϖ_{0cj} and parameters (indexed with i) p_{cij} of the phase function P_{cj}:

$$\partial_{\beta_c}\Gamma_n \quad = \quad -\left[l_n + l_n^*\right]_c \tag{5.52}$$

$$\partial_{\varepsilon_{cj}}\Gamma_n \quad = \quad -\left[l_n + l_n^*\right]_c + S_n \circ \left[\frac{\varpi_{0j}P_j}{\varepsilon_s P}\right]_c \tag{5.53}$$

$$\partial_{\varpi_{0cj}}\Gamma_n \quad = \quad S_n \circ \left[\frac{\varepsilon_j P_j}{\varepsilon_s P}\right]_c \tag{5.54}$$

$$\partial_{p_{cij}}\Gamma_n \quad = \quad S_n \circ \left[\frac{\varpi_{0j}\varepsilon_j \partial_{p_{ij}} P_j}{\varepsilon_s P}\right]_c \tag{5.55}$$

Eq. (5.52) is the length of the sub trajectory n in the cluster c as it is obtained from the derivative of the sum of Eq. (5.45) (resulting in $-l_n$) and $\tau^*_{\vec{r}_n \to \vec{r}_{\text{Sun}}}$ (contributing $-l_n^*$) with respect to the cluster absorption coefficient and is also contained in the aerosol particle derivatives. The additional summands in Eqs. (5.53-5.55) result from the logarithmic derivatives of Eq. (5.46). According to Eq. (5.50) the bracketed expressions are equally

evaluated for the first $n-1$ scatter events (beginning at the detector) on the sub trajectory of order n. At the last scatter event the angle (i.e. the μ_n^*) inserted into the phase function is the angle between the Sun direction and the sub trajectory.

5.2.1.3. 2ⁿᵈ Order Derivatives

Second order derivatives decompose into 1ˢᵗ and 2ⁿᵈ order logarithmic derivatives as follows:

$$\partial_{12}^2 g \; = \; \partial_1\left(g \cdot \partial_2 \log(g)\right) \tag{5.56}$$

$$= \; \partial_2 \log(g) \cdot \partial_1 g + g \cdot \partial_{12}^2 \log(g) \tag{5.57}$$

$$= \; g \cdot \left(\partial_1 \log(g) \cdot \partial_2 \log(g) + \partial_{12}^2 \log(g)\right) \tag{5.58}$$

i.e. the 2ⁿᵈ order derivative contains a product of 1ˢᵗ order logarithmic derivatives. A usefull consequence is that for different clusters $c_1 \neq c_2$ follows $\partial_{x_{c_1} x_{c_2}}^2 \Gamma_n = 0$, i.e.

$$c_1 \neq c_2 \quad \Rightarrow \partial_{x_{c_1} x_{c_2}}^2 e^{\Gamma_n} = e^{\Gamma_n} \cdot \left(\partial_{x_{c_1}} \Gamma_n\right) \cdot \left(\partial_{x_{c_2}} \Gamma_n\right). \tag{5.59}$$

This is particularly interesting while investigating how optical property derivatives with respect to one cell depend on optical properties derivatives with respect to other (distinct) cells. Furthermore, if one derivative is given with respect to the absorption coefficient, 2ⁿᵈ order logarithmic derivatives for quantities associated with a single cluster even vanish:

$$\partial_{X \beta_c}^2 \Gamma_n = 0 \quad \text{for all} \quad X \in \{\beta_c, \varepsilon_{cj}, \omega_{0cj}, p_{cij}\}. \tag{5.60}$$

The reason is that in Eq. (5.47) only the τ contributions depend on the absorption coefficients β_c. All other cases are listed in the following:

$$\partial_{\varepsilon_j \varepsilon_i}^2 \Gamma_n \; = \; -S_n \circ \left[\frac{(\omega_{0j} P_j)(\omega_{0i} P_i)}{(\varepsilon_s P)^2}\right]_c \tag{5.61}$$

$$\partial_{\omega_{0j} \varepsilon_i}^2 \Gamma_n \; = \; S_n \circ \left[\frac{\varepsilon_s P \delta_{ij} P_i - (\omega_{0i} P_i)(\varepsilon_j P_j)}{(\varepsilon_s P)^2}\right]_c \tag{5.62}$$

$$\partial_{p_{jm} \varepsilon_i}^2 \Gamma_n \; = \; S_n \circ \left[\frac{\varepsilon_s P \delta_{ij} \omega_{0j} \partial_{p_{jm}} P_j - \omega_{0i} P_i \varepsilon_j \omega_{0j} \partial_{p_{jm}} P_j}{(\varepsilon_s P)^2}\right]_c \tag{5.63}$$

$$\partial_{\omega_{0j} \omega_{0i}}^2 \Gamma_n \; = \; -S_n \circ \left[\frac{(\varepsilon_i P_i)(\varepsilon_j P_j)}{(\varepsilon_s P)^2}\right]_c \tag{5.64}$$

$$\partial_{p_{jm} \omega_{0i}}^2 \Gamma_n \; = \; S_n \circ \left[\frac{\varepsilon_s P \varepsilon_i \delta_{ij} \partial_{p_{jm}} P_j - \varepsilon_i P_i \omega_{0j} \varepsilon_j \partial_{p_{jm}} P_j}{(\varepsilon_s P)^2}\right]_c \tag{5.65}$$

$$\partial_{p_{jm} p_{il}}^2 \Gamma_n \; = \; S_n \circ \left[\frac{\varepsilon_s P \omega_{0i} \varepsilon_i \delta_{ij} \partial_{p_{jm} p_{il}}^2 P_i - (\omega_{0i} \varepsilon_i \partial_{p_{il}} P_i)(\omega_{0j} \varepsilon_j \partial_{p_{jm}} P_j)}{(\varepsilon_s P)^2}\right]_c. \tag{5.66}$$

5.2.1.4. Derivatives Local Estimate Structure

Once derivatives $\partial^D \Gamma_n$ (where D = 1 or 2, see previous sections 5.2.1.2 and 5.2.1.3) are available, the local estimate calculation can be performed:

$$\partial^D I \approx \sum_{n=1}^{N} e^{-\tau^*(\vec{r}_n)} P(\vec{r}_n, \mu_n^*) \partial^D \Gamma_n \tag{5.67}$$

The result is, similar as Eq. (5.31), a sum over scatter orders.

5.3. Validation of Functionals

A forward model simulates quantities that are measures of a physical process. Using a different formulation, it is the specific implementation of an algorithm which is capable of solving a differential equation (DE) describing the physics of the process. With respect to the reliability of the forward model predictions in comparison with measured values, some important questions must be addressed. The first question is, if the physics of the process is assessed entirely in the formulation of the DE. Sometimes this question can be answered in parts by preparing specials cases for which the differential equation reduces to simpler form. Then, potentially analytic solutions are available and simultaneously measurable. For example one could test the validity of the Bouguer-Lambert-Beer term in the RTE by measuring the radiative flux through a small medium for which multiple scattering contributions can nearly be ruled out, i.e. the integral term is small. Another example is to compare measured and modeled stratospheric radiances for wavelengths for which single scattering is the dominant and prevailing process. In comparisons for all cases containing the full complexity of the physics the question whether the implementation, i.e. the technical realization of the solution method is correct is crucial. To summarize, a forward model validation contains two important steps. In a first step, it must be proven that the implementation is correct and the solution obtained by the program obeys the DE. If a direct proof is not possible, comparison with other methods (i.e. models) to solve the same DE very likely allows to test, whether this is the case. The fidelity of the test then relies on the assumption that an ensemble of models operating on the same input data yields correct predictions. The second important validation step is to test whether the physics is assessed correctly. This can only be done by comparisons to measurements and it is a challenging task. Most difficulties arise in preparing a case which can be simulated *in principle* by the forward model. In principle here means, that a finite set of parameters (the *state*) needs to be known in order to compare measured and simulated quantities within a certain accuracy range. Conclusions on the validity of the modeled physics can then only be drawn if the degree of the state uncertainty propagation into the simulated quantities is significantly less then the sensitivity of the simulated quantities with respect to the physical aspect to be tested.

In this thesis methods in radiative transfer modeling are investigated. With respect to the validity of the concept of elastic and polarized scattering it is trustfully referred to publications of Michael I. Mishchenko et al. [Lacis et al., 1998, Mishchenko, 2002, Mishchenko, 2003, Mishchenko, 2008, Mishchenko et al., 2006, Mishchenko, 2009], who thoroughly analyzed the limits of applicability of the vector radiative transfer equation. McArtim calculates scalar and vector radiances and first and second order scalar radiance derivatives. The aim of the following section in this chapter is to test whether the implementation of some functional estimation methods is correct. Previous comparisons [Deutschmann et al., 2011] already showed that scalar radiances and first order derivatives are implemented correctly. What remains is the validation of vector radiances and second order derivatives.

5.3.1. Validation of Vector Radiances

[Kokhanovsky et al., 2010] published benchmark results for vector radiative transfer simulations. Fig. 5.3 shows inter comparison results with the RTM SCIATRAN [Rozanov et al., 2005]. SCIATRAN showed perfect agreement with 2 other models and it is thus taken as a reference model. The plot shows the Stokes vectors I, Q and U components obtained from a limb scan between the zenith and the ground through a purely molecular Rayleigh scattering atmosphere. The signals around VZA 90° correspond to the horizontal directions. As a result of the inter comparison, no obvious systematic deviations from the reference data are present. In addition to comparing with other models, other tests are carried out. Fig. 5.4 shows how scalar radiances compare with vector radiances. The differences are smallest for the cases with 90° relative azimuth angle between the Sun and the viewing direction. For all other cases the deviations range between zero and a few percent. The same benchmark results are taken to test whether the intersection point calculation of the ray tracer works as expected. In order to test this, the atmosphere is subdivided into 10 smaller layers with the same Rayleigh scattering coefficient. Tests show no deviation from results obtained in a single layer atmosphere.

5.3.2. Validation of Radiance Derivatives

In order to validate 2nd order derivatives, self consistency test as described in [Deutschmann et al., 2011] are applied. Such a test is, to systematically vary a parameter x influencing a function $f(x)$, to fit a function $g(x)$
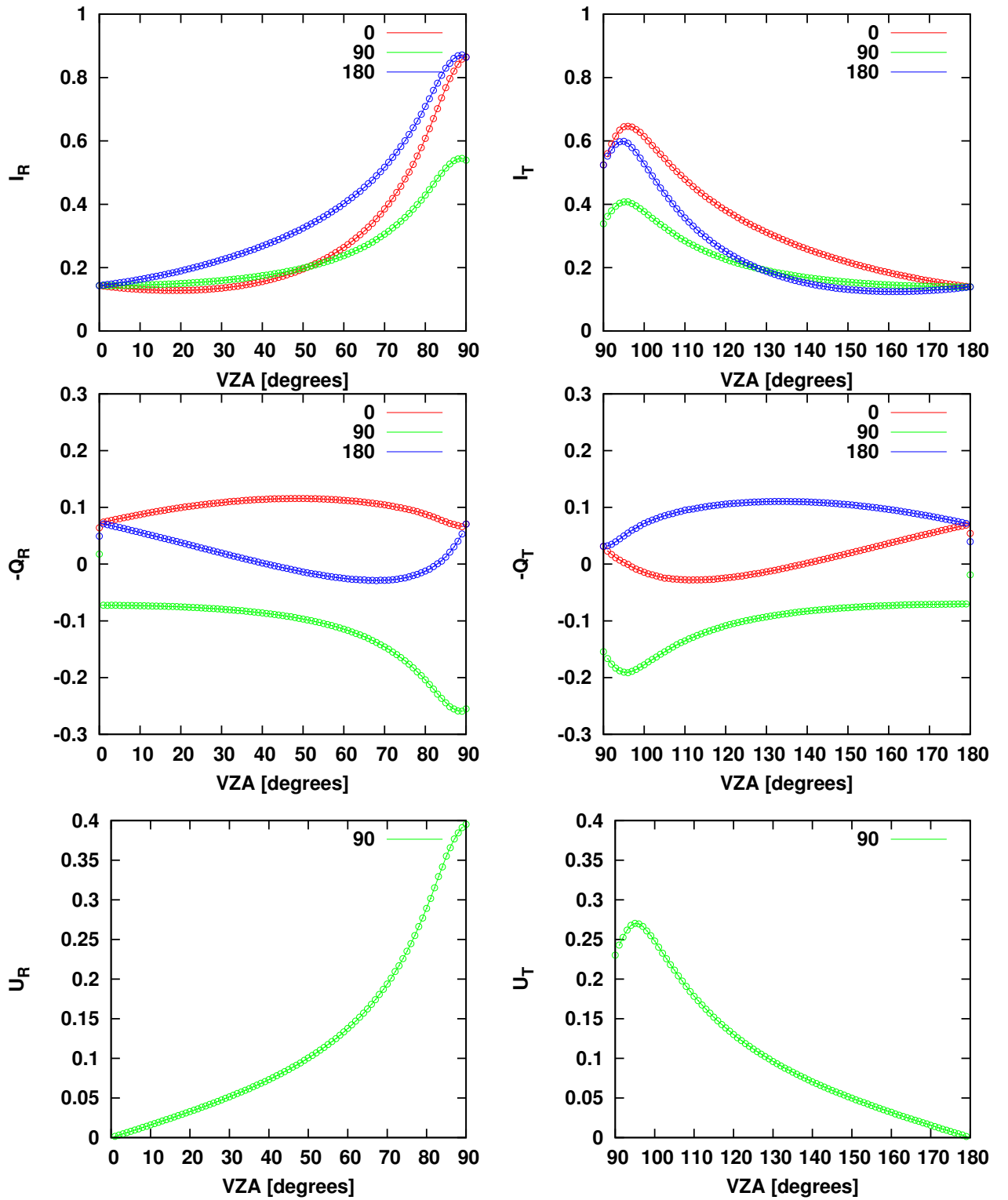
Figure 5.3.: Reproduction of Fig. 2 from [Kokhanovsky et al., 2010] with McArtim results. The solid lines are results from the SCIATRAN model, points and error bars are McArtim results. Shown are reflected (**left column**) and transmitted (**right column**) Stokes vector radiance components for a one layered plane parallel pure molecular (Rayleigh) atmosphere. The surface albedo is set to zero and no scattering particles nor any gaseous absorbers are present. For more details it is referred to the cited publication.
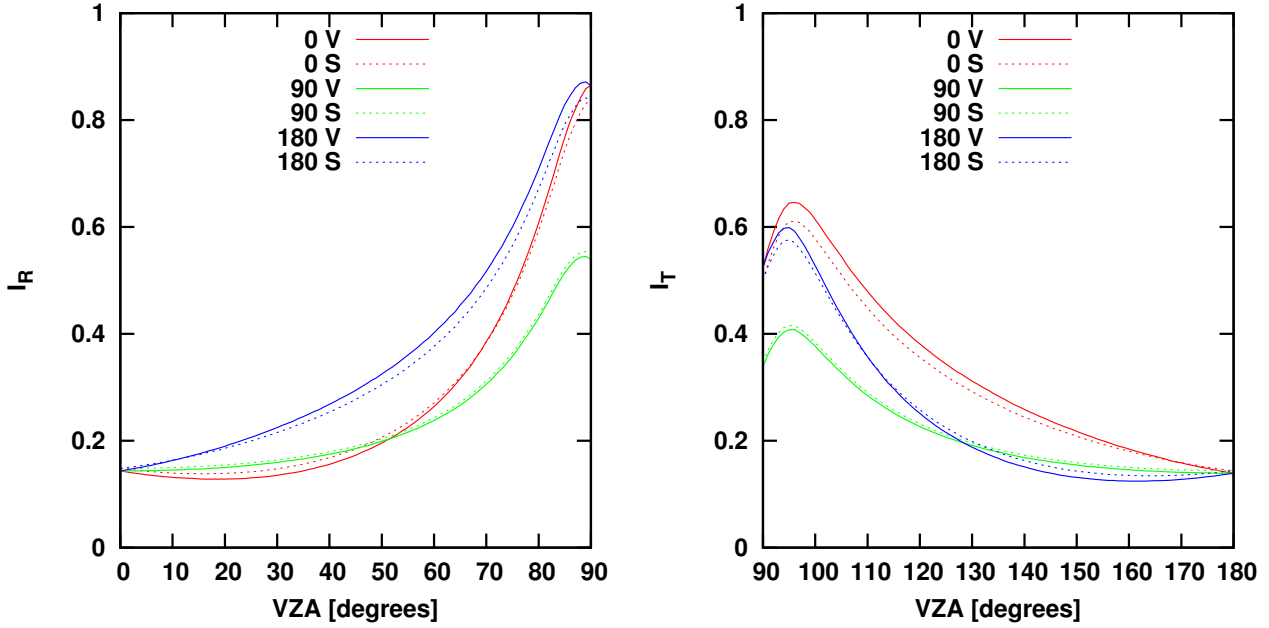
Figure 5.4.: Comparison between scalar (dotted lines) and vector (solid lines) radiances. The setup is identical to Fig. 5.3.

to $f(x)$ and to compare the derivatives $f'(x)$ and $g'(x)$. In case of an agreement the model outputs $f(x)$ and $f'(x)$ are consistent. Fig. 5.5 shows the self consistency tests of the first order scalar radiance derivatives with respect to the cluster extinction coefficient, the single scattering albedo and the asymmetry parameter. Discrepancies can be explained by a too low or also too high polynomial degree used in the test. The next step is to validate the 2$^{\text{nd}}$ order scalar radiance derivatives. Fig. 5.6 shows the corresponding self consistency tests. Again, the implementation seems to be correct and only statistical fluctuations let the model output deviate from the self consistent prediction.
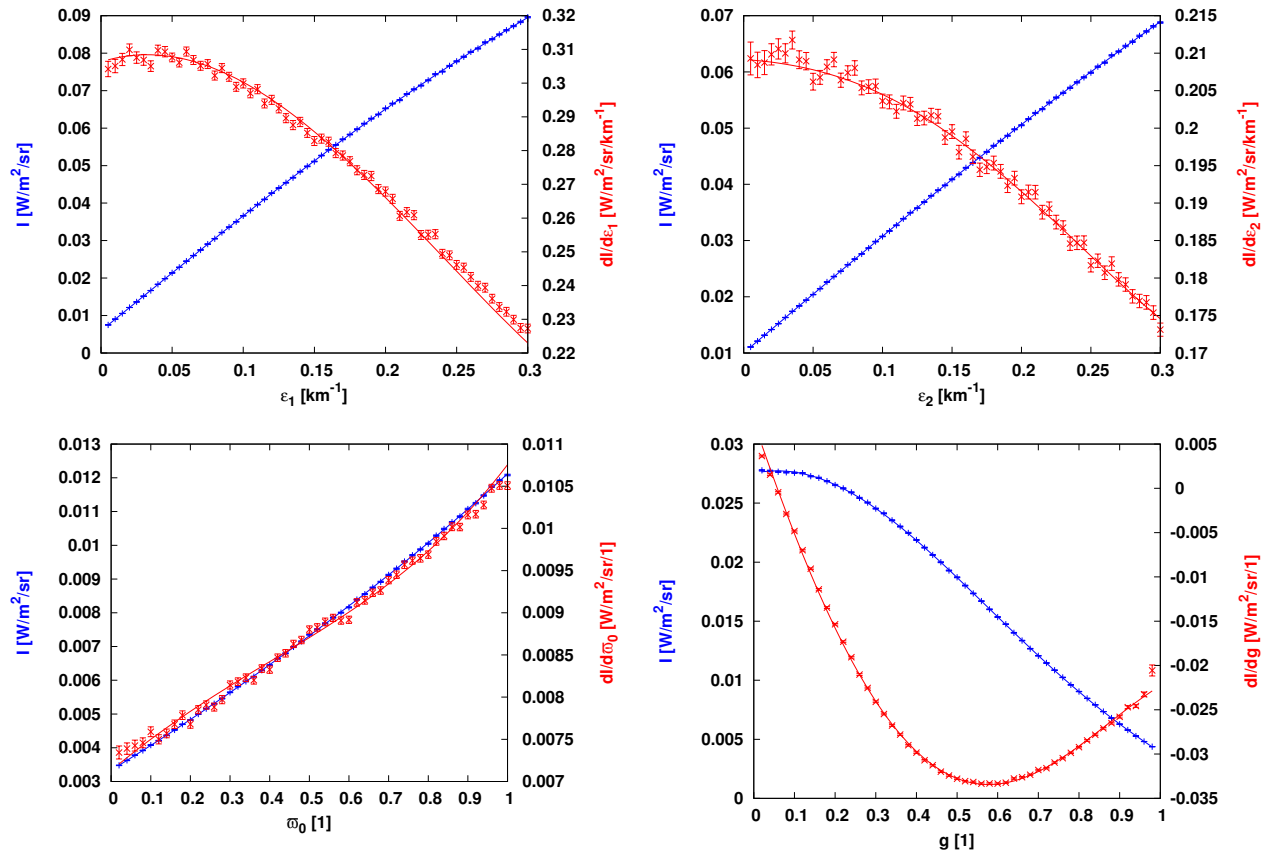
Figure 5.5.: Validation of 1st order scalar radiance derivatives.
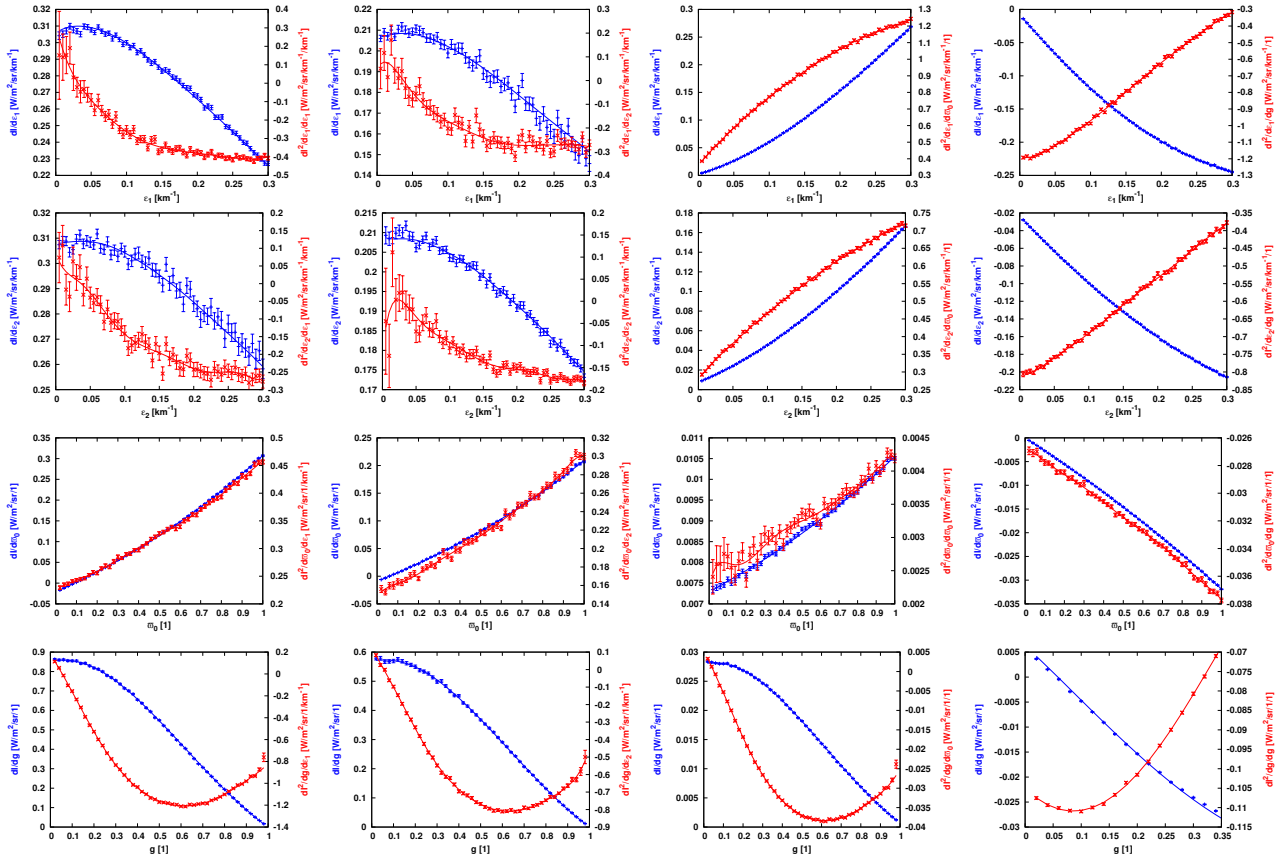
Figure 5.6.: Self consistency test for second order scalar radiance derivatives. In each row, the optical parameter that is varied is shown in the x axis caption of the respective plot. From top panel row until the bottom panel row the optical parameters are the particle extinction coefficients ε_1, ε_2, the single scattering albedo ϖ_0 and the asymmetry parameter g.

6

Optical Absorption Spectroscopy

This chapter contains a mathematical analysis of the concept of optical absorption spectroscopy. The purpose of writing this chapter is to reveal, how the optical absorption spectroscopy method (OAS) and especially the differential OAS method (DOAS) appears from a radiative transfer modeler's perspective. New perspectives for looking at existing numerical methods to retrieve information on spatial abundances of not necessarily weak gaseous absorbers from scattered Sun light spectra are given. Some considerations assume to have a perfect measurement device and measurement setup (e.g. exact information on measurement geometry). It is attempted to include these uncertainties of the measurement process into the discussion, but the focus is on discussing information that is available *in principle* for wide spread grating spectrometers. The analysis should be carefully compared to the mathematical part of Chapter 6 in [Platt and Stutz, 2008]. In addition to the more profound model of the scattered light intensity based on the Neumann series used in this work also spectra for a model spectrometer are presented in order to illustrate the analysis. Details on currently widespread types of spectrometers, the current theory and to some extent also the basis of the discussion are found in [Platt and Stutz, 2008]. In order to have a visual impression of the so called Czerny-Turner configuration of grating spectrometers and for introducing the used terminology it is referred to Fig. 6.1.
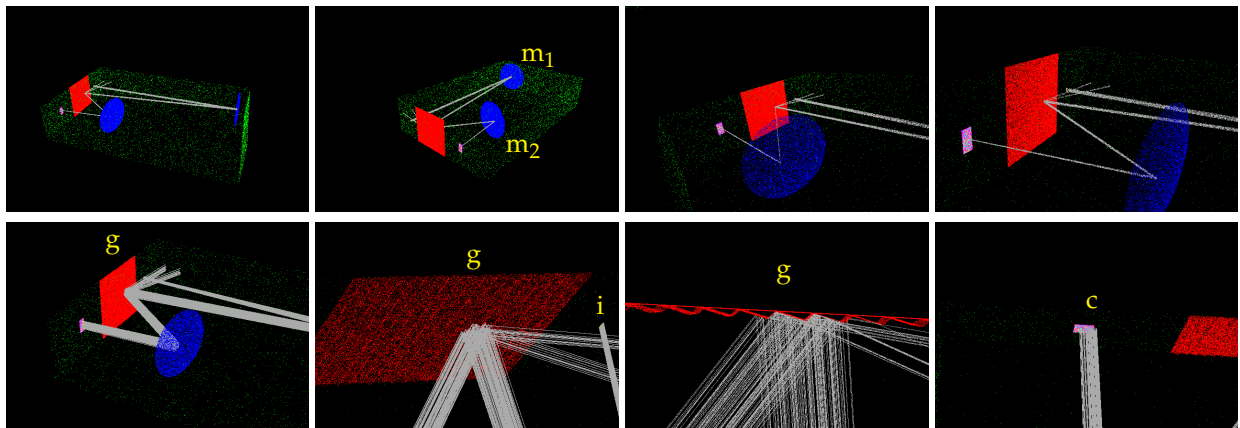
Figure 6.1.: Schematic showing different perspectives on a grating spectrometer housing with a Czerny-Turner configuration of optical elements. The light path inside the housing begins at the inlet (i) which usually consists of a slit. Then a spherical mirror (m_1) follows which serves collimating the divergent beam emerging from the slit at the inlet i. The parallel light then irradiates the grating (g) and is reflected into the direction of the second spherical mirror (m_2) where it is focused on the CCD camera (c). For many applications the camera is a vertically (related to the grating) aligned array of charged coupled photo effect detector. The different pixels of the camera are also called channels.
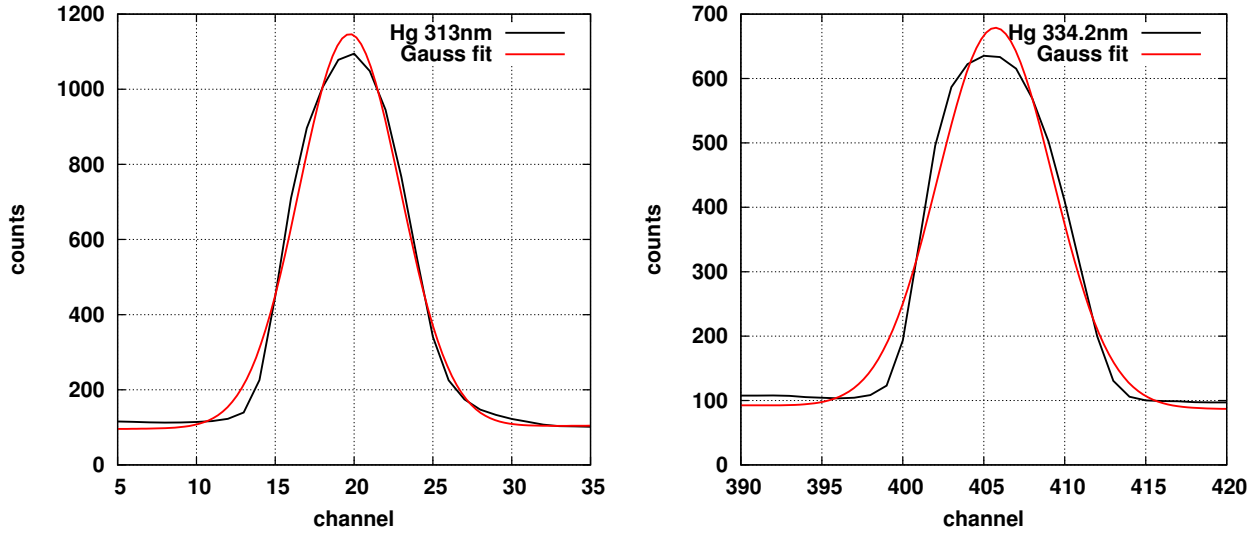
Figure 6.2.: Mercury emission line shapes recorded on a typical grating spectrometer. The background socket is caused by a difference in the temperature at which the dark current was obtained. The temperature at which the spectrometer was exposed to the mercury lamp light was higher. The slit function $s_c(\lambda)$ is obtained from the recorded spectrum by removing the background and normalizing the resulting line shape with the area under the curve.

6.1. A Simply Structured Instrument Forward Model

After correcting a recorded spectrum for dark current and offset (see e.g. [Platt and Stutz, 2008]), the signal S_c of a grating spectrometers channel c can be described by

$$S_c = \int_0^\infty \int_{\Omega_{\text{FOV}}} R(\lambda)\eta(\lambda)s_c(\lambda)\,\mathrm{d}\omega\,\mathrm{d}\lambda \tag{6.1}$$

$$\approx \int_0^\infty I(\lambda)\eta(\lambda)s_c(\lambda) \tag{6.2}$$

$$\approx \Delta\lambda \sum_i \eta(\lambda_i)I(\lambda_i)s_c(\lambda_i) \tag{6.3}$$

where $R(\lambda)$ is the radiance the spectrometers telescope lens is exposed to, I is the intensity which is the radiance integrated over the small (!) FOV[1], $\eta(\lambda)$ accounts for the detectors quantum efficiency and the grating efficiency, lens and band pass filter transmission and other broad band instrument features, except stray light. Furthermore, for sake of simplicity, it is supposed that optical fibers mix light portions coming from different regions of the field of view. For the model result obtained in this chapter, as the slit function

$$s_c(\lambda) = \frac{1}{\sigma_c\sqrt{2\pi}}\exp\left\{-\frac{1}{2}\left(\frac{\lambda-\mu_c}{\sigma_c}\right)^2\right\} \tag{6.4}$$

a Gaussian line shape is assumed centering around the channel center wavelength μ_c with a width of σ_c (see Fig. 6.2). As is obvious in the plot to approximate the true line shape of a typical spectrometer with a Gaussian line shape is only to some extent justified. The systematic error of this approximation is also subject of the discussion in Section 7.4.4.1 of the following Chapter 7. The wavelength discretization $\{\lambda_i, \Delta\lambda_i\}$ is chosen such that there are some 10 wavelengths (avoidance of under sampling, [Platt and Stutz, 2008]) within the $4\sigma_c$ range of the slit function center wavelength. Since it is experimentally a challenging task to measure all these instrument parameters (especially $\eta(\lambda)$) with sufficient accuracy, the calibration of the spectrometer can be done by fitting simultaneously all instrument parameters (i.e. η, f and the channel to wavelength polynomial) together with a simulated (high resolution) atmospheric spectrum $I(\lambda)$ with lowest possible atmospheric uncertainties to the measured spectrum in a least squares fit[2]. In appendix C derivatives

---

[1]see Chapter 5.1 with respect to the definition of I

[2]A fit also employing atmospheric RT forward model derivatives is implemented but not applied due to lack of time.

of the spectrometer forward function involved in the fit are listed. Another approximation in the following sections is that grating efficiency and quantum yield $\eta(\lambda)$ are approximately constant for one channel. In reality consideration of the wavelength dependence cause small deviations depending on the slope of the wavelength dependence. In the following sections the instrument property function associated with a channel c is symbolized by

$$f_c(\lambda) = \eta(\lambda)s_c(\lambda, \mu, \sigma) \tag{6.5}$$

and the signal of channel c is written as

$$S_c = \int f_c(\lambda)I(\lambda)\,\mathrm{d}\lambda. \tag{6.6}$$

6.2. Pure Atmospheric Spectra and Absorption

One way to describe the method of optical absorption spectroscopy (OAS) is to start with the direct light experiment (Section 6.2.1) and then to apply the evaluation algorithm to scattered Sun light (Section 6.2.2) [Rozanov and Rozanov, 2010, Deutschmann, 2009]. In such measurement constellation, the spectrometer is exposed to the light source directly, i.e. by far the major part of the measured signal is attributed to direct Sun radiation.

6.2.1. Direct Light Spectra

In the direct light experiment, the intensity can be described as follows:

$$I_{\mathrm{DL}}(\lambda) := I_0(\lambda)\exp\left(-\int\limits_{\mathrm{telescope}}^{\mathrm{light\ source}}\left[\varepsilon_{\mathrm{mol}} + \varepsilon_{\mathrm{part}} + \sum_i N_i\sigma_i\right](l,\lambda)\,\mathrm{d}l\right) \tag{6.7}$$

Here $\varepsilon_{\mathrm{mol}}$ and $\varepsilon_{\mathrm{part}}$ denote the extinction coefficients for molecular and particle scattering, N_i is the number density of the ith gaseous species and σ_i is its absorption cross section. $I_0(\lambda)$ describes the spectral signature of the light source, i.e. in the atmospheric direct Sun light experiment $I_0(\lambda)$ is the extraterrestrial solar irradiance. In the terminology of inverse modelling Eq. (6.7) constitutes a so called forward model. How does the direct light intensity in Eq. (6.7) depend on the concentration N_i of the the absorber of interest? This question can be addressed by calculating derivatives. Derivatives with respect to the absorption coefficient are related to other derivatives by a change of variables based on $\beta_i = \sigma_i N_i$:

$$\frac{\partial}{\partial\beta_i}\overset{\sigma_i=const.}{=}\frac{1}{\sigma_i}\frac{\partial}{\partial N_i}\leftrightarrow\frac{\partial}{\partial N_i}\overset{\sigma_i=const.}{=}\sigma_i\frac{\partial}{\partial\beta_i}, \tag{6.8}$$

σ_i is the cross section at the respective wavelength. The structure of Eq. (6.7) also suggests to apply a negative logarithmic derivative with respect to the number density. The negative logarithmic derivative is applied to $I_{\mathrm{DL}}(\lambda)$:

$$-\frac{\partial}{\partial N_i}\log\left(\frac{I_{\mathrm{DL}}(\lambda)}{I_0(\lambda)}\right) = \sigma_i\frac{\partial}{\partial\beta_i}\int\limits_{\mathrm{telescope}}^{\mathrm{light\ source}}\left[\varepsilon_{\mathrm{mol}} + \varepsilon_{\mathrm{part}} + \sum_i \underbrace{N_i\sigma_i}_{\beta_i}\right](l,\lambda)\,\mathrm{d}l \tag{6.9}$$

$$= \sigma_i\int\limits_{\mathrm{telescope}}^{\mathrm{light\ source}}\mathrm{d}l. \tag{6.10}$$

The result of application of the derivative is a volume. Switching to the negative logarithmic derivative with respect to the absorption coefficient yields the light path traversed by measured light:

$$-\frac{\partial}{\partial\beta_i}\log\left(\frac{I_{\mathrm{DL}}(\lambda)}{I_0(\lambda)}\right) = \int\limits_{\mathrm{telescope}}^{\mathrm{light\ source}}\mathrm{d}l. \tag{6.11}$$

It is remarkable that the right side of the derivative does not depend on the species i for which the derivative is calculated. As a summarizing statement the following note is made:

> *Taking the negative logarithmic derivative of the intensity with respect to the absorption coefficient in a region of the radiation transport process yields the light path in the region traversed by the observed radiation.*

In the following section it is analyzed which form the right side of the Eq. (6.11) assumes if a scattered Sun light intensity is inserted on the left side.

6.2.2. Scattered Sun Light Spectra

It is common practice to measure scattered Sun light. In comparison to the direct light case, the intensity spectrum assumes a different form because the light path is more complex. In the direct light configuration of light source, optical medium and detector only very similar paths needs to be taken into account in order to describe the measured signal whereas when observing scattered sunlight, a manifold of very different paths have to be considered. Actually there is no longer "a light path" but an infinte sized set of piecewise straight polygons consisting of a variable number of vertices, the scatter events. If an element of that set, a single polygon, has n scatter events, the trajectory is said to be of order n. In this section the effect of absorption on the intensity *before the measurement device* is investigated. Instrument effects on the the intensities are discussed further below in Section 6.3.1.

The Monte Carlo formalism allows to express the intensity in terms of contributions of scatter orders (the adjoint Neumann series in this work, see Chapter 5.1.2):

$$I(\lambda) = \left\langle \sum_{n=1}^{\infty} c_n(\lambda) \right\rangle = \left\langle \sum_{n=1}^{\infty} c_n^*(\lambda) w_n(\lambda) \right\rangle, \tag{6.12}$$

where c_n is the local estimate of the scatter order n (compare to Eq. (5.31)). The intensity $I(\lambda)$ is given in units of $[I(\lambda)] = \text{W/m}^2/\text{nm}$ (irradiance). In the following discussion the logarithm of the intensity appears in many equations. Since the logarithmic derivative of the pure number of the intensity $I(\lambda)$ with respect to an optical parameter ζ of the atmosphere is identical to the logarithmic derivative of the so called Sun normalized intensity, i.e.

$$\frac{\partial}{\partial \zeta} \log \left(\frac{I(\lambda)}{[I(\lambda)]} \right) = \frac{\partial}{\partial \zeta} \log \left(\frac{I(\lambda)}{I_0(\lambda)} \right) \tag{6.13}$$

the unit of the intensity is loosely ignored in the equations and its logarithm is taken. Using the importance sampling technique (Chapter 4.3) in Eq. (6.12), the trace gas of interest is excluded from the path sampling and local estimation, and included in the corresponding importance sampling weights w_n. The associated local estimate is c_n^*. From this artificial separation follows:

$$\frac{\partial}{\partial \beta_{vi}} c_n^* = 0 \tag{6.14}$$

because only the importance sampling weight $w_n(\lambda)$ contains information on the species i:

$$w_n(\lambda) = e^{-\tau_{i,n}(\lambda)} \tag{6.15}$$

with

$$\tau_{i,n}(\lambda) = \int_{\text{trajectory } n} \sigma_i(\lambda, \vec{r}(l_n(\lambda))) N_i(\vec{r}(l_n(\lambda))) \, \mathrm{d}l_n(\lambda) = \int_{\text{trajectory } n} \beta_i(\lambda, \vec{r}(l_n(\lambda))) \, \mathrm{d}l_n(\lambda). \tag{6.16}$$

and where l_n symbolizes the parametrization value for the light path $\vec{r}(l)$. In the discretized model atmosphere the expression translates as follows:

$$\tau_{i,n}(\lambda) = \sum_v \sigma_i(\lambda) N_{i,v} l_{v,n}(\lambda) = \sum_v \beta_{iv}(\lambda) l_{v,n}(\lambda) \tag{6.17}$$

where the index v stands for volume or voxel and $l_{v,n}$ is the length of the trajectory of the nth scatter order through the volume v. In case of weak absorption the importance sampling weight is approximately

$$w_n(\lambda) \approx 1 - \tau_{i,n}(\lambda) \tag{6.18}$$

In order to understand how (much) the scattered light intensity Eq. (6.12) depends on the number density, it is again derived for the absorption coefficient, but this time for the absorption coefficient β_v of a certain

volume (layer or cluster in general) v:

$$-\frac{\partial \log\left(I(\lambda)\right)}{\partial \beta_v} = -\frac{1}{I(\lambda)}\frac{\partial}{\partial \beta_v}\left\langle \sum_{n=1}^{\infty} c_n^*(\lambda)w_n(\lambda)\right\rangle \tag{6.19}$$

$$\overset{\text{Eqs. 6.14-6.17}}{=} \frac{1}{I(\lambda)}\left\langle \sum_{n=1}^{\infty} c_n^*(\lambda)w_n(\lambda)l_{v,n}(\lambda)\right\rangle \tag{6.20}$$

$$\overset{c_n(\lambda)=c_n^*(\lambda)w_n(\lambda)}{=} \frac{\left\langle \sum_{n=1}^{\infty} c_n(\lambda)l_{v,n}(\lambda)\right\rangle}{\left\langle \sum_{n=1}^{\infty} c_n(\lambda)\right\rangle}. \tag{6.21}$$

The expression obtained is an intensity weighted light path

$$s_v(\lambda) = -\frac{\partial \log\left(I(\lambda)\right)}{\partial \beta_v} = -\frac{1}{I(\lambda)}\frac{\partial I(\lambda)}{\partial \beta_v}. \tag{6.22}$$

$s_v(\lambda)$ is called sensitivity[3] for the volume v and deserves a closer inspection.

6.2.2.1. The 3D Sensitivity in Scattered Sun Light Measurements

The s_v are of central importance for any absorption spectroscopy based retrieval of spatial absorber concentration profiles in the atmosphere. It is common practice to restrict modeling the radiation transport process for deriving s_v to one dimension. Using the radiatioin transport model presented in this work it is possible to understand the 3D composition of these sensitivities. For basic instructions how to interpret the plots see Fig. 6.3. The three dimensional (3D) sensitivity of a measurement towards a volume indexed with xyz in
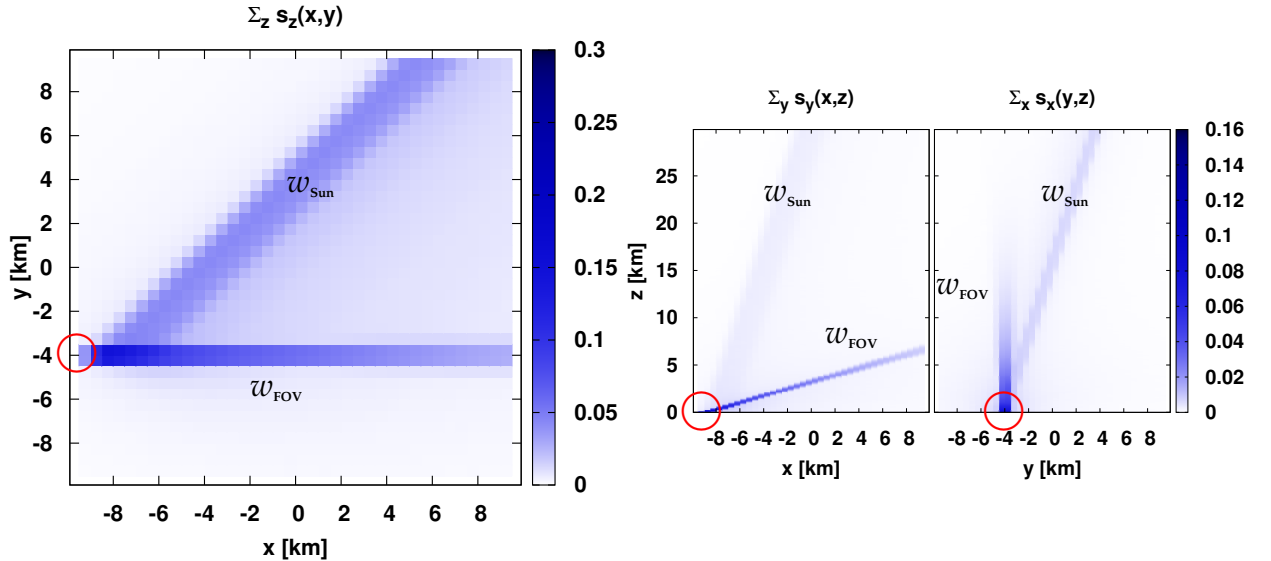
Figure 6.3.: Instructions for the interpretation of figures 6.4 and 6.5. Trajectories originate at the detector position (red). Many, but not all, scatter events are located in the FOV. The corresponding feature in the plot is called w_{FOV}. The second feature w_{Sun} originates from the evaluation of the local estimate at the respective scatter event and is directly related to the incident Sun light.

the atmosphere can be expressed in terms of the derivative of the intensity with respect to the absorption coefficient β_{xyz} in the volume:

$$s_{xyz} = -\frac{\partial \log\left(I\right)}{\partial \beta_{xyz}} = -\frac{1}{I}\frac{\partial I}{\partial \beta_{xyz}}. \tag{6.23}$$

In 1D radiative transfer modeling the atmosphere is discretized into horizontal layers for which logarithmic derivatives are calculated. The corresponding 1D sensitivities are usually expressed as so called box air

---

[3]$s_v(\lambda)$ is related to the box air mass factor $b_v(\lambda)$ for the volume v only in case of spherical shell layer volumina: $b_v(\lambda) = \frac{s_v(\lambda)}{h_v}$ where h_v is the vertical extension of the layer.

mass factors $b_z = s_z/h_z$, where s_z is the sensitivity of the layer z and h_z is the layers vertical extension. The relationship between s_z and the individual sensitivities s_{xyz} in the same horizontal layer is $s_z = \sum_x \sum_y s_{xyz}$. In that respect it is calculated and presented how conventional 1D sensitivities decompose into horizontal portions. Fig. 6.4 shows sums of 3D sensitivities for all coordinate directions. The plot on top shows vertically added 3D sensitivities $s_{xy} = \sum_z s_{xyz}$ which are calculated from an ensemble of trajectories as follows:

$$s_{xyz} \approx \frac{\sum_i \sum_j^{n_i} l_{ij,xyz} c_{ij}}{\sum_i \sum_j^{n_i} c_{ij}} = \underbrace{\frac{\sum_{i \in S_{xyz}} \sum_j^{n_i} l_{ij,xyz} c_{ij}}{\sum_{i \in S_{xyz}} \sum_j^{n_i} c_{ij}}}_{L_{xyz}} \underbrace{\frac{\sum_{i \in S_{xyz}} \sum_j^{n_i} c_{ij}}{\sum_i \sum_j^{n_i} c_{ij}}}_{p_{xyz}} = L_{xyz} p_{xyz}, \qquad (6.24)$$

where $l_{ij,xyz}$ is the light path length of the scatter order j of the trajectory i associated to the volume xyz and c_{ij} is the corresponding local estimate. In total the sampled trajectory i has n_i scatter events. Given a representative trajectory ensemble, the trajectories can be sorted into two sets: the first set S_{xyz} consists of trajectories traversing the volume, whereas trajectories of the complement don't. Only S_{xyz} trajectories contribute to the sensitivity, thus $l_{(i \notin S_{xyz})j,xyz} = 0$. A sensitivity (intensity weighted light path length) is thus always the product of the light path length in the volume L_{xyz} and the probability that light traverses the volume p_{xyz}. The sensitivities s_{xyz} can directly be used to estimate the effect of the (weak) absorption coefficient β_{xzy} on the intensity:

$$I = I^* e^{-\beta_{xyz} s_{xyz}} \qquad (6.25)$$

where I^* is the intensity without the gas of interest. In Fig. 6.4, four atmospheric situations at 440nm are
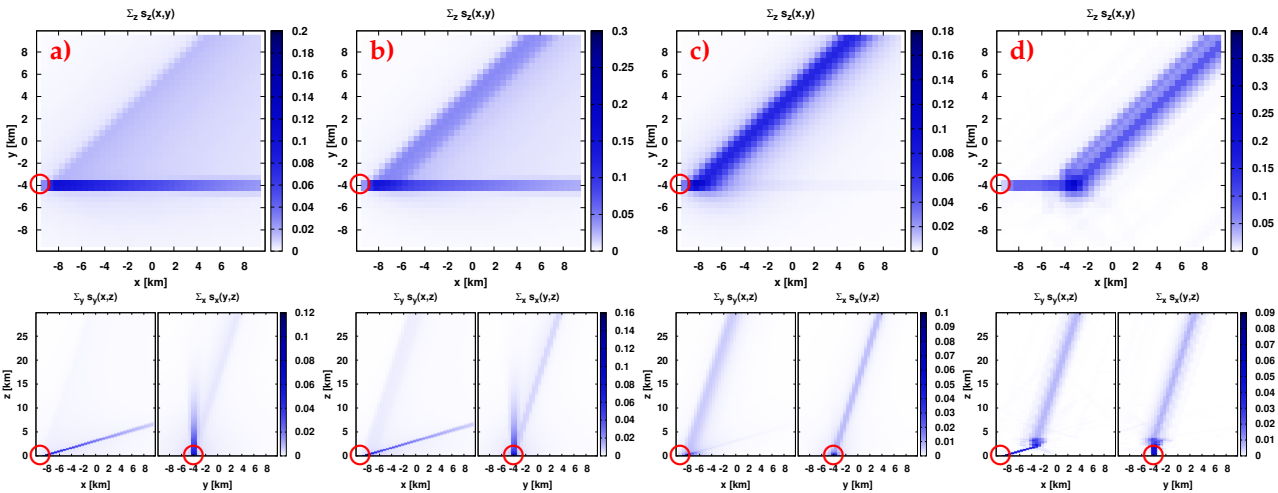
Figure 6.4.: Sun position SZA 30°, SRAA 45°. **a) - d)**: $\lambda = 440$nm, detector on the ground (red circle) at x=-8.75km, y=-3.75km, elevation 10°. **a)** pure Rayleigh atmosphere, **b)** low aerosol, **c)** high aerosol, **d)** cloud in 2-4km.

shown: a pure Rayleigh case in a) a high b) and a low c) aerosol load case and a cloud case d). Fig. 6.5 shows a limb observation geometry and 3D sensitivities for a satellite measurement.

6.2.2.2. Interpretation of the 3D Sensitivity

A spectroscopic measurement selects certain spatial portions of the radiation field, i.e. only some regions in the atmosphere influence the measurement. These regions respectively contribute to the measurement with a certain weight (sensitivities). The spatial distribution of weights is determined by the measurement geometry, the wavelength and the chemical composition of the atmosphere. The plots all show two distinct features: one is associated with the detector field of view w_{FOV} and the other with the incoming light beam w_{Sun}. In the ground based observations a-d, w_{FOV} is determined most by the scattering components in the boundary layer and the corresponding visibility. In the cases c and d, w_{FOV} is even spatially limited and terminated by the presence of scattering particles, whereas in the cloudless cases e and f, w_{FOV} is determined by the
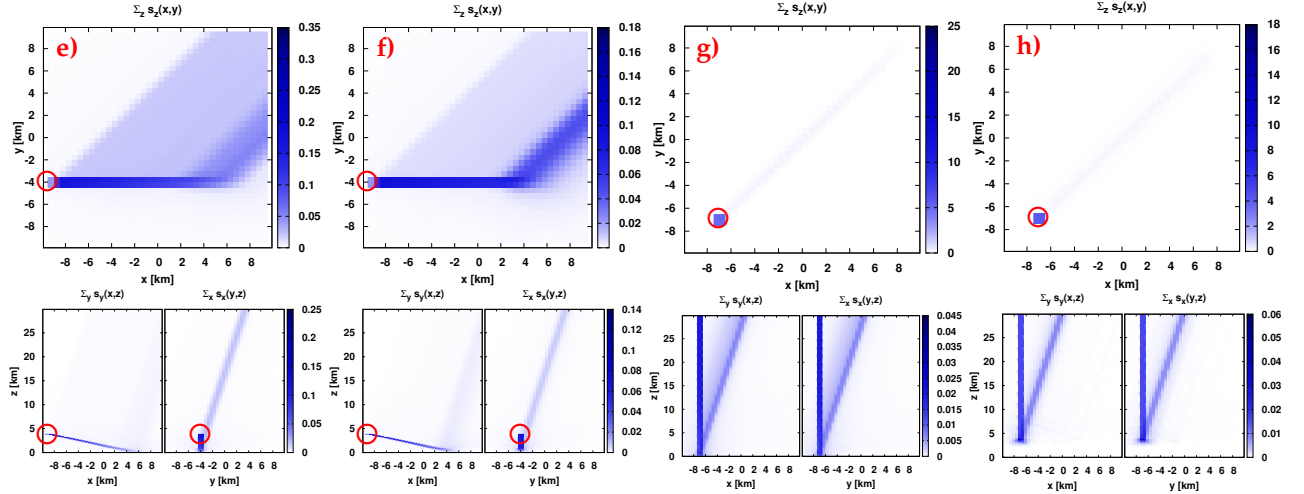
Figure 6.5.: Same Sun position as in Fig. 6.4. **e)** and **f)** limb geometries, detector at 4km oriented at -15° relative to the horizon. Low aerosol load in **e)**, high aerosol load in **f)**. **g)** and **h)** satellite nadir observation geometry, satellite over x=y=-6.75km. High aerosol in **g)**, cloud (as in case d) in **h)**.

FOV segment between the detector and the ground. Viewed from the (technical) perspective of the Monte Carlo method, the density of the w_{Sun} feature is directly related to the density of scatter events contributing to the measurement, since for every scatter event a intensity contribution is calculated. In the cases g and h a satellite nadir geometry was assumed. Both features can be distinguished clearly. In the x and y projections of the cloud case h it is obvious that an absorber below the cloud base can not be detected (cloud shielding effect). By choosing a certain measurement geometry an investigator can influence w_{FOV} more then w_{Sun}.

6.3. (D)OAS from the Perspective of Radiative Transfer Modeling

In this section the DOAS method is approached from radiation transport theory. The definition of the standard DOAS method is given in the course of the discussion. As in the previous section, the language of the Monte Carlo formalism, in particular the Neumann series, serves as a mathematical tool to describe intensities. First it is discussed in section 6.3.1, how weak absorber signatures appear on typical spectrometers. The spectrometer forward model is described in the previous Section 6.1. The absorber signatures appear as narrow band (so called *differential*) structures in the measured spectra and are target of the DOAS fit method. In the following Section 6.3.2, their strengths are quantitatively assessed using the importance sampling technique (as already prepared in the previous section 6.2.2) and then compared to the strength of related structures that are extracted by the standard DOAS technique.

6.3.1. (Rest) Signatures of Weakly Absorbing Gases

Before investigating the effect of DOAS fitting algorithms, an important approximation, the weak absorption approximation, is discussed. As the "weak absorber" also a difference in the concentration profile of a simulated absorber can be considered, i.e. the results derived here may also serve in a case of strong absorption for which only a small difference in the spatial concentration profile, leading to a small difference in the absorption, is considered. Starting point is Eq. (6.6) in combination with Eq. (6.12) expressed as the logarithm of the device unit normalized channel signal $L_c = \log\left(\frac{S_c}{DN}\right)$. The device norm DN is omitted in the following (compare to Eq. (6.13) and its context).

$$L_c \quad = \quad \log\left(\int f_c(\lambda) \left\langle \sum_{n=1}^{\infty} c_n^*(\lambda) w_n(\lambda) \right\rangle d\lambda\right) \tag{6.26}$$

$$\overset{Eq. (6.18)}{\approx} \quad \log\left(\int f_c(\lambda) \left\langle \sum_{n=1}^{\infty} c_n^*(\lambda)(1 - \tau_{i,n}(\lambda)) \right\rangle d\lambda\right) \tag{6.27}$$

6.3. (D)OAS from the Perspective of Radiative Transfer Modeling

At this point the channel signal as it occurs in the absence of the absorber i is introduced:

$$S_c^* = \int f_c(\lambda) \left\langle \sum_{n=1}^{\infty} c_n^*(\lambda) \right\rangle d\lambda \quad \text{and} \quad L_c^* = \log(S_c^*). \tag{6.28}$$

Further,

$$L_c = \log\left(S_c^* \cdot (1 - \frac{1}{S_c^*} \int f_c(\lambda) \left\langle \sum_{n=1}^{\infty} c_n^*(\lambda)\tau_{i,n}(\lambda) \right\rangle d\lambda) \right) \tag{6.29}$$

$$= L_c^* + \log\left(1 - \frac{1}{S_c^*} \int f_c(\lambda) \left\langle \sum_{n=1}^{\infty} c_n^*(\lambda)\tau_{i,n}(\lambda) \right\rangle d\lambda \right) \tag{6.30}$$

$$\overset{\log(1-x)\overset{x\ll 1}{\approx}-x}{\approx} L_c^* - \frac{1}{S_c^*} \int f_c(\lambda) \left\langle \sum_{n=1}^{\infty} c_n^*(\lambda)\tau_{i,n}(\lambda) \right\rangle d\lambda \tag{6.31}$$

$$\overset{\text{Eq. (6.17)}^*}{=} L_c^* - \sum_v N_{i,v} \frac{1}{S_c^*} \int f_c(\lambda)\sigma_{i,v}(\lambda) \left\langle \sum_{n=1}^{\infty} c_n^*(\lambda)l_{v,n}(\lambda) \right\rangle d\lambda \tag{6.32}$$

$$= L_c^* + \sum_v N_{i,v} \frac{1}{S_c^*} \int f_c(\lambda)\sigma_{i,v}(\lambda) \frac{\partial \log(I^*(\lambda))}{\partial \beta_v} I^*(\lambda) d\lambda \tag{6.33}$$

$$= L_c^* - \sum_v N_{i,v} \frac{1}{S_c^*} \int f_c(\lambda)\sigma_{i,v}(\lambda)s_v(\lambda)I^*(\lambda) d\lambda. \tag{6.34}$$

In Eq. (6.17)* an additional index at the cross section i is added in order to account for pressure and temperature dependence. The basic principle of this derivation is also presented in [Kern et al., 2012]. The derivation for the case of weak absorption is summarized as follows:

$$L_c \approx L_c^* - \sum_v N_{i,v} V_{i,v,c} = L_c^* - \sum_v N_{i,v} \langle \sigma_{i,v} s_v \rangle_c \tag{6.35}$$

with the slant absorber volume $V_{i,v,c}$ of the atmospheric region v:

$$V_{i,v,c} = \frac{\int f_c(\lambda)I^*(\lambda)\sigma_{i,v}(\lambda)s_v(\lambda) d\lambda}{\int f_c(\lambda)I^*(\lambda) d\lambda} = \langle \sigma_{i,v} s_v \rangle_c. \tag{6.36}$$

Fig. 6.6 shows slant absorber volumes normalized with layer vertical extension times channel absorption
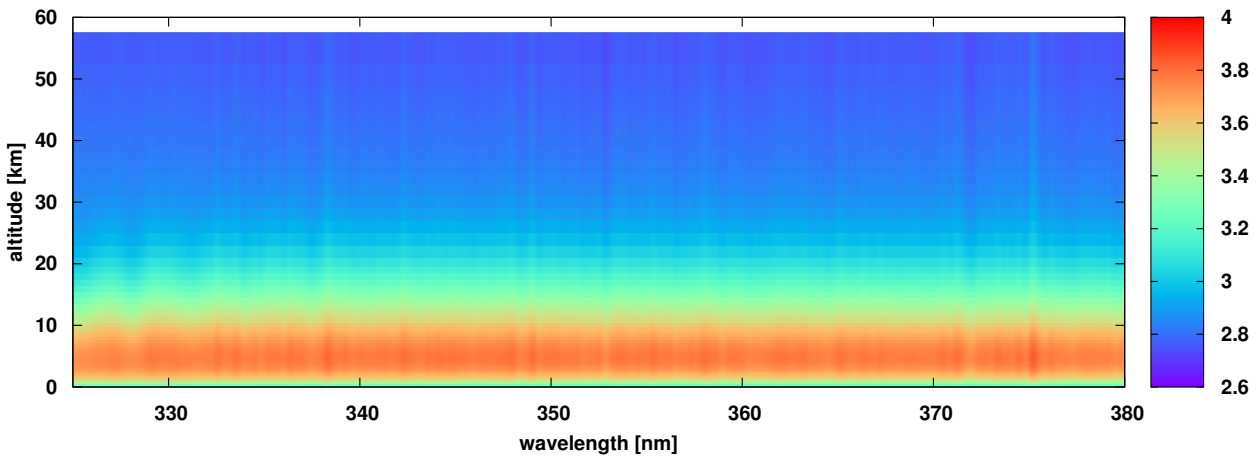
Figure 6.6.: Approximate BoxAMF spectrum serving as a proxy for $V_{i,v,c}$. High frequent artefacts stem from the missing intensity $I_*(\lambda)$ in the cross section convolution of Eq. (6.37). The oscillating structures are caused by shortening of light paths due to absorption by O_3 and NO_2.

cross section

$$b_v(\lambda) \approx \frac{\langle \sigma_{i,v} s_v \rangle_c}{h_v \int f_c(\lambda) \sigma_{i,v}(\lambda) \, d\lambda} \tag{6.37}$$

being approximately the box air mass factor $b_v(\lambda) = s_v(\lambda)/h_v$ of the respective layer (volume) and wavelength. Fitting the measured spectra with $V_{i,v,c}$ resolved for different atmospheric volumina would yield respective volume number densities, i.e. detailed profile information coming from a single spectrum, but of course only if all relevant atmospheric parameters would be known. The expression $V_{i,v,c}$ can be obtained from a linearized RTM without knowledge of the spatial concentration profile of the absorber of interest if its absorption is weak. In vector form the difference $L_c - L_c^*$ becomes:

$$\Delta \vec{L} = \vec{L} - \vec{L}^* = \log \left(\frac{S}{S^*} \right) = \mathbf{V}_i \vec{N}_i \tag{6.38}$$

with

$$\mathbf{V}_i = \begin{pmatrix} \langle \sigma_{i,1} s_1 \rangle_1 & \langle \sigma_{i,2} s_2 \rangle_1 & \cdots & \langle \sigma_{i,\#v-1} s_{\#v-1} \rangle_1 & \langle \sigma_{i,\#v} s_{\#v} \rangle_1 \\ \langle \sigma_{i,1} s_1 \rangle_2 & \cdots & \cdots & \cdots & \langle \sigma_{i,\#v} s_{\#v} \rangle_2 \\ \vdots & \cdots & \cdots & \cdots & \vdots \\ \langle \sigma_{i,1} s_1 \rangle_{\#c-1} & \cdots & \cdots & \cdots & \langle \sigma_{i,\#v} s_{\#v} \rangle_{\#c-1} \\ \langle \sigma_{i,1} s_1 \rangle_{\#c} & \langle \sigma_{i,2} s_2 \rangle_{\#c} & \cdots & \langle \sigma_{i,\#v-1} s_{\#v-1} \rangle_{\#c} & \langle \sigma_{i,\#v} s_{\#v} \rangle_{\#c} \end{pmatrix} \tag{6.39}$$

where #v is the number of volumina (or clusters) the atmosphere is discretized into and #c is the number of spectrometer channels. In order to show the order of magnitude of the spectral signatures, $\Delta \vec{L}$ for different profiles of the trace gas NO_2 are shown in Fig. 6.7. Probably the most remarkable thing is that $\Delta \vec{L}$ scales approximately with the vertical columns (VCD_A=5.59, VCD_B=4.4, VCD_C=3.14 in [$10^{15}cm^{-2}$]). When observing number density profiles with identical VCD (middle and bottom panel of Fig. 6.7), differences in the order of some 10^{-4} optical thickness appear. These differences are directly related to differences in the number densities and become visible because light paths through the volumes (layers) are different at different wavelengths.

6.3.2. Spectroscopic Measurements and Standard DOAS

The key idea of DOAS is, to numerically decompose the absorption cross section of the absorber of interest into a smoothly varying fraction $\sigma_{bb,i}$ (bb for broad band, terminology from FT signal processing, low pass filtering) and a rapidly varying unique fraction $\sigma_{nb,i}$ (nb for narrow band, please study [Platt and Stutz, 2008] for details). By non-linear least square fitting a modeled signal containing $\sigma_{i,n}$ to the measured signal, the DOAS algorithm then "filters" the signal fraction attributed to the amount of the species i. The standard DOAS equation is usually written as follows (see chapters 6 and 8 of [Platt and Stutz, 2008] and [Rozanov and Rozanov, 2010] for a discussion on equivalent forms):

$$\log \left(\frac{S_c}{S_c^r} \right) = - \sum_{i=1}^{\#species} (\sigma_{i,c}^{f,bb} + \sigma_{i,c}^{f,nb}) DSCD_i + \sum_{k=0}^{N_k} p_k \lambda_c^k \tag{6.40}$$

Here, $\sigma_{i,c}^{f,x}$ are the respective species absorption cross sections (f for fit) at channel resolution separated into respective broad band x = bb and narrow band (or differential) x = nb fractions (see Fig. 6.8). The left side is the logarithm of two measured spectra (compare to Eq. (6.6)), where r stands for reference. The standard way to obtain the absorption cross sections at instrument resolution is to convolve high resolution "literature" cross sections with the normalized instrument slit function $f_{slit,c}(\lambda)$ (where often a constant function for the whole wavelength range is taken), i.e.

$$\sigma_{i,c}^f = \int f_{slit,c}(\lambda) \sigma_i(\lambda) \, d\lambda. \tag{6.41}$$

The p_k in Eq. (6.40) are polynomial fit coefficients. Their purpose is to describe the wavelength dependence of molecular and particulate scattering but in a fit, p_k will contain all broad band features in the fit range, which can be described by a polynomial. There are some other important fit parameters, which are not shown in the DOAS equation. Some parameters are motivated by the following difficulties (the list does not claim to be complete):

- Literature cross sections sometimes exhibit a wavelength shift or squeeze.
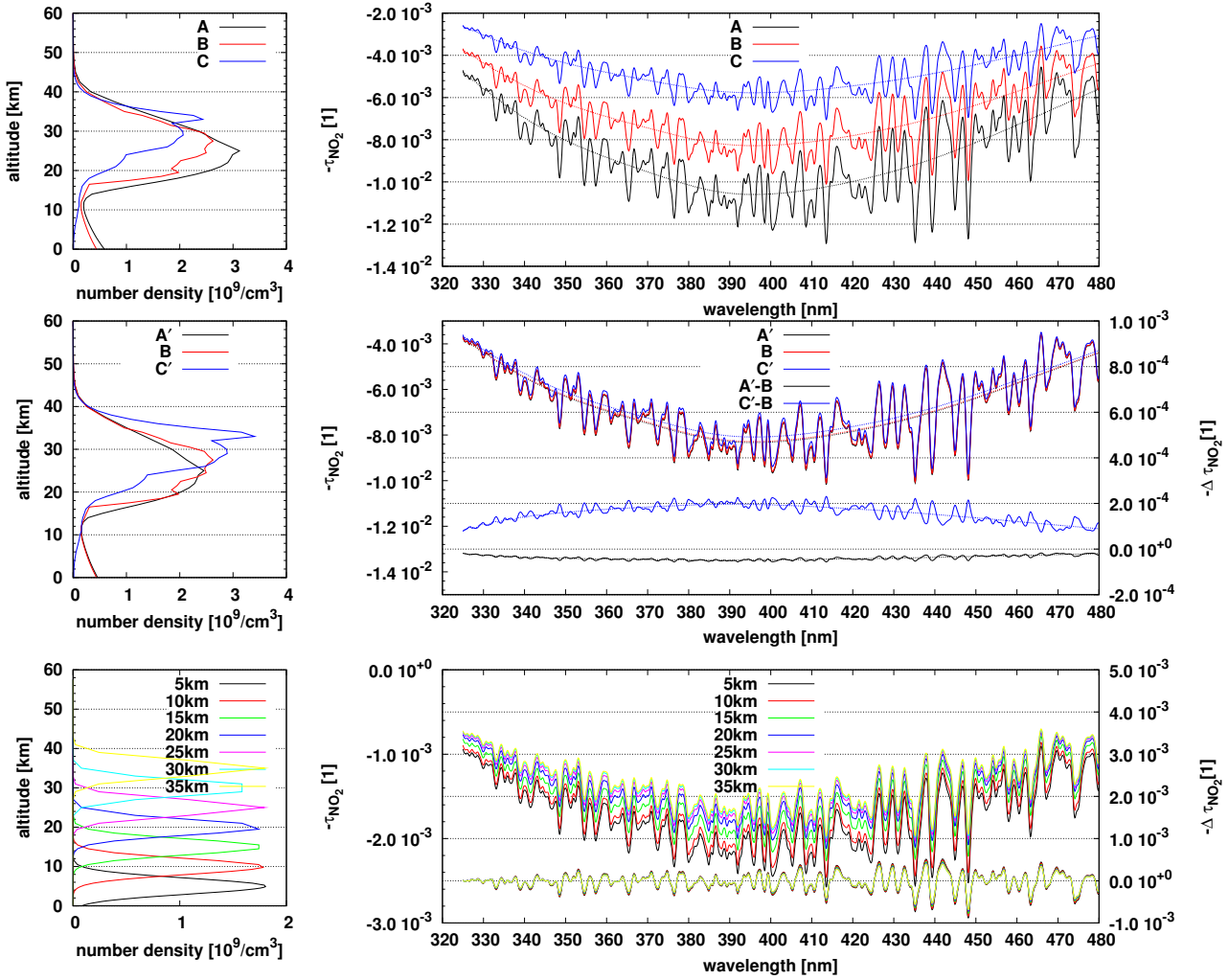
Figure 6.7.: Negative optical thickness $-\tau_{NO_2}$ spectra calculated for different vertical concentration profiles. **Top**: $\Delta\vec{L} = \mathbf{V}\vec{N}_{NO_2}^{\mathbf{A,B,C}} = -\tau_{NO_2}^{\mathbf{A,B,C}}$ on the right panel for three different number density vertical profiles (labeled as **A**, **B** and **C**) shown on the left panel with VCD_A=5.59, VCD_B=4.4 and VCD_C=3.14 in 10^{15}cm^{-2}. **Middle**: same as top panel, but number densities of A' and C' profiles are re-scaled to the VCD of B. The detector is on the ground, pointing 20° above the horizon, SZA 70° and SRAA 30°, no aerosols or clouds are present. **Bottom**: differential and absolute τ signatures for artificial NO$_2$ number density profiles each normalized to a VCD of $9 \cdot 10^{14}$cm^{-2} and with maxima as shown in the legend.

- The channel-to-wavelength association is usually done by calibration with Fraunhofer lines, or known elemental emission lines. The calibration is described by a polynomial and in the analyzed wavelength region the calibration is often not fine enough such that also general shift and squeeze (i.e. the first to coefficients of the channel-to-wavelength polynomial) parameters needs to be fitted.

- Residual structures of some percent (see next chapter 7) caused by inelastic scattering can not be assessed accurately. There are some approximate methods to generate Ring spectra suitable for improving the residual.

The fit itself is done including a range of channels minimizing the sum of the squared differences of both sides of Eq. (6.40): the left side is the logarithm of two measured spectra which are selected in way that the projected (i.e. expected) difference in absorption signatures is as large as possible for the respective measurement geometries. The key idea is the separation of differential and broad band structures:

$$\log\left(\frac{S_c}{S_c^r}\right) = -\sum_{i=1}^{\#species} \sigma_{i,c}^{f,nb}\text{DSCD}_i + \sum_{k=0}^{N_k} p_k'\lambda_c^k + R_c \tag{6.42}$$
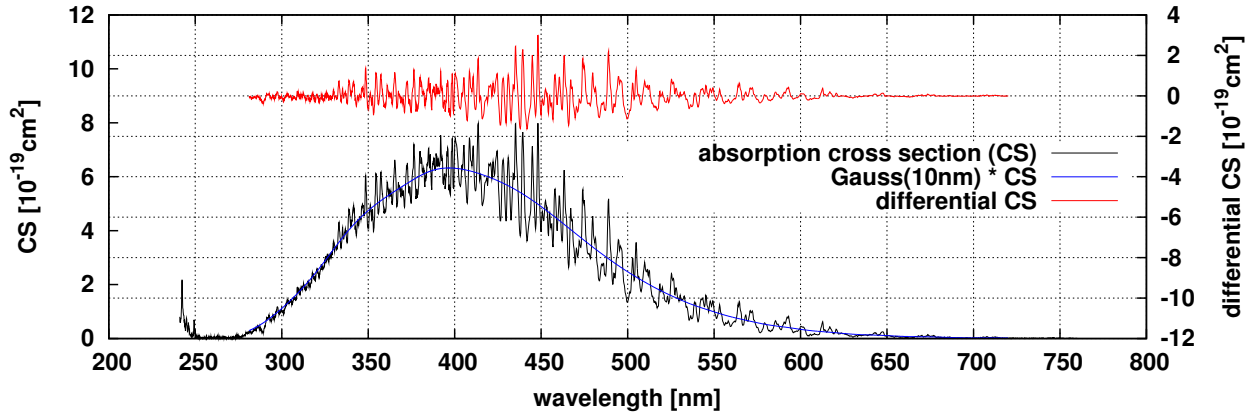
Figure 6.8.: Separation of the NO_2 absorption cross section (black) into a broad band part (blue) and a differential or narrow band part (red) using a Gauss convolution with $\sigma = 10nm$.

After the fit, residual structures R_c remain that look like noise at best. Broad band absorber structures are contained in the polynomial fit coefficients p'_k. In order to analyze DOAS, Eq. (6.38) is written down for both
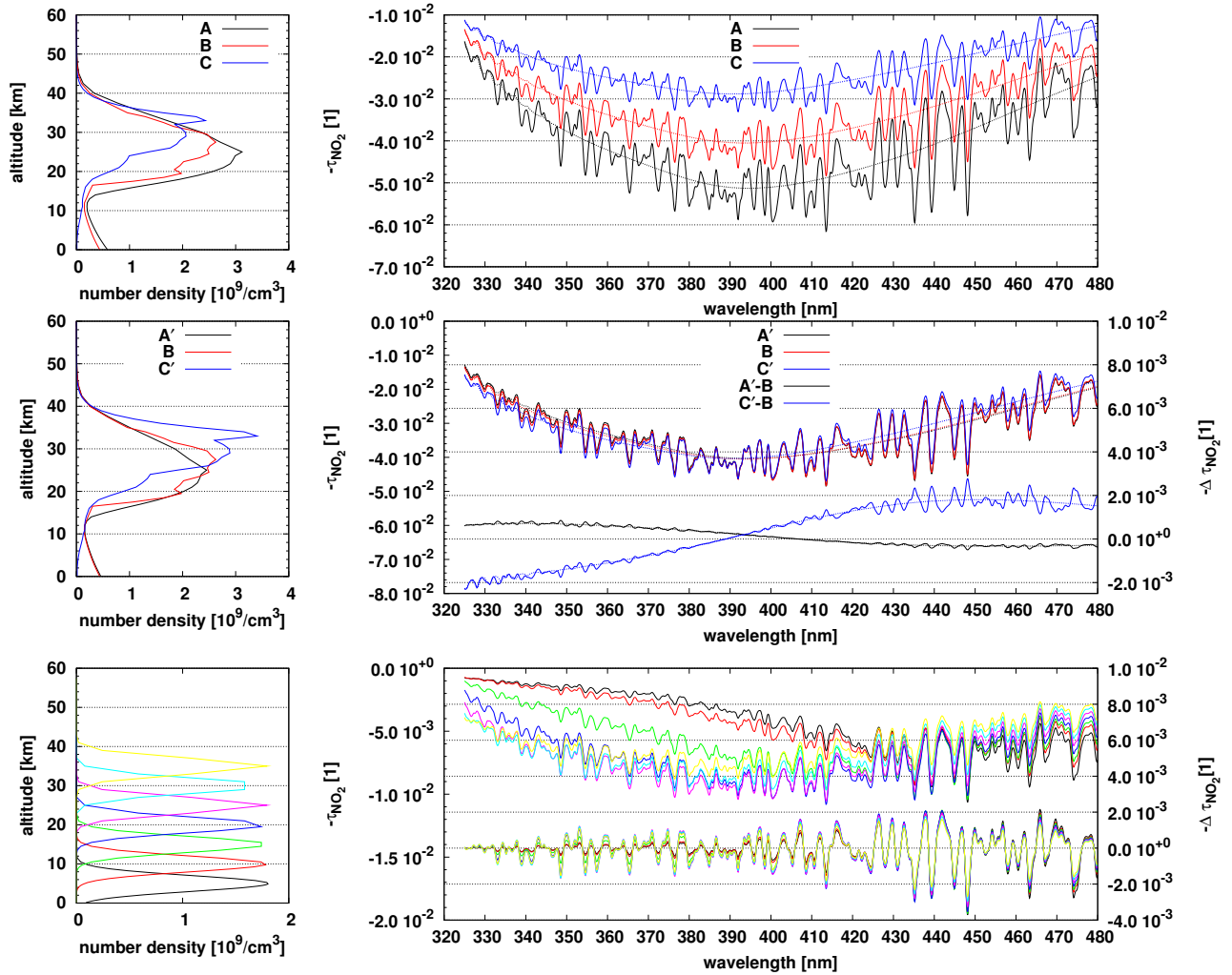
Figure 6.9.: Same as Fig. 6.7 but with altered geometry: The detector is on the ground pointing 2° over the horizon, SZA 89 ° and SRAA 10°.

spectra $\vec{S}$ and $\vec{S}_r$ respectively their (channel wise) logarithms $\vec{L} = \log\left(\vec{S}\right)$ and $\vec{L}_r = \log\left(\vec{S}_r\right)$):

$$\Delta\vec{L} - \Delta\vec{L}_r = \mathbf{V}\vec{N}_i - \mathbf{V}_r\vec{N}_{i,r} \overset{\vec{N}_i \approx \vec{N}_{i,r}}{\approx} (\mathbf{V} - \mathbf{V}_r)\vec{N}_i. \tag{6.43}$$

In the approximation on the right hand side it is assumed, that the number densities encountered by measured light in both measurement geometries are equal. This is only the case in horizontally homogeneous atmospheres. As is shown in the bottom panels of Fig. 6.7 differences in concentration profiles with equal VCD show up in a broad band structure in the signatures. These broad band number density profile information is inevitably put into the polynomial coefficients by DOAS and are not considered in the DSCDs. In order to model this, slant absorber volumina in Eq. (6.36) are also separated into a broad band and a narrow band part

$$V_{i,v,c} = \frac{1}{S_c^*} \int f_c(\lambda) I^*(\lambda) (\sigma_{i,v}^{\mathrm{bb}}(\lambda) + \sigma_{i,v}^{\mathrm{nb}}(\lambda)) s_v(\lambda)\,\mathrm{d}\lambda \tag{6.44}$$

$$= \langle \sigma_{i,v}^{\mathrm{bb}} s_v \rangle_c + \langle \sigma_{i,v}^{\mathrm{nb}} s_v \rangle_c \tag{6.45}$$

$$= V_{i,v,c}^{\mathrm{bb}} + V_{i,v,c}^{\mathrm{nb}}. \tag{6.46}$$

The resulting broad band structures are dotted lines in the top and middle panel of Fig. 6.7. Fig. 6.9 shows results for the same atmosphere of Fig. 6.7 but for a different observation geometry. In the latter figure, the detector is oriented $2°$ over the horizon and the Sun is at $89°$ SZA. In this geometry the light paths through the volumes (layers) are considerably longer (see Fig. 6.10), causing an order of magnitude more absorption signatures (compare top panels). Also for number density profiles with equal VCD (middle and bottom
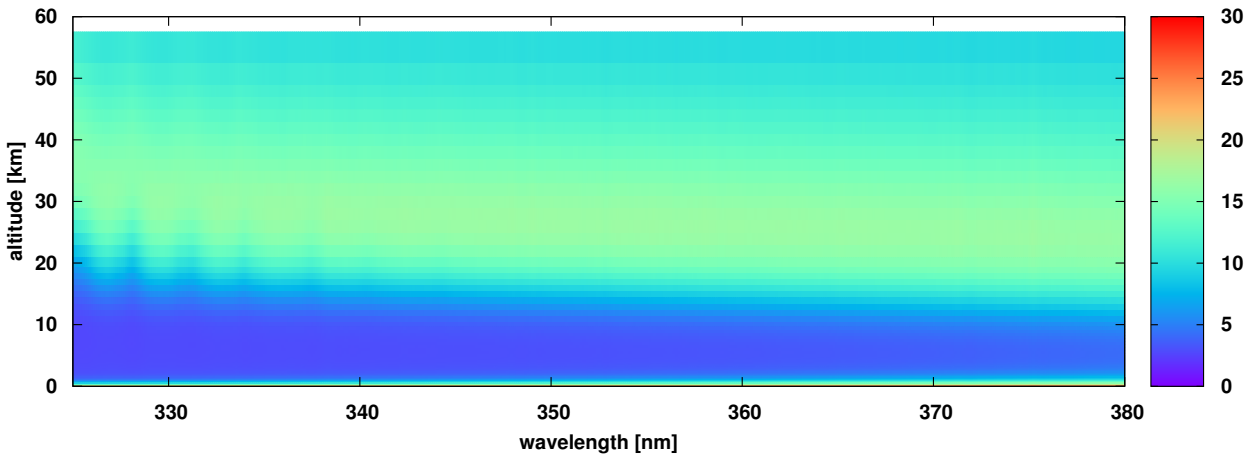
Figure 6.10.: Approximate BoxAMF spectrum serving as a proxy for $V_{r,i,v,c}$. Same atmosphere as in Fig. 6.6 but for different geometry (see text or caption of Fig. 6.9).

panels of the figures) differences in the signatures are found. Obviously, there is a weak positive correlation of the location of the profile maximum with the wavelength. At this point in the analysis it is possible to directly compare the DOAS Ansatz with results from radiative transfer modeling and derive formulas for correcting DSCDs. In order to do this, the narrow band structure in Eq. (6.42), which are identified by the DOAS fit when applied to a number of spectrometer channels of two spectra, is compared to the corresponding structure derived from radiation transport theory:

$$\sigma_{i,c}^{\mathrm{f,nb}}\mathrm{DSCD}_i = \sum_{v=1}^{\#v} N_{i,v}(V_{i,v,c}^{\mathrm{nb}} - V_{r,i,v,c}^{\mathrm{nb}}) \tag{6.47}$$

$$= \sum_{v=1}^{\#v} \frac{N_{i,v}}{S_{r,c}^* S_c^*} \int f_c(\lambda) (S_{r,c}^* I^*(\lambda) s_v(\lambda) - S_c^* I_r^*(\lambda) s_{r,v}(\lambda)) \sigma_{i,v}^{\mathrm{nb}}(\lambda)\,\mathrm{d}\lambda. \tag{6.48}$$

The χ^2-fit can be interpreted as a linear averaging procedure in the following sense: in principle Eq. (6.48) can be written for each channel of the fit window. The channels of the fit window contribute all with the

same weight to the χ^2 cost function. The partial contribution of Eq. (6.48) to the global cost function χ^2 can be written as follows:

$$\chi_i^2(\text{DSCD}_i) = \sum_{c=c_1}^{c_2-c_1+1} \left(\sigma_{i,c}^{\text{f,nb}} \text{DSCD}_i - \sum_{v=1}^{\#v} N_{i,v}(V_{i,v,c}^{\text{nb}} - V_{r,i,v,c}^{\text{nb}}) \right)^2. \tag{6.49}$$

If considered as a partially linear (sub) problem, the solution of Eq. (6.49) is readily found by deriving for DSCD_i and setting the derivative to zero:

$$\text{DSCD}_i \sum_{c=c_1}^{c_2-c_1+1} \sigma_{i,c}^{\text{f,nb}} = \sum_{c=c_1}^{c_2-c_1+1} \sum_{v=1}^{\#v} N_{i,v}(V_{i,v,c}^{\text{nb}} - V_{r,i,v,c}^{\text{nb}}). \tag{6.50}$$

The result is:

$$\text{DSCD}_i = \left\langle \sigma_i^{\text{f,nb}} \right\rangle^{-1} \cdot \left\langle \sum_{v=1}^{\#v} N_{i,v}(V_{i,v}^{\text{nb}} - V_{r,i,v}^{\text{nb}}) \right\rangle \tag{6.51}$$

where the averaging takes place in the fit window. Therefore, in order to precisely model DOAS fit results, the way of correct averaging is in principle prescribed by Eq. (6.51).

6.3.2.1. Strong Absorption

The derivation of the Eq. (6.35) can also be done using the Taylor expansion of the intensity $I(\lambda, \vec{N}_i)$ around the intensity $I^*(\lambda)$ without the absorber of interest:

$$I^*(\lambda) = I(\lambda, \vec{N}_i = \vec{0}), \tag{6.52}$$

where $\vec{N}_i = (N_{i,1}, \ldots, N_{i,\#v})^T$ is the volume number density profile. Therewith, the Taylor expansion is:

$$I(\lambda, \vec{N}_i) = I^*(\lambda) + \vec{\nabla}_N I(\lambda, \vec{N}_i = \vec{0})\vec{N}_i + \frac{1}{2}\vec{N}_i^T \vec{\nabla}_N^T \vec{\nabla}_N I(\lambda, \vec{N}_i = \vec{0})\vec{N}_i + \cdots \tag{6.53}$$

where $\vec{\nabla}_N^T \vec{\nabla}_N I(\lambda, \vec{N})$ is the Hessian of $I(\lambda)$ with respect to the volume number density. It is related to the absorption coefficient Hessian as follows:
$\vec{\nabla}_N^T \vec{\nabla}_N I(\lambda, \vec{N}) =$

$$\begin{pmatrix} \sigma_1 \frac{\partial^2 I(\vec{\beta})}{\partial\beta_1\partial\beta_1}\sigma_1 & \sigma_1 \frac{\partial^2 I(\vec{\beta})}{\partial\beta_1\partial\beta_2}\sigma_2 & \cdots & \sigma_1 \frac{\partial^2 I(\vec{\beta})}{\partial\beta_1\partial\beta_{\#v-1}}\sigma_{\#v-1} & \sigma_1 \frac{\partial^2 I(\vec{\beta})}{\partial\beta_1\partial\beta_{\#v}}\sigma_{\#v} \\ \sigma_2 \frac{\partial^2 I(\vec{\beta})}{\partial\beta_2\partial\beta_1}\sigma_1 & \cdots & \cdots & \cdots & \sigma_2 \frac{\partial^2 I(\vec{\beta})}{\partial\beta_2\partial\beta_{\#v}}\sigma_{\#v} \\ \vdots & \cdots & \cdots & \cdots & \vdots \\ \sigma_{\#v-1} \frac{\partial^2 I(\vec{\beta})}{\partial\beta_{\#v-1}\partial\beta_1}\sigma_1 & \cdots & \cdots & \cdots & \sigma_{\#v-1} \frac{\partial^2 I(\vec{\beta})}{\partial\beta_{\#v-1}\partial\beta_{\#v}}\sigma_{\#v} \\ \sigma_{\#v} \frac{\partial^2 I(\vec{\beta})}{\partial\beta_{\#v}\partial\beta_1}\sigma_1 & \sigma_{\#v} \frac{\partial^2 I(\vec{\beta})}{\partial\beta_{\#v}\partial\beta_2}\sigma_2 & \cdots & \sigma_{\#v} \frac{\partial^2 I(\vec{\beta})}{\partial\beta_{\#v}\partial\beta_{\#v-1}}\sigma_{\#v-1} & \sigma_{\#v} \frac{\partial^2 I(\vec{\beta})}{\partial\beta_{\#v}\partial\beta_{\#v}}\sigma_{\#v} \end{pmatrix}, \tag{6.54}$$

see chapter 5.2.1.3 for details on calculating $\frac{\partial^2 I(\vec{\beta})}{\partial\beta_k\partial\beta_l}$. For simplicity the index i is omitted in the following. Inserting the expansion into Eq. (6.6) yields

$$\begin{aligned} S_c &= \overbrace{\int f_c(\lambda)\sigma_v(\lambda)I(\lambda, \vec{N} = \vec{0})\,d\lambda}^{S_c^*} + \cdots \\ &+ \sum_{v=1}^{\#v} N_v \int f_c(\lambda)\sigma_v(\lambda)\frac{\partial I^*(\lambda)}{\partial\beta_v}\,d\lambda \cdots \\ &+ \sum_{v_1=1}^{\#v} \sum_{v_2=1}^{\#v} N_{v_1}N_{v_2} \int f_c(\lambda)\sigma_{v_1}(\lambda)\sigma_{v_2}(\lambda)\frac{\partial^2 I^*(\lambda)}{\partial\beta_{v_1}\partial\beta_{v_2}}\,d\lambda \cdots \\ &+ \cdots, \end{aligned} \tag{6.55}$$

Modeled and measured intensity fits based on this expansion would need knowledge on the absolute calibration of the instrument. Taking logarithms of ratios of signals for two measurements as a basis to some extent avoids this problem. The Taylor series expansion of the logarithm of the channel signal with respect to the absorption coefficient is:

$$
L_c = L_c^* + \frac{1}{S_c^*} \vec{\nabla}_N S_c^* \vec{N} + \frac{1}{2} \vec{N}^T \left(\frac{S_c^* \vec{\nabla}_N^T \vec{\nabla}_N S_c^*}{S_c^{*2}} - \frac{(\vec{\nabla}_N^T S_c^*)(\vec{\nabla}_N S_c^*)}{S_c^{*2}} \right) \vec{N} + \cdots \tag{6.56}
$$

$$
\begin{aligned}
= \; & L_c^* + \cdots \\
& + \frac{1}{S_c^*} \sum_{v=1}^{\#v} N_v \int f_c(\lambda)\sigma_v(\lambda) \frac{\partial I^*}{\partial \beta_v} \, \mathrm{d}\lambda + \cdots \\
& + \frac{1}{S_c^{*2}} \sum_{v_1=1}^{\#v} \sum_{v_2=1}^{\#v} N_{v_1} N_{v_2} \left\{ S_c^* \int f_c(\lambda)\sigma_{v_1}(\lambda)\sigma_{v_2}(\lambda) \frac{\partial^2 I^*(\lambda)}{\partial \beta_{v_1} \partial \beta_{v_2}} \, \mathrm{d}\lambda \cdots \right. \\
& \left. - \sum_{v_1=1}^{\#v} \sum_{v_2=1}^{\#v} \left(\int f_c(\lambda)\sigma_{v_1}(\lambda) \frac{\partial I^*}{\partial \beta_{v_1}} \, \mathrm{d}\lambda \right) \left(\int f_c(\lambda)\sigma_{v_2}(\lambda) \frac{\partial I^*}{\partial \beta_{v_2}} \, \mathrm{d}\lambda \right) \right\}
\end{aligned} \tag{6.57}
$$

In [Puķīte et al., 2009] also a Taylor series approach is presented, but the derivatives are calculated with respect to wavelength and absorption coefficient improving therewith the DOAS fit residual. Using second order derivatives, the two approaches outlined in this work may serve as alternatives.

6.4. DOAS Analysis Summary

The findings of the previous sections are summarized as follows. DOAS is a mathematical technique which is able to retrieve light path integrated spatial number density information of weak absorbers using ratios of uncalibrated (in absolute intensities) scattered Sun light spectra without radiation transport modeling. The key method is, to separate broad band and unique narrow band (differential) absorption features from each other and to fit them together with a polynomial describing the influence of molecular and particulate scattering and the broad band absorber structures to the spectra ratio.

6.4.1. DSCD Retrieval

The detailed analysis of the spectral signatures of weak absorbers using the Neumann series from Monte Carlo RTM combined with the importance sampling technique reveals that the DOAS Ansatz Eq. (6.42) is well justified provided that sufficient knowledge on the instrument operation (especially knowledge of the slit function) is given. It seems however, that current approaches to calculate cross sections at instrument resolution could be improved, but this would require a more sophisticated model or even RTM. Although information on the shape of the number density profile of a weak absorber is in principle contained in the spectra, the information is put to the polynomial coefficients and is therewith indistinguishable from other broad band structures. The experimental reality (especially degradation or temperature or vibration induced change of the slit function) however allows only for retrieving light path integrated number densities, so called DSCDs. In view of the small differences in the differential structures shown in the bottom panels of Fig.s 6.7 and 6.9 it is advisable to have sufficient knowledge of the instrument in order to conserve valuable information in the spectra. Eq. (6.51) is suitable to analyze the stability of DSCDs and their dependence on choice of the fit window [Vogel et al., 2012].

6.4.2. Inversion

By varying the observation geometry, it is possible to significantly change the light path [Hönninger et al., 2004]. Through comparison with radiation transport theory as summarized in Eq. (6.51) it becomes obvious that the interpretation of DSCDs in the framework of inversion schemes is delicate, since only the time consuming wavelength integration could yield correct (or at least effective) volume (or layer) sensitivity functions and this step would also require knowledge on other atmospheric parameters. However, recent publications [Zieger et al., 2011] show that DOAS can compete with other methods and with the further development of forward models also strong absorption cases can be expected to be addressable by DOAS

fitting algorithms. On the other side, also the knowledge on the instrument operation (slit function and absolute calibration) has to be improved.

<div align="right">

7

</div>

The Ring Effect

In the previous Chapters 5.1.1 and 5.1.3 only elastic scattering processes are considered. In chapter 3.2.2.4 the (inelastic) rotational Raman scattering (RRS) process is introduced. In this chapter a procedure is described, with which RRS can be simulated. In literature (e.g. [Landgraf et al., 2004]), the effect of RRS is described as a perturbation of elastic radiation transport intensities [Shefov, 1959, Grainger and Ring, 1962]. The deviations are quantified by a so called Ring signal or also filling-in (FI) defined as

$$S_{\text{RRS}}(\lambda) = \frac{I(\lambda) - I_{\text{el}}(\lambda)}{I_{\text{el}}(\lambda)} \tag{7.1}$$

where $I_{\text{el}}(\lambda)$ is the intensity that is obtained when treating Rayleigh scattering as an elastic scattering processes and $I(\lambda)$ accounts for the wavelength shift in RRS events. In the following, it is described how to *simultaneously* obtain estimates of $I(\lambda)$ and $I_{\text{el}}(\lambda)$ from the same path ensemble in an efficient way. The goal is to obtain $S_{\text{RRS}}(\lambda)$ from a single model run.

7.1. RRS-Modified RTE

The elastic, monochromatic and scalar radiative transfer equation at the wavelength λ and location $\vec{r}$ is:

$$\vec{\omega}\vec{\nabla}R(\vec{r},\vec{\omega},\lambda) = -\varepsilon_{\text{el}}(\vec{r},\lambda)R(\vec{r},\vec{\omega},\lambda) + \frac{\varepsilon_{\text{S,el}}(\vec{r},\lambda)}{4\pi}\int_{4\pi} P_{\text{el}}(\vec{r},\mu,\lambda)R(\vec{r},\vec{\omega}',\lambda)\,\mathrm{d}\vec{\omega}', \tag{7.2}$$

where $\mu = \vec{\omega}' \cdot \vec{\omega}$ and ε_{el} is the coefficient for elastic extinction and $\varepsilon_{\text{S,el}}$ is the elastic scattering coefficient. In order to account for inelastic scattering the right hand side of the equation is modified as follows. The deduction of the vector form is analogous to the deduction in the scalar case. For sake of readability, the location dependence $\vec{r}$ is dropped in the notation but it is kept in mind that all optical properties and the radiance are quantities depending on the position $\vec{r}$.

7.1.1. RRS Cross Sections for Scattering out and into a Wavelength

On the right hand side of the "elastic" RTE Eq. (7.2) the first term (the loss term) contains the total extinction coefficient. A part of that coefficient is the total cross section of light scattered out of the center wavelength. In the second term on the right side (the source term) the scattering coefficient and the phase functions appear. The overall source term must also contain contributions of light of other wavelengths rotational Raman scattered into the considered wavelength. A mathematical object is needed which serves the description of both cases. From the introducing Chapter 3.2.2.4 the following expression is derived by combining Eq. (3.114) with the selection rule for wavelengths Eq. (3.111):

$$\Sigma_{\text{X,RRS}}(\lambda_i \to \lambda_f) = \frac{256\pi^5}{27\lambda_f^4}\gamma_X^2(\lambda_i)b_J^{\pm}w_X(J,T)\delta\left(\lambda_f - \frac{hc\lambda_i}{hc - \lambda_i\Delta E_{\text{X,rot}}^{\pm}(J)}\right). \tag{7.3}$$

where X is the species index , i.e. $X=N_2$, O_2, $w_X(J,T)$ is the thermodynamic probability of encountering a molecule of a gas of temperature T in rotational state J, γ_X is the molecular anisotropy of the polarizability and $\Delta E_{\text{X,rot}}^{\pm}(J)$ is the respective rotational energy difference for Stokes $(+)$ and Anti-Stokes $(-)$ RRS. The delta function assures selection of wavelengths according to the selection rule for RRS. In order to investigate Eq.
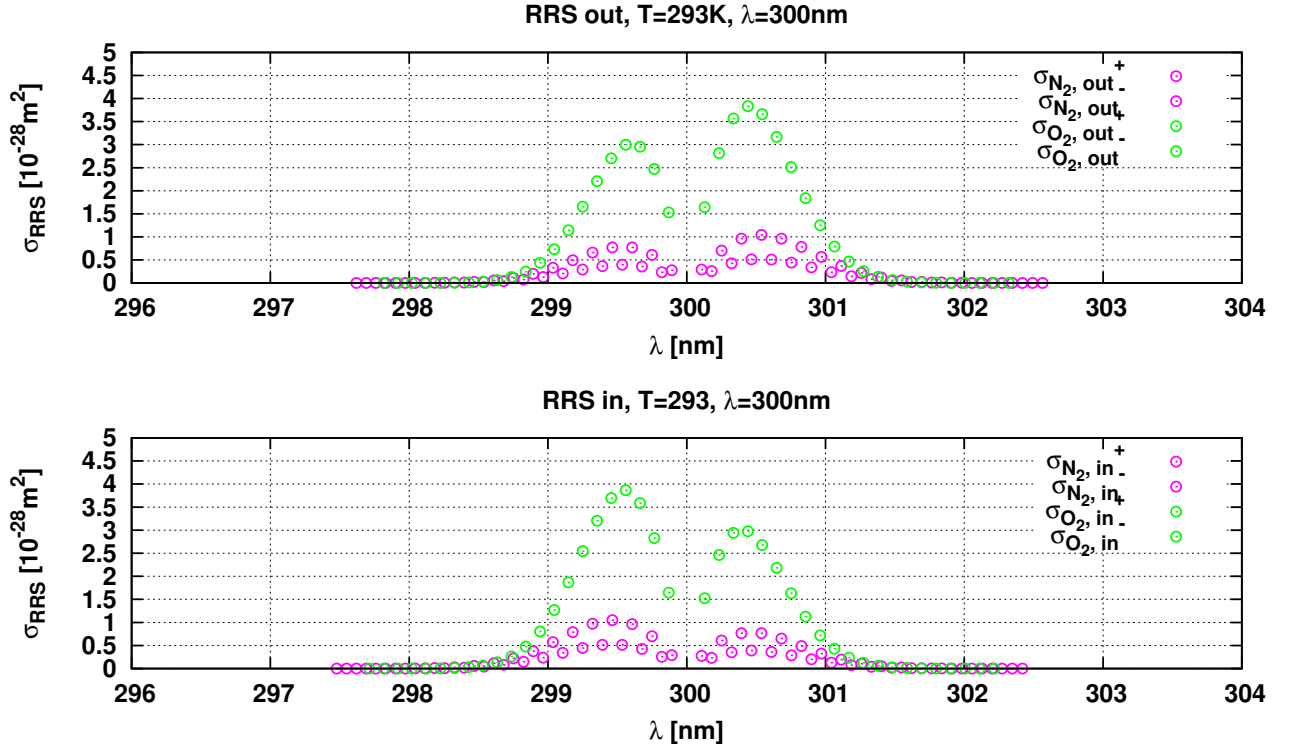
Figure 7.1.: Individual RRS cross sections of Eq. (7.5) for N_2 and O_2 on top, and of Eq. (7.6) in the bottom panel. The central wavelength is 300nm and the temperature 20°C.

(7.3) further, the argument of the delta function in Eq. (7.3), i.e. the selection rule Eq. (3.110), is solved for λ_f and λ_i:

$$\lambda_f - \frac{hc\lambda_i}{hc - \lambda_i \Delta E_{\text{rot}}^{\pm}(J)} = 0 = \lambda_i + \frac{hc\lambda_f}{hc + \lambda_f \Delta E_{\text{rot}}^{\pm}(J)}. \tag{7.4}$$

This leads to the definition of the following four wavelengths:

$$\lambda_{X,\text{out}}^{+}(\lambda, J) = \frac{hc\lambda}{hc - \lambda \Delta E_{\text{rot}}^{+}(J)} \quad \text{final wavelength after Stokes RRS with initial wavelength } \lambda$$

$$\lambda_{X,\text{out}}^{-}(\lambda, J) = \frac{hc\lambda_i}{hc - \lambda \Delta E_{\text{rot}}^{-}(J)} \quad \text{final wavelength after Anti-Stokes RRS with initial wavelength } \lambda$$

$$\lambda_{X,\text{in}}^{+}(\lambda, J) = \frac{hc\lambda}{hc + \lambda \Delta E_{\text{rot}}^{+}(J)} \quad \text{initial wavelength before Stokes RRS with final wavelength } \lambda$$

$$\lambda_{X,\text{in}}^{-}(\lambda, J) = \frac{hc\lambda_i}{hc + \lambda \Delta E_{\text{rot}}^{-}(J)} \quad \text{initial wavelength before Anti-Stokes RRS with final wavelength } \lambda$$

To assure energy conservation, the delta function "selects" wavelengths fitting according to the selection rule of RRS. In the following RTE modification two cross sections are of importance:

$$\sigma_{X,\text{out}}(\lambda) := \int \Sigma_{X,\text{RRS}}(\lambda \to \lambda')\, d\lambda' = \frac{256\pi^5}{27} \gamma_X^2(\lambda) \sum_{J=0}^{\infty} w_X(J, T) \left\{ \frac{b_J^+}{\lambda_{X,\text{out}}^{+4}(\lambda, J)} + \frac{b_J^-}{\lambda_{X,\text{out}}^{-4}(\lambda, J)} \right\} \tag{7.5}$$

$$\sigma_{X,\text{in}}(\lambda) := \int \Sigma_{X,\text{RRS}}(\lambda' \to \lambda)\, d\lambda' = \frac{256\pi^5}{27\lambda^4} \sum_{J=0}^{\infty} w_X(J, T) \left\{ b_J^+ \gamma_X^2(\lambda_{X,\text{in}}^{+}(\lambda, J)) + b_J^- \gamma_X^2(\lambda_{X,\text{in}}^{-}(\lambda, J)) \right\}. \tag{7.6}$$

Eq. (7.5) is the cross section of light being rotational Raman scattered away from a considered wavelength λ and Eq. (7.6) can be interpreted similarly as the cross section of light rotational Raman scattered to a considered wavelength λ. The individual constituents of both equations are shown in Fig. 7.1. A consequence of the inverse symmetry of the cross sections $\sigma_{X,\text{in}}(\lambda)$ and $\sigma_{X,\text{out}}(\lambda)$ with respect to the center wavelength is that RR scattered light is distributed more likely to higher wavelengths, i.e. to wavelengths with less energy and is also arriving the center wavelength through RRS from smaller wavelengths. The net effect of RRS on the molecules is thus an effective heating, i.e. in total energy is transferred from the radiation field into the

thermal reservoir of the gaseous matter.

7.1.1.1. Effective RRS Coefficients of Air

Effective RRS scattering coefficients of air are obtained by a number-density-weighted summation over species:

$$\varepsilon_{\text{RRS}}(\lambda_i \to \lambda_f) = \sum_{X=N_2,O_2} N_X \Sigma_{X,\text{RRS}}(\lambda_i \to \lambda_f), \tag{7.7}$$

where N_X are the respective number densities. It needs to be emphasized that the unit of $\varepsilon_{\text{RRS}}(\lambda_i, \lambda_f)$ is one over length over wavelength, i.e. $1/(\text{km} \cdot \text{nm})$, in contrast to the unit of ordinary extinction coefficients of $1/\text{km}$. The last quantities necessary to be defined for the modification of the RTE are the RRS coefficients for in- and out-scattering:

$$\varepsilon_{\text{RRS, out}}(\lambda) := \sum_{X=N_2,O_2} N_X \int \Sigma_{X,\text{RRS}}(\lambda \to \lambda')\, d\lambda' \quad = \quad \sum_{X=N_2,O_2} N_X \sigma_{X,\text{out}}(\lambda) \tag{7.8}$$

$$\varepsilon_{\text{RRS, in}}(\lambda) := \sum_{X=N_2,O_2} N_X \int \Sigma_{X,\text{RRS}}(\lambda' \to \lambda)\, d\lambda' \quad = \quad \sum_{X=N_2,O_2} N_X \sigma_{X,\text{in}}(\lambda) \tag{7.9}$$

which have ordinary extinction coefficient units $1/\text{km}$.

7.1.2. Modification of the RTE Loss and Source Terms

The modified extinction coefficient in the loss term of the RTE is

$$\varepsilon(\lambda) = \varepsilon_{\text{el}}(\lambda) + \varepsilon_{\text{RRS,out}}(\lambda). \tag{7.10}$$

The second modification is to add an additional source term considering RRS

$$\frac{1}{4\pi} \int \int_{4\pi} \varepsilon_{\text{RRS}}(\lambda' \to \lambda) P_{\text{RRS}}(\mu) R(\vec{\omega}', \lambda')\, d\vec{\omega}'\, d\lambda' \tag{7.11}$$

to the right side of the RTE. The elastic source function is rewritten using a delta function:

$$\frac{1}{4\pi} \int \int_{4\pi} \varepsilon_{S,\text{el}}(\lambda') P_{\text{el}}(\mu, \lambda') R(\vec{\omega}', \lambda') \delta(\lambda' - \lambda)\, d\vec{\omega}'\, d\lambda'. \tag{7.12}$$

Both source functions are combined to obtain the following inelastic RTE:

$$\vec{\omega} \vec{\nabla} R(\vec{\omega}, \lambda) = -\varepsilon(\lambda) R(\vec{\omega}, \lambda) + \frac{\varepsilon_S(\lambda)}{4\pi} \int \int_{4\pi} P(\mu, \lambda' \to \lambda) R(\vec{\omega}', \lambda')\, d\vec{\omega}'\, d\lambda'. \tag{7.13}$$

where

$$P(\mu, \lambda' \to \lambda) = \frac{\varepsilon_{S,\text{el}}(\lambda') P_{\text{el}}(\mu, \lambda') \delta(\lambda' - \lambda) + \varepsilon_{\text{RRS}}(\lambda' \to \lambda) P_{\text{RRS}}(\mu)}{\varepsilon_S(\lambda)} \tag{7.14}$$

and

$$\varepsilon_S(\lambda) = \varepsilon_{S,\text{el}}(\lambda) + \varepsilon_{\text{RRS,out}}(\lambda). \tag{7.15}$$

Written in this form the algebraic structure is identical to the elastic RTE such that the deduction of the inelastic IRTE (i.e. the basis of the Monte Carlo method) can be conducted analogously.

7.2. Intensity Estimates Considering Rotational Raman Scattering

According to the modified RTE with RRS, the backward Monte Carlo method has to be modified in order to account for inelastic scattering. The implications of the RTE modifications concern the path sampling which is described in section 7.2.1 and the local estimates modification in section 7.2.3.

7.2.1. RRS in the Path Sampling Procedure

The resulting procedure differs in two points: the extinction coefficient is modified according to Eq. (7.10), therefore free path length and single scattering albedo sampling has to account for an additional scatterer.

The second difference is the modified phase function in Eq. (7.14) which is accounted for by carrying the wavelength integration in the source function of Eq. (7.13):

$$\int P(\mu, \lambda' \to \lambda) R(\vec{\omega}', \lambda') \, d\lambda'$$

$$= \int \frac{\varepsilon_{S,el}(\lambda') P_{el}(\mu, \lambda') \delta(\lambda' - \lambda) + \varepsilon_{RRS}(\lambda' \to \lambda) P_{RRS}(\mu)}{\varepsilon_S(\lambda)} \cdot R(\vec{\omega}', \lambda') \, d\lambda' \tag{7.16}$$

$$= \frac{\varepsilon_{S,el}(\lambda)}{\varepsilon_S(\lambda)} P_{el}(\mu, \lambda) R(\vec{\omega}', \lambda) + \frac{\varepsilon_{RRS,out}(\lambda)}{\varepsilon_S(\lambda)} \frac{\int \varepsilon_{RRS}(\lambda' \to \lambda) P_{RRS}(\mu) R(\vec{\omega}', \lambda') \, d\lambda'}{\varepsilon_{RRS,out}(\lambda)} \tag{7.17}$$

$$= (1 - p_{RRS}(\lambda)) P_{el}(\mu, \lambda) R(\vec{\omega}', \lambda) + p_{RRS}(\lambda) \frac{\varepsilon_{RRS,in}(\lambda)}{\varepsilon_{RRS,out}(\lambda)} P_{RRS}(\mu) \frac{\int \varepsilon_{RRS}(\lambda' \to \lambda) R(\vec{\omega}', \lambda') \, d\lambda'}{\int \varepsilon_{RRS}(\lambda' \to \lambda) \, d\lambda'}, \tag{7.18}$$

where

$$p_{RRS}(\lambda) = \frac{\varepsilon_{RRS,out}(\lambda)}{\varepsilon_S(\lambda)}. \tag{7.19}$$

Using the Monte Carlo integration technique, the phase function (i.e. the density of scatter angles in the MC path tracing framework) can be estimated (i.e. sampled) as follows:

1. Calculate $p_{RRS}(\lambda)$ at the current wavelength λ and location.

2. With a probability of $1 - p_{RRS}(\lambda)$ sample the new direction from $P_e(\lambda, \mu)$ and leave the wavelength unchanged.

3. With probability $p_{RRS}(\lambda)$ sample the new direction from $P_{RRS}(\mu)$, and the new wavelength λ' from the density

$$p_{\Delta\lambda_{RRS}}(\lambda') = \frac{\varepsilon_{RRS}(\lambda' \to \lambda)}{\int \varepsilon_{RRS}(\lambda' \to \lambda) \, d\lambda'} \tag{7.20}$$

and consider in all subsequent estimates the weight $\frac{\varepsilon_{RRS,in}(\lambda)}{\varepsilon_{RRS,out}(\lambda)}$ from the normalization.

In practice, the density $p_{\Delta\lambda_{RRS}}$ (similarly as the densities shown in Fig. (3.11) in Chapter 3.2.2.4) has a discrete and finite form. More precisely, the set of possible wavelength transitions is countable and allows the definition of a cut-off criterion which is the maximum number of rotational quantum number considered. Therefore, sampling from it is straight forward:

$$\frac{\int \varepsilon_{RRS}(\lambda' \to \lambda) R(\vec{\omega}', \lambda') \, d\lambda'}{\int \varepsilon_{RRS}(\lambda' \to \lambda) \, d\lambda'} = \sum_{X=N_2, O_2} \sum_{J=0}^{\infty} \left(p_{RRS,in,X,J}^+(\lambda) R(\vec{\omega}', \lambda_{X,in}^+(\lambda, J)) + p_{RRS,in,X,J}^-(\lambda) R(\vec{\omega}', \lambda_{X,in}^-(\lambda, J)) \right) \tag{7.21}$$

where

$$p_{RRS,in,X,J}^{\pm}(\lambda) = N_X w_X(J, T) \frac{256\pi^5}{\varepsilon_{RRS,in}(\lambda) 27\lambda^4} b_J^{\pm} \gamma_X^2(\lambda_{X,in}^{\pm}(\lambda, J)). \tag{7.22}$$

7.2.2. Adjoint RRS Correction Weights

The estimation of intensities (and functionals in general) can be thought separated into two stages: The path generation stage as described in the previous Section 7.2.1 and functional estimation using the generated path ensemble, see Fig. 7.3. When considering the forward (i.e. natural) time direction, i.e. when physically interpreting the sampled paths in the functional estimation stage one has to account for additional importance sampling weights correcting for the reversal of trajectories. As described in Chapter 4.2.6 the single order transition density $k(\vec{x}_n \to \vec{x}_{n+1}) =: k_{n \to n+1}$ simulation consist of three parts: simulation of the free path length (FPL), simulation of the single scattering albedo (SSA, i.e. simulation of the survival in an extinction event) and simulation of the phase function (PF) i.e. the scalar RT scatter angle density), see Fig. 4.6. The path generation algorithm described before in this chapter correctly (i.e. even when considering RRS) simulates the FPL at a certain wavelength and SSA and PF in case of elastic scattering. In case of sampling an RRS event, an error occurs when performing local estimation which needs to be corrected for (see Fig. 7.2). As presented, the path generation actually simulates RT in the way the RTE suggests it and the trajectories originate at the detector position. During the local estimation the propagation direction is reversed and the path ensemble must be re-weighted in accounting for the reversal of the path elements. The problem is entirely analog to the usage of a backward trajectory ensemble in order to simulate polarization effects
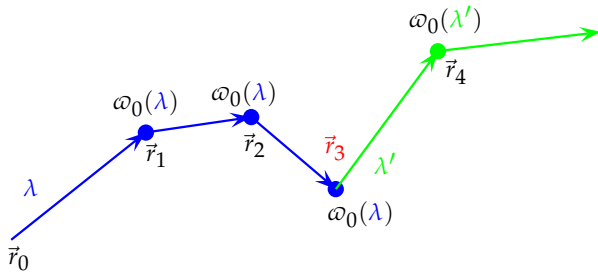
path generation: **local estimation:**
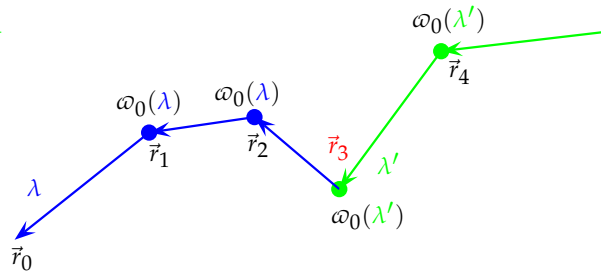
Figure 7.2.: Correction of the single scattering albedo in the local estimation. In the path generation (**left**) phase the model photon starts at $\vec{r}_0$ with wavelength λ. The ray tracer samples scatter events using the respective single scattering albedos ω_0. At the scatter event no. 3 at $\vec{r}_3$ (red), a RRS event occurs and the wavelength of the model photon changes to λ'. For sampling of the scatter event ω_0 at $\vec{r}_3$ is calculated at wavelength λ. In the local estimation phase (**right**), the orientation of the trajectory elements is reversed and at $\vec{r}_3$, the single scattering albedo must be calculated for the wavelength λ'. Compare this figure to Fig. 5.2.

(Chapter 5.1.3.1). Similarly as in Eq. (5.32) the necessary importance sampling weights are given as the ratio of the desired transition density (i.e. $k_{n\to n-1} \cdot k_{n-1\to n-2} \cdot \cdots \cdot k_{1\to 0}$) with the path generation transition density $k_{0\to 1} \cdot k_{1\to 2} \cdot \cdots \cdot k_{n-1\to n}$. Since the problem occurs only in case of RRS, the calculation of the corresponding importance weights reduces to calculating the ratio of probabilities for the change of wavelength for both propagation directions.

Given a backward trajectory and the density of the occurrence of a RRS event at a coordinate $\vec{r}$ during path generation which leads to a wavelength change from $\lambda \to \lambda'$ is:

$$k_{\lambda\to\lambda'} = \varepsilon(\lambda) \cdot \omega_0(\lambda) \cdot p_{\text{RRS}}(\lambda) \cdot \frac{\varepsilon_{\text{RRS}}(\lambda' \to \lambda)}{\varepsilon_{\text{RRS,in}}(\lambda)} \tag{7.23}$$

$$= \varepsilon(\lambda) \cdot \frac{\varepsilon_S(\lambda)}{\varepsilon(\lambda)} \cdot \frac{\varepsilon_{\text{RRS,out}}(\lambda)}{\varepsilon_S(\lambda)} \cdot \frac{\varepsilon_{\text{RRS}}(\lambda' \to \lambda)}{\varepsilon_{\text{RRS,in}}(\lambda)} \tag{7.24}$$

$$= \frac{\varepsilon_{\text{RRS,out}}(\lambda)}{\varepsilon_{\text{RRS,in}}(\lambda)} \cdot \varepsilon_{\text{RRS}}(\lambda' \to \lambda) \tag{7.25}$$

For local estimation instead one needs the "physical transition density" $\varepsilon_{\lambda'\to\lambda}$:

$$k_{\lambda'\to\lambda} = \varepsilon(\lambda') \cdot \omega_0(\lambda') \cdot p_{\text{RRS}}(\lambda') \cdot \frac{\varepsilon_{\text{RRS}}(\lambda' \to \lambda)}{\varepsilon_{\text{RRS,out}}(\lambda')} \tag{7.26}$$

$$= \varepsilon(\lambda') \cdot \frac{\varepsilon_S(\lambda')}{\varepsilon(\lambda')} \cdot \frac{\varepsilon_{\text{RRS,out}}(\lambda')}{\varepsilon_S(\lambda')} \cdot \frac{\varepsilon_{\text{RRS}}(\lambda' \to \lambda)}{\varepsilon_{\text{RRS,out}}(\lambda')} \tag{7.27}$$

$$= \varepsilon_{\text{RRS}}(\lambda' \to \lambda). \tag{7.28}$$

The importance sampling weight which corrects for the aforementioned problem is thus

$$w_{\text{IS, RRS}}(\lambda' \to \lambda) = \frac{k_{\lambda'\to\lambda}}{k_{\lambda\to\lambda'}} = \frac{\varepsilon_{\text{RRS,in}}(\lambda)}{\varepsilon_{\text{RRS,out}}(\lambda)}. \tag{7.29}$$

Note that the ratio $\frac{\varepsilon_{\text{RRS,in}}(\lambda)}{\varepsilon_{\text{RRS,out}}(\lambda)}$ is the one following also from the derivation of point 3 of the path sampling procedure in Section 7.2.1 as a normalizing factor. The fact that $\varepsilon_{\text{RRS}}(\lambda' \to \lambda)$ cancels in the importance sampling weight is the reason to simulate RRS events in a mixed form of forward and backward sampling. The path sampling procedure as it is described is thus neither perfectly "forward" nor "adjoint" in the mathematical sense. In the estimation of intensities, the weights $w_{\text{IS, RRS}}$ for each scatter order are gradually updated (i.e. multiplied) and accumulated into a total correction weight.
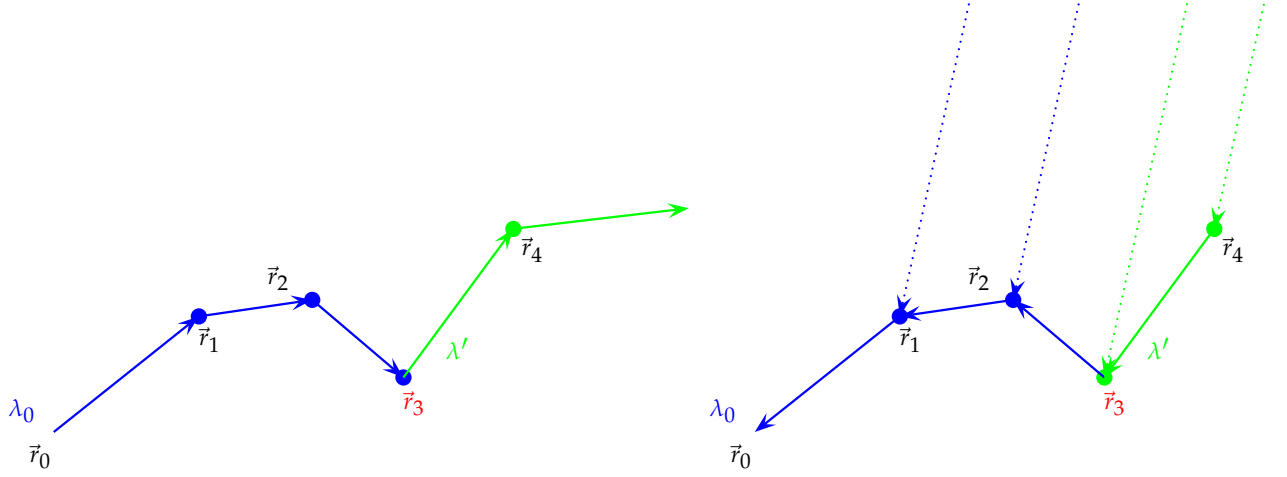
Figure 7.3.: Path generation with an RRS event at $\vec{r}_3$ (**left**) and the local estimation stage (**right**). The raytracing starts at the detector position at $\vec{r}_0$ with wavelength λ_0. Scatter events are sampled (solid circles: elastic events) until a RRS event occurs ($\vec{r}_3$). Local estimates are calculated for the wavelength λ' sampled in the RRS event. The single scattering albedo at $\vec{r}_3$ is corrected (circle color changes from blue to green).

7.2.3. Local Estimates of Intensities with RRS

The path ensemble that is generated by the previously described procedure is used as usual (see Chapter 5.1.2.2) to obtain intensity estimates. Such estimates are obtained by summation over the contributions $c_{\text{l.e.}}$ of scatter orders. A single contribution consists of the product of the transmission probability according to the optical thickness (obtained by integrating the extinction coefficient between a scatter event of a trajectory sample and the Sun) and the phase function evaluated for the angle $\theta_* = \arccos(\mu^*)$ between the direction of the trajectory and the Sun direction. Similarly as for the direction sampling in the path generation procedure, given a scatter event with probability $\varpi_0(\lambda)$, the local estimate is calculated by the following formula:

$$c_{\text{l.e.}} \overset{\lambda' \text{ from Eq. (7.20)}}{\approx} (1 - p_{\text{RRS}}(\lambda)) \frac{P_{\text{el}}(\mu^*, \lambda)}{4\pi} F(\lambda) + p_{\text{RRS}}(\lambda) w_{\text{IS, RRS}}(\lambda' \to \lambda) \frac{P_{\text{RRS}}(\mu^*)}{4\pi} F(\lambda') \tag{7.30}$$

where

$$F(\lambda) = F_0(\lambda) e^{-\tau(\lambda)} \tag{7.31}$$

and the correction weight Eq. (7.29). This is interpreted as follows: according to Eq. (7.30), with a probability of $1 - p_{\text{RRS}}(\lambda)$, the local estimate of the intensity is the elastic intensity local estimate and with a probability $p_{\text{RRS}}(\lambda)$ it is an estimate containing the solar irradiance (the light source in general) obtained at the wavelength λ' sampled from the same density as in point 3 of the path sampling procedure:

$$\frac{\int \varepsilon_{\text{RRS}}(\lambda' \to \lambda) F(\lambda') \, d\lambda'}{\int \varepsilon_{\text{RRS}}(\lambda' \to \lambda) \, d\lambda'} = \sum_{X=N_2,O_2} \sum_{J=0}^{\infty} \left(p_{\text{RRS,in},X,J}^{-}(\lambda) F(\lambda_{X,\text{in}}^{-}(\lambda, J)) + p_{\text{RRS,in},X,J}^{+}(\lambda) F(\lambda_{X,\text{in}}^{+}(\lambda, J)) \right) \tag{7.32}$$

using Eq. (7.22).

7.2.4. Intensity Estimates

Fig. 7.3 summarizes the procedure described in Sections 7.2.1, 7.2.2 and 7.2.3. Intensity estimates are then obtained from the following formula:

$$I \approx \sum_{n=1}^{N} \prod_{i=1}^{n-1} w_{\text{IS, RRS}}(\lambda_i \to \lambda_{i-1}) c_{\text{l.e.},n}(\lambda_{n-1}, \lambda_n) \tag{7.33}$$

where

$$c_{\text{l.e.},n}(\lambda_{n-1}, \lambda_n) = \begin{cases} \frac{P_{\text{el}}(\mu_n^*, \lambda_{n-1})}{4\pi} F(\lambda_{n-1}) & \text{elastic scattering, i.e. } \lambda_{n-1} = \lambda_n \\ w_{\text{IS, RRS}}(\lambda_n \rightarrow \lambda_{n-1}) \frac{P_{\text{RRS}}(\mu_n^*)}{4\pi} F(\lambda_n) & \text{with probability } p_{\text{RRS}}(\lambda_{n-1}) \end{cases} \quad (7.34)$$

are the local estimates according to Eq. (7.30) and the sampling of λ_n.

7.3. Ring Spectra

Including RRS in the estimation of intensities is described in previous sections. For the calculation of a Ring signal (or filling-in) according to Eq. (7.1) one has to run the model once in order to obtain an intensity with RRS and a second time for the elastic intensity (i.e. without RRS). Since for two runs the trajectory samples are statistically entirely independent, the application of Eq. (7.1) yields a result with large and even unacceptable standard deviation whenever the difference in the intensities is within the respective intensity noise range.

7.3.1. Elastic Biasing of the Local Estimates

A method to overcome this efficiency problem is again importance sampling. Importance sampling is in this case to treat RT with purely elastic scattering as a perturbation to RT with RRS. As already described in Chapters 4.3 and in an applied form in Chapter 5.1.3, for importance sampling one needs appropriate weights to correct for the differences in the sampling kernels. In order to derive the importance sampling weight, consider a section in the event chain:

$$\cdots \rightarrow \begin{pmatrix} \vec{r}_{n-1} \\ \vec{\omega}_{n-1} \\ \lambda_{n-1} \end{pmatrix} \rightarrow \begin{pmatrix} \vec{r}_n \\ \vec{\omega}_n \\ \lambda_n \end{pmatrix} \rightarrow \cdots \quad (7.35)$$

According to the path sampling procedure (Section 7.2.1) the kernel for the transition Eq. (7.35) is

$$k_{\text{el + RRS}, \vec{r}_{n-1} \rightarrow \vec{r}_n} = \exp\left(-\tau_{\vec{r}_{n-1} \rightarrow \vec{r}_n}(\lambda_{n-1})\right) \cdot \varepsilon_S(\vec{r}_n, \lambda_{n-1}) \cdot \frac{P(\vec{r}_n, \mu_n, \lambda_{n-1})}{4\pi} \quad (7.36)$$

or in words: transmission from $\vec{r}_{n-1}$ to $\vec{r}_n$ **and** (then) scattering (i.e. not absorption) at $\vec{r}_n$ **and** selection of the new direction and wavelength. For the physically correct interpretation the propagation direction is reversed:

$$\cdots \rightarrow \begin{pmatrix} \vec{r}_n \\ -\vec{\omega}_n \\ \lambda_0 \end{pmatrix} \rightarrow \begin{pmatrix} \vec{r}_{n-1} \\ -\vec{\omega}_{n-1} \\ \lambda_0 \end{pmatrix} \rightarrow \cdots . \quad (7.37)$$

The corresponding transition probability density at the center wavelength λ_0 is

$$k_{\text{el}, \vec{r}_n \rightarrow \vec{r}_{n-1}} = \varepsilon_{S,\text{el}*}(\vec{r}_n, \lambda_0) \cdot \frac{P_{\text{el}*}(\vec{r}_n, \mu_n, \lambda_0)}{4\pi} \cdot \exp\left(-\tau_{\text{el}*, \vec{r}_n \rightarrow \vec{r}_{n-1}}(\lambda_0)\right) \quad (7.38)$$

where $P_{\text{el}*}$, $\varepsilon_{S,\text{el}*}$ are the purely elastic effective phase function and scattering coefficient, in which RRS is part of Rayleigh scattering, but treated approximately as an elastic scattering process (see the also the note below Eq. (7.41)). The importance sampling weight for the elastic biasing is therefore:

$$w_{\text{IS,el},n} = \frac{k_{\text{el}*, \vec{r}_n \rightarrow \vec{r}_{n-1}}}{k_{\text{el + RRS}, \vec{r}_{n-1} \rightarrow \vec{r}_n}} \quad (7.39)$$

$$= \exp\left(-\Delta\tau_{0,n}\right) \cdot \frac{\varepsilon_{S,\text{el}*}(\vec{r}_n, \lambda_0) P_{\text{el}*}(\vec{r}_n, \mu_n, \lambda_0)}{\varepsilon_S(\vec{r}_n, \lambda_{n-1}) P(\vec{r}_n, \mu_n, \lambda_{n-1})}, \quad (7.40)$$

where

$$\Delta\tau_{0,n} = \tau_{\text{el}*, \vec{r}_n \rightarrow \vec{r}_{n-1}}(\lambda_0) - \tau_{\vec{r}_{n-1} \rightarrow \vec{r}_n}(\lambda_{n-1}) \quad (7.41)$$

It has to be noted that the elastic cross sections for molecular scattering in the equations above differ. for the "elastic + RRS" case the elastic cross section is the Cabannes cross section, whereas in the elastic biasing case the Rayleigh cross section comprises of the Cabannes fraction plus the RR cross section treated as a "pseudo elastic" scattering cross section.

7.3.2. Cumulative Weights and Local Estimates

The cumulative weights consist of two parts: one is for the trajectory and is cumulatively updated at each scatter order and the second is for the local estimate, respectively it is a modified local estimate. The weights for the elastic biasing (elb) are (compare to Eq. (5.32))

$$
w_{\text{elb},n} = \prod_{i=1}^{n-1} w_{\text{IS,el},i} = e^{-\Delta\tau_{0,n,\text{total}}} \cdot \prod_{i=1}^{n-1} \left[\begin{cases} \dfrac{[\varepsilon_{S,\text{el}} * P_{\text{el}} * (\mu_i)](\lambda_0)}{[\varepsilon_{S,\text{el}} P_{\text{el}}(\mu_i)](\lambda_{i-1})} & \text{elastic event} \\[2ex] \dfrac{[\varepsilon_{S,\text{el}} * P_{\text{el}} * (\mu_i)](\lambda_0)}{[\varepsilon_{\text{RRS}} P_{\text{RRS}}(\mu_i)](\lambda_{i-1})} & \text{else} \end{cases} \right] (\vec{r}_i) \tag{7.42}
$$

with the difference in the integrated optical thickness (piece-wise at the respective RRS sampled wavelength λ_i) $\Delta\tau_{0,n,\text{total}}$ along the trajectory between the perturbed case and the case with RRS:

$$
\Delta\tau_{0,n,\text{total}} = \sum_{i=1}^{n-1} \Delta\tau_{0,n} = \tau_{\text{el}*,\vec{r}_0 \to \cdots \to \vec{r}_n}(\lambda_0) - \sum_{i=0}^{n-1} \tau_{\vec{r}_i \to \vec{r}_{i+1}}(\lambda_i) \tag{7.43}
$$

where n is the scatter order. $w_{\text{elb},n}$ accounts for the elastic biasing along the backward trajectory until the nth scatter order. In practice the w_{elb} is gradually updated at each scatter event. The modified elastic local estimate is thus:

$$
c_{\text{elastic l.e.},n} = w_{\text{elb},n} \cdot e^{-\tau_{\text{el}*,\vec{r} \to \vec{r}_{\text{Sun}}}(\lambda_0)} P_{\text{el}*}(\vec{r}_n, \mu_n^*, \lambda_0). \tag{7.44}
$$

Both local estimates Eq. (7.30) and Eq. (7.44) are separately added along the trajectory to their respective intensities with and without RRS. After a sufficient large number of trajectories is sampled, Eq. (7.1) can be evaluated.

7.3.3. Test of the Elastic Biasing

In order to test the correct implementation of the biasing, a simple atmosphere with three layers over a black surface (i.e. surface albedo 0) is set up. The atmosphere consists of a Rayleigh scattering gas and an artificial absorber. The absorber is expected to influence most the difference in optical thickness along the trajectory Eq. (7.43). The solar irradiance is artificially set to a distinctive structure (purple line in panel c of Fig. 7.4). Other relevant parameters are listed in Tab. 7.1. In panel b of Fig. 7.4 it becomes obvious,

3 spherical layers	0-2, 2-4 and 4-8km
X number density	0.02, 0.05 and 0.02 $N \cdot cm^{-3}$
p & T	std. atm. evaluated at layer middle altitudes
Altitude	0.0001km
Elevation	12°
SZA	24°
SRAA	90°

Table 7.1.: settings for Chapter 7.3.3

that the difference of importance sampled I_e and I_e obtained from a separate run fluctuates randomly. These fluctuations are attributed to Monte Carlo noise. The lowermost panel d shows the filling-in of structures of the solar irradiance. The degree of polarization (DOP) is shown in panel d. In the comparison with measurements (the following section), the difference between the scalar Ring effect and the vector Ring effect is investigated. In panel b three peaks appear as a consequence of rotational Raman scattering: the structures at 406 and 408nm are caused by filling-in of absorption cross section structures of the artificial absorber (compare to panel c) and the Ring peak at 402nm is RRS filling-in of a solar irradiance structure.
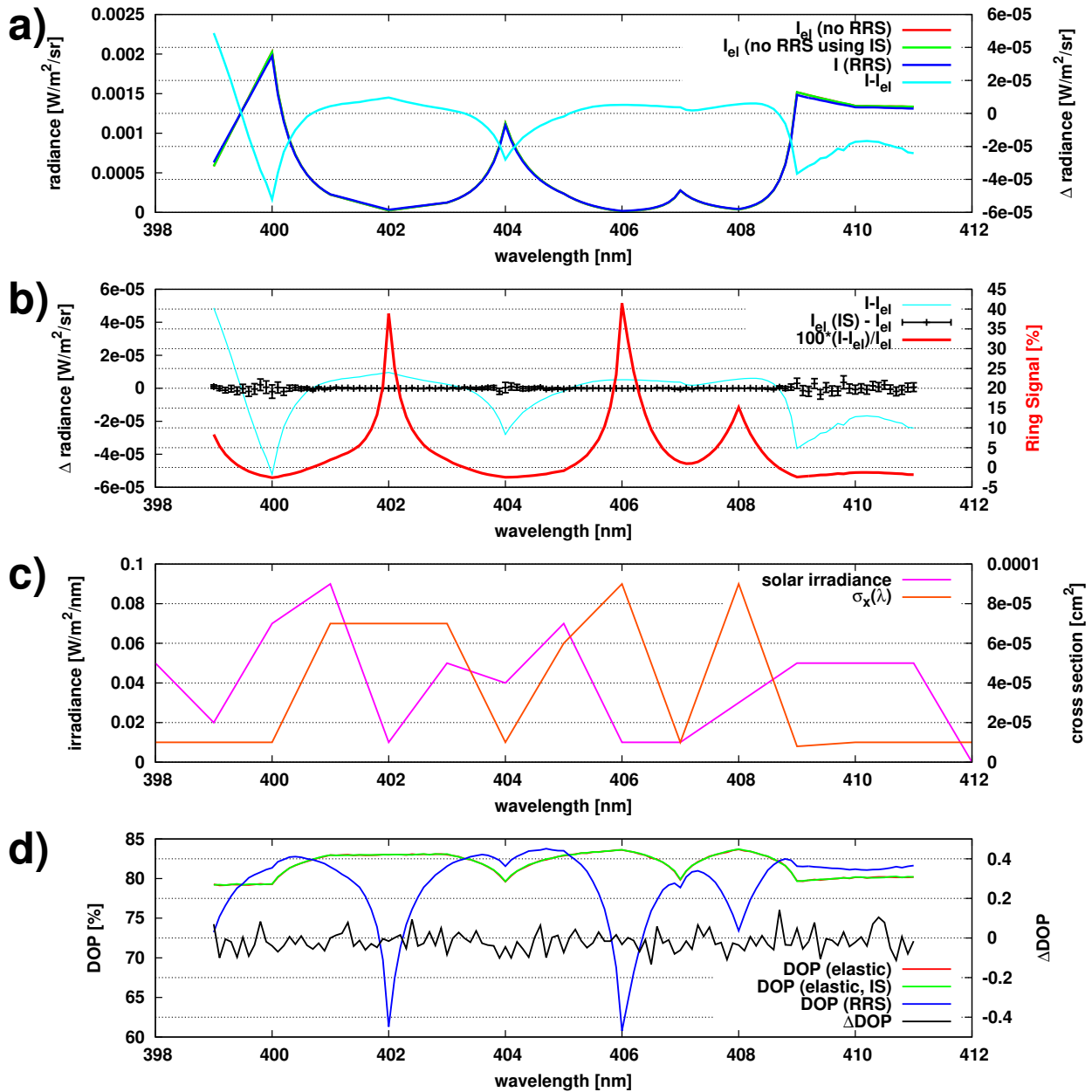
Figure 7.4.: Validation of the elastic biasing. **Panel a):** the blue, green and red curves show I, I_{el} from IS and I_{el} from a separate run without importance sampling. **Panel b):** difference of importance sampled I_e and I_e from a different run (black) and the difference $I - I_e$ in turquoise. Additionally, the corresponding Ring spectrum is shown. In **panel c)** the solar irradiance (pink) and the absorption cross section of the artificial absorber (brown) are shown. **Panel d):** Validation of elastic biasing for the Stokes vector components in form of the degree of polarization (DOP). The deviations of the separate elastic intensity run and the importance sampled elastic intensity is the black curve.

7.4. Validation

In this section validation of the implementation is done through comparison with a single scattering code (section 7.4.1), comparison with two other radiative transfer models (section 7.4.3) and by comparison to a measurement (section 7.4.4). Comparing model results has always the problem that only the way of solving a differential equation is compared, but not if the underlying physics is correctly described or if physics in complete. New physics can only be found by testing known physics against reality.

7.4.1. Comparison to an Analytic Single Scattering Code

There are situations in the atmospheric radiation transport, where the single scattering approximation holds (compare to introducing Chapter 3.3.6). Such a case is for example the spectral region of the O_2 absorption around 755nm-780nm (the so called oxygen A band, see [Funk, 2000] for a detailed treatment of relevant physics in the spectral region) if no aerosols or clouds are present. The validity of the single scattering assumption is presented in Fig. 7.5. The single scattering model is described in Chapter 3.3.6 and its extension
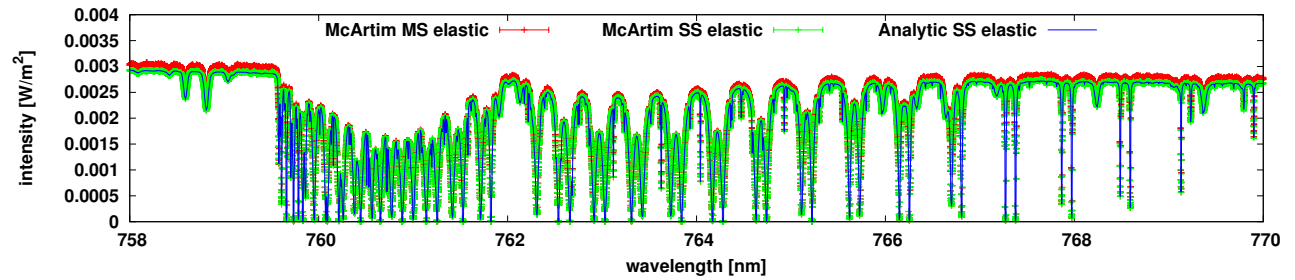
Figure 7.5.: Simulated O2 A band spectrum for a satellite nadir geometry with 45° SZA and δ-FOV. The surface albedo is zero and no aerosols or clouds are present. The red curve shows the (multiple scattering) RTE solution, green is the result from the single scattering approximation (Neumann series truncation) and the blue line shows the result of the analytic single scattering model.

to inelastic scattering in Chapter 7.4.2. Fig. 7.5 also shows the results of the single scattering code: the blue line perfectly fits to the error envelope of the Monte Carlo code results obtained by truncating the Neumann series. The SSA code is therefore considered as validated.

7.4.2. Single Scattering Model Including Rotational Raman Scattering

The simple single scattering model described in chapter 3.3.6 is extended with respect to rotational Raman scattering. Since historically RRS is part of the Rayleigh scattering cross section when considering a wavelength resolution large compared to the typical RRS wavelength shifts, the modifications of the molecular scattering cross sections in Eq. (3.168) with respect to RRS will affect the transmission terms (Section 7.4.2.1) only slightly[Penney et al., 1974]. The major differences of the inelastic single scattering model in comparison with its elastic version result from the modified source terms (Section 7.4.2.2).

7.4.2.1. Elastic and Inelastic Optical Thicknesses

The elastic optical thickness contains in the integral the absorption coefficients $\varepsilon_a(\vec{r}, \lambda)$ and the elastic scattering coefficients $\varepsilon_{s,\text{el}}(\vec{r}, \lambda)$ including the molecular Cabannes cross sections and the super molecular particle cross sections.

$$\tau_{\text{el}}(\vec{r}_1 \to \vec{r}_2, \lambda) = \int_0^{|\vec{r}_2 - \vec{r}_1|} [\varepsilon_a + \varepsilon_{s,\text{el}}](\vec{r}_{1 \to 2}(l), \lambda)\, dl. \tag{7.45}$$

where $\vec{r}_{1 \to 2}(l)$ is the parametrization of the straight line between $\vec{r}_1$ and $\vec{r}_2$. Considered separately (the optical thickness is additive with respect to the coefficients in one grid cell), the RRS optical thickness is:

$$\tau_{\text{RRS}}(\vec{r}_1 \to \vec{r}_2, \lambda) = \int_0^{|\vec{r}_2 - \vec{r}_1|} \varepsilon_{\text{RRS}}^{\text{out}}(\vec{r}_{1 \to 2}(l), \lambda)\, dl = \int_0^{|\vec{r}_2 - \vec{r}_1|} \int_{-\infty}^{+\infty} \varepsilon_{\text{RRS}}(\vec{r}, \lambda \to \lambda')\, d\lambda'\, dl \tag{7.46}$$

where

$$\varepsilon_{\text{RRS}}^{\text{out}}(\vec{r}, \lambda) = \int_{-\infty}^{+\infty} \varepsilon_{\text{RRS}}(\vec{r}, \lambda \to \lambda')\, d\lambda' \tag{7.47}$$
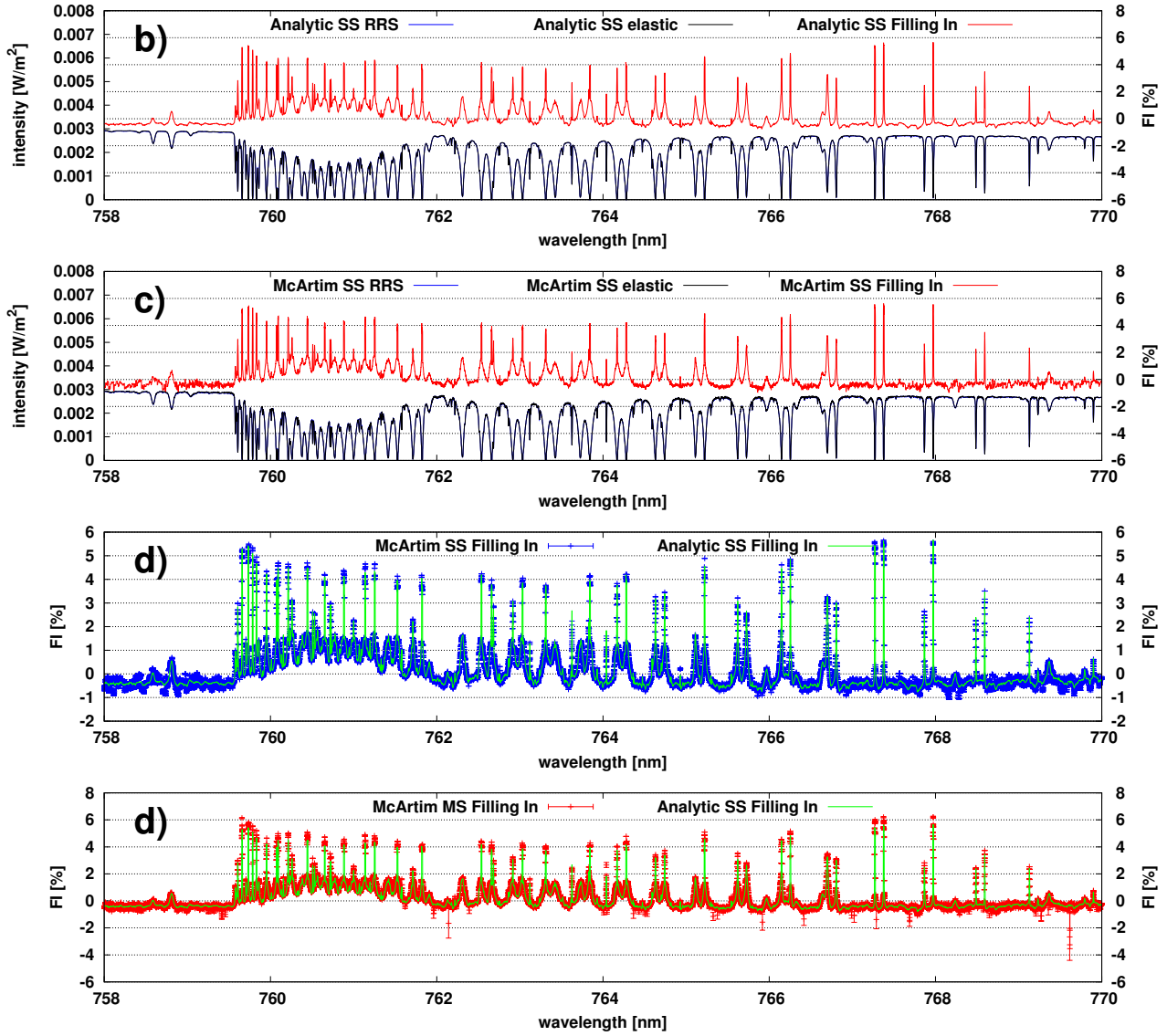
Figure 7.6.: Elastic and inelastic intensities and filling-in for the analytic SSA model (**panel a**) and for McArtim truncating the Neumann series after the first scatter event (**panel b**). Observation geometry and atmosphere as described Fig. 7.5. **Panel c** shows direct inter comparison of the filling in from the analytic model (green) and McArtim (blue). The last **panel d** again the analytic model results are plot, but this time against the multiple scattering filling-in result of McArtim.

contains the sum of cross sections of all RRS events, which change the incident wavelength to all possible wavelengths except the incident wavelength. In the total optical thickness τ_{el} and τ_{RRS} add:

$$\tau_{el+RRS}(\vec{r}_1 \to \vec{r}_2, \lambda) = [\tau_{RRS} + \tau_{el}](\vec{r}_1 \to \vec{r}_2, \lambda) = \int_0^{|\vec{r}_2 - \vec{r}_1|} [\varepsilon_a + \varepsilon_{S,el} + \varepsilon_{RRS}^{out}](\vec{r}_{1\to 2}(l), \lambda)\, dl. \tag{7.48}$$

It has to be noted that $\tau = \tau_{el+RRS}$ (see [Penney et al., 1974] for a discussion), i.e. that the modifications presented here are only a separation of the optical thickness into elastic and inelastic contributions.

7.4.2.2. RRS Source Terms

The elastic source term Eq. (3.160) is rewritten in a different form introducing a wavelength integration which is needed for the RRS source term using a δ function:

$$
R_{S,\mathrm{el}}(\vec{r}, \vec{\omega}, \lambda) = \frac{1}{4\pi} \int_0^{4\pi} R(\vec{r}, \vec{\omega}', \lambda) \cdot \varepsilon_{S,\mathrm{el}}(\vec{r}, \lambda) P_{\mathrm{el}}(\vec{r}, \vec{\omega}' \to \vec{\omega}, \lambda) \, \mathrm{d}\vec{\omega}' \tag{7.49}
$$

$$
= \frac{1}{4\pi} \int_\infty^\infty \delta(\lambda - \lambda') \int_0^{4\pi} R(\vec{r}, \vec{\omega}', \lambda') \cdot \varepsilon_{S,\mathrm{el}}(\vec{r}, \lambda') P_{\mathrm{el}}(\vec{r}, \vec{\omega}' \to \vec{\omega}, \lambda') \, \mathrm{d}\vec{\omega}' \, \mathrm{d}\lambda'. \tag{7.50}
$$

Similar as in the modified transmission the previous section the elastic phase function comprises of the Cabannes phase function and of the phase functions of particles. $R_{S,\mathrm{RRS}}$ RRS source term:

$$
R_{S,\mathrm{RRS}}(\vec{r}, \vec{\omega}, \lambda) = \frac{1}{4\pi} \int_{-\infty}^{+\infty} \int_0^{4\pi} R(\vec{r}, \vec{\omega}', \lambda') \cdot \varepsilon_{\mathrm{RRS}}(\vec{r}, \lambda' \to \lambda) P_{\mathrm{RRS}}(\vec{r}, \vec{\omega}' \to \vec{\omega}, \lambda') \, \mathrm{d}\vec{\omega}' \, \mathrm{d}\lambda'. \tag{7.51}
$$

As a consequence of RRS, light of other wavelengths λ' then the center wavelength λ contribute to the source term respectively weighted by the RRS cross section $\varepsilon_{\mathrm{RRS}}(\vec{r}, \lambda' \to \lambda)$. The total source term is:

$$
R_{S,\mathrm{el}+\mathrm{RRS}}(\vec{r}, \vec{\omega}, \lambda) = R_{S,\mathrm{el}}(\vec{r}, \vec{\omega}, \lambda) + R_{S,\mathrm{RRS}}(\vec{r}, \vec{\omega}, \lambda). \tag{7.52}
$$

7.4.2.3. The Intensity Including RRS in the Single Scattering Approximation

For sake of completeness, the intensity is given explicitly in similar form as Eq. (3.168):

$$
F_{\mathrm{ssa}} = \frac{1}{4\pi} \int_0^{l_{\max}} T(\vec{r}_l \to \vec{r}_\bullet) \left[\varepsilon_{S,\mathrm{el}}(\vec{r}, \lambda) \int_{\Delta\Omega^*(\vec{r})} P_{\mathrm{el}}(\vec{r}, \vec{\omega}' \to \vec{\omega}, \lambda) \cdot F_0(\lambda) \cdot T(\vec{r}_*(\vec{\omega}') \to \vec{r}_l, \lambda) \, \mathrm{d}\vec{\omega}' + \cdots \right.
$$

$$
\left. \int_{\Delta\Omega^*(\vec{r})} \int_{-\infty}^{+\infty} \varepsilon_{\mathrm{RRS}}(\vec{r}, \lambda' \to \lambda) P_{\mathrm{RRS}}(\vec{r}, \vec{\omega}' \to \vec{\omega}, \lambda') \cdot F_0(\lambda') \cdot T(\vec{r}_*(\vec{\omega}') \to \vec{r}_l, \lambda') \, \mathrm{d}\lambda' \, \mathrm{d}\vec{\omega}' \right] \mathrm{d}l. \tag{7.53}
$$

7.4.2.4. Discussion

In Fig. 7.6 the upper two panels show respectively intensities with and without inelastic scattering and the associated filling-in. The direct inter comparison of analytic and Monte Carlo single scattering results show agreement within the statistical noise. Finally, the lowermost panel shows the strength of the Ring effect for the multiple scattering case in comparison with the analytic single scattering solution. Due to the same reasons why the single scattering approximation is valid, it can according to the lowermost plot be said that the Monte Carlo calculated multiple scattering filling-in is valid at least for a case with few multiple scattering.

7.4.3. Multiple Scattering Model Comparison

The results of the Monte Carlo method are compared against two other models radiative transfer models. Both models, the UVSPEC model [Kylling et al., 2010] and SCIATRAN [Rozanov et al., 2005] calculate the Ring effect in the single scattering approximation using discrete ordinate techniques. The Monte Carlo method presented here solves the integro-differential equation Eq. (7.13). The solution also contains the effect of multiple scattering and filling in of absorption structures of atmospheric constituents like O_3.

7.4.3.1. Molecular Atmosphere With Physical Solar Irradiance

The first test is, whether the models yield equal radiances for the case of a purely Rayleigh scattering atmosphere (see Fig. 7.7) and the solar irradiance spectrum after [Chance and Kurucz, 2010]. The ground albedo is set to zero and the atmosphere does not contain any absorbing species. The detector is at 29.9km altitude

in the nadir geometry and the Sun's zenith angle is 20°. The top panel of Fig. 7.7 shows the model results for
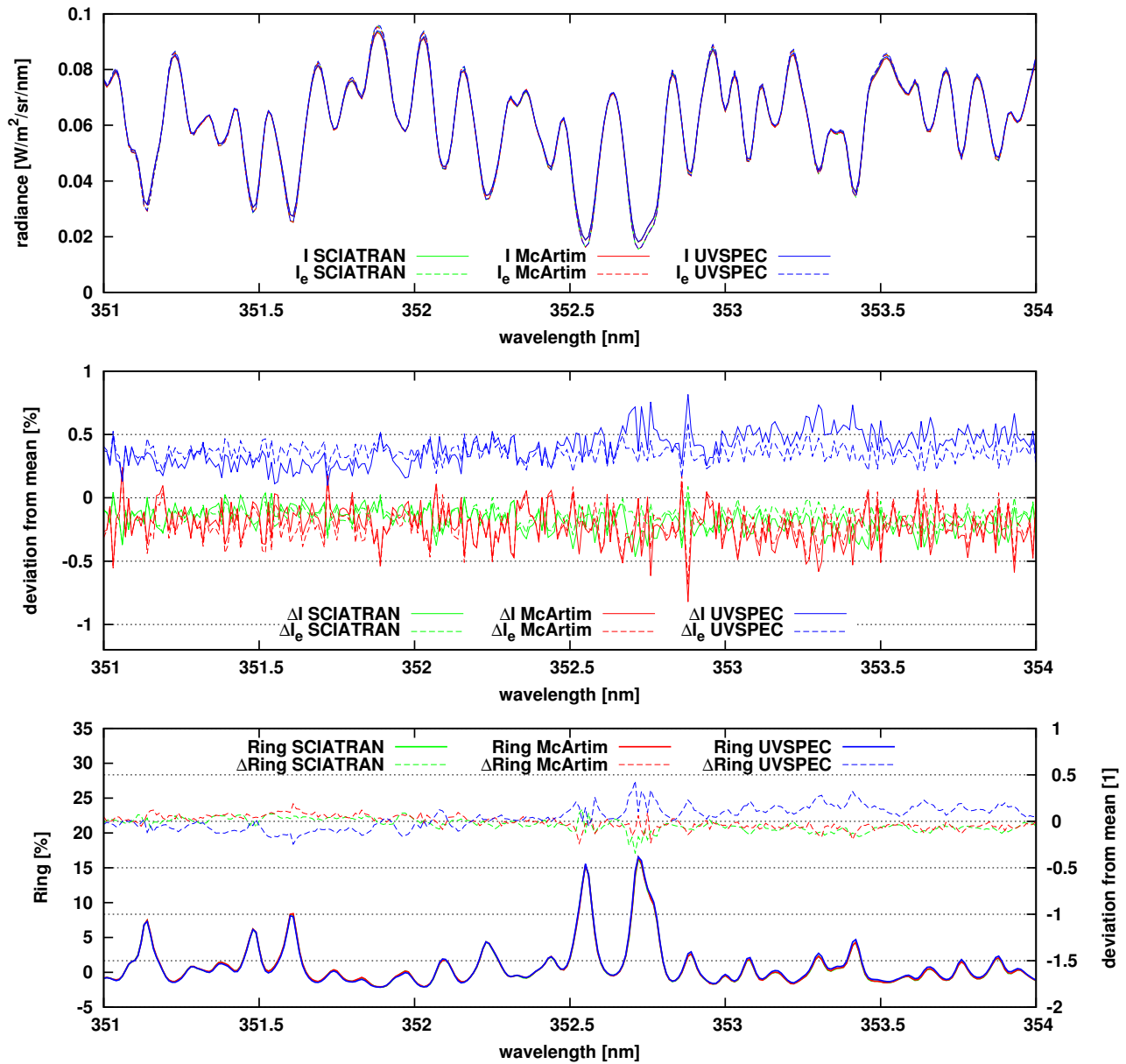
Figure 7.7.: **Top panel:** comparison of elastic (I) and inelastic radiances (I_{el}) for a pure Rayleigh atmosphere in satellite, nadir geometry, SZA=20, ground albedo 0. **Middle panel:** deviations of the model results for I and I_{el} from the respective arithmetic mean in percent. **Bottom panel:** the solid curves show Ring spectra of the models. Dashed curves are deviations from the arithmetic mean Ring signal.

elastic radiances I_{el} and radiances considering RRS I. In the plot, the Ring effect appears in form of deviations of I and I_{el} (e.g. in the wavelength range 352.5nm and 353nm). The corresponding Ring signals S_{rrs} calculated according to Eq. (7.1) are shown as the solid curves in the bottom panel of Fig. 7.7. In order to compare the models, the arithmetic mean is calculated for I, I_{el} and S_{RRS}. Deviations of the models results for I and I_{el} are shown in the middle panel. The plot reveals that SCIATRAN and McArtim results are close to each other and agree within the Monte Carlo noise. The agreement between all three models is 2% peak-to-peak. The deviations of the models from the mean can also be seen in the bottom plot, where only the Ring signals are inter compared. There also the results of the UVSPEC differ a little bit from the results of McArtim and SCIATRAN.

7.4.3.2. Artificial Solar Irradiance

The solar irradiance is replaced by an artificial irradiance spectrum in order to study the effect on the shape of S_{rrs}. The bottom panel of Fig. 7.8 shows the corresponding Ring spectra. Obviously, the Ring structure is asymmetric for a symmetric irradiance. This is caused by the asymmetry of Stokes and Anti-Stokes scattering cross sections (see Fig. 7.1). In order to investigate the influence of multiple rotational Raman scattering on
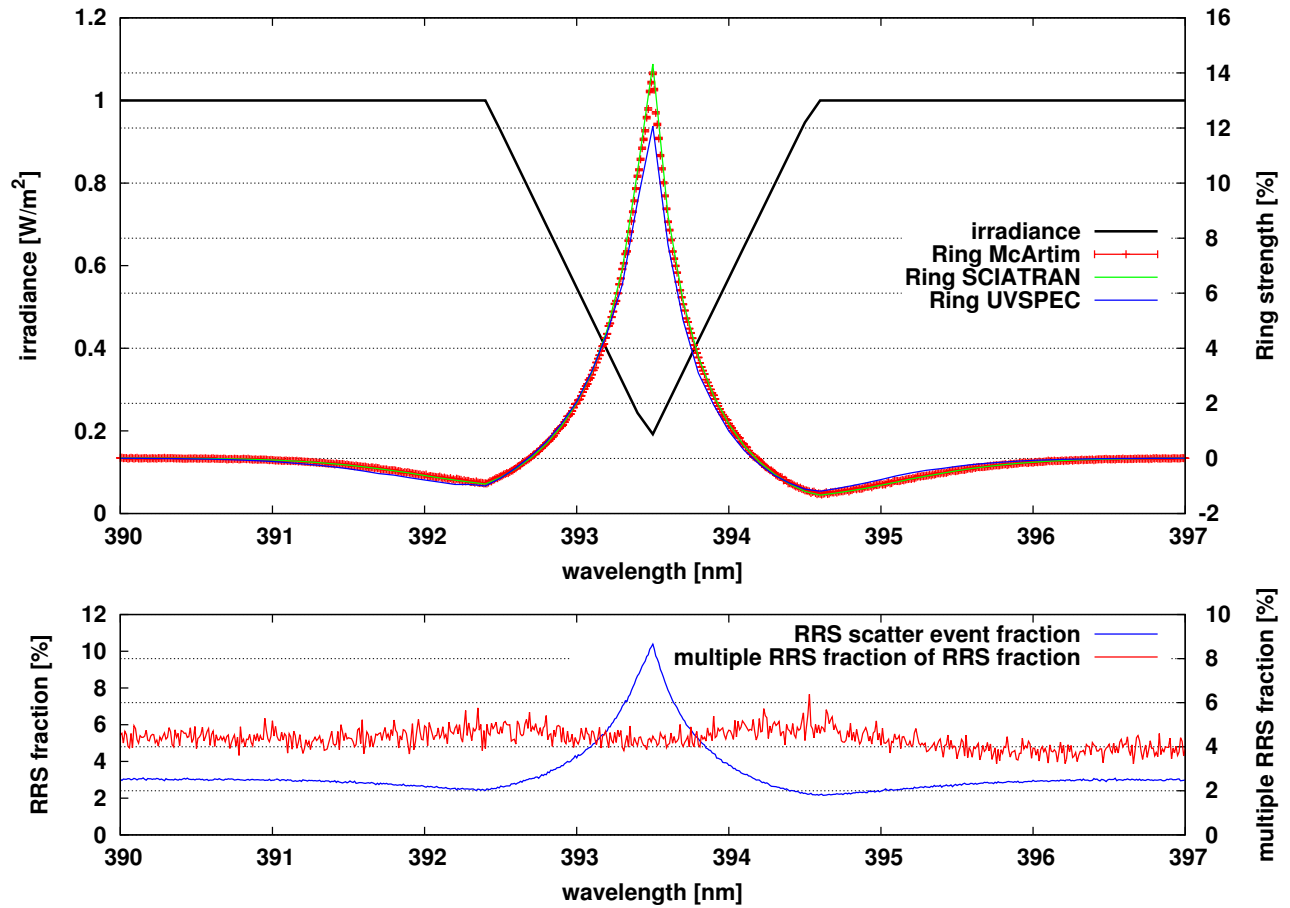
Figure 7.8.: **Top panel:** Modeled Ring effect for an artificial irradiance spectrum (black curve). The **bottom panel** shows the contribution of RRS events as a fraction of the total number of scatter events (blue) and the fraction of the multiply RR scattered model photons of the RRS scattered model photons.

the Ring structure, effective (i.e. intensity weighted) number of scatter events are calculated (see bottom panel of Fig. 7.8). As the figure shows, the fraction of RRS scatter events of all scatter event is around 2.7% in the wings of the irradiance line. This is approximately the fraction of the RRS cross section with respect the Rayleigh cross section but contains additionally (and in a non trivial form) a contribution of the RRS phase function. In the center of the artificial solar irradiance line at 393.5nm the fraction of RR scattered light reaches a total amount of approximately 10.5%. The fraction of multiple RRS on the total RRS fraction is shown by the red curve in the bottom panel of Fig. 7.8. According to the figure, the total fraction of multiple rotational Raman scattered light (red curve in the plot) accounts for 4.5% of the Ring signal and is has thus is $\approx 0.045 \cdot 0.105 = 0.0047$ i.e. 0.5% of the total signal. At the maximum of the Ring structure at 393.5nm the difference between the McArtim model and UVSPEC is about 15% of the Ring signal. According to the previous considerations, multiple RRS scattering can explain about 25% of the differences in the model results. The comparison of elastic radiances from the (from a mathematical or technical point of view) similar RT models SCIATRAN and UVSPEC however shows that small differences in the parametrization of Rayleigh scattering (see e.g. [Eberhard, 2010] for common systematic errors in the calculation) solely can explain some of the deviations. Details which are particularly influencing the inter comparison are the parametrization of the polarizabilities $\alpha(\lambda)$ of N_2 and O_2, their anisotropies $\gamma(\lambda)$, the maximum number of rotational quantum

Figure 7.9.: The measurement site is marked with a pin. The measurement took place 05.11.11 at around 17:48:52UTC.

numbers considered amongst others. From personal communicatioin with the author of the SCIATRAN model it is known that a compensation for the neglect of single scattering or even a different technical approach compared to the UVSPEC mode is implemented. Therefore the difference between UVSPEC and SCIATRAN could also be attributed entirely to the effect of multiple RRS.

7.4.4. Comparison with A Measurement

In the previous section an disagreement between the Ring effect models of approximately 10% is found. Physical knowledge basis of all models is the radiative transfer equation including inelastic scattering. In this section the strength of the Ring effect and the amount of filling-in of structures in the solar irradiance is compared for simulated and measured spectra. Measured spectra were recorded during the TASK campaign employing a rebuilt military drone (the global hawk) equipped with an UV spectrometer from Ocean Optics. In order to compare measured and modeled spectra the spectrometer function (i.e. the spectrometer forward model) has to be modeled. See Chapter 6.1 for details on the model. The comparison is done in the following way. The Ring effect appears in a spectral fitting routine as a residual structure in the order of some percent (of the by-channel spectrum) The model which is fit to the data (DOAS) implicitly treats radiation transport elastically (compare to chapter 6). Therefore residual structures $S_{\text{measured}} - S_{\text{elastic}}$ in the spectra are caused by missing physics or a missing knowledge on the atmospheric state in the model. The signal per channel is calculated according to Eq. (6.6), i.e. the modeled signals per channel with (S) and without (S_{elastic}) RRS are obtained from the high resolution radiance spectra I and I_{el} by convolution with the instrument function per channel. The instrument parameters quantum yield and grating efficiency η (chapter 6) and the channel to wavelength mapping function are obtained from a fit (see appendix C for details on the derivatives). Using the instrument parameters and with the radiances I and I_{el} the result of the fit is a modeled S_{elastic} in instrument units. The comparison is done by comparing the purely modeled Ring spectrum $S - S_{\text{elastic}}$ with the residual $S_{\text{measured}} - S_{\text{elastic}}$.

The analyzed spectrum was recorded 05.11.11 at around 17:48:52 over the pacific in the vicinity of Los Angeles. The geographic coordinates are shown in Tab. 7.2. The telescope elevation angle was -2.5° relative to the

SZA	57.4°
SRAA	-106.25°
CoLatitude	56.1077°
Longitude	-121.3527°
Altitude	16.36835km
Elevation	-2.5°
time	05.11.11 17:48:52 (UTC)
total exposure	19.904s
scans	16

Table 7.2.: Geometry parameters for the inter comparison of measured and simulated Ring effect.
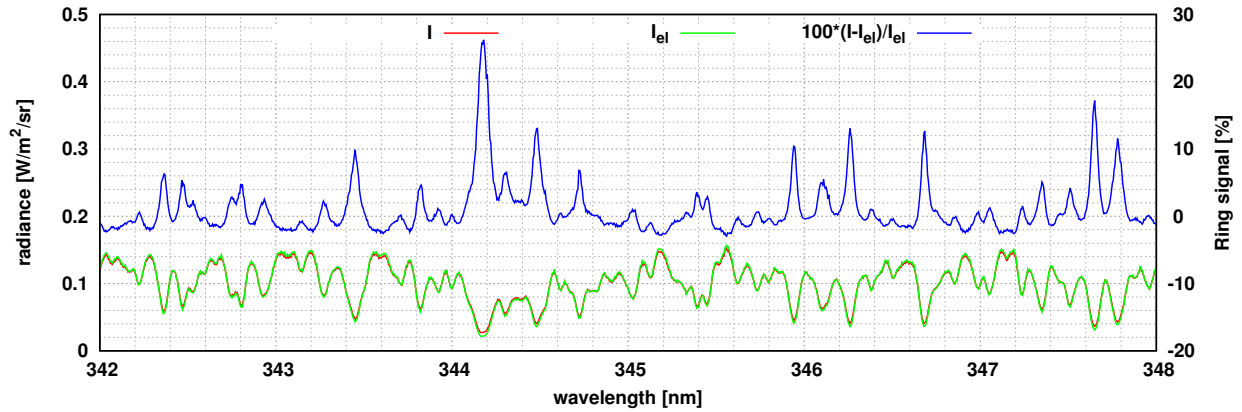
Figure 7.10.: The spectral range 342nm to 348nm of the modeled high resolution scalar spectra I (red) and I_{el} (green) and the corresponding Ring signal (blue) for the observation geometry selected for the comparison with a measured spectrum.

local horizontal, the SZA was 57.4° and the telescope relative solar azimuth -106.25°. Relevant parameters are summarized in Tab. 7.2. Due to the atmospheric uncertainties (mainly due to O_3, NO_2, stratospheric aerosols and surface optical properties) it can not be expected that the absolute calibration obtained in the fit is reliable. For the Ring effect validation most of these uncertainties except those from the gases are very likely not much relevant, since only differential structures are compared. Fig. 7.10 shows a slice of the high resolution modeled spectrum in the UV range. Fig. 7.11 shows the comparison of the relative residuals. If the differences in the fit can be attributed to missing RRS in the model, the difference should at least correlate with the modeled Ring spectrum. The visual inspection shows that this is indeed the case. The following facts could explain some of the differences:

- The spectrometer slit function is not Gaussian. Indeed, the spectral analysis of single mercury lines exhibit a line shape which is better described by a Gauss convoluted with a box function. (see Fig. 7.12 and the following section 7.4.4.1).

- There are etalon structures from the passivation layer of the CCD chip. In the manufacturer manual the etalon effect is shown at NIR wavelengths, suggesting small effects in the UV. However, a small influence in the UV fine structures can not be ruled out.

- Structures in the actual quantum yield and grating efficiency curves, that can not be modeled by a cubic spline could propagate into the simulated spectrum.

- Differential structures of gaseous absorbers O_3, NO_2 etc., are not modeled correctly by McArtim due to lack of knowledge of the spatial concentration profile.

7.4.4.1. Influence of the Instrument Line Shape

As it is shown in this short section, a crucial point in the DOAS fitting process is choosing the correct slit function, for down convolution literature absorption cross sections and other high resolution spectra to instrument resolution. DOAS analysts often choose line shapes obtained from observations of monochromatic
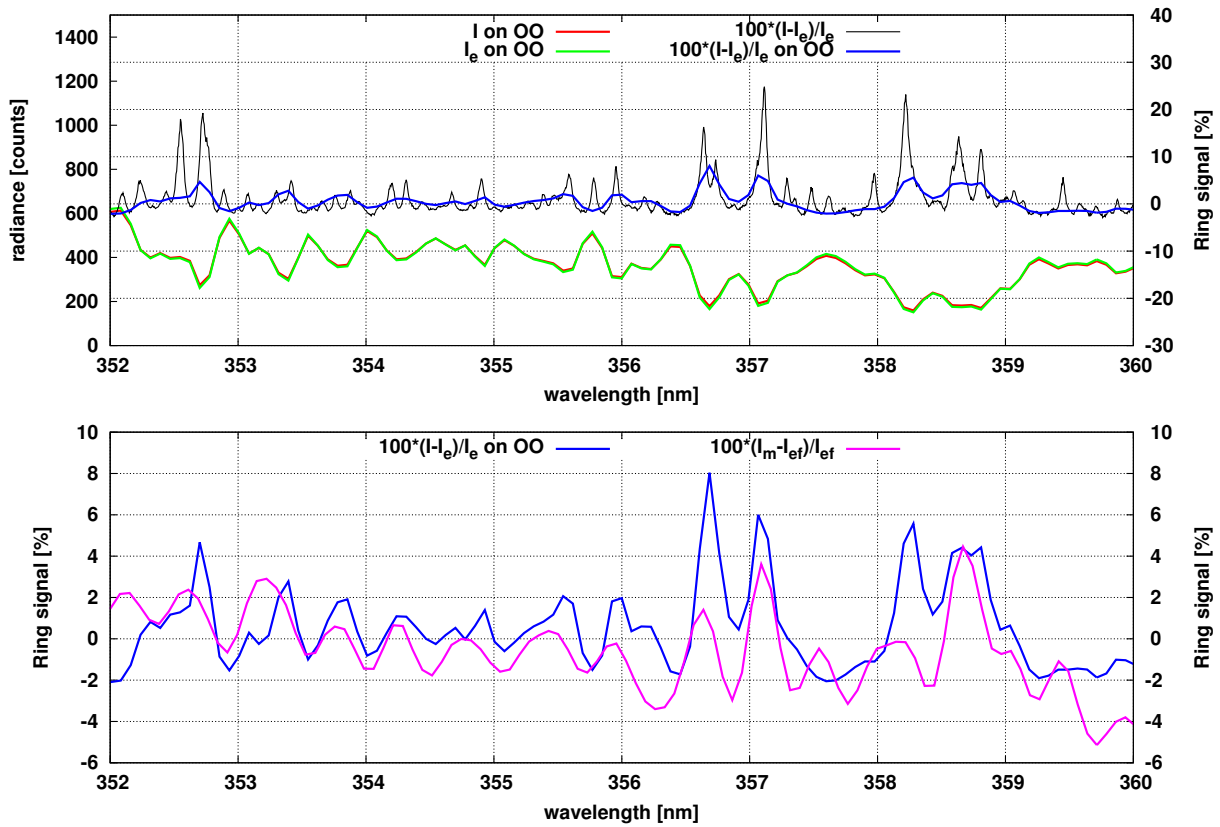
Figure 7.11.: Comparison of measured and modeled Ring spectrum. The **top panel** shows in green and red *I* and I_{el} "convoluted" to instrument resolution. The blue graph is the corresponding Ring signal. In the **bottom panel**, the Ring spectrum at instrument resolution is shown in blue. The pink line shows the "measured" Ring signal as it appears in the fit residual using an elastic RTM.

emission lines (e.g. mercury lamps) as slit functions. Since these emission lines are usually not present over the hole spectral range or, even worth, overlap on a wavelength range scale unresolvable for the instrument, the common practice is often to select an emission line from an adjacent wavelength region. The effect of deviations from the instrumental line shape in DOAS modeling in combination with the Ring effect is shown in Fig. 7.12. If the deviations are symmetric around the center of the emission line, the residual is "Ring-like".
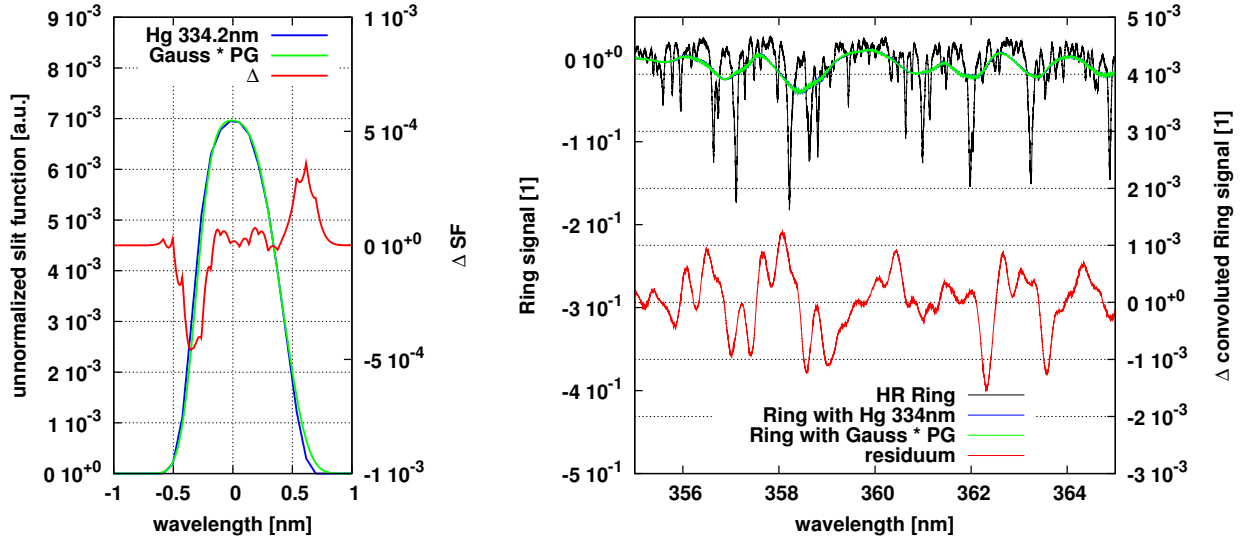
Figure 7.12.: The effect of choosing the wrong slit function for DOAS modeling. **Left panel:** a mercury lamp emission line as it is observed on a typical spectrometer (green) and a Gaussian fit to its shape (blue). The **right panel** shows a high resolution Shefov-Ring spectrum (black) as it would be measured with the slit functions shown in the left panel (same colors) and the corresponding DOAS fit residuum (red) of relative strength of $2.5 \cdot 10^{-3}$ peak-to-peak.

In the case presented, the deviations are asymmetric. The residual therefore seems to be uncorrelated with the Ring effect. A DOAS fitting routine misinterprets the structures as artificial absorbers, or it cancels with a high residual.

7.4.5. Validation of Approximate Methods For Ring Effect Modeling

In the application of DOAS, the Ring effect appears in the logarithmic spectra ratios $\log(I/I_r)$ as a structure at the 10^{-2} optical thickness scale. A common approximation to correct for the Ring structure is to calculate a Ring correction spectrum by convolving the measured reference spectrum I_r with the RRS cross section of air. Another method is to apply the convolution to a high resolution solar irradiance spectrum. The resulting Ring spectra are then used as an additional fit component in the DOAS fitting algorithm. In this section, an approximate Ring spectrum based on the former approach of convolving a simulated spectrum with the effective (out-scattering) RRS cross section (see Fig. 7.1) of air is compared to a simulated Ring spectrum. In panel **a)** of Fig. 7.13 high resolution spectra with (I, blue) and without ($I_{w/o Ring}$, black) RRS and the same spectra respectively convolved with a mercury emission line (slit function) are shown. The convoluted spectra are also shown in panel **b** together with a corresponding modeled Ring spectrum (red). Panel **c)** shows the RT modeled Ring spectrum (red) and a Ring spectrum obtained from the DOASIS software [Kraus, 2005] using I as an input spectrum blue curve in panel **b)**. After removing a polynomial structure the fit result (green) is shown in panel **d)**. The residual structure is shown in turquoise and has a peak-to-peak magnitude of $1.5 \cdot 10^{-3}$. According to the structure of the residual it is expected that the DOAS fit algorithm interpret structures in the systematic Ring error (the aforementioned residual) as trace gas absorption cross section if there is a similarity to the absorption cross section structure of the respective trace gas. Concludingly, fit coefficients related to optical thickness abundances of less then 10^{-3} obtained from the DOAS algorithm applied to the investigated spectral range should be handled with care. However since, first, the agreement of models is also in the same regime (see Fig. 7.7) and second, missing knowledge of the precise slit function also lead to errors in the same order of magnitude (see Fig. 7.12), the investigated approximation method is simple, fast and accurate above the $2 \cdot 10^{-3}$ scale.

7.5. Summary and Discussion

To which extent is the RRS Monte Carlo algorithm able to describe reality? In Chapter 5.3 some general considerations with respect to the validation of a model are presented. In view of these considerations, the weaknesses of the approach are discussed here.

At first, does the underlying differential equation, i.e. the modified RTE (Section 7.1) respectively its vector version, contain all known physics? This is hard to answer. The commonly accepted theoretical structure describing RT is the set of Maxwell equations together with known material properties such as the molecular polarizability tensor which RRS is related to. [Mishchenko, 2002] showed that it is possible to derive the (in other respects merely postulated) vector RTE from the Maxwell equations using the assumption of countable scattering particles with distinct (from the environment) refractive indices, however Rayleigh (wave) scattering has so far not been described in this way which would need stochastic fluctuations in the local refractive index in order to cause scattering. A microscopic theory, on the other side would need localizable (particle like) photons a concrete description of which is not allowed by the uncertainty principles. In so far basing the theory on the still postulated vector RTE still means accepting a gap in taking into account physical knowledge in RTM. A detailed derivation from first principles would require a more sophisticated description of the optical medium, especially with respect to the dielectric properties of air. I believe that, at the moment and in the form of Eq. (7.13), the physics is described sufficiently accurately although it is postulated.

Secondly, the derivation of the path generation algorithm from the integral form (compare to Chapter 4.2.2) is not done rigorously, but the elastic path generation algorithm is modified (Section 7.2.1) and corrected for "nonphysical" biases (Section 7.2.2) applying the importance sampling method of Monte Carlo integration theory. Thus, the mathematical method to obtain the relative difference in intensity with and without modeling of RRS is exact and unbiased (panel b of Fig. 7.4).

All inter compared models aim at solving the same integro-differential equation (compare Chapter 7.1 and Eq. (7.13) to [M.Vountas et al., 1998, Kylling et al., 2010]), but from at least the UVSPEC model method it is known that it does not account for multiple RRS. A direct comparison with a Monte Carlo code implementing the presented approach will therefore not yield exactly identical results. It therefore can not be concluded by using results from the presented inter comparison that the algorithm solves Eq. (7.13) exactly, but that there is agreement of the Ring signals within some few percent (see Fig. 7.8). In order to assess whether physics is described completely and modeled correctly only comparisons with measurements are suitable. Currently, these comparisons (see Fig. 7.11) suffer from missing knowledge on instrument and atmospheric parameters (Sections 7.4.4 and 7.4.4.1). Only a sophisticated fit and further rigorous characterization of the measurement device is believed to decrease the fit residual and allow for concluding on physical correctness of the model.
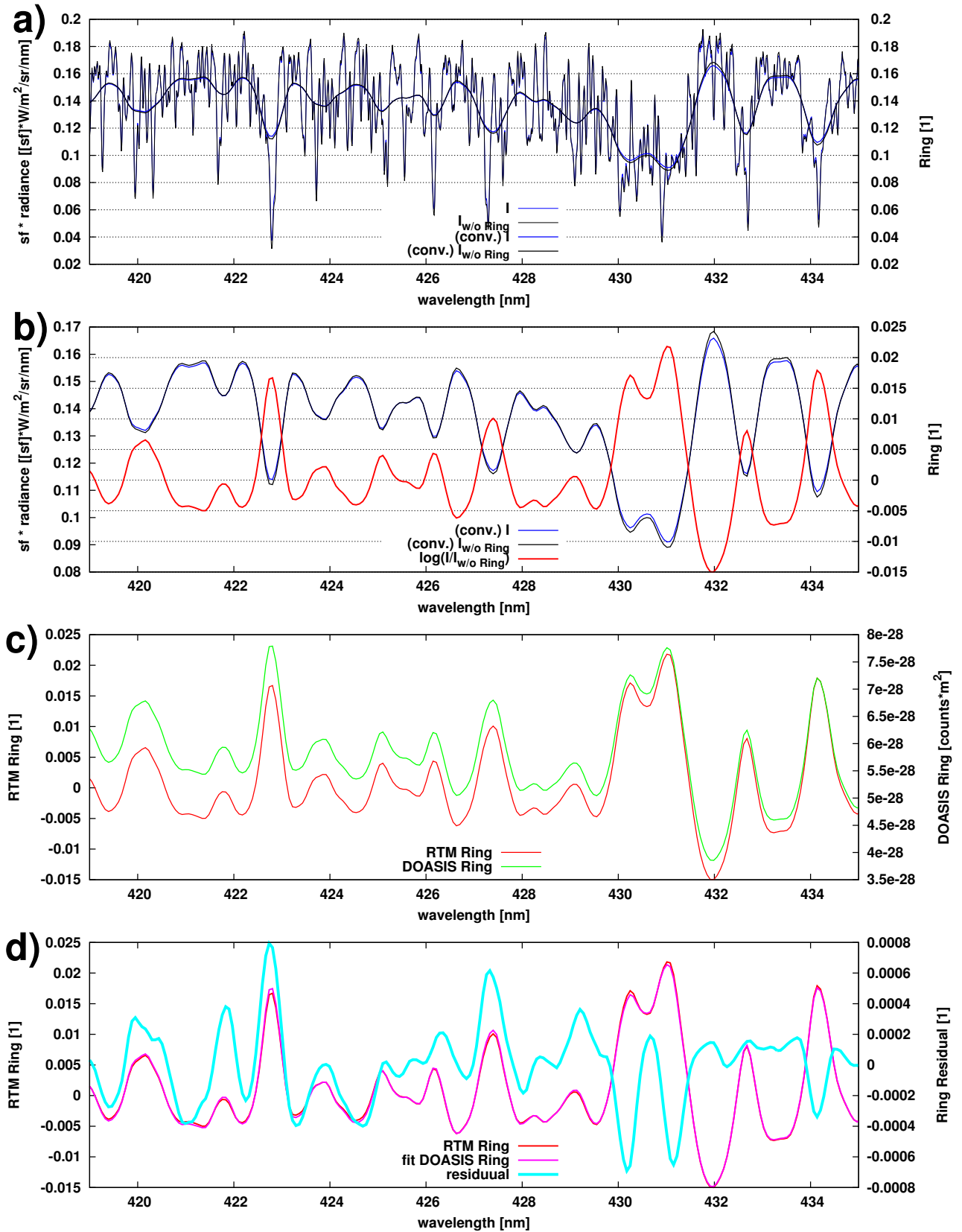
Figure 7.13.: Comparison of approximate and RT modeled Ring spectra. The detailed description of the panels is given in the main text. The plot shows the progression from high resolution spectra in **a** resulting in a RTM Ring spectrum at instrument resolution (the red curve in **b**), the DOASIS modeled Ring (green curve in c) and the resulting fit residual using either of the two spectra in **d**. The residual structure peak-to-peak magnitude is $\approx 1.5 \cdot 10^{-3}$.

<div align="right">

8

</div>

Consolidation

In the following chapter the achievements of the work are summarized into a portfolio of some partially advanced possibilities in atmospheric radiation transport modeling with regard to UV/vis/NIR spectroscopy at spectral resolutions of approximately 10^{-10}m.

8.1. Status and Summary

Passive spectroscopy with grating spectrometers at the 10^{-10}m scale is complicated in particular by the necessity of knowing physical instrument parameters. These parameters are the detector quantum yield, the grating efficiency combined into the $\eta(\lambda)$ function (see Chapter 6.1), the slit function and channel-to-wavelength mapping function among others. The influence of missing or only approximate knowledge of the detailed slit function on the spectrum at instrument resolution is investigated in Chapter 7.4.4.1. The instrument function $f_c(\lambda)$ (chapter 6.1) can be determined in way that the major uncertainty is the $\eta(\lambda)$. In a realistic measurement it also would not make much sense to have a calibration in terms of absolute radiation power per channel in the targeted gas absorption detection range of 10^{-3} to 10^{-4} because spectral artefacts at that range can easily occur by perturbation of the instrument assembly, e.g. pollution of the optical elements or vibration induced displacements of elements of the assembly. Instead, relative structures in the spectra are used as information sources and the effect of the uncertainties in the absolute instrument calibration (in particular η) and those with respect to particulate and molecular scattering are addressed by a low order polynomial (e.g. [Platt and Stutz, 2008] or [Rozanov and Rozanov, 2010]). The so called differential signal resulting from structures in the solar irradiance, (trace) gas absorption (chapter 6.3.2) and the Ring effect (chapter 7.4.4) convoluted channel-wise with the $f_c(\lambda)$, is then in the range of some 10^{-2} and $10^{-4} - 10^{-5}$, where the lower limit 10^{-5} is often given by the photon and instrumental noise. By using a Monte Carlo RTM in a standard way it is, due to inherent noise, unfeasible to obtain radiances at that precision scale in a reasonable computation time.

8.1.1. Ring-Effect and Absorption Corrected Radiances

With the mathematical technique of importance sampling presented in this thesis it is possible to obtain a spectrum containing only the differential structures (as a function of the atmospheric state) attributed to RRS and absorption with a feasible relative accuracy. The absolute accuracy of these simulated differential structures is then in the range of the differential signal magnitude times the relative accuracy. Using the concept of air mass sensitivities (i.e. so called box air mass factors) the validity of the approach is not surprising. However, for Ring structures it has not been done before. From a mathematical point of view the removal of RRS and absorption structures is based on the modification of Eq. (7.42) by the removal of the transmission due to absorption:

$$w^*_{\text{elb},n} = \exp\left(\tau_{\text{abs},n}\right)w_{\text{elb},n} \tag{8.1}$$

where $\tau_{\text{abs},n}$ is the integrated absorption density, i.e. the optical thickness of absorption, along the nth sub-trajectory. This is also done with the off-splitting of the transmission of one species in Eq. (6.15) from the local estimates in Eq. (6.12), but here it is done for all absorbing gaseous species. Fig. 8.1 shows sun normalized spectra which are normal radiance spectra divided by the solar irradiance spectrum $F_0(\lambda)$. The unit of these normalized spectra is thus sr^{-1}. It is obvious that the DOAS Ansatz of describing the scatterers by a polynomial is well justified (black curve). The structures in the difference spectrum (red curve) result
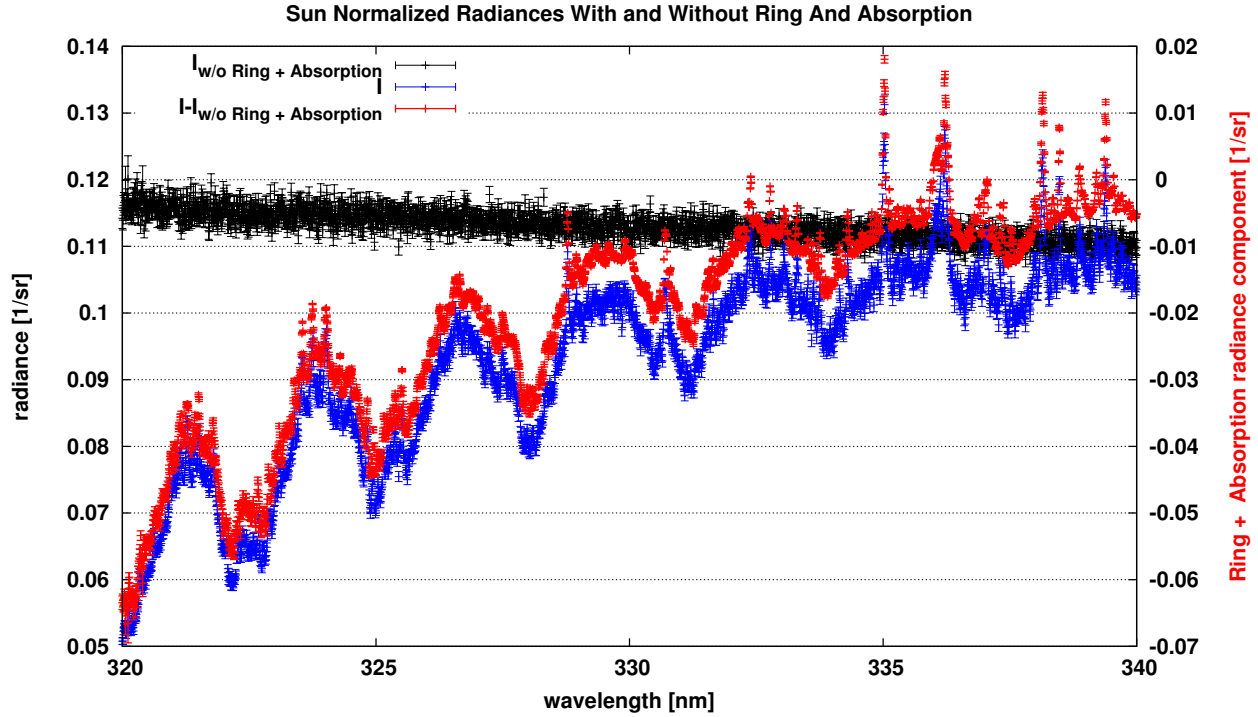
Figure 8.1.: Sun normalized radiance spectrum *I* for the wavelength range 320-340nm in blue. After removing the trace gas absorption and the Ring effect the black curve remains. The substracted spectrum is shown in red.

from O_3 absorption and RRS. In order to test the computational efficiency of the approach the spectral range 390-400nm containing the famous Calcium absorption lines in the solar irradiance spectrum is simulated. On a Intel(R) Core (TM) i5-2410M CPU @ 2.30GHz CPU the calculation of 1000 wavelength takes approximately 8.5 minutes. Fig. 8.2 shows the resulting spectra. The absolute relative accuracy of the differential spectrum is in the order of 10^{-3} to 10^{-4}, but the computation time corresponds to 1% relative accuracy, i.e. the computation time is reduced by a factor of 10^4.

8.1.2. Derivatives of Radiometric Quantities Accessible Through Spectroscopy

Spectra of scattered sun light are used as information sources (the *measurement* or observables) in order to retrieve spatial abundances of atmospheric constituents (the *state*) as for example trace gas or aerosol concentration profiles. In such a retrieval derivatives (in 1st order also called sensitivities) of the measurement with respect to the state are required. 3D Sensitivities (chapter 6.2.2.1) can be used to obtain a visual impression for which spatial regions a spectroscopic measurement is actually sensitive. The availability of 2nd order derivatives (the Hesse matrix) even allows accounting for curvature information in a retrieval and accelerate it therewith. As demonstrated in Chapter 5.2.1 the RTM presented in this work is able to calculate 1st and 2nd order derivatives of radiances with respect to the *optical* state.

8.1.2.1. 1st and 2nd Order Radiance Derivatives

The DOAS analysis yields as a result (observation geometry-relative) light path integrals (so called slant column densities, SCDs). Using the output of the program it is possible to obtain 1st order derivatives of the SCDs with respect to the optical state, which is demonstrated in the following. To give an example, let the trace gas of interest be O_4 and its slant column SCD_{O_4}. From the DOAS analysis the optical thickness of O_4 is known: calculated at one wavelength:

$$\tau_{O_4} = \sigma_{O_4} SCD_{O_4} = \sigma_{O_4} \sum_{c=1}^{N} l_c \cdot [O_4]_c = \sum_{c=1}^{N} l_c \beta_{c,O_4} \tag{8.2}$$
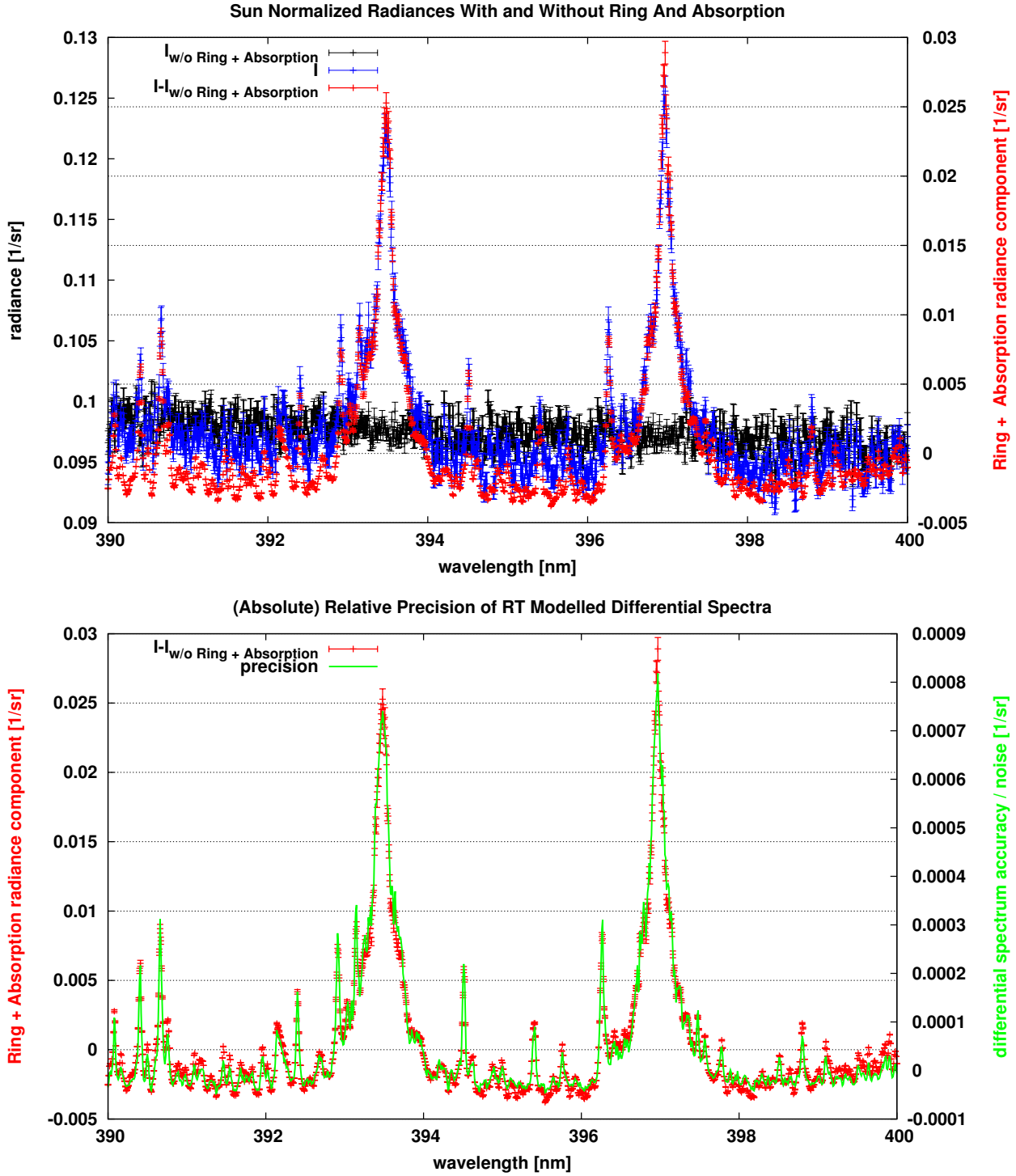
Figure 8.2.: **Top panel:** the Calcium lines in the range 390-400nm. The relative precision of all simulated quantities is ≈1% on their relative scales. The error of the differential spectrum with respect to the Sun normalized radiance is shown in the **bottom panel** in green. The accuracy of the differential structure is at some 10^{-3} to 10^{-4}.

where l_c is the sensitivity, $[O_4]_c$ is the (unknown) number density of O_4 in the cluster c and σ_{O_4} is the (unknown) absorption cross section. Only the product $\beta_{c,O_4} = \sigma_{O_4}[O_4]_c$ is known from dedicated measurements. There are N clusters. l_c can be expressed as:

$$l_c = -\frac{d \log (I)}{d\beta_{c,O_4}} = -\frac{1}{I}\frac{dI}{d\beta_{c,O_4}}. \tag{8.3}$$
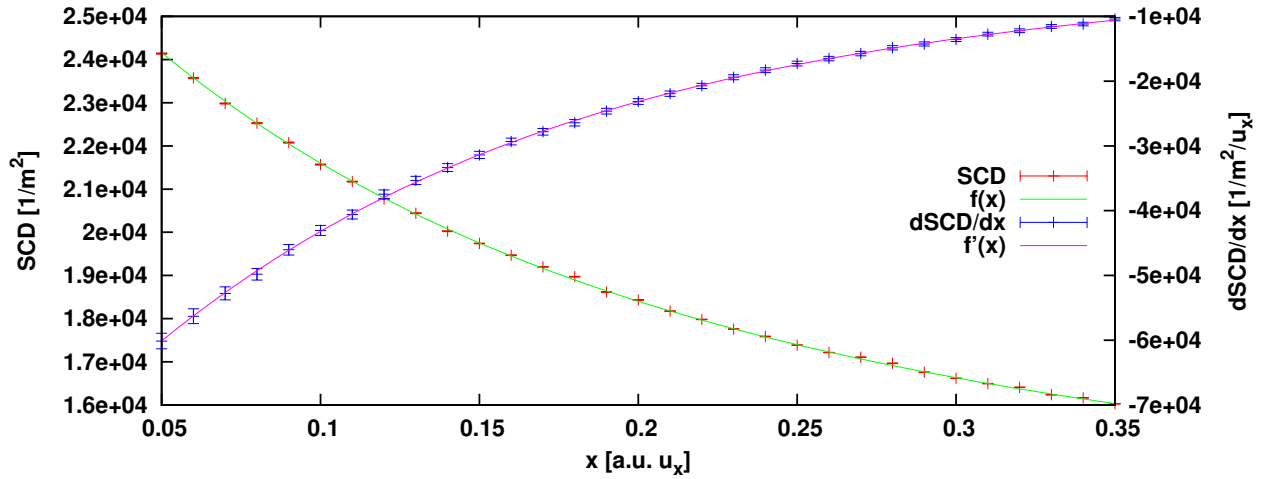
Figure 8.3.: Self-consistence test for the derivative of the SCD of an artificial tracegas with respect to an aerosol optical parameter in an arbitrary cluster.

The 1ˢᵗ derivative of τ_{O_4} with respect an optical property $x_{c'}$ in the cluster c' is:

$$\frac{d\tau_{O_4}}{dx_{c'}} = -\frac{d}{dx_{c'}} \sum_{c=1}^{N} \frac{\beta_{c,O_4}}{I} \frac{dI}{d\beta_{c,O_4}} = \frac{1}{I^2} \sum_{c=1}^{N} \beta_{c,O_4} \left(\frac{dI}{d\beta_{c,O_4}} \frac{dI}{dx_{c'}} - I \frac{d^2 I}{d\beta_{c,O_4} \, dx_{c'}} \right). \tag{8.4}$$

In order to calculate this expression, one needs the radiance I, the 1ˢᵗ order derivatives $dI/d\beta_{c,O_4}$ and $dI/dx_{c'}$ and the 2ⁿᵈ order derivatives (Hesse matrix elements) $d^2I/d\beta_{c,O_4}\,dx_{c'}$. The validation is done with a self consistence test (see for example Fig. 8.3). The method of self consistence tests is described in Chapter 5.3.2 where all radiance derivatives are validated. As concluded in the chapter the derivatives don't show any systematic biases.

8.1.2.2. Inversion and Clusters

The concept of clusters presented in Chapter 4.2.1 allows to obtain 1ˢᵗ and 2ⁿᵈ order radiances derivatives with respect to optical properties in nearly arbitrarily shaped spatial regions and therewith enables designing inversion schemes targeting at concentration profiles on arbitrary spatial sub-divisions. For example, the spatial volume of a volcanic exhaust plume can be sub-divided into slices orthogonal to the local wind speed in order to align slices to the chemical age spatial axis (respectively along wind direction) relative to the crater position (see Fig. 8.4).

8.1.3. Polarization

The third achievement of this work is the inclusion of polarization effects into the model. In a purely molecular atmosphere, the errors induced by the neglect of polarization is easily in the 10^{-2} range of the radiance (see Fig. 5.3). A major obstacle on the way to a realistic simulation is the availability of a physically realistic model of the phase matrices. Using the spherical particle approximation, which is to some extent justified by the orientation averaging of non spherical particle optical properties, results from Mie's theory can be used as a parametrization (chapter 3.2.4) and the modification of the size integration formulas (chapter 3.2.4.4) allow for a calculation of Mie optical properties in the initialization phase of the program. The phase matrices of RRS (chapter 3.2.2.7) allow to simulate the Ring effect in the Stokes vector components. In addition to Mie phase matrices, arbitrary phase matrices can be simulated.

8.1.4. Time Integrated Sensitivities for 3D UV/vis/NIR Remote Sensing

For moving air or space borne platforms such as NASA's Global Hawk or satellite instruments the motion of the spectrometer and the spectrometer integration time requires time integration of the functionals. For non Monte Carlo models this averaging procedure requires time discretisation of the flight track and the
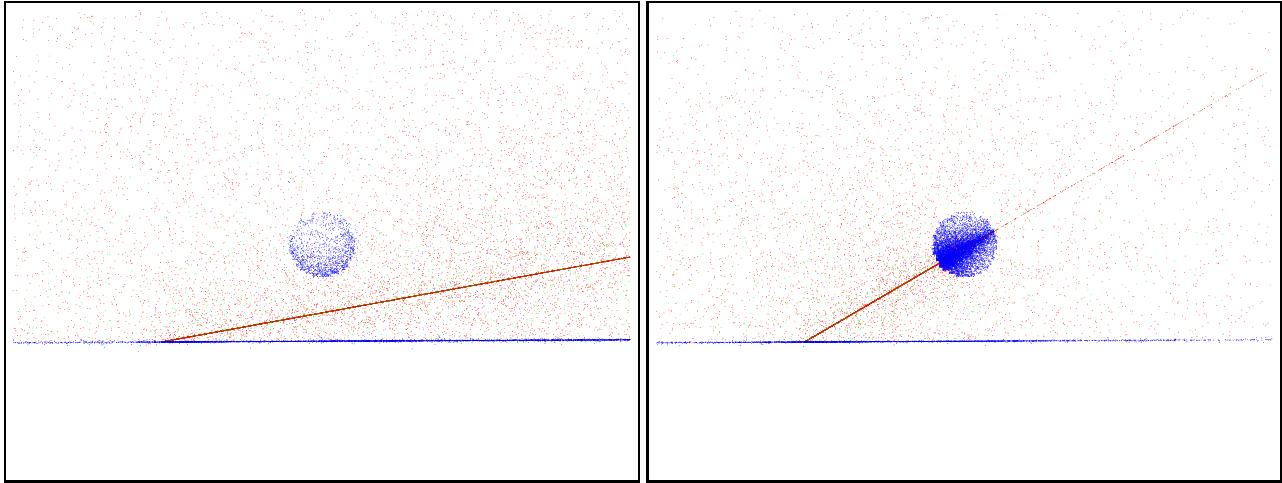
Figure 8.4.: Ray tracing events occurring in the simulated observation of a pure SO_2 plume at 1.5km on a strong absorption line (315nm) in the UV. Blue points are absorption events, red points symbolize molecular scattering. The ground has an albedo of 0.04 and comprises of the blue points at the bottom of the scene. **Left:** observation with elevation angle 10°, **right:** detector pointing at the plume directly with an elevation angle 30°. McArtim configuration with courtesy of Peter Lübcke.

associated observation geometries and subsequent integration of the respective functionals. For a Monte Carlo code integrals are trivial to obtain. One only has to take samples of time points within the integration time frame and take them as estimates of the whole integral.

8.1.4.1. 3D Sensitivities

Results from such a time integration are shown in Fig. 8.5 for a Global Hawk flight SF2 in 2013. The plot shows time integrated / averaged 3D sensitivities respectively integrated over longitude, colatitude or altitude cell indices, i.e. 2D sensitivites in principle. The potential of these depictions lies in the identification of spatial regions for which the measurement is most sensitive and the resulting clustering allows therewith for improving the residuals of 3D inversion schemes.
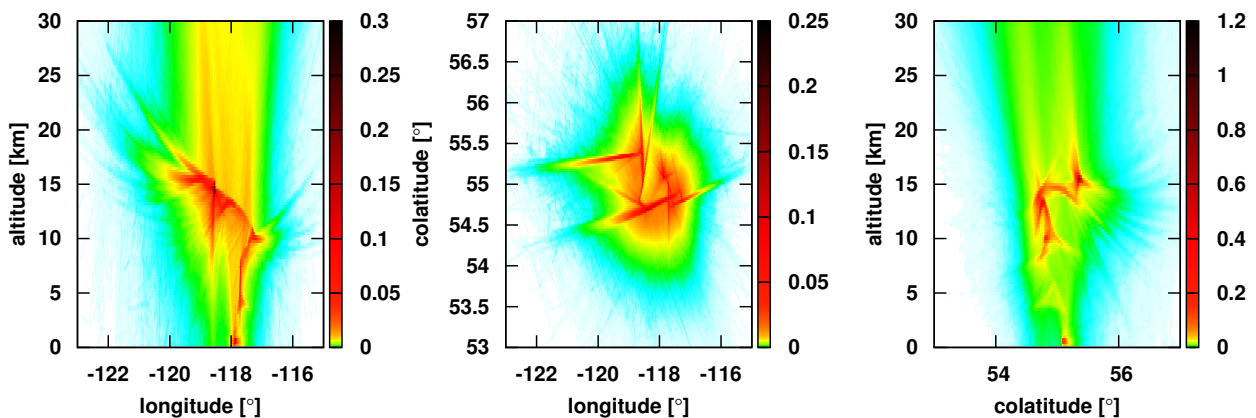
Figure 8.5.: Altitude, longitude and colatitude projections of 3D sensitivities in a pure Rayleigh scattering atmosphere for NASA Global Hawk flight 2013 SF2 integrated over 1 hour of trajectory data. 3D sensitivities are intensity weighted cellular light paths or derivatives of the intensity with respect to the absorption coefficient in the cell. Long straight flight passages cause spot-like FOV footprints in the 3D sensitivity. Wavelength 350nm, surface albedo 0.4.

8.1.4.2. 3D Scatter Event Visualisation

For debugging and visualisation purposes the program 'PathViewer' was designed. Events occuring during the raytracing procedure are shown in different colors, see Fig. 8.6 for details. The 'eps' output of the program can be used as a basis for discussions of radiation effects and allows the user to develop an intuitive understanding of the 3D UV/vis/NIR radiation physics.
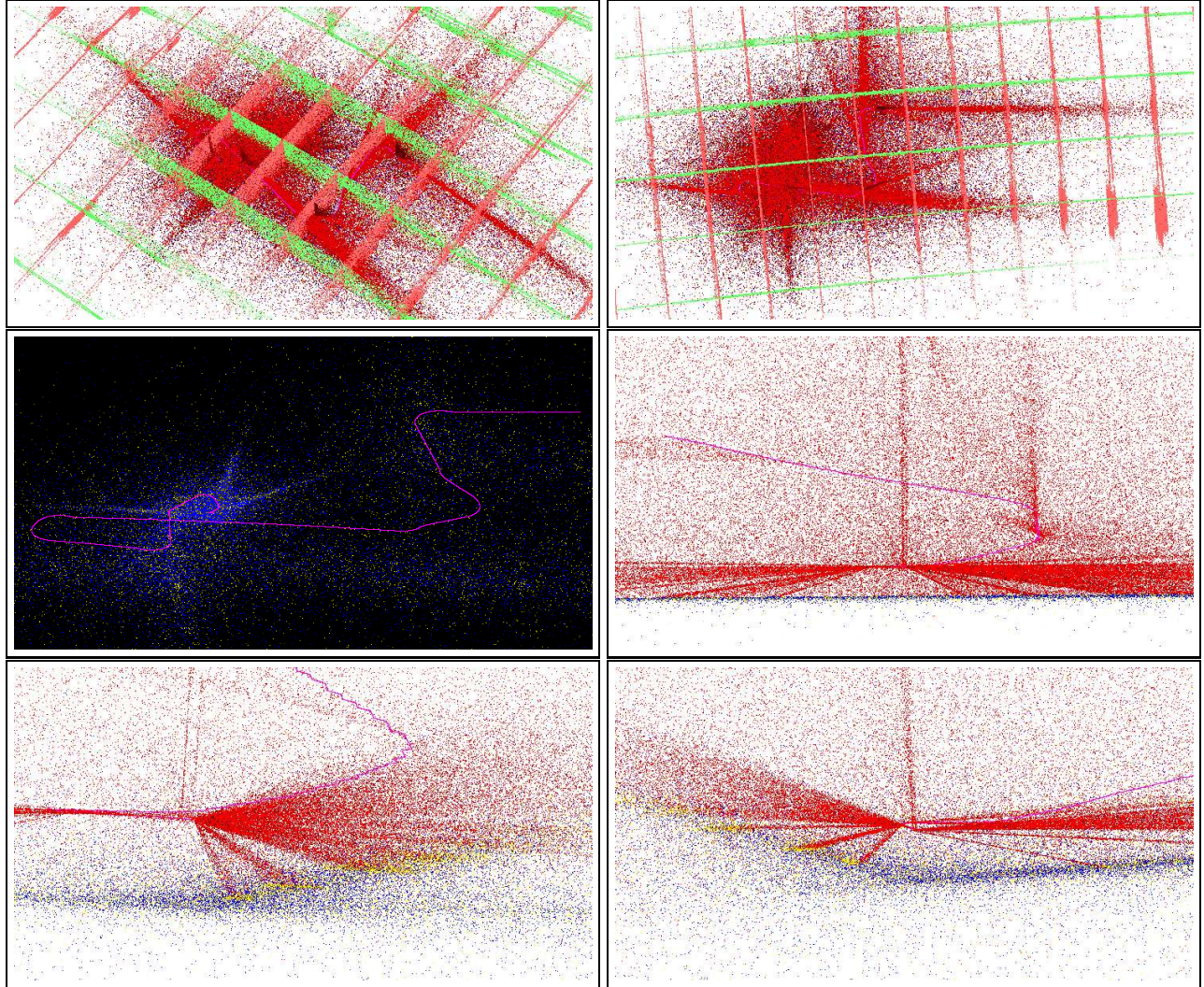
Figure 8.6.: Screenshots of the Global Hawk 2013 flight SF2 created with the 'PathViewer' debugging and 3D visualisation tool (compare to Fig. 8.5). The panels on top show Rayleigh scatter events in dark red and ray intersection points with longitude (light red) and colatitude (light green) grid edges. Absorption events are blue and ground scatter event are yellow. The right panel in the middle row shows the flight track in purple. In the lowermost panels Rayleigh scatter events within the FOV for different limb angles can be identified. The associated elevation angles relative to the plane are 90°, 1°, 0°, -0.5°, -1°,-1.5°, -2°, -2.5°,-3°, -4°,-7° and -15°.

8.2. Outlook

In order to to accurately simulate radiation transport modeling in the UV/vis/NIR spectral range attention must be paid to all optically relevant elements of the atmosphere. This thesis focusses on the accurate simulation of differential spectral structures in the 10^{-2} to 10^{-4} range of scattered sun light spectra originating from narrow band absorption structures and the effect of rotational Raman scattering. It is now possible to simulate these differential structures in a reasonable computation time. These modeling capabilities offer several new ways of directly evaluating scattered sun light spectra. In the mathematical frame work of the radiative

transfer equation a significant amount of physics is now contained in the model. In the course of directly fitting this known physics to reality, more emphasis has to be put on advanced instrument characterization (especially on measuring the slit function) in order to distinguish atmospheric properties from instrumental effects in the spectra. A spectral retrieval replacing the conventional "DOAS + subsequent RTM" combination has to be written and its applicability for automated procession of data has to be investigated.

Further, more physics needs to be included into the model in future:

- **Vibrational Raman scattering in air and in the ocean**. More then two third of Earth's surface is covered with ocean. Vibrational Raman scattering on water molecules form a significant spectral obstacle on the way to residuals smaller then 10^{-3}.

- **Simulation of optical anistropy.** Cirrus and thunderstorm clouds contain in the uppermost regions of the cloud ice crystals. The particles are oriented and their optical properties depend on such orientation. As a consequence, all optical properties in the RTE become dependent on the direction.

- **Implementation of the BRDF for different surface types.** Due to the availability of more a sophisticated optical representation of the surface the implementation of the BRDF (**B**idirectional **R**eflectance **D**istribution **F**unction) allows for more realistic simulations of the lowermost atmospheric layer.

- **Refraction.** In the model a fast and accurate method of the simulation of atmospheric refraction is still missing.

- **Thermal IR.** In the infrared spectral range the thermal emission of gaseous absorber become significant and must be simulated. In the Monte Carlo frame work the simulation of emission is achieved by considering the absorption events and treat them as emission events.

- **Adaptive variance reduction techniques.** If for example optically thick clouds are simulated, the models computation time dramatically increases. New adaptive ways of reducing the variance need to be found and implemented.

There is no doubt that future computer architectures are parallel, therefore all these additional capabilities and refinements will likely be implemented for such an architecture.

A

Monte Carlo Sampling

A.1. Zero Variance Estimates

$$I = \int_a^b f(x)\,dx = \int_a^b h(x)p(x)\,dx \quad \text{with} \quad h(x) = \frac{f(x)}{p(x)} \tag{A.1}$$

The question is, which quadrature of $[a,b]$ represents the most efficient Monte Carlo algorithm. Or in other words: How can $p(x)$ be chosen in order to minimise the variance of the estimates? John Kahn [Kahn, 1950] proved about 1950, that

$$\hat{p}(x) = \frac{|f(x)|}{\int_a^b |f(x)|\,dx} \tag{A.2}$$

is the best choice to achieve this. This can be proven as follows. In order to minimise the variance one can use the Lagrange multiplier λ for the normalisation condition $\int_a^b p(x)\,dx = 1$ and minimise the function

$$\xi = \text{var}(\langle h(x) \rangle) + \lambda \left(\int_a^b p(x)\,dx - 1 \right). \tag{A.3}$$

$$\delta_p \xi = \delta_p \left\{ \langle (h(x))^2 \rangle - \langle h(x) \rangle^2 + \lambda \left(\int_a^b p(x)\,dx - 1 \right) \right\} \tag{A.4}$$

$$\overset{\delta_p \langle h(x) \rangle = 0}{=} \delta_p \int_a^b (h(x))^2 p(x)\,dx + \delta_p \lambda \int_a^b p(x)\,dx \tag{A.5}$$

$$= -\int_a^b (h(x))^2\,dx + \lambda \int_a^b dx \tag{A.6}$$

$$= \int_a^b \left[\lambda - \left(\frac{f(x)}{p(x)} \right)^2 \right] \overset{!}{=} 0. \tag{A.7}$$

Thus $\hat{p}(x) = \lambda^{-\frac{1}{2}} |f(x)|$ and the normalisation yields $\lambda^{-\frac{1}{2}} = \left(\int_a^b |f(x)|\,dx \right)^{-1}$. For the variance of estimates drawn from $\hat{p}(x)$ zero is obtained.

A.2. Free Path Length Sampling in a Homogeneous Medium

Suppose that the medium in which the transport takes place is homogeneous with extinction ε and unbounded. The free path length pdf is then

$$p_{\text{fpl}}(l) = \varepsilon \exp{(-\varepsilon l)} \tag{A.8}$$

with respect to any point and any direction in the medium. $p_{\text{fpl}}(l)$ is normalized

$$\int_0^\infty p_{\text{fpl}}(l)\,dl = -\varepsilon \left[\frac{1}{\varepsilon} \exp{(-\varepsilon l)} \right]_0^\infty = 1 \tag{A.9}$$

and has the expectation of the free path length

$$\int_0^\infty l\, p_{\text{fpl}}(l)\,dl = \varepsilon \int_0^\infty l \exp{(-\varepsilon l)}\,dl = -\varepsilon \frac{\partial}{\partial \varepsilon} \int_0^\infty \exp{(-\varepsilon l)}\,dl = \frac{1}{\varepsilon}. \tag{A.10}$$

In such a medium, a path length sample is obtained by application of the ITS method. The CDF of the free path length is

$$P_{\text{fpl}}(l) = \int_0^l p_{\text{fpl}}(l)\,dl = 1 - \exp{(-\varepsilon l)} \tag{A.11}$$

and path length samples are accordingly obtained with

$$l(\alpha) = -\frac{1}{\varepsilon} \log{(1 - \alpha)}. \tag{A.12}$$

A.3. Cumulative Differential Scatter Cross Sections

A.3.1. Cardanic formulas

For Rayleigh and Rotational Raman phase functions, one has to solve the cubic equation

$$ax^3 + bx^2 + cx + d = 0 \tag{A.13}$$

for x. The substitution $u = x + \frac{b}{3a}$

$$p = \frac{3ac - b^2}{3a^2} \tag{A.14}$$

$$q = \frac{2b^3}{27a^3} - \frac{bc}{3a^2} + \frac{d}{a} \tag{A.15}$$

yields the simplier form

$$u^3 + pu + q = 0. \tag{A.16}$$

Define the discriminant

$$D = \left(\frac{q}{2}\right)^2 + \left(\frac{p}{3}\right)^3 \tag{A.17}$$

There are three cases for solutions u_i now, from which x_i can be determined by backsubstitution

$$x = u - \frac{b}{3a} \tag{A.18}$$

The only important case for this work is $D > 0$. Define:

$$D_1 = \sqrt[3]{-\frac{q}{2} + \sqrt{\left(\frac{q}{2}\right)^2 + \left(\frac{p}{3}\right)^3}} \tag{A.19}$$

$$D_2 = \sqrt[3]{-\frac{q}{2} - \sqrt{\left(\frac{q}{2}\right)^2 + \left(\frac{p}{3}\right)^3}} \tag{A.20}$$

The solution for x is:

$$x = D_1 + D_2 - \frac{b}{3a} \tag{A.21}$$

source: `http://de.wikipedia.org/wiki/Cardanische_Formeln`

A.3.2. Rayleigh and Raman Phase Functions

phase function	formula	$z_1(\alpha)$	z_2
Rayleigh phase function with isotropic polarizability	$p(\mu) = \frac{3}{4}(1+\mu^2)$	$2 - 4\alpha$	1
rotational raman phase function	$p(\mu) = \frac{3}{40}(13+\mu^2)$	$20 - 40\alpha$	13
Rayleigh phase function with anisotropic polarizability[Goody and Yung, 1989]	$p(\mu) = y_1 + y_2\mu^2$	$\frac{\frac{3}{2}-3\alpha}{y_2}$	$\frac{y_1}{y_2}$

The cosine of the scatter angle ϑ is calculated with the primitive inverse parameter according to the table above and a random number $\alpha \in [0,1]$ by

$$\mu = \sqrt[3]{a(\alpha) - z_1(\alpha)} - \sqrt[3]{a(\alpha) + z_1(\alpha)} \quad \text{with} \quad a(\alpha) = \sqrt{z_1^2(\alpha) + z_2^3} \tag{A.22}$$

For the anisotropic Rayleigh phase function after [Goody and Yung, 1989] the parameters y_i are

$$y_{1/2} = \frac{3(1 \pm \rho(\lambda))}{2(2 + \rho(\lambda))} \tag{A.23}$$

where $\rho(\lambda)$ is the wavelength depolarisation correction parameter

$$\rho(\lambda) = 6\frac{F_\lambda - 1}{3 + 7F_\lambda} \tag{A.24}$$

with the King correction factor F_λ according to [Bates, 1984]:

$$F_\lambda = 1.0367 + 5.381 \cdot 10^{-12} v_{\text{vac}}^2 + 0.304 \cdot 10^{-20} v_{\text{vac}}^4 \tag{A.25}$$

$$v_{\text{vac}} = 10^{-2} \cdot \lambda^{-1} \tag{A.26}$$

A.3.3. Henyey Greenstein Model

A simplification of aerosol phase functions is the Henyey Greenstein model. Originally invented for astronomical radiative transfer problems[Henyey and Greenstein, 1941] it is now widely used in other disciplines as in atmospheric RT. The phase function is

$$P(\mu) = \frac{1 - g^2}{(1 - g(2\mu - g))^{\frac{3}{2}}} \tag{A.27}$$

n	$P_n(x)$	$\int P_n(x)$
0	1	x
1	x	$\frac{1}{2}x^2$
2	$\frac{1}{2}(3x^2 - 1)$	$\frac{1}{2}(x^3 - x)$
3	$\frac{1}{2}(5x^3 - 3x)$	$\frac{1}{2}(\frac{5}{4}x^4 - \frac{3}{2}x^2)$
4	$\frac{1}{8}(35x^4 - 30x^2 + 3)$	$\frac{1}{8}(7x^5 - 10x^3 + 3x)$
5	$\frac{1}{8}(63x^5 - 70x^3 + 15x)$	$\frac{1}{8}(\frac{63}{6}x^6 - \frac{70}{4}x^4 + \frac{15}{2}x^2)$

Table A.1.: Legendre polynomials and integrals of Legendre polynomials.

The asymmetry parameter is defined as the first moment of the phase function to be approximated:

$$g = \langle \mu \rangle = \frac{1}{2} \int_{-1}^{+1} \mu P(\mu) \, d\mu \tag{A.28}$$

the factor $\frac{1}{2}$ comes from the phase function normalization, which is usually 2. Scatter angles for Henyey-Greenstein type scatter events can be sampled from

$$\mu = \frac{1 + g^2 - \left(\frac{1-g^2}{1+g(2\alpha-1)} \right)^2}{2g} \tag{A.29}$$

A.3.4. Legendre Polynomial Phase Function Model

Legendre polynomials are a system of orthogonal functions. They can be obtained by the formula of Rodrigues:

$$P_n(x) = \frac{1}{2^n n!} \frac{d^n}{dx^n} (x^2 - 1)^n. \tag{A.30}$$

Alternatively and for practical purposes the following "three term recurrence relation" can be used to construct Legendre polynomials:

$$P_{n+1}(x) = \frac{2n+1}{n+1} x P_n(x) - \frac{n}{n+1} P_{n-1}(x) \tag{A.31}$$

To deduce the integral of a Legendre polynomial using $P_{n-1}(x)$ and $P_n(x)$ the following relation is transformed

$$(2n+1)P_n(x) = \frac{d}{dx}(P_{n+1}(x) - P_{n-1}(x)) \tag{A.32}$$

$$= \frac{d}{dx}\left(\frac{2n+1}{n+1} x P_n(x) - \frac{n}{n+1} P_{n-1}(x) - P_{n-1}(x) \right) \tag{A.33}$$

$$= \frac{1}{n+1} \frac{d}{dx}((2n+1)x P_n(x) - (2n+1)P_{n-1}(x)) \tag{A.34}$$

to obtain

$$\int P_n(x) = \frac{1}{n+1}(x P_n(x) - P_{n-1}(x)). \tag{A.35}$$

The first Legendre polynomials and integrals are listed in table A.1. A phase function can be expressed in terms of Legendre polynomials

$$P(\mu) = \sum_{n=0}^{N} c_n P_n(\mu). \tag{A.36}$$

For $P(\mu)$ in (A.36) to describe a phase function, one must require

$$P(\mu \in [-1,1]) \geq 0 \quad \text{and} \quad \int_{-1}^{+1} P(\mu) \, d\mu = 2 \tag{A.37}$$

The norm of $P(\mu)$ for arbitrary coefficients is given by

$$C = \int_{-1}^{+1} P(\mu) \, d\mu = \sum_{n=0}^{N} c_n \int_{-1}^{+1} P_n(\mu) \, d\mu \tag{A.38}$$

$$= \sum_{n=0}^{N} \frac{c_n}{n+1} \left[\mu P_n(\mu) - P_{n-1}(\mu) \right]_{-1}^{+1} \tag{A.39}$$

$$= 2c_0 \tag{A.40}$$

since $P_n(1) = 1$ and $P_n(-1) = (-1)^n$. This means, if $P(\mu) \geq 0$ and $c_0 = 1$, $P(\mu)$ is a valid phase function. Unfortunately, the inverse of the cumulative phase function is not given explicitly. So to use $P(\mu)$ in McArtim a quadrature $\{\mu_i\}_{i \in \{1,\cdots,R\}}$ of $[-1,1]$ with a resolution of R has to be found, such that

$$F(\mu_i) := \int_{-1}^{\mu_i} P(\mu) \, d\mu = \frac{2i+1}{R} =: 2\alpha_i \tag{A.41}$$

which approximates $F(\mu) = 2\alpha$. To find the root $\tilde{x} = \mu_i$ of the function $F(x) - 2\alpha_i$ the Newton method is used:

$$x_{j+1} = x_j - \frac{F(x_j) - 2\alpha_i}{P(x_j)}. \tag{A.42}$$

The resulting quadrature $\{\mu_i\}$ can be used by sampling a random number α and selecting an μ-estimate by

$$\mu \approx \mu_i \quad \text{with} \quad i = \text{ceil}(\alpha R), \tag{A.43}$$

where the $\text{ceil}(x)$ function yields the smallest integer greater then or equal to x. This estimate can be refined by linearisation of the cumulative phase function around the estimate:

$$\mu = \mu_i + \frac{2\alpha - F(\mu_i)}{P(\mu_i)} \tag{A.44}$$

A.3.5. Table Methods

The most flexible way to define phase functions is by using tables. In McArtim there are three types of tabulated phase fuctions. The first type is to provide a phase function in form of a linearly interpolated polygon by defining N pairs of $(\mu_i, U_i = U(\mu_i))$ with $\mu_1 = -1$ and $\mu_N = 1$. It is not neccessary that the function is normalised. The norm of the arbitrary user function is:

$$C = \sum_{i=1}^{N-1} \underbrace{\frac{1}{2}(\mu_{i+1} - \mu_i)(U_{i+1} + U_i)}_{=:b_i(U)} = \sum_{i=1}^{N-1} b_i(U), \tag{A.45}$$

where normalised phase function is

$$P_i = \frac{2}{C} U_i. \tag{A.46}$$

By a random number α an estimate of the cosine of the scatter angle is given by $\mu \in [\mu_j, \mu_{j+1}]$ with j according to:

$$F_j := \sum_{i=1}^{j} b_j(P) < 2\alpha < \sum_{i=1}^{j+1} b_j(P) =: F_{j+1}. \tag{A.47}$$

In the interval $[\mu_j, \mu_{j+1}]$ the phase function is

$$P(\mu) = (\mu - \mu_j) \underbrace{\frac{P_{j+1} - P_j}{\mu_{j+1} - \mu_j}}_{=:m_j} + P_j \tag{A.48}$$

and the cumulative phase function is

$$F(\mu \in [\mu_j, \mu_{j+1}]) = \int_{-1}^{\mu} P(\mu')\,d\mu' = \frac{1}{2}m_j(\mu - \mu_j)^2 + P_j(\mu - \mu_j) + F_j(P) \tag{A.49}$$

Consequently, the cosine of the scatter angle is given by $F_j(\mu) = 2\alpha$:

$$\mu = \mu_j + \frac{1}{m_j}\left(\pm\sqrt{2m_j(2\alpha - F_j) + P_j^2} - P_j\right) \tag{A.50}$$

where only the solution in $[\mu_j, \mu_{j+1}]$ is selected. Fig. A.1 shows a linearely interpolated phase functions and samples of the μ drawn with the method described above. The method is quite fast because m_j, and F_j may be precalculated table form. The other possibility of
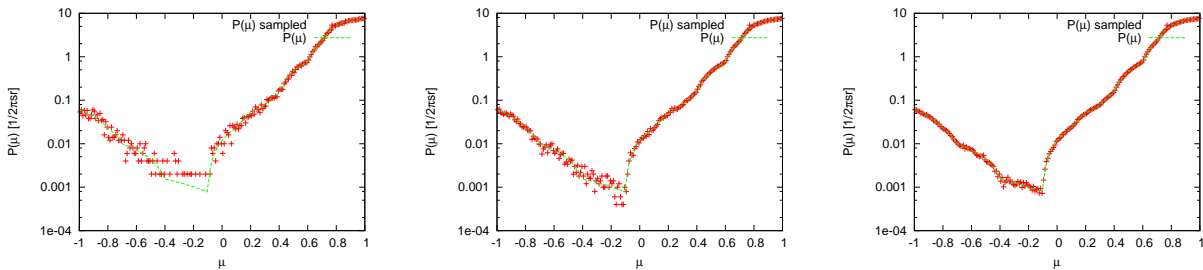
Figure A.1.: Example of a linearely interpolated phase function. For (left to right) 10^5, 10^6 and 10^7 samples.

phase function specification is to provide the quadrature $\mu(\alpha)$ of the phase function directly. The phase function itself can be obtained by numerical inversion and differentiation, similar as described above.

A.4. Greens Function in the Derivation of the IRTE

Without loss of generality only a certain direction $\vec{\omega}$ involving a certain path $\vec{r}(x) = \vec{r}' + (x - x')\vec{\omega}$ from $\vec{r}$ to the boundary of the medium at $x = b$ into direction $\vec{\omega}$ is considered. For the operator L one chooses:

$$L_x = 1 + \frac{1}{\alpha(x)}\frac{d}{dx}. \tag{A.51}$$

The extinction coeffcient $\varepsilon(\vec{r})$ has been replaced by $\alpha(x)$. The problem is of the simple form

$$L_x f(x) = u(x), \tag{A.52}$$

where $f(x)$ is the radiance and $u(x)$ is the right side of the 4.57. The Green's function of (A.52) can be found by assuming

$$f(x) = \int_a^b k(x, x')u(x')\,dx' \tag{A.53}$$

for the solution $f(x)$, where $x = a$ is the position of the boundary along $-\vec{\omega}$. Applying L_x to Eq. (A.53) yields:

$$L_x f(x) = L_x \int_a^b k(x, x')u(x')\,dx' = \int_a^b L_x k(x, x')u(x')\,dx' = u(x) \tag{A.54}$$

This implies:

$$L_x k(x, x') = k(x, x') + \frac{1}{\alpha(x)}\frac{d}{dx}k(x, x') = \delta(x - x') \tag{A.55}$$

or

$$\alpha(x)k(x, x') + \frac{d}{dx}k(x, x') = \alpha(x)\delta(x - x'). \tag{A.56}$$

For $x \neq x'$, the right side is zero and therefore

$$k(x \neq x', x') = c(x \neq x')\exp\left(-\int_{x'}^x \alpha(t)|dt|\right), \tag{A.57}$$

where $c(x \neq x')$ is a constant in both regions $x < x'$ and $x > x'$ where the solution is expected to be continous. The δ function in the integral form of (A.56) implies, that $k(x, x')$ makes a jump of $\alpha(x')$. Therefore a step function in c is found, $c(x \neq x') = \alpha(x')\Theta(x - x')$ and hence for $G(x, x')$ (compare to Fig. A.2)

$$k(x, x') = \alpha(x')\Theta(x - x')\exp\left(-\int_{x'}^x \alpha(t)dt\right). \tag{A.58}$$

A.5. Source Code For Stokes Vector Transformation Plot

The following three octave functions generate tex code for Fig. 3.1. The required LATEXpackages are `pstricks`, `pstricks-add`, `pst-3dplot`, `pst-plot` and `pst-tools`.
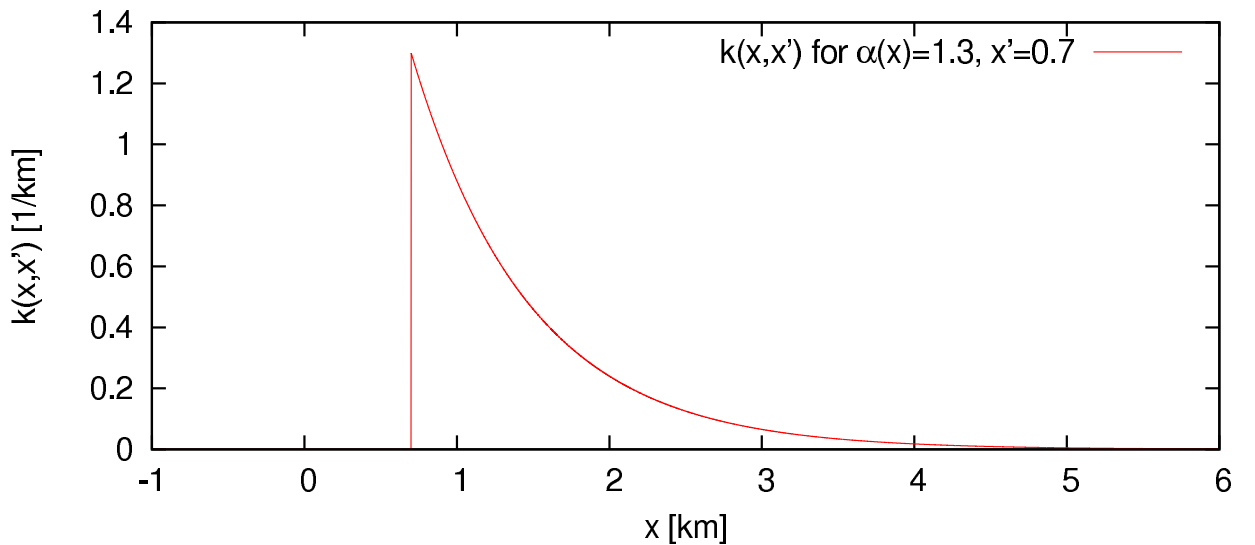
Figure A.2.: Example of a Green's Function for a medium with $\alpha = 1.3$ and $x' = 0.7$

A.5. Source Code For Stokes Vector Transformation Plot

Listing A.1: createPSPictureInput.m

```
1  function createPSPictureInput(phi_in_D, theta_in_D, phi_out_D, theta_out_D)
2
3    addpath('retrieval/clouds/octave/3D/');
4
5    % correction of angles
6
7    f = pi / 180 ;
8
9    phi_in = phi_in_D * f ;
10   theta_in = theta_in_D * f ;
11   phi_out = phi_out_D * f ;
12   theta_out = theta_out_D * f ;
13
14   % calculate k_in, k_out, k_sp
15   k_in = create3DVectorFromPolar(theta_in, phi_in);
16   k_out = create3DVectorFromPolar(theta_out, phi_out);
17
18   k_sp = vectorProduct3D( k_in, k_out );
19
20   printPSScatteringPlane(k_sp, 'red');
21   printPSVector('inc', 'blue', phi_in_D, theta_in_D, 3);
22   printPSVector('sca', 'green', phi_out_D, theta_out_D, 3);
23
24   % calculate spherical angles
25   mu_s=k_in'*k_out;
26
27   cos_theta_in=cos(theta_in);
28   sin_theta_in=sin(theta_in);
29   cos_theta_out=cos(theta_out);
30   sin_theta_out=sin(theta_out);
31   sdp=sin(phi_out-phi_in);
32
33   % NOTE: I ommit division through sin(theta_s) due
34   % to the later use of atan2
35
36   c_in=(cos_theta_out-cos_theta_in*mu_s)/sin_theta_in;
37   s_in=sdp*sin_theta_out;
38   c_out=(cos_theta_in-cos_theta_out*mu_s)/sin_theta_out;
39   s_out=sdp*sin_theta_in;
40
41   % calculate sigmas
42   sigma_in = atan2(s_in, c_in);
43   sigma_out = atan2(s_out, c_out);
44
45   % show angles
46   f = pi / 180;
47   fd = 1 / f;
48   alpha_sp = (20) * f;
49
50   C = [k_in k_out k_sp];
51   R = createZRotationMatrix(-phi_in);
52   R = createYRotationMatrix(0.5*pi-theta_in) * R;
53
54   C_in_z = R * C; % k_in -> x
55   theta_sp = atan2 (sqrt(C(1,3)^2+C(2,3)^2) , C(3,3));
56   Rx = createXRotationMatrix(-theta_sp);
57
58   R = Rx * R;
59   C = Rx * C;
60
61   % draw sigma 1
62   x = cos (alpha_sp) * 3;
63   r = sin (alpha_sp) * 3;
64
65   % label
66   xl = cos (0.5 * alpha_sp) * 3;
67   rl = 0.55 * sin (0.5 * alpha_sp) * 8;
68
69   % sigma_in
70   printf('\\pstThreeDCircle[RotY=%f,RotZ=%f,linestyle=dashed,linecolor=red,beginAngle=0,endAngle=%f]', theta_in_D, phi_in_D, fd * sigma_in);
71   printf('(0,0,%f)(-%f,0, 0)(0,%f,0)\n', x, r, r);
72
73   % sigma_out
74   printf('\\pstThreeDCircle[RotY=%f,RotZ=%f,linestyle=dashed,linecolor=red,beginAngle=0,endAngle=%f]', theta_out_D, phi_out_D, fd * sigma_out);%, fd *
          sigma_out);
75   printf('(0,0,%f)(-%f,0,0)(0,-%f,0)\n', x, r, r);
76
77   % put labels
78   x = -cos(-0.5 * sigma_in) * rl;
79   y = -sin(-0.5 * sigma_in) * rl;
80   printf('\\pstThreeDPut[RotY=%f,RotZ=%f](%f,%f,%f){$i_{\\hbox{\\tiny inc}}$}%%.\n', theta_in_D, phi_in_D, x, y, xl);
81
82   x = -cos(0.5 * sigma_out) * rl;
83   y = -sin(0.5 * sigma_out) * rl;
84   printf('\\pstThreeDPut[RotY=%f,RotZ=%f](%f,%f,%f){$i_{\\hbox{\\tiny sca}}$}%%.\n', theta_out_D, phi_out_D, x, y, xl);
85
86 endfunction
```

Listing A.2: printPSScatteringPlane.m

```
1  function printPSScatteringPlane(k_sp, color)
2
3    fd = 180 / pi ;
4
5    % calculate polar angles
6    phi = fd * atan2 ( k_sp(2), k_sp(1) );
7    theta = fd * atan2 ( sqrt(k_sp(2)^2 + k_sp(1)^2),  k_sp(3));
8
9    printf('\\pstThreeDLine[RotY=%.1f,RotZ=%.1f,arrows=->,linewidth=2pt,linecolor=red](0,0,0)(0,0,5)\n', theta, phi);
10   printf('\\pstThreeDPut[RotY=%.1f,RotZ=%.1f](0,0,5.6){$\\vec{k}_{\\hbox{\\tiny sp}}$}\n', theta, phi);
11
12   printf('\\pstThreeDCircle[RotY=%f,RotZ=%f,dotsep=1pt,linestyle=dotted,linecolor=%s,beginAngle=0,endAngle=360](0,0,0)(3,0,0)(0,3,0)\n', theta, phi, color)
        ;
13
14 endfunction
```

Listing A.3: printPSVector.m

```
1  function printPSVector(name, color, phi_D, theta_D, r)
2    printf('\\pstThreeDLine[RotY=%.1f,RotZ=%.1f,arrows=->,linewidth=2pt,linecolor=%s](0,0,0)(0,0,5)\n', theta_D, phi_D, color);
3    printf('\\pstThreeDPut[RotY=%.1f,RotZ=%.1f](0,0,5.6){$\\vec{k}_{\\hbox{\\tiny {%s}}}$}\n', theta_D, phi_D, name);
4    printf('\\pstThreeDLine[RotZ=%.1f,linestyle=dashed,linecolor=%s](0,0,0)(%.1f,0,0)\n', phi_D, color, r);
5    printf('\\pstThreeDCircle[linestyle=dashed,linecolor=%s,beginAngle=0,endAngle=%.1f](0,0,0)(%.1f,0,0)(0,%.1f,0)\n', color, phi_D, r, r);
6    printf('\\pstThreeDCircle[RotZ=%.1f,linestyle=dashed,linecolor=%s,beginAngle=0,endAngle=%.1f](0,0,0)(0,0,%.1f)(%.1f,0,0)\n', phi_D, color, theta_D, r, r)
     ;
7    %printf('\\pstThreeDCircle[RotZ=%.1f,linestyle=dotted](0,0,0)(%.1f,0,0)(0,0,%.1f)\n', phi_D, r, r);
8    printf('\\pstThreeDPut[RotY=%.1f,RotZ=%.1f](0,0,%.1f){$\\vartheta_{\\hbox{\\tiny %s}}$}%%.\n', theta_D/2, phi_D, 0.5*r, name);
9    printf('\\pstThreeDPut[RotZ=%.1f](%.1f,0,0){$\\varphi_{\\hbox{\\tiny %s}}$}%%.\n\n', phi_D/2, 0.8*r, name);
10 endfunction
```

Basic Principle to Obtain Derivative Estimates

Again it is instructive to reduce the problem to calculate derivatives to a case in one dimension:

$$I(y) = \int g(x,y) p(x,y) \, \mathrm{d}x =: \int [gp](x,y) \, \mathrm{d}x. \tag{B.1}$$

The integral is carried out over x and both kernel p and scoring function g depend on y such that the integral I is a function of y too. Estimates of $I(y)$ are given by evaluating $g(x,y)$ at samples x_n drawn from $p(x,y)$:

$$I(y) \approx g(x_n, y) \quad \text{with} \quad x_n \sim p(x,y) \tag{B.2}$$

In the following it is discussed, how estimates of derivatives $\frac{\partial I}{\partial y}$ are obtained. The key intention is to take $p(x,y)$ samples (in Monte Carlo RT $f^{(\dagger)}$ samples) as estimates for the derivative kernels and correct for the error with the appropriate importance sampling weight. Thus, in the derivative estimate formulas samples x_n are always taken from $p(x,y)$

$$x_n \sim p(x,y). \tag{B.3}$$

In order to stay clear about the reduction of complexity, analogous expressions are listed in the following table:

1D example (chapter B)	RT
$g(x)$	$\Psi(\vec{x})$ resp. $\Psi^{\dagger}(\vec{x}) = \varphi(\vec{x})$
$p(x)$	$f^{(\dagger)} = \Psi^{(\dagger)}(\vec{x}_0) \sum\limits_{n=1}^{\cdots} k^{(\dagger)}[\vec{x}_{n-1} \to \vec{x}_n]$

In chapter B, the basic derivative estimation principle is discussed in reduced complexity (1D). In chapter 5.2.1, these principles are applied to radiance derivative estimation.

B.1. 1st Order Derivatives

The y derivative is applied to the right side of Eq. (B.1)

$$\frac{\partial I}{\partial y} = \frac{\partial}{\partial y} \int [gp](x,y) \, \mathrm{d}x = \int [g'p + gp'](x,y) \, \mathrm{d}x \tag{B.4}$$

where the prime denotes taking the derivative with respect to y. Estimates of the first part of Eq. (B.4) (i.e. $\int [g'p](x,y) \, \mathrm{d}x$) are readily obtained by evaluating Eq. (B.2) analogously with the scoring function g'. The second part $\int [gp'](x,y) \, \mathrm{d}x$ is evaluated with the importance sampling technique by taking $p(x,y)$ samples and correct for the difference with respect to the kernel $p'(x,y)$ with the corresponding weight $\frac{p'}{p}$:

$$\frac{\partial I}{\partial y} \approx g'(x_n, y) + g(x_n, y) \frac{p'(x_n, y)}{p(x_n, y)}. \tag{B.5}$$

At this point an important relationship is shown. The importance sampling weight for the kernel derivative p' is equal to its logarithmic derivative:

$$\frac{\partial}{\partial y} \log\left(p(x,y)\right) = \frac{p'(x,y)}{p(x,y)}. \tag{B.6}$$

This fact is important, since logarithms of the RT (transport) kernels assume mathematically simple forms.

B.2. 2nd Order Derivatives

In order to evaluate 2nd order derivatives, $\frac{\partial^2}{\partial y^2}$ is applied to the right side of Eq. (B.1):

$$\frac{\partial^2 I}{\partial y^2} = \int [g''p + 2g'p' + gp''](x,y) \, \mathrm{d}x \tag{B.7}$$

The first two summands are

$$\int [g''p](x,y)\,\mathrm{d}x \approx g''(x_n,y) \tag{B.8}$$

and

$$\int [g'p'](x,y)\,\mathrm{d}x \approx \left[g'\frac{p'}{p}\right](x_n,y). \tag{B.9}$$

For the 2nd derivatives of the kernel p, the following identities are usefull:

$$\left(\frac{p'}{p}\right)' = \frac{pp'' - p'p'}{p^2} \tag{B.10}$$

$$\frac{p''}{p} = \left(\frac{p'}{p}\right)^2 + \left(\frac{p'}{p}\right)'. \tag{B.11}$$

Inserting the importance sampling weight Eq. (B.11) in the estimate for the third summand of Eq. (B.7) yields

$$\int [gp''](x,y)\,\mathrm{d}x \quad \approx \quad \left[g\frac{p''}{p}\right](x_n,y) \tag{B.12}$$

$$\overset{\text{Eq. (B.11)}}{=} \left[g\left(\left(\frac{p'}{p}\right)^2 + \left(\frac{p'}{p}\right)'\right)\right](x_n,y). \tag{B.13}$$

In total, 2nd order derivative estimates are:

$$\frac{\partial^2}{\partial y^2}I(y) \approx \left[g'' + 2g'\frac{p'}{p} + g\left(\left(\frac{p'}{p}\right)^2 + \left(\frac{p'}{p}\right)'\right)\right](x_n,y). \tag{B.14}$$

As aforementioned, the expressions $\frac{p'}{p} = \log(p)'$ are well known quantities, for which derivatives can also be calculated easily. Therewith the 2nd order derivative estimates are

$$\frac{\partial^2}{\partial y^2}I(y) \approx g'' + 2g'\log'(p) + g\left((\log'(p))^2 + (\log'(p))'\right). \tag{B.15}$$

B.3. Hessian of Integrals Depending on Many Variables

Eq. (B.1) is modified as follows:

$$I(y_i, y_j) = \int [gp](x, y_i, y_j)\,\mathrm{d}x \tag{B.16}$$

It is introduced the following notation for derivatives:

$$\partial_i h(y_i, y_j) := \frac{\partial}{\partial y_i}h(y_i, y_j) \tag{B.17}$$

and

$$\partial_{ij}^2 h(y_i, y_j) := \frac{\partial^2}{\partial y_i \partial y_j}h(y_i, y_j). \tag{B.18}$$

1st derivatives are estimated accordings to Eq. (B.5). The Hessian is formally:

$$\partial_{ij}^2 I(y_i, y_j) = \int [\partial_{ij}^2 gp + \partial_j g\partial_i p + \partial_i g\partial_j p + g\partial_{ij}^2 p](x, y_i, y_j)\,\mathrm{d}x \tag{B.19}$$

Similiary as in Eq. (B.11) one obtains the identity

$$\frac{\partial_{ij}^2 p}{p} = \partial_i \left(\frac{\partial_j p}{p}\right) + \left(\frac{\partial_i p}{p}\right)\left(\frac{\partial_j p}{p}\right) \tag{B.20}$$

and obtain therewith

$$\partial_{ij}^2 I \approx \left[\partial_{ij}^2 g + \partial_j g\frac{\partial_i p}{p} + \partial_i g\frac{\partial_j p}{p} + g\left(\partial_i \left(\frac{\partial_j p}{p}\right) + \left(\frac{\partial_i p}{p}\right)\left(\frac{\partial_j p}{p}\right)\right)\right](x_n, y_i, y_j). \tag{B.21}$$

C

Spectrometer Forward Function Derivatives

C.1. Slit Function f Derivatives

1st derivatives

$$\frac{\partial}{\partial \sigma} f(\lambda, \mu, \sigma) = f(\lambda, \mu, \sigma) \left(\frac{(\lambda - \mu)^2}{\sigma^3} - \frac{1}{\sigma} \right) \tag{C.1}$$

$$\frac{\partial}{\partial \mu} f(\lambda, \mu, \sigma) = f(\lambda, \mu, \sigma) \frac{\lambda - \mu}{\sigma^2} \tag{C.2}$$

$$\tag{C.3}$$

2nd derivatives

$$\frac{\partial^2}{\partial \sigma^2} f(\lambda, \mu, \sigma) = f(\lambda, \mu, \sigma) \left(\frac{(\lambda - \mu)^4}{\sigma^6} - \frac{5(\lambda - \mu)^2}{\sigma^4} + \frac{2}{\sigma^2} \right) \tag{C.4}$$

$$\frac{\partial^2}{\partial \mu \partial \sigma} f(\lambda, \mu, \sigma) = f(\lambda, \mu, \sigma) \left(\frac{(\lambda - \mu)^3}{\sigma^5} - \frac{3(\lambda - \mu)}{\sigma^3} \right) \tag{C.5}$$

$$\frac{\partial^2}{\partial \mu^2} f(\lambda, \mu, \sigma) = f(\lambda, \mu, \sigma) \left(\frac{(\lambda - \mu)^2}{\sigma^4} - \frac{1}{\sigma^2} \right) \tag{C.6}$$

C.2. Signal S_n Derivatives

The channel index c is in this section replaced by the index n. 1st derivatives:

$$\frac{\partial S_n}{\partial \eta} = \Delta \lambda \sum_i L(\lambda_i) f(\lambda_i, \mu_n, \sigma_n) \tag{C.7}$$

$$\frac{\partial S_n}{\partial \mu_n} = \Delta \lambda \sum_i \eta(\lambda_i) L(\lambda_i) \frac{\partial f(\lambda_i, \mu_n, \sigma_n)}{\partial \mu_n} \tag{C.8}$$

$$\frac{\partial S_n}{\partial \sigma_n} = \Delta \lambda \sum_i \eta(\lambda_i) L(\lambda_i) \frac{\partial f(\lambda_i, \mu_n, \sigma_n)}{\partial \sigma_n} \tag{C.9}$$

2nd derivatives:

$$\frac{\partial^2 S_n}{\partial \eta^2} = 0 \tag{C.10}$$

$$\frac{\partial^2 S_n}{\partial \mu_n \partial \eta} = \Delta \lambda \sum_i L(\lambda_i) \frac{\partial}{\partial \mu_n} f(\lambda_i, \mu_n, \sigma_n) \tag{C.11}$$

$$\frac{\partial^2 S_n}{\partial \sigma_n \partial \eta} = \Delta \lambda \sum_i L(\lambda_i) \frac{\partial}{\partial \sigma_n} f(\lambda_i, \mu_n, \sigma_n) \tag{C.12}$$

$$\frac{\partial^2 S_n}{\partial \mu_n^2} = \Delta \lambda \sum_i \eta(\lambda_i) L(\lambda_i) \frac{\partial^2 f(\lambda_i, \mu_n, \sigma_n)}{\partial \mu_n^2} \tag{C.13}$$

$$\frac{\partial^2 S_n}{\partial \sigma_n \partial \mu_n} = \Delta \lambda \sum_i \eta(\lambda_i) L(\lambda_i) \frac{\partial^2 f(\lambda_i, \mu_n, \sigma_n)}{\partial \sigma_n \partial \mu_n} \tag{C.14}$$

$$\frac{\partial^2 S_n}{\partial \sigma_n^2} = \Delta \lambda \sum_i \eta(\lambda_i) L(\lambda_i) \frac{\partial^2 f(\lambda_i, \mu_n, \sigma_n)}{\partial \sigma_n^2} \tag{C.15}$$

C.3. $\eta(\lambda)$ Spline Fitting

C.3.1. Constrained Non-Linear Least Square Problem

cost or misfit function: $\chi^2(\vec{x})$ along with the equality constraints $c_n(\vec{x}) = 0$. Lagrange function:

$$L(\vec{x}, \vec{\lambda}) = \chi^2(\vec{x}) + \sum_n \lambda_n c_n(\vec{x}) = \chi^2(\vec{x}) + \vec{\lambda}^T \vec{C}(\vec{x}) \tag{C.16}$$

for minimizing χ^2 it is necessary that

$$\vec{\nabla}_{\vec{x}} L(\vec{x}, \vec{\lambda}) = \vec{\nabla}_{\vec{x}} \chi^2(\vec{x}) + \vec{\lambda}^T \left(\vec{\nabla}_{\vec{x}} \vec{C}(\vec{x}) \right) = \vec{0} \tag{C.17}$$

the solution $\vec{x}_*$ must satisfy:

$$\lim_{\vec{\lambda} \to \infty} L(\vec{x}_*, \vec{\lambda}) = \chi^2(\vec{x}_*) \tag{C.18}$$

So during the fit/minimization process the constraint strength/weight can be controlled by the Lagrange multipliers. The contribution ratio of the λ-normalised constraints and the unconstrained cost function to the Lagrange function is:

$$R(\vec{x}) = \frac{\sum_n \lambda_n c_n(\vec{x})}{\chi^2(\vec{x}) \sqrt{\sum_n \lambda_n^2}} \tag{C.19}$$

This ratio could be modelled with the overal relative convergence rate so:

$$R_i = \frac{L_{i-1} - L_i}{L_i} \tag{C.20}$$

The Lagrange multiplier are kept

$$\lambda_{i,n} \geq \lambda_{\min} \quad \text{and} \quad \sqrt{\sum_n \lambda_{i,n}^2} = \frac{L(\vec{x}_i, \vec{\lambda}_i) \sum_n \lambda_{i,n} c_n(\vec{x}_i)}{\chi^2(\vec{x}_i)(L(\vec{x}_i, \vec{\lambda}_i) - L(\vec{x}_{i-1}, \vec{\lambda}_{i-1}))} \tag{C.21}$$

C.3.2. Spline Fitting

spline:

$$s_k(x) = \sum_{n=0}^{3} s_{k,n}(x - \xi_k)^n = s_{k,0} + s_{k,1}(x - \xi_k) + s_{k,2}(x - \xi_k)^2 + s_{k,3}(x - \xi_k)^3 \tag{C.22}$$

$$\frac{d}{dx} s_k(x) = s_{k,1} + 2s_{k,2}(x - \xi_k) + 3s_{k,3}(x - \xi_k)^2 \tag{C.23}$$

$$\frac{d^2}{dx^2} s_k(x) = 2s_{k,2} + 6s_{k,3}(x - \xi_k) \tag{C.24}$$

cost function:

$$\chi^2 = \lambda_a \left(\frac{d^2}{dx^2} s_0(\xi_0) \right)^2 \tag{C.25}$$

$$+ \sum_{m=1}^{M} \sum_{k=0}^{N-1} \Theta_k(x_m)(s_k(x_m) - y_m)^2 \tag{C.26}$$

$$+ \sum_{k=0}^{N-2} \sum_{j=0}^{2} \lambda_{kj} \left(\frac{d^j}{dx^j} s_k(\xi_{k+1}) - \frac{d^j}{dx^j} s_{k+1}(\xi_{k+1}) \right)^2 \tag{C.27}$$

$$+ \lambda_b \left(\frac{d^2}{dx^2} s_{N-1}(\xi_N) \right)^2 \tag{C.28}$$

with

$$\Theta_k(x) = \begin{cases} 1 & \text{if } x \in [\xi_k, \xi_{k+1}] \\ 0 & \text{else} \end{cases} \tag{C.29}$$

in detail:

$$
\begin{aligned}
\chi^2 \;=\;& \lambda_a(2s_{0,2})^2 && \text{(C.30)}\\
+\;& \sum_{m=1}^{M}\sum_{k=0}^{N-1}\Theta_k(x_m)\bigl(s_{k,0}+s_{k,1}(x_m-\xi_k)+s_{k,2}(x_m-\xi_k)^2+s_{k,3}(x_m-\xi_k)^3-y_m\bigr)^2 && \text{(C.31)}\\
+\;& \sum_{k=0}^{N-2} && \\
& \{ \\
& \quad \lambda_{k,0}\left(s_{k,0}+s_{k,1}(\xi_{k+1}-\xi_k)+s_{k,2}(\xi_{k+1}-\xi_k)^2+s_{k,3}(\xi_{k+1}-\xi_k)^3-s_{k+1,0}\right)^2 && \text{(C.32)}\\
& \quad \lambda_{k,1}\left(s_{k,1}+2s_{k,2}(\xi_{k+1}-\xi_k)+3s_{k,3}(\xi_{k+1}-\xi_k)^2-s_{k+1,1}\right)^2 && \text{(C.33)}\\
& \quad \lambda_{k,2}\left(2s_{k,2}+6s_{k,3}(\xi_{k+1}-\xi_k)-2s_{k+1,2}\right)^2 && \text{(C.34)}\\
& \} \\
+\;& \lambda_b(2s_{N-1,2}+6s_{N-1,3}(\xi_N-\xi_{N-1}))^2 && \text{(C.35)}
\end{aligned}
$$

C.3.3. Jacobians and Hessian

helpers:

$$
\begin{aligned}
\Delta x_{k,m} &= x_m-\xi_k && \text{(C.36)}\\
\Delta y_{k,m} &= s_k(x_m)-y_m && \text{(C.37)}\\
\Delta \xi_k &= \xi_{k+1}-\xi_k && \text{(C.38)}
\end{aligned}
$$

$$
\begin{aligned}
C_{k,0} &= s_{k,0}+s_{k,1}(\xi_{k+1}-\xi_k)+s_{k,2}(\xi_{k+1}-\xi_k)^2+s_{k,3}(\xi_{k+1}-\xi_k)^3-s_{k+1,0} && \text{(C.39)}\\
C_{k,1} &= s_{k,1}+2s_{k,2}(\xi_{k+1}-\xi_k)+3s_{k,3}(\xi_{k+1}-\xi_k)^2-s_{k+1,1} && \text{(C.40)}\\
C_{k,2} &= 2s_{k,2}+6s_{k,3}(\xi_{k+1}-\xi_k)-2s_{k+1,2} && \text{(C.41)}
\end{aligned}
$$

$$
\frac{d\chi^2}{ds_{0,0}} = 2\sum_{m=1}^{M}\Theta_0(x_m)\Delta y_{0,m}+2\lambda_{0,0}C_{0,0} \tag{C.42}
$$

$$
\begin{aligned}
\frac{d^2\chi^2}{ds_{0,0}ds_{0,0}} &= 2\sum_{m=1}^{M}\Theta_0(x_m)+2\lambda_{0,0} && \text{(C.43)}\\
\frac{d^2\chi^2}{ds_{0,1}ds_{0,0}} &= 2\sum_{m=1}^{M}\Theta_0(x_m)\Delta x_{0,m}+2\lambda_{0,0}\Delta\xi_0 && \text{(C.44)}\\
\frac{d^2\chi^2}{ds_{0,2}ds_{0,0}} &= 2\sum_{m=1}^{M}\Theta_0(x_m)\Delta x_{0,m}^2+2\lambda_{0,0}\Delta\xi_0^2 && \text{(C.45)}\\
\frac{d^2\chi^2}{ds_{0,3}ds_{0,0}} &= 2\sum_{m=1}^{M}\Theta_0(x_m)\Delta x_{0,m}^3+2\lambda_{0,0}\Delta\xi_0^3 && \text{(C.46)}\\
\frac{d^2\chi^2}{d\lambda_{0,0}ds_{0,0}} &= 2C_{0,0} && \text{(C.47)}\\
\frac{d^2\chi^2}{ds_{1,0}ds_{0,0}} &= -2\lambda_{0,0} && \text{(C.48)}
\end{aligned}
$$

$$
\frac{d\chi^2}{ds_{0,1}} = 2\sum_{m=1}^{M}\Theta_0(x_m)\Delta y_{0,m}\Delta x_{0,m}+2\lambda_{0,0}C_{0,0}\Delta\xi_0+2\lambda_{0,1}C_{0,1} \tag{C.49}
$$

$$\frac{d^2\chi^2}{ds_{0,0}ds_{0,1}} = 2\sum_{m=1}^{M}\Theta_0(x_m)\Delta x_{0,m}+2\lambda_{0,0}\Delta\xi_0 \tag{C.50}$$

$$\frac{d^2\chi^2}{ds_{0,1}ds_{0,1}} = 2\sum_{m=1}^{M}\Theta_0(x_m)\Delta x_{0,m}^2+2\lambda_{0,0}\Delta\xi_0^2 + 2\lambda_{0,1} \tag{C.51}$$

$$\frac{d^2\chi^2}{ds_{0,2}ds_{0,1}} = 2\sum_{m=1}^{M}\Theta_0(x_m)\Delta x_{0,m}^3+2\lambda_{0,0}\Delta\xi_0^3 + 4\lambda_{0,1}\Delta\xi_0 \tag{C.52}$$

$$\frac{d^2\chi^2}{ds_{0,3}ds_{0,1}} = 2\sum_{m=1}^{M}\Theta_0(x_m)\Delta x_{0,m}^4+2\lambda_{0,0}\Delta\xi_0^4 + 6\lambda_{0,1}\Delta\xi_0^2 \tag{C.53}$$

$$\frac{d^2\chi^2}{d\lambda_{0,0}ds_{0,1}} = 2C_{0,0}\Delta\xi_0 \tag{C.54}$$

$$\frac{d^2\chi^2}{d\lambda_{0,1}ds_{0,1}} = 2C_{0,1} \tag{C.55}$$

$$\frac{d^2\chi^2}{ds_{1,0}ds_{0,1}} = -2\lambda_{0,0}\Delta\xi_0 \tag{C.56}$$

$$\frac{d^2\chi^2}{ds_{1,1}ds_{0,1}} = -2\lambda_{0,1} \tag{C.57}$$

$$\frac{d\chi^2}{ds_{0,2}} = 8\lambda_a s_{0,2} + 2\sum_{m=1}^{M}\Theta_0(x_m)\Delta y_{0,m}\Delta x_{0,m}^2+2\lambda_{0,0}C_{0,0}\Delta\xi_0^2+4\lambda_{0,1}C_{0,1}\Delta\xi_0+4\lambda_{0,2}C_{0,2} \tag{C.58}$$

$$\frac{d^2\chi^2}{d\lambda_a ds_{0,2}} = 8s_{0,2} \tag{C.59}$$

$$\frac{d^2\chi^2}{ds_{0,0}ds_{0,2}} = 2\sum_{m=1}^{M}\Theta_0(x_m)\Delta x_{0,m}^2+2\lambda_{0,0}\Delta\xi_0^2 \tag{C.60}$$

$$\frac{d^2\chi^2}{ds_{0,1}ds_{0,2}} = 2\sum_{m=1}^{M}\Theta_0(x_m)\Delta x_{0,m}^3+2\lambda_{0,0}\Delta\xi_0^3 + 4\lambda_{0,1}\Delta\xi_0 \tag{C.61}$$

$$\frac{d^2\chi^2}{ds_{0,2}ds_{0,2}} = 8\lambda_a+2\sum_{m=1}^{M}\Theta_0(x_m)\Delta x_{0,m}^4+2\lambda_{0,0}\Delta\xi_0^4 + 8\lambda_{0,1}\Delta\xi_0^2 + 8\lambda_{0,2} \tag{C.62}$$

$$\frac{d^2\chi^2}{ds_{0,3}ds_{0,2}} = 2\sum_{m=1}^{M}\Theta_0(x_m)\Delta x_{0,m}^5+2\lambda_{0,0}\Delta\xi_0^5 + 12\lambda_{0,1}\Delta\xi_0^3 + 24\lambda_{0,2}\Delta\xi_0 \tag{C.63}$$

$$\frac{d^2\chi^2}{d\lambda_{0,0}ds_{0,2}} = 2C_{0,0}\Delta\xi_0^2 \tag{C.64}$$

$$\frac{d^2\chi^2}{d\lambda_{0,1}ds_{0,2}} = 4C_{0,1}\Delta\xi_0 \tag{C.65}$$

$$\frac{d^2\chi^2}{d\lambda_{0,2}ds_{0,2}} = 4C_{0,2} \tag{C.66}$$

$$\frac{d^2\chi^2}{ds_{1,0}ds_{0,2}} = -2\lambda_{0,0}\Delta\xi_0^2 \tag{C.67}$$

$$\frac{d^2\chi^2}{ds_{1,1}ds_{0,2}} = -4\lambda_{0,1}\Delta\xi_0 \tag{C.68}$$

$$\frac{d^2\chi^2}{ds_{1,2}ds_{0,2}} = -8\lambda_{0,2} \tag{C.69}$$

$$\frac{d\chi^2}{ds_{0,3}} = 2\sum_{m=1}^{M}\Theta_0(x_m)\Delta y_{0,m}\Delta x_{0,m}^3+2\lambda_{0,0}C_{0,0}\Delta\xi_0^3+6\lambda_{0,1}C_{0,1}\Delta\xi_0^2+12\lambda_{0,2}C_{0,2}\Delta\xi_0 \tag{C.70}$$

CHAPTER C: SPECTROMETER FORWARD FUNCTION DERIVATIVES

$$\frac{d^2\chi^2}{ds_{0,0}ds_{0,3}} \quad = \quad 2\sum_{m=1}^{M} \Theta_0(x_m)\Delta x_{0,m}^3 + 2\lambda_{0,0}\Delta\zeta_0^3 \tag{C.71}$$

$$\frac{d^2\chi^2}{ds_{0,1}ds_{0,3}} \quad = \quad 2\sum_{m=1}^{M} \Theta_0(x_m)\Delta x_{0,m}^4 + 2\lambda_{0,0}\Delta\zeta_0^4 + 6\lambda_{0,1}\Delta\zeta_0^2 \tag{C.72}$$

$$\frac{d^2\chi^2}{ds_{0,2}ds_{0,3}} \quad = \quad 2\sum_{m=1}^{M} \Theta_0(x_m)\Delta x_{0,m}^5 + 2\lambda_{0,0}\Delta\zeta_0^5 + 12\lambda_{0,1}\Delta\zeta_0^3 + 24\lambda_{0,2}\Delta\zeta_0 \tag{C.73}$$

$$\frac{d^2\chi^2}{ds_{0,3}ds_{0,3}} \quad = \quad 2\sum_{m=1}^{M} \Theta_0(x_m)\Delta x_{0,m}^6 + 2\lambda_{0,0}\Delta\zeta_0^6 + 18\lambda_{0,1}\Delta\zeta_0^4 + 72\lambda_{0,2}\Delta\zeta_0^2 \tag{C.74}$$

$$\frac{d^2\chi^2}{d\lambda_{0,0}ds_{0,3}} \quad = \quad 2C_{0,0}\Delta\zeta_0^3 \tag{C.75}$$

$$\frac{d^2\chi^2}{d\lambda_{0,1}ds_{0,3}} \quad = \quad 6C_{0,1}\Delta\zeta_0^2 \tag{C.76}$$

$$\frac{d^2\chi^2}{d\lambda_{0,2}ds_{0,3}} \quad = \quad 12C_{0,2}\Delta\zeta_0 \tag{C.77}$$

$$\frac{d^2\chi^2}{ds_{1,0}ds_{0,3}} \quad = \quad -2\lambda_{0,0}\Delta\zeta_0^3 \tag{C.78}$$

$$\frac{d^2\chi^2}{ds_{1,1}ds_{0,3}} \quad = \quad -6\lambda_{0,1}\Delta\zeta_0^2 \tag{C.79}$$

$$\frac{d^2\chi^2}{ds_{1,2}ds_{0,3}} \quad = \quad -24\lambda_{0,2}\Delta\zeta_0 \tag{C.80}$$

$$\frac{d\chi^2}{ds_{k,0}} \overset{k\in[1,...,N-2]}{=} 2\sum_{m=1}^{M} \Theta_k(x_m)\Delta y_{k,m} + 2\lambda_{k,0}C_{k,0} - 2\lambda_{k-1,0}C_{k-1,0} \tag{C.81}$$

$$\frac{d^2\chi^2}{ds_{k-1,0}ds_{k,0}} \overset{k\in[1,...,N-2]}{=} -2\lambda_{k-1,0} \tag{C.82}$$

$$\frac{d^2\chi^2}{ds_{k-1,1}ds_{k,0}} \overset{k\in[1,...,N-2]}{=} -2\lambda_{k-1,0}\Delta\zeta_{k-1} \tag{C.83}$$

$$\frac{d^2\chi^2}{ds_{k-1,2}ds_{k,0}} \overset{k\in[1,...,N-2]}{=} -2\lambda_{k-1,0}\Delta\zeta_{k-1}^2 \tag{C.84}$$

$$\frac{d^2\chi^2}{ds_{k-1,3}ds_{k,0}} \overset{k\in[1,...,N-2]}{=} -2\lambda_{k-1,0}\Delta\zeta_{k-1}^3 \tag{C.85}$$

$$\frac{d^2\chi^2}{d\lambda_{k-1,0}ds_{k,0}} \overset{k\in[1,...,N-2]}{=} -2C_{k-1,0} \tag{C.86}$$

$$\frac{d^2\chi^2}{ds_{k,0}ds_{k,0}} \overset{k\in[1,...,N-2]}{=} 2\sum_{m=1}^{M} \Theta_k(x_m) + 2\lambda_{k,0} + 2\lambda_{k-1,0} \tag{C.87}$$

$$\frac{d^2\chi^2}{ds_{k,1}ds_{k,0}} \overset{k\in[1,...,N-2]}{=} 2\sum_{m=1}^{M} \Theta_k(x_m)\Delta x_{k,m} + 2\lambda_{k,0}\Delta\zeta_k \tag{C.88}$$

$$\frac{d^2\chi^2}{ds_{k,2}ds_{k,0}} \overset{k\in[1,...,N-2]}{=} 2\sum_{m=1}^{M} \Theta_k(x_m)\Delta x_{k,m}^2 + 2\lambda_{k,0}\Delta\zeta_k^2 \tag{C.89}$$

$$\frac{d^2\chi^2}{ds_{k,3}ds_{k,0}} \overset{k\in[1,...,N-2]}{=} 2\sum_{m=1}^{M} \Theta_k(x_m)\Delta x_{k,m}^3 + 2\lambda_{k,0}\Delta\zeta_k^3 \tag{C.90}$$

$$\frac{d^2\chi^2}{d\lambda_{k,0}ds_{k,0}} \overset{k\in[1,...,N-2]}{=} 2C_{k,0} \tag{C.91}$$

$$\frac{d^2\chi^2}{ds_{k+1,0}ds_{k,0}} \overset{k\in[1,...,N-2]}{=} -2\lambda_{k,0} \tag{C.92}$$

$$\frac{d\chi^2}{ds_{k,1}} \overset{k\in[1,...,N-2]}{=} 2\sum_{m=1}^{M} \Theta_k(x_m)\Delta y_{k,m}\Delta x_{k,m} + 2\lambda_{k,0}C_{k,0}\Delta\zeta_k + 2\lambda_{k,1}C_{k,1} - 2\lambda_{k-1,1}C_{k-1,1} \tag{C.93}$$

CHAPTER C: SPECTROMETER FORWARD FUNCTION DERIVATIVES

$$\frac{d^2\chi^2}{ds_{k-1,1}ds_{k,1}} \stackrel{k\in[1,...,N-2]}{=} -2\lambda_{k-1,1} \tag{C.94}$$

$$\frac{d^2\chi^2}{ds_{k-1,2}ds_{k,1}} \stackrel{k\in[1,...,N-2]}{=} -4\lambda_{k-1,1}\Delta\tilde{\zeta}_{k-1} \tag{C.95}$$

$$\frac{d^2\chi^2}{ds_{k-1,3}ds_{k,1}} \stackrel{k\in[1,...,N-2]}{=} -6\lambda_{k-1,1}\Delta\tilde{\zeta}_{k-1}^2 \tag{C.96}$$

$$\frac{d^2\chi^2}{d\lambda_{k-1,1}ds_{k,1}} \stackrel{k\in[1,...,N-2]}{=} -2C_{k-1,1} \tag{C.97}$$

$$\frac{d^2\chi^2}{ds_{k,0}ds_{k,1}} \stackrel{k\in[1,...,N-2]}{=} 2\sum_{m=1}^{M}\Theta_k(x_m)\Delta x_{k,m}+2\lambda_{k,0}\Delta\tilde{\zeta}_k \tag{C.98}$$

$$\frac{d^2\chi^2}{ds_{k,1}ds_{k,1}} \stackrel{k\in[1,...,N-2]}{=} 2\sum_{m=1}^{M}\Theta_k(x_m)\Delta x_{k,m}^2+2\lambda_{k,0}\Delta\tilde{\zeta}_k^2 + 2\lambda_{k,1}+2\lambda_{k-1,1} \tag{C.99}$$

$$\frac{d^2\chi^2}{ds_{k,2}ds_{k,1}} \stackrel{k\in[1,...,N-2]}{=} 2\sum_{m=1}^{M}\Theta_k(x_m)\Delta x_{k,m}^3+2\lambda_{k,0}\Delta\tilde{\zeta}_k^3 + 4\lambda_{k,1}\Delta\tilde{\zeta}_k \tag{C.100}$$

$$\frac{d^2\chi^2}{ds_{k,3}ds_{k,1}} \stackrel{k\in[1,...,N-2]}{=} 2\sum_{m=1}^{M}\Theta_k(x_m)\Delta x_{k,m}^4+2\lambda_{k,0}\Delta\tilde{\zeta}_k^4 + 6\lambda_{k,1}\Delta\tilde{\zeta}_k^2 \tag{C.101}$$

$$\frac{d^2\chi^2}{d\lambda_{k,0}ds_{k,1}} \stackrel{k\in[1,...,N-2]}{=} 2C_{k,0}\Delta\tilde{\zeta}_k \tag{C.102}$$

$$\frac{d^2\chi^2}{d\lambda_{k,1}ds_{k,1}} \stackrel{k\in[1,...,N-2]}{=} 2C_{k,1} \tag{C.103}$$

$$\frac{d^2\chi^2}{ds_{k+1,0}ds_{k,1}} \stackrel{k\in[1,...,N-2]}{=} -2\lambda_{k,0}\Delta\tilde{\zeta}_k \tag{C.104}$$

$$\frac{d^2\chi^2}{ds_{k+1,1}ds_{k,1}} \stackrel{k\in[1,...,N-2]}{=} -2\lambda_{k,1} \tag{C.105}$$

$$\frac{d\chi^2}{ds_{k,2}} \stackrel{k\in[1,...,N-2]}{=} 2\sum_{m=1}^{M}\Theta_k(x_m)\Delta y_{k,m}\Delta x_{k,m}^2+2\lambda_{k,0}C_{k,0}\Delta\tilde{\zeta}_k^2+4\lambda_{k,1}C_{k,1}\Delta\tilde{\zeta}_k+4\lambda_{k,2}C_{k,2}-4\lambda_{k-1,2}C_{k-1,2} \tag{C.106}$$

$$\frac{d^2\chi^2}{ds_{k-1,2}ds_{k,2}} \stackrel{k\in[1,...,N-2]}{=} -8\lambda_{k-1,2} \tag{C.107}$$

$$\frac{d^2\chi^2}{ds_{k-1,3}ds_{k,2}} \stackrel{k\in[1,...,N-2]}{=} -24\lambda_{k-1,2}\Delta\tilde{\zeta}_{k-1} \tag{C.108}$$

$$\frac{d^2\chi^2}{d\lambda_{k-1,2}ds_{k,2}} \stackrel{k\in[1,...,N-2]}{=} -4C_{k-1,2} \tag{C.109}$$

$$\frac{d^2\chi^2}{ds_{k,0}ds_{k,2}} \stackrel{k\in[1,...,N-2]}{=} 2\sum_{m=1}^{M}\Theta_k(x_m)\Delta x_{k,m}^2+2\lambda_{k,0}\Delta\tilde{\zeta}_k^2 \tag{C.110}$$

$$\frac{d^2\chi^2}{ds_{k,1}ds_{k,2}} \stackrel{k\in[1,...,N-2]}{=} 2\sum_{m=1}^{M}\Theta_k(x_m)\Delta x_{k,m}^3+2\lambda_{k,0}\Delta\tilde{\zeta}_k^3 + 4\lambda_{k,1}\Delta\tilde{\zeta}_k \tag{C.111}$$

$$\frac{d^2\chi^2}{ds_{k,2}ds_{k,2}} \stackrel{k\in[1,...,N-2]}{=} 2\sum_{m=1}^{M}\Theta_k(x_m)\Delta x_{k,m}^4+2\lambda_{k,0}\Delta\tilde{\zeta}_k^4 + 8\lambda_{k,1}\Delta\tilde{\zeta}_k^2 + 8\lambda_{k,2}+8\lambda_{k-1,2} \tag{C.112}$$

$$\frac{d^2\chi^2}{ds_{k,3}ds_{k,2}} \stackrel{k\in[1,...,N-2]}{=} 2\sum_{m=1}^{M}\Theta_k(x_m)\Delta x_{k,m}^5+2\lambda_{k,0}\Delta\tilde{\zeta}_k^5 + 12\lambda_{k,1}\Delta\tilde{\zeta}_k^3 + 24\lambda_{k,2}\Delta\tilde{\zeta}_k \tag{C.113}$$

$$\frac{d^2\chi^2}{d\lambda_{k,0}ds_{k,2}} \stackrel{k\in[1,...,N-2]}{=} 2C_{k,0}\Delta\tilde{\zeta}_k^2 \tag{C.114}$$

$$\frac{d^2\chi^2}{d\lambda_{k,1}ds_{k,2}} \stackrel{k\in[1,...,N-2]}{=} 4C_{k,1}\Delta\tilde{\zeta}_k \tag{C.115}$$

$$\frac{d^2\chi^2}{d\lambda_{k,2}ds_{k,2}} \stackrel{k\in[1,...,N-2]}{=} 4C_{k,2} \tag{C.116}$$

$$\frac{d^2\chi^2}{ds_{k+1,0}ds_{k,2}} \stackrel{k\in[1,...,N-2]}{=} -2\lambda_{k,0}\Delta\tilde{\zeta}_k^2 \tag{C.117}$$

$$\frac{d^2\chi^2}{ds_{k+1,1}ds_{k,2}} \stackrel{k\in[1,...,N-2]}{=} -4\lambda_{k,1}\Delta\tilde{\zeta}_k \tag{C.118}$$

$$\frac{d^2\chi^2}{ds_{k+1,2}ds_{k,2}} \stackrel{k\in[1,...,N-2]}{=} -8\lambda_{k,2} \tag{C.119}$$

$$\frac{d\chi^2}{ds_{k,3}} \overset{k\in[1,...,N-2]}{=} 2\sum_{m=1}^{M} \Theta_k(x_m)\Delta y_{k,m}\Delta x_{k,m}^3 + 2\lambda_{k,0}C_{k,0}\Delta\xi_k^3 + 6\lambda_{k,1}C_{k,1}\Delta\xi_k^2 + 12\lambda_{k,2}C_{k,2}\Delta\xi_k \tag{C.120}$$

$$\frac{d^2\chi^2}{ds_{k,0}ds_{k,3}} \overset{k\in[1,...,N-2]}{=} 2\sum_{m=1}^{M} \Theta_k(x_m)\Delta x_{k,m}^3 + 2\lambda_{k,0}\Delta\xi_k^3 \tag{C.121}$$

$$\frac{d^2\chi^2}{ds_{k,1}ds_{k,3}} \overset{k\in[1,...,N-2]}{=} 2\sum_{m=1}^{M} \Theta_k(x_m)\Delta x_{k,m}^4 + 2\lambda_{k,0}\Delta\xi_k^4 + 6\lambda_{k,1}\Delta\xi_k^2 \tag{C.122}$$

$$\frac{d^2\chi^2}{ds_{k,2}ds_{k,3}} \overset{k\in[1,...,N-2]}{=} 2\sum_{m=1}^{M} \Theta_k(x_m)\Delta x_{k,m}^5 + 2\lambda_{k,0}\Delta\xi_k^5 + 12\lambda_{k,1}\Delta\xi_k^3 + 24\lambda_{k,2}\Delta\xi_k \tag{C.123}$$

$$\frac{d^2\chi^2}{ds_{k,3}ds_{k,3}} \overset{k\in[1,...,N-2]}{=} 2\sum_{m=1}^{M} \Theta_k(x_m)\Delta x_{k,m}^6 + 2\lambda_{k,0}\Delta\xi_k^6 + 18\lambda_{k,1}\Delta\xi_k^4 + 72\lambda_{k,2}\Delta\xi_k^2 \tag{C.124}$$

$$\frac{d^2\chi^2}{d\lambda_{k,0}ds_{k,3}} \overset{k\in[1,...,N-2]}{=} 2C_{k,0}\Delta\xi_k^3 \tag{C.125}$$

$$\frac{d^2\chi^2}{d\lambda_{k,1}ds_{k,3}} \overset{k\in[1,...,N-2]}{=} 6C_{k,1}\Delta\xi_k^2 \tag{C.126}$$

$$\frac{d^2\chi^2}{d\lambda_{k,2}ds_{k,3}} \overset{k\in[1,...,N-2]}{=} 12C_{k,2}\Delta\xi_k \tag{C.127}$$

$$\frac{d^2\chi^2}{ds_{k+1,0}ds_{k,3}} \overset{k\in[1,...,N-2]}{=} -2\lambda_{k,0}\Delta\xi_k^3 \tag{C.128}$$

$$\frac{d^2\chi^2}{ds_{k+1,1}ds_{k,3}} \overset{k\in[1,...,N-2]}{=} -6\lambda_{k,1}\Delta\xi_k^2 \tag{C.129}$$

$$\frac{d^2\chi^2}{ds_{k+1,2}ds_{k,3}} \overset{k\in[1,...,N-2]}{=} -24\lambda_{k,2}\Delta\xi_k \tag{C.130}$$

$$\frac{d\chi^2}{ds_{N-1,0}} = 2\sum_{m=1}^{M} \Theta_{N-1}(x_m)\Delta y_{N-1,m} - 2\lambda_{N-2,0}C_{N-2,0} \tag{C.131}$$

$$\frac{d^2\chi^2}{ds_{N-2,0}ds_{N-1,0}} = -2\lambda_{N-2,0} \tag{C.132}$$

$$\frac{d^2\chi^2}{ds_{N-2,1}ds_{N-1,0}} = -2\lambda_{N-2,0}\Delta\xi_{N-2} \tag{C.133}$$

$$\frac{d^2\chi^2}{ds_{N-2,2}ds_{N-1,0}} = -2\lambda_{N-2,0}\Delta\xi_{N-2}^2 \tag{C.134}$$

$$\frac{d^2\chi^2}{ds_{N-2,3}ds_{N-1,0}} = -2\lambda_{N-2,0}\Delta\xi_{N-2}^3 \tag{C.135}$$

$$\frac{d^2\chi^2}{d\lambda_{N-2,0}ds_{N-1,0}} = -2C_{N-2,0} \tag{C.136}$$

$$\frac{d^2\chi^2}{ds_{N-1,0}ds_{N-1,0}} = 2\sum_{m=1}^{M} \Theta_{N-1}(x_m) + 2\lambda_{N-2,0} \tag{C.137}$$

$$\frac{d^2\chi^2}{ds_{N-1,1}ds_{N-1,0}} = 2\sum_{m=1}^{M} \Theta_{N-1}(x_m)\Delta x_{N-1,m} \tag{C.138}$$

$$\frac{d^2\chi^2}{ds_{N-1,2}ds_{N-1,0}} = 2\sum_{m=1}^{M} \Theta_{N-1}(x_m)\Delta x_{N-1,m}^2 \tag{C.139}$$

$$\frac{d^2\chi^2}{ds_{N-1,3}ds_{N-1,0}} = 2\sum_{m=1}^{M} \Theta_{N-1}(x_m)\Delta x_{N-1,m}^3 \tag{C.140}$$

$$\frac{d\chi^2}{ds_{N-1,1}} = 2\sum_{m=1}^{M} \Theta_{N-1}(x_m)\Delta y_{N-1,m}\Delta x_{N-1,m} - 2\lambda_{N-2,1}C_{N-2,1} \tag{C.141}$$

$$\frac{d^2\chi^2}{ds_{N-2,1}ds_{N-1,1}} = -2\lambda_{N-2,1} \tag{C.142}$$

$$\frac{d^2\chi^2}{ds_{N-2,2}ds_{N-1,1}} = -4\lambda_{N-2,1}\Delta\zeta_{N-2} \tag{C.143}$$

$$\frac{d^2\chi^2}{ds_{N-2,3}ds_{N-1,1}} = -6\lambda_{N-2,1}\Delta\zeta_{N-2}^2 \tag{C.144}$$

$$\frac{d^2\chi^2}{d\lambda_{N-2,1}ds_{N-1,1}} = -2C_{N-2,1} \tag{C.145}$$

$$\frac{d^2\chi^2}{ds_{N-1,0}ds_{N-1,1}} = 2\sum_{m=1}^{M}\Theta_{N-1}(x_m)\Delta x_{N-1,m} \tag{C.146}$$

$$\frac{d^2\chi^2}{ds_{N-1,1}ds_{N-1,1}} = 2\sum_{m=1}^{M}\Theta_{N-1}(x_m)\Delta x_{N-1,m}^2 + 2\lambda_{N-2,1} \tag{C.147}$$

$$\frac{d^2\chi^2}{ds_{N-1,2}ds_{N-1,1}} = 2\sum_{m=1}^{M}\Theta_{N-1}(x_m)\Delta x_{N-1,m}^3 \tag{C.148}$$

$$\frac{d^2\chi^2}{ds_{N-1,3}ds_{N-1,1}} = 2\sum_{m=1}^{M}\Theta_{N-1}(x_m)\Delta x_{N-1,m}^4 \tag{C.149}$$

$$\tag{C.150}$$

$$\frac{d\chi^2}{ds_{N-1,2}} = 2\sum_{m=1}^{M}\Theta_{N-1}(x_m)\Delta y_{N-1,m}\Delta x_{N-1,m}^2 - 4\lambda_{N-2,2}C_{N-2,2} + 4\lambda_b(2s_{N-1,2}+6s_{N-1,3}\Delta\zeta_{N-1}) \tag{C.151}$$

$$\frac{d^2\chi^2}{ds_{N-2,2}ds_{N-1,2}} = -8\lambda_{N-2,2} \tag{C.152}$$

$$\frac{d^2\chi^2}{ds_{N-2,3}ds_{N-1,2}} = -24\lambda_{N-2,2}\Delta\zeta_{N-2} \tag{C.153}$$

$$\frac{d^2\chi^2}{d\lambda_{N-2,2}ds_{N-1,2}} = -4C_{N-2,2} \tag{C.154}$$

$$\frac{d^2\chi^2}{ds_{N-1,0}ds_{N-1,2}} = 2\sum_{m=1}^{M}\Theta_{N-1}(x_m)\Delta x_{N-1,m}^2 \tag{C.155}$$

$$\frac{d^2\chi^2}{ds_{N-1,1}ds_{N-1,2}} = 2\sum_{m=1}^{M}\Theta_{N-1}(x_m)\Delta x_{N-1,m}^3 \tag{C.156}$$

$$\frac{d^2\chi^2}{ds_{N-1,2}ds_{N-1,2}} = 2\sum_{m=1}^{M}\Theta_{N-1}(x_m)\Delta x_{N-1,m}^4 + 8\lambda_{N-2,2} + 8\lambda_b \tag{C.157}$$

$$\frac{d^2\chi^2}{ds_{N-1,3}ds_{N-1,2}} = 2\sum_{m=1}^{M}\Theta_{N-1}(x_m)\Delta x_{N-1,m}^5 + 24\lambda_b\Delta\zeta_{N-1} \tag{C.158}$$

$$\frac{d^2\chi^2}{d\lambda_b ds_{N-1,2}} = 4(2s_{N-1,2}+6s_{N-1,3}\Delta\zeta_{N-1}) \tag{C.159}$$

$$\tag{C.160}$$

$$\frac{d\chi^2}{ds_{N-1,3}} = 2\sum_{m=1}^{M}\Theta_{N-1}(x_m)\Delta y_{N-1,m}\Delta x_{N-1,m}^3 + 12\lambda_b(2s_{N-1,2}+6s_{N-1,3}\Delta\zeta_{N-1})\Delta\zeta_{N-1} \tag{C.161}$$

$$\frac{d\chi^2}{ds_{N-1,0}ds_{N-1,3}} = 2\sum_{m=1}^{M}\Theta_{N-1}(x_m)\Delta x_{N-1,m}^3 \tag{C.162}$$

$$\frac{d\chi^2}{ds_{N-1,1}ds_{N-1,3}} = 2\sum_{m=1}^{M}\Theta_{N-1}(x_m)\Delta x_{N-1,m}^4 \tag{C.163}$$

$$\frac{d\chi^2}{ds_{N-1,2}ds_{N-1,3}} = 2\sum_{m=1}^{M}\Theta_{N-1}(x_m)\Delta x_{N-1,m}^5 + 24\lambda_b\Delta\zeta_{N-1} \tag{C.164}$$

$$\frac{d\chi^2}{ds_{N-1,3}ds_{N-1,3}} = 2\sum_{m=1}^{M}\Theta_{N-1}(x_m)\Delta x_{N-1,m}^6 + 72\lambda_b\Delta\zeta_{N-1}^2 \tag{C.165}$$

$$\frac{d\chi^2}{d\lambda_b ds_{N-1,3}} = 12(2s_{N-1,2}+6s_{N-1,3}\Delta\zeta_{N-1})\Delta\zeta_{N-1} \tag{C.166}$$

$$\frac{d\chi^2}{d\lambda_a} = 4s_{02}^2 \tag{C.167}$$

$$\frac{d^2\chi^2}{ds_{02}d\lambda_a} = 8s_{02} \tag{C.168}$$

$$\frac{d\chi^2}{d\lambda_{k,0}} \stackrel{k\in[0,...,N-2]}{=} \left(s_{k,0} + s_{k,1}\Delta\zeta_k + s_{k,2}\Delta\zeta_k^2 + s_{k,3}\Delta\zeta_k^3 - s_{k+1,0}\right)^2 \tag{C.169}$$

$$\frac{d^2\chi^2}{ds_{k,0}d\lambda_{k,0}} \stackrel{k\in[0,...,N-2]}{=} 2C_{k,0} \tag{C.170}$$

$$\frac{d^2\chi^2}{ds_{k,1}d\lambda_{k,0}} \stackrel{k\in[0,...,N-2]}{=} 2C_{k,0}\Delta\zeta_k \tag{C.171}$$

$$\frac{d^2\chi^2}{ds_{k,2}d\lambda_{k,0}} \stackrel{k\in[0,...,N-2]}{=} 2C_{k,0}\Delta\zeta_k^2 \tag{C.172}$$

$$\frac{d^2\chi^2}{ds_{k,3}d\lambda_{k,0}} \stackrel{k\in[0,...,N-2]}{=} 2C_{k,0}\Delta\zeta_k^3 \tag{C.173}$$

$$\frac{d^2\chi^2}{ds_{k+1,0}d\lambda_{k,0}} \stackrel{k\in[0,...,N-2]}{=} -2C_{k,0} \tag{C.174}$$

$$\frac{d\chi^2}{d\lambda_{k,1}} \stackrel{k\in[0,...,N-2]}{=} \left(s_{k,1} + 2s_{k,2}\Delta\zeta_k + 3s_{k,3}\Delta\zeta_k^2 - s_{k+1,1}\right)^2 \tag{C.175}$$

$$\frac{d^2\chi^2}{ds_{k,1}d\lambda_{k,1}} \stackrel{k\in[0,...,N-2]}{=} 2C_{k,1} \tag{C.176}$$

$$\frac{d^2\chi^2}{ds_{k,2}d\lambda_{k,1}} \stackrel{k\in[0,...,N-2]}{=} 4C_{k,1}\Delta\zeta_k \tag{C.177}$$

$$\frac{d^2\chi^2}{ds_{k,3}d\lambda_{k,1}} \stackrel{k\in[0,...,N-2]}{=} 6C_{k,1}\Delta\zeta_k^2 \tag{C.178}$$

$$\frac{d^2\chi^2}{ds_{k+1,1}d\lambda_{k,1}} \stackrel{k\in[0,...,N-2]}{=} -2C_{k,1} \tag{C.179}$$

$$\frac{d\chi^2}{d\lambda_{k,2}} \stackrel{k\in[0,...,N-2]}{=} \left(2s_{k,2} + 6s_{k,3}\Delta\zeta_k - 2s_{k+1,2}\right)^2 \tag{C.180}$$

$$\frac{d^2\chi^2}{ds_{k,2}d\lambda_{k,2}} \stackrel{k\in[0,...,N-2]}{=} 4C_{k,2} \tag{C.181}$$

$$\frac{d^2\chi^2}{ds_{k,3}d\lambda_{k,2}} \stackrel{k\in[0,...,N-2]}{=} 12C_{k,2}\Delta\zeta_k \tag{C.182}$$

$$\frac{d^2\chi^2}{ds_{k+1,2}d\lambda_{k,2}} \stackrel{k\in[0,...,N-2]}{=} -4C_{k,2} \tag{C.183}$$

$$\frac{d\chi^2}{d\lambda_b} = \left(2s_{N-1,2} + 6s_{N-1,3}\Delta\zeta_{N-1}\right)^2 \tag{C.184}$$

$$\frac{d^2\chi^2}{ds_{N-1,2}d\lambda_b} = 4\left(2s_{N-1,2} + 6s_{N-1,3}\Delta\zeta_{N-1}\right) \tag{C.185}$$

$$\frac{d^2\chi^2}{ds_{N-1,3}d\lambda_b} = 12\left(2s_{N-1,2} + 6s_{N-1,3}\Delta\zeta_{N-1}\right)\Delta\zeta_{N-1} \tag{C.186}$$

Bibliography

[Bates, 1984] Bates, D. (1984). Rayleigh scattering by air. *Planet. Space Sc.*, 32, No.6:785–790.

[Ben-Dor et al., 2013] Ben-Dor, E., Schläpfer, D., Plaza, A. J., and Malthus, T. (2013). *Hyperspectral Remote Sensing*, pages 413–456. Wiley-VCH Verlag GmbH & Co. KGaA.

[Bodhaine et al., 1999] Bodhaine, B. A., Wood, N. B., Dutton, E. G., and Slusser, J. R. (1999). On rayleigh optical depth calculations. *Journal of Atmospheric and Oceanic Technology*, 16(11):1854–1861.

[Bussemer, 1993] Bussemer, M. (1993). Der ring effekt: Ursachen und einfluss auf die spektrokopische messung stratosphärischer spurenstoffe. Master's thesis, University of Heidelberg.

[Caballero, 2006] Caballero (2006). Existence of solutions of an integral equation chandrasekhar type in the theory of radiative transfer. *Electronic Journal of Differential Equations*, 57:1–11. ISSN: 1072-6691.

[Cahalan et al., 2005] Cahalan, R., Oreopoulos, L., Marshak, A., Evans, K., Davis, A., Pincus, R., Yetzer, K., Mayer, B., Davies, R., Barker, T. A. H., Clothiaux, E., Ellingson, R., Garay, M., Assianov, E. K., Kinne, S., Macker, A., O'Hirok, W., Partain, P., Prigarin, S., Rublev, A., Stephens, G., Szczap, F., Takara, E., Várnai, T., Wen, G., and Zhuravleva, T. (2005). The international intercomparison of 3d radiation codes (i3rc): Bringing together the most advanced radiative transfer tools for cloudy atmospheres. *Bull. Amer. Meteor. Soc.*, 86 (9):1275–1293.

[Chance and Kurucz, 2010] Chance, K. and Kurucz, R. L. (2010). An improved high-resolution solar reference spectrum for earth's atmosphere measurements in the ultraviolet, visible, and near infrared. *J. Quant. Spec. Rad. Trans.*, 111:1289–1295.

[Chance and Spurr, 1997] Chance, K. and Spurr, R. (1997). Ring effect studies: Rayleigh scattering, including molecular parameters for rotational raman scattering, and the fraunhofer spectrum. *Appl. Opt.*, 36:5224–5230.

[Chandrasekhar, 1960] Chandrasekhar, S. (1960). *Radiative Transfer*. Dover, New York.

[Chapman, 1930] Chapman, S. (1930). A theory of upper atmosphere ozone. *Mem. R. Meteorol. Soc.*, 3:103–125.

[Ciddor, 1996] Ciddor, P. (1996). Refractive index of air: new equations for the visible and near infrared. *Appl. Opt.*, 35:1566–1573.

[Clarke and Kapustin, 2010] Clarke, A. and Kapustin, V. (2010). Hemispheric aerosol vertical profiles: Anthropogenic impacts on optical depth and cloud nuclei. *Science*, 329(5998):1488–1492.

[Cornet et al., 2010] Cornet, C., Szczap, F., and C-Labonnote, L. (2010). Three-dimensional polarized monte carlo atmospheric radiative transfer model (3dmcpol): 3d effects on polarized visible reflectances of a cirrus cloud. *J. Quant. Spec. Rad. Trans.*, 111:174–186.

[Davis and Marshak, 2010] Davis, A. and Marshak, A. (2010). Solar radiation transport in the cloudy atmosphere: a 3d perspective on observations and climate impacts. *Reports on progress in Physics*, 73:026801pp.

[Deutschmann, 2009] Deutschmann, T. (2009). Atmospheric radiative transfer modelling with monte carlo methods. Master's thesis, University of Heidelberg.

[Deutschmann et al., 2011] Deutschmann, T., Beirle, S., Frieß, U., Grzegorski, M., Kern, C., Kritten, L., Platt, U., Prados-Román, C., Puķīte, J., Wagner, T., Werner, B., and Pfeilsticker, K. (2011). The monte carlo atmospheric radiative transfer model mcartim: Introduction and validation of jacobians and 3d features. *Journal of Quantitative Spectroscopy and Radiative Transfer*, 112(6):1119 – 1137.

[Draine and Flatau, 1994] Draine, B. T. and Flatau, P. J. (1994). Discrete-dipole approximation for scattering calculations. *J. Opt. Soc. Am. A*, 11(4):1491–1499.

[Eberhard, 2010] Eberhard, W. L. (2010). Correct equations and common approximations for calculating rayleigh scatter in pure gases and mixtures and evaluation of differences. *Appl. Opt.*, 49(7):1116–1130.

[Emde et al., 2010] Emde, C., Buras, R., Mayer, B., and Blumthaler, M. (2010). The impact of aerosols on polarized sky radiance: model development, validation and applications. *Atmos. Chem. Phys.*, 10:383–396.

[Eötvös, 1886] Eötvös, L. (1886). "". *Annalen der Physik*, 27:448.

[Frankenberg, 2004] Frankenberg, C. (2004). *Retrieval of methane and carbon monoxide using near infrared spectra recorded by SCIAMACHY onboard ENVISAT, Algorithm development and data analysis*. PhD thesis, University of Heidelberg.

[Funk, 2000] Funk, O. (2000). *Photon Pathlengths Distributions for Cloudy Skies - Oxygen A-Band Measurements and Radiative Transfer Model Calculations*. PhD thesis, University of Heidelberg.

[Gilardoni et al., 2011] Gilardoni, S., Vignati, E., Marmer, E., Cavalli, F., Belis, C., Gianelle, V., Loureiro, A., and Artaxo, P. (2011). Sources of carbonaceous aerosol in the amazon basin. *Atmospheric Chemistry and Physics*, 11(6):2747–2764.

[Goody and Yung, 1989] Goody, R. and Yung, Y. (1989). *Atmospheric Radiation - Theoretical Basis*. Oxford University Press.

[Grainger and Ring, 1962] Grainger, J. and Ring, J. (1962). Anomalous fraunhofer line profiles. *Nature London*, 193:762pp.

[Green and Mira, 1999] Green, P. J. and Mira, A. (1999). Delayed rejection in reversible jump metropolis-hastings. *Biometrika*, 88:1035–1053.

[Guo et al., 2010] Guo, Z., Li, Z., Farquhar, J., Kaufman, A. J., Wu, N., Li, C., Dickerson, R. R., and Wang, P. (2010). Identification of sources and formation processes of atmospheric sulfate by sulfur isotope and scanning electron microscope measurements. *J. Geophys. Res.*, 115:D00K07.

[Haken and Wolf, 2006] Haken, H. and Wolf, H. C. (2006). Molekülphysik und quantenchemie.

[Hastings, 1970] Hastings, W. K. (1970). Monte carlo sampling methods using markov chains and their applications. *Biometrika*, 57(1):97–109.

[Henyey and Greenstein, 1941] Henyey, L. and Greenstein, J. (1941). Diffuse radiation in the galaxy. *J. Astrophys.*, 93:70–83.

[Hoffmann et al., 2007] Hoffmann, T., Zetsch, C., and Rossi, M., J. (2007). Chemie von aerosolen. *Chemie Unserer Zeit*, 41:232–246.

[Hohm and Kerl, 1990] Hohm, U. and Kerl, K. (1990). Interferometric measurements of the dipole polarizability α of molecules between 300 k and 1100 k. *Molecular Physics*, 69(5):803–817.

[Hollas, 2004] Hollas, J. M. (2004). *Modern Spectroscopy*. Wiley, Chichester, England, 4 edition.

[Hovenier et al., 2004] Hovenier, J., van der Mee, C., and Domke, H., editors (2004). *Transfer of Polarized Light in Planetary Atmospheres, Basic Concepts and Practical Methods.* Kluwer Academic.

[Huffman and Bohren, 1983] Huffman, C. and Bohren, D. (1983). *Absorption and Scattering of Light by Small Particles*. John Wiley and Sons, New York.

[Hönninger et al., 2004] Hönninger, G., von Friedeburg, C., and Platt, U. (2004). Multi axis differential optical absorption spectroscopy (max-doas). *Atmos. Chem. Phys.*, 4:231–254.

[Joiner et al., 1995] Joiner, J., Bhartia, P. K., Cebula, R. P., Hilsenrath, E., McPeters, R. D., and Park, H. (1995). Rotational raman scattering (ring effect) in satellite backscatter ultraviolet measurements. *Appl. Opt.*, 34(21):4513–4525.

[Kahn, 1950] Kahn, H. (1950). Random sampling (monte carlo) techniques in neutron attenuation problems. *Nucleonics*, 6(5,6).

[Kattawar et al., 1981] Kattawar, G., Young, A., and Humphreys, T. (1981). Inelastic scattering in planetary atmospheres i. the ring effect without aerosols. *J. Astrophys.*, 243(3):1049–1057.

[Kattawar et al., 1973] Kattawar, G. W., Hitzfelder, S. J., and Binstock, J. (1973). An explicit form of the mie phase matrix for multiple scattering calculations in the i, q, u and v representation. *Journal of the Atmospheric Sciences*, 30(2):289–295.

[Kern et al., 2012] Kern, C., Deutschmann, T., Werner, C., Sutton, A. J., Elias, T., and Kelly, P. J. (2012). Improving the accuracy of so2column densities and emission rates obtained from upward-looking uv-spectroscopic measurements of volcanic plumes by taking realistic radiative transfer into account. *Journal of Geophysical Research: Atmospheres*, 117(D20):2156–2202.

[Kokhanovsky et al., 2010] Kokhanovsky, A., Budak, V., Cornet, C., Duan, M., Emde, C., Katsev, I., Klyukov, D., Korkin, S., C-Labonnote, L., Mayer, B., Min, Q., Nakajima, T., Ota, Y., Prikhach, A., Rozanov, V., Yokota, T., and Zege, E. (2010). Benchmark results in vector atmospheric radiative transfer. *J. Quant. Spec. Rad. Trans.*, 111:1931–1946.

[Koponen, 2003] Koponen, I. (2003). *Observation of Tropospheric Aerosol Size Distributions*. PhD thesis, University of Helsinki.

[Kraus, 2005] Kraus, S. (2005). *DOASIS: A framework design for DOAS*. PhD thesis, University of Mannheim.

[Kylling et al., 2010] Kylling, A., Mayer, B., and Blumthaler, M. (2010). Technical note: Cloud and aerosol effects on rotational raman scattering: measurement comparisons and sensitivity studies. *Atmospheric Chemistry and Physics Discussions*, 10(10):22515–22552.

[Lacis et al., 1998] Lacis, A., Chowdhary, J., Mishchenko, M., and Cairns, B. (1998). Modeling errors in diffuse-sky radiation: vector vs. scalar treatment. *Geophys. Res. Lett.*, 25:135–138.

[Landgraf et al., 2004] Landgraf, J., Hasekamp, O., van Deelen, R., and Aben, I. (2004). Rotational raman scattering of polarized light in the earth atmosphere: a vector radiative transfer model using the radiative transfer pertubation theory approach. *J. Quant. Spec. Rad. Trans.*, 87:399–433.

[Li et al., 2010] Li, W., Shao, L., Wang, Z., Shen, R., Yang, S., and Tang, U. (2010). Size, composition, and mixing state of individual aerosol particles in a south china coastal city. *Journal of Environmental Sciences*, 22(4):561 – 569.

[Liou, 1980] Liou, K.-N. (1980). Chapter 3 {ABSORPTION} {AND} {SCATTERING} {OF} {SOLAR} {RADIATION} {IN} {THE} {ATMOSPHERE}. In Liou, K.-N., editor, *An Introduction to Atmospheric Radiation*, volume 26 of *International Geophysics*, pages 50 – 86. Academic Press.

[Liu et al., 2000] Liu, J. S., Liang, F., and Wong, W. H. (2000). The multiple-try method and local optimization in metropolis sampling. *Journal of the American Statistical Association*, 95(449):121–134.

[Liu and Weng, 2006] Liu, Q. and Weng, F. (2006). Advanced doubling: Adding method for radiative transfer in planetary atmospheres. *Journal of the Atmospheric Sciences*, 63(12):3459–3465.

[Marchuk et al., 1976] Marchuk, G., Mikhailov, G., Nazaraliev, M., Darbinyan, R., Kargin, B., and Elepov, B. (1976). *Monte-Carlo Method in Atmospheric Optics*. Springer.

[Marshak and Davis, 2005] Marshak, A. and Davis, A. (2005). *3D Radiative Transfer in Cloudy Atmospheres*. Springer.

[Mayer, B., 2009] Mayer, B. (2009). Radiative transfer in the cloudy atmosphere. *EPJ Web of Conferences*, 1:75–99.

[Metropolis et al., 1953] Metropolis, N., Rosenbluth, A. W., Rosenbluth, M. N., Teller, A. H., and Teller, E. (1953). Equation of State Calculations by Fast Computing Machines. *jcp*, 21:1087–1092.

[Mie, 1908] Mie, G. (1908). Beiträge zur optik trüber medien, speziell kolloidaler metallösungen. *Annalen der Physik*, 25:377–445.

[Mishchenko, 2002] Mishchenko, M. (2002). Vector radiative transfer equation for arbitrarily shaped and arbitrarily oriented particles: a microphysical derivation from statistical electromagnetics. *Appl. Opt.*, 41:7114–7134.

[Mishchenko, 2003] Mishchenko, M. (2003). Microphysical approach to polarized radiative transfer: extension to the case of an external observation point. *Appl. Opt.*, 42:4963–4967.

[Mishchenko, 2008] Mishchenko, M. (2008). Multiple scattering, radiative transfer and weak localisation in discrete random media: Unified microphysical approach. *Rev. Geophys.*, 46:RG2003.

[Mishchenko, 2009] Mishchenko, M. (2009). Gustav mie and the fundamental concept of electromagnetic scattering by particles: a perspective. *J. Quant. Spec. Rad. Trans.*, 110:1210–1222.

[Mishchenko et al., 2006] Mishchenko, M., Travis, L., and Lacis, A. (2006). *Multiple Scattering of Light by Particles: Radiative Transfer and Coherent Backscattering*. Cambridge University Press.

[Mishchenko et al., 1996] Mishchenko, M. I., Travis, L. D., and Mackowski, D. W. (1996). T-matrix computations of light scattering by nonspherical particles: A review. *Journal of Quantitative Spectroscopy and Radiative Transfer*, 55(5):535 – 575. Light Scattering by Non-Spherical Particles.

[M.Vountas et al., 1998] M.Vountas, Rozanov, V., and Burrows, J. (1998). Ring effect: Impact of rotational raman scattering on radiative transfer in earth's atmosphere. *J. Quant. Spec. Rad. Trans.*, 60(6):943 – 961.

[Nolting, 1997] Nolting, W. (1997). *Grundkurs Theoretische Physik 3 Elektrodynamik*. Friedr. Vieweg & Sohn Verlagsgesellschaft, Braunschweig/Wiesbaden.

[Norval et al., 2007] Norval, M., Cullen, A. P., de Gruijl, F. R., Longstreth, J., Takizawa, Y., Lucas, R. M., Noonan, F. P., and van der Leun, J. C. (2007). The effects on human health from stratospheric ozone depletion and its interactions with climate change. *Photochem. Photobiol. Sci.*, 6:232–251.

[O'Dowd et al., 2012] O'Dowd, C., Ceburnis, D., Ovadnevaite, J., Martucci, G., Bialek, J., Monahan, C. ., Berresheim, H., Vaishya, A., Grigas, T., Jennings, S. G., McVeigh, P., Varghese, S. ., Flanagan, R., Martin, D., Moran, E., Lambkin, K., Semmler, T., Perrino, C., and McGrath, R. (2012). The eyjafjallajökull ash plume - part i: Physical, chemical and optical characteristics. *Atmospheric Environment*, 48(0):129 – 142.

[O'Hirok and Gautier, 1998] O'Hirok, W. and Gautier, C. (1998). A three-dimensional rradiative transfer model to investigate the solar radiation within a cloudy atmosphere. part i: Spatial effects. *J. Atmos. Sci.*, 55:2162–2179.

[Pallamraju et al., 2000] Pallamraju, D., Baumgardner, J., and Chakrabarti, S. (2000). A multiwavelength investigation of the ring effect in the day sky spectrum. *Geophys. Res. Lett.*, 27(13):1875–1878.

[Penney et al., 1974] Penney, C., Peters, R. S., and Lapp, M. (1974). Absolute rotational raman cross sections for n2, o2, and co2. *Opt. Soc. Am.*, 64:712–716.

[Pincus and Evans, 2009] Pincus, R. and Evans, K. (2009). Computational cost and accuracy in calculating three-dimensional radiative transfer: Results for new implementations of monte carlo and shdom. *J. Atmos. Sci.*, 66:3131–3146.

[Placzek and Teller, 1933] Placzek, G. and Teller, E. (1933). Die rotationsstruktur der ramanbanden mehratomiger moleküle. *Zeitschrift für Physik*, 81(3-4):209–258.

[Platt and Stutz, 2008] Platt, U. and Stutz, J. (2008). *Differential Optical Absorption Spectroscopy: Principles and Application*. Springer.

[Postylyakov, 2004] Postylyakov, O. (2004). Linearized vector radiative transfer model mcc++ for a spherical atmosphere. *J. Quant. Spec. Rad. Trans.*, 88(1-3):297–317.

[Pruppacher and Klett, 2010] Pruppacher, H. R. and Klett, J. D. (2010). *Microphysics of clouds and precipitation*. Springer, Dordrecht; New York.

[Puķīte et al., 2009] Puķīte, J., Kühl, S., Deutschmann, T., Platt, U., and Wagner, T. (2009). Extending differential optical absorption spectroscopy for limb measurements in the uv. *Atmospheric Measurement Techniques Discussions*, 2(6):2919–2982.

[Ramamoorthi and Hanrahan, 2001] Ramamoorthi, R. and Hanrahan, P. (2001). On the relationship between radiance and irradiance: determining the illumination from images of a convex lambertian object. *J. Opt. Soc. Am. A*, 18(10):2448–2459.

[Rodgers, 2000] Rodgers, C. (2000). *Inverse Methods for Atmospheric Sounding: Theory and Practice*. Series on Atmospheric Oceanic and Planetary Physics, Volume 2. World Scientific Publishing Company, Incorporated.

[Rogers and Yau, 2000] Rogers, R. R. and Yau, M. (2000). *A Short Course in Cloud Physics*, volume 113 of *International Series In Nataural Philosophy*. Pergamon Press.

[Rozanov et al., 2005] Rozanov, A., Rozanov, V., Buchwitz, M., Kokhanovsky, A., and Burrows, J. (2005). Sciatran 2.0 - a new radiative transfer model for geophysical applications in the 175-2400nm spectral region. *Advances in Space Research*, 36(5):1015 – 1019.

[Rozanov and Rozanov, 2010] Rozanov, V. V. and Rozanov, A. V. (2010). Differential optical absorption spectroscopy (doas) and air mass factor concept for a multiply scattering vertically inhomogeneous medium: theoretical consideration. *Atmospheric Measurement Techniques Discussions*, 3(1):697–784.

[Rödel, 2000] Rödel, W. (2000). *Physik unserer Umwelt - Die Atmosphäre*. Springer.

[Schwabl, 2004] Schwabl, F. (2004). *Statitische Mechanik*. Springer Verlag Berlin-Heidelberg.

[Seinfeld and Pandis, 2006] Seinfeld, J. and Pandis, S. (2006). *Atmospheric Chemistry and Physics - From Air Pollution to Climate Change*. John Wiley & Sons.

[Shefov, 1959] Shefov, N. (1959). Spectroscopic, photoelectric, and radar investigations of the aurora and the nightglow. *Izd. Akad. Nauk.*, 1.

[Spurr, 2006] Spurr, R. J. (2006). Vlidort: A linearized pseudo-spherical vector discrete ordinate radiative transfer code for forward model and retrieval studies in multilayer multiple scattering media. *Journal of Quantitative Spectroscopy and Radiative Transfer*, 102(2):316 – 342.

[Stamnes, 1986] Stamnes, K. (1986). The theory of multiple scattering of radiation in plane parallel atmospheres. *Rev. Geophys.*, 24(2):299–310.

[Tarantola, 2005] Tarantola, A. (2005). *Inverse Problem Theory and Methods for Model Parameter Estimation*. SIAM.

[Thomas and Bowman, 1969] Thomas, L. and Bowman, M. (1969). Atmospheric penetration of ultra-violet and visible solar radiations during twilight periods. *Journal of Atmospheric and Terrestrial Physics*, 31(11):1311 – 1322.

[Thuillier et al., 2003] Thuillier, G., Hers´e, M., Labs, D., Foujols, T., Peetermans, W., Gillotay, D., Simon, P., and Mandel, H. (2003). The solar spectral irradiance from 200 to 2400 nm as measured by the solspec spectrometer from the atlas 1-2-3 and eureca missions. *Sol. Phys.*, 214:1–22.

[van Deelen et al., 2005] van Deelen, R., Landgraf, J., and Aben, I. (2005). Multiple elastic and inelastic light scattering in the earth's atmosphere: a doubling-adding method to include rotational raman scattering by air. *J. Quant. Spec. Rad. Trans.*, 95(3):309 – 330.

[Veach and Guibas, 1997] Veach, E. and Guibas, L. J. (1997). Metropolis light transport. In *Computer Graphics (SIGGRAPH '97 Proceedings)*, pages 65–76. Addison Wesley.

[Vogel et al., 2012] Vogel, L., Sihler, H., Lampel, J., Wagner, T., and Platt, U. (2012). Retrieval interval mapping, a tool to optimize the spectral retrieval range in differential optical absorption spectroscopy. *Atmospheric Measurement Techniques Discussions*, 5(3):4195–4247.

[von Neumann, 1951] von Neumann, J. (1951). Various techniques used in connection with random digits. *Nat. Bureau Stand. Appl. Math.*, 12:36–38.

[Vountas et al., 1998] Vountas, M., Rozanov, V., and Burrows, J. (1998). Ring effect: Impact of rotational raman scattering on radiative transfer in earths atmosphere. *J. Quant. Spec. Rad. Trans.*, 60, No. 6:943–961.

[Wagner et al., 2009] Wagner, T., Beirle, S., and Deutschmann, T. (2009). Three-dimensional simulation of the ring effect in observations of scattered sun light using monte carlo radiative transfer models. *Atmos. Meas. Tech.*, 2:113–124.

[Wagner et al., 2011] Wagner, W., Riethmann, T., Feistel, R., and Harvey, A. H. (2011). New equations for the sublimation pressure and melting pressure of h[sub 2]o ice ih. *Journal of Physical and Chemical Reference Data*, 40(4):043103.

[Wendisch et al., 2013] Wendisch, M., Pilewskie, P., Bohn, B., Bucholtz, A., Crewell, S., Harlow, C., Jäkel, E., Schmidt, K. S., Shetter, R., Taylor, J., Turner, D. D., and Zöger, M. (2013). *Atmospheric Radiation Measurements*, pages 343–411. Wiley-VCH Verlag GmbH & Co. KGaA.

[Wendisch and Yang, 2012] Wendisch, M. and Yang, P. (2012). *Theory of atmospheric radiative transfer: a comprehensive introduction*. Physics textbook. Wiley, Singapore.

[Wiscombe, 1979] Wiscombe, W. (1979). Mie scattering calculations: Advances in technique and fast, vector-speed computer codes. Technical note, NCAR.

[Witschas, 2012] Witschas, B. (2012). Light scattering on molecules in the atmosphere. In Schumann, U., editor, *Atmospheric Physics*, Research Topics in Aerospace, pages 69–83. Springer Berlin Heidelberg.

[Young, 1981] Young, A. T. (1981). Rayleigh scattering. *Appl. Opt.*, 20(4):533–535.

[Zieger et al., 2011] Zieger, P., Weingartner, E., Henzing, J., Moerman, M., de Leeuw, G., Mikkilä, J., Ehn, M., Petäjä, T., Clémer, K., van Roozendael, M., Yilmaz, S., Frieß, U., Irie, H., Wagner, T., Shaiganfar, R., Beirle, S., Apituley, A., Wilson, K., and Baltensperger, U. (2011). Comparison of ambient aerosol extinction coefficients obtained from in-situ, max-doas and lidar measurements at cabauw. *Atmospheric Chemistry and Physics*, 11(6):2603–2624.

Index